

**Spectroscopic Investigation of Conformational Transitions  
in the Copper-transporting P1B-ATPase CopA from  
*Legionella pneumophila***

**DISSERTATION**

**zur Erlangung des akademischen Grades  
Doctor rerum naturalium  
(Dr. rer. nat.)**

**Vorgelegt**

**der Fakultät Mathematik und Naturwissenschaften  
der Technischen Universität Dresden**

**Von**

**Ahmed Moustafa Taha Sayed**

geboren am 17.05.1983 in Giza, Egypt

**Gutachter:**

**Prof. Dr. Gerhard Rödel**, TU Dresden

**Prof. Dr. Martin Hof**, J. Heyrovský Institute-Prag

Eingereicht am 10.10.2014

Datum der Verteidigung: 23.03.2015



2015

**This thesis is dedicated to my father's soul who his words of inspiration and encouragement in pursuit of excellence, still linger all the way long.**

## Summary

All cells maintain essential metal nutrients at optimal levels by metal homeostasis. P-type ATPases, a crucial superfamily of integral membrane proteins, are involved in the active transport of metal ions across biological membranes driven by the motive force of ATP- hydrolysis. The P<sub>1B</sub>-type ATPase subfamily, also called CP<sub>X</sub>-ATPases, fulfills a key role in heavy metal homeostasis among the most widespread species from bacteria to human. In humans, the defect in copper transporters is the direct cause of severe neurological and hepatic disorders such as Wilson and Menkes diseases, therefore, understanding the molecular function of these pumps is of paramount importance in human health. Cu<sup>+</sup>-ATPases have two transmembrane metal binding sites (TM-MBS) and three cytosolic domains, namely the actuator (A-domain) and phosphorylation and nucleotide-binding domain (PN), and regulatory N-terminal heavy metal binding domain (HMBD).

Here, we have studied the *Legionella pneumophila* CopA (LpCopA) and its isolated cytosolic domains to improve our understanding of the functional interaction of the protein domains during metal transport relate this to the known structure of this ATPase. To elucidate how cytosolic ligands (Cu<sup>+</sup> and nucleotide) stimulate the interactions among the cytosolic domains and may transmit conformational changes to the TM-MBS, the interactions among recombinant isolated cytosolic domains were first examined biochemically by co-purification and spectroscopically by circular dichroism, time-resolved fluorescence and site-directed fluorescent labeling assays. The Cu<sup>+</sup>-dependent interaction between the A-domain and HMBD has been postulated as a mechanism for activating the ATPase cycle. This question was addressed here by studying copper-dependent interactions between the isolated expressed domains. Spectroscopic evidence is provided that an HMBD-A complex is formed in the presence of Cu<sup>+</sup> which binds with 100-200 nM affinity to the recombinant HMBD. In contrast, the A-domain interacts with the PN domain in a nucleotide-dependent fashion. This molecular recognition is required for the dephosphorylation step in the catalytic cycle. The interaction was investigated in more detail by the use of a decameric peptide derived from the PN-binding interface of the A-domain and carrying the conserved TGE-motif involved in dephosphorylation. Its binding to the isolated PN domain in a weakly nucleotide-dependent manner, is demonstrated here by stopped-flow

fluorescence spectroscopy. Several ATPase assays were modified to assess the functionality of the PN-domain and full length LpCopA. The peptide was found to reduce the catalytic turnover of full length LpCopA. This agrees with the expected slowing down of the reformation of the PN-A-domain interaction since the peptide occupies their binding interface. Thus, the synthetic peptide provides a means to study specifically the influence of PN-A-domain interactions on the structure and function of LpCopA. This was done by time-correlated single photon counting (TCSPC) method. The time-dependent Stokes shift of the environmentally sensitive fluorophore BADAN which was covalently attached to the conserved CPC-motif in the TM-MBS was measured. The data indicate that the interior of the ATPase is hydrated and the mobility of the intra-protein water varies from high to low at C382 at the “luminal side” and C384 at the “cytosolic side” of the TM-MBS, respectively. This finding is consistent with the recent MD simulation of LpCopA, bringing the first experimental evidence on a luminal-open conformation of *E2~P* state. The A-domain-derived decapeptide, although binding to the cytosolic head piece, induces structural changes also at the TM-MBS. The peptide-stabilized state (with a disrupted PN-A interface) renders the C384 environment more hydrophobic as evidenced by TCSPC.

Taken together, the data from cytosolic domain interactions, ATPase assays and of time-dependent Stoke shift analyses of BADAN-labeled LpCopA reveal the presence of hydrated intramembraneous sites whose degree of hydration is regulated by the rearrangement of cytosolic domains, particularly during the association and dissociation of the PN-A domains. Copper affects this arrangement by inducing the linkage of the A-domain to the HMBD. The latter appears to play not only an autoinhibitory but also a chaperone-like role in transferring  $\text{Cu}^+$  to the TM-MBS during catalytic turnover.

## Table of Contents

|                                                                |             |
|----------------------------------------------------------------|-------------|
| <b>SUMMARY</b> .....                                           | <b>3</b>    |
| <b>LIST OF FIGURES</b> .....                                   | <b>I</b>    |
| <b>LIST OF TABLES</b> .....                                    | <b>V</b>    |
| <b>PREFACE</b> .....                                           | <b>VI</b>   |
| <b>ACKNOWLEDGEMENT</b> .....                                   | <b>VII</b>  |
| <b>ABBREVIATIONS</b> .....                                     | <b>VIII</b> |
| <b>CHAPTER 1 INTRODUCTION AND BACKGROUND</b> .....             | <b>1</b>    |
| <b>1.1 COPPER AND LIFE</b> .....                               | <b>1</b>    |
| <b>1.2 ION TRANSPORT IN CELL</b> .....                         | <b>2</b>    |
| <b>1.3 COPPER HOMEOSTASIS IN <i>E. COLI</i> BACTERIA</b> ..... | <b>3</b>    |
| <b>1.4 P-TYPE ATPASE SUPERFAMILY</b> .....                     | <b>4</b>    |
| <b>1.5 STRUCTURAL ASPECTS OF P1B-ATPASES</b> .....             | <b>6</b>    |
| 1.5.1 METAL-BINDING DOMAIN AND CU-CHAPERONES .....             | 9           |
| 1.5.2 PHOSPHORYLATION-/NUCLEOTIDE-BINDING DOMAINS .....        | 13          |
| 1.5.3 ACTUATOR DOMAIN .....                                    | 16          |
| 1.5.4 TRANSMEMBRANE HELICES DOMAIN .....                       | 18          |
| <b>1.6 CATALYTIC MECHANISM OF P-TYPE ATPASES</b> .....         | <b>19</b>   |
| <b>AIM OF THIS STUDY</b> .....                                 | <b>23</b>   |
| <b>CHAPTER 2 MATERIALS AND METHODS</b> .....                   | <b>24</b>   |
| <b>2.1 MATERIALS</b> .....                                     | <b>24</b>   |
| 2.1.1 CULTURE MEDIA AND ANTIBIOTICS.....                       | 24          |
| 2.1.2 OLIGONUCLEOTIDES AND VECTORS.....                        | 25          |
| 2.1.3 DNA CONSTRUCTS.....                                      | 27          |
| 2.1.4 COMMON BUFFERS .....                                     | 28          |
| <b>2.2 MOLECULAR CLONING METHODS</b> .....                     | <b>29</b>   |
| 2.2.1 OLIGONUCLEOTIDES DESIGN .....                            | 29          |
| 2.2.2 POLYMERASE CHAIN REACTIONS .....                         | 29          |
| 2.2.3 AGAROSE GELS .....                                       | 30          |
| 2.2.4 GEL EXTRACTION .....                                     | 30          |
| 2.2.5 DNA CLONING.....                                         | 31          |
| 2.2.5.1 Restriction enzyme digestion.....                      | 31          |
| 2.2.5.2 Ligation.....                                          | 31          |
| 2.2.5.3 Ligation independent cloning (LIC) .....               | 31          |
| 2.2.6 SITE-DIRECTED MUTAGENESIS .....                          | 31          |

|            |                                                                                                    |           |
|------------|----------------------------------------------------------------------------------------------------|-----------|
| 2.2.7      | THE PRODUCTION OF COMPETENT <i>ESCHERICHIA COLI</i> CELLS .....                                    | 32        |
| 2.2.8      | TRANSFORMATION OF COMPETENT <i>ESCHERICHIA COLI</i> DH5A CELLS .....                               | 33        |
| 2.2.8.1    | Glycerol stocks .....                                                                              | 33        |
| <b>2.3</b> | <b>MOLECULAR BIOLOGICAL METHODS .....</b>                                                          | <b>33</b> |
| 2.3.1      | EXPRESSION OF RECOMBINANT PROTEINS .....                                                           | 33        |
| 2.3.2      | PURIFICATION OF HIS-TAGGED CYTOSOLIC DOMAINS .....                                                 | 34        |
| 2.3.3      | PURIFICATION OF STREP-TAGGED CYTOSOLIC DOMAINS.....                                                | 34        |
| 2.3.4      | ANION-EXCHANGE CHROMATOGRAPHY .....                                                                | 35        |
| 2.3.5      | THE SOLUBILIZATION OF MEMBRANE PROTEINS.....                                                       | 35        |
| 2.3.6      | PURIFICATION OF MEMBRANE PROTEINS.....                                                             | 35        |
| 2.3.7      | RECONSTITUTION OF MEMBRANE PROTEIN IN LIPID .....                                                  | 36        |
| 2.3.8      | SDS POLYACRYLAMIDE GEL ELECTROPHORESIS (SDS-PAGE).....                                             | 36        |
| 2.3.9      | PROTEIN CONCENTRATION DETERMINATION.....                                                           | 37        |
| <b>2.4</b> | <b>BIOPHYSICAL AND BIOCHEMICAL ANALYSIS.....</b>                                                   | <b>38</b> |
| 2.4.1      | ATPASE ASSAY .....                                                                                 | 38        |
| 2.4.1.1    | Fluorimetric enzyme-coupled ATPase assay.....                                                      | 38        |
| 2.4.1.2    | Malachite green assay .....                                                                        | 39        |
| 2.4.2      | BCA Cu <sup>+</sup> ASSAY .....                                                                    | 40        |
| 2.4.2.1    | Cu <sup>+</sup> Loading to Proteins.....                                                           | 40        |
| 2.4.2.2    | Cu <sup>+</sup> -Binding Affinity .....                                                            | 40        |
| 2.4.3      | CO-PURIFICATION ASSAY FOR DOMAIN-DOMAIN INTERACTION STUDY.....                                     | 40        |
| 2.4.4      | CIRCULAR DICHROISM MEASUREMENTS .....                                                              | 41        |
| 2.4.4.1    | Secondary structure determination of cytosolic domains .....                                       | 41        |
| 2.4.4.2    | Thermal stability of cytosolic domains with additives.....                                         | 41        |
| 2.4.5      | ISOTHERMAL TITRATION CALORIMETRY (ITC).....                                                        | 42        |
| 2.4.6      | CYSTEINE ACCESSIBILITY ASSAY OF A CPC MOTIF .....                                                  | 42        |
| 2.4.6.1    | Fluorescent CPM Assay.....                                                                         | 42        |
| 2.4.6.2    | Colorimetric 4-DPS assay .....                                                                     | 43        |
| 2.4.7      | STEADY-STATE FLUORESCENCE MEASUREMENTS .....                                                       | 43        |
| 2.4.7.1    | TNP-nucleotides affinity of PN domain.....                                                         | 43        |
| 2.4.7.2    | Interaction of actuator-derived peptides with the PN domain .....                                  | 44        |
| 2.4.7.3    | Binding kinetics of actuator-derived peptides to the PN domain: Stopped-Flow<br>Fluorescence ..... | 44        |
| 2.4.8      | FLUORESCENCE LIFETIME MEASUREMENTS .....                                                           | 44        |
| 2.4.8.1    | Labeling of LpCopAΔHMBD and C384S mutant with BADAN .....                                          | 45        |
| 2.4.8.2    | On-column BADAN labeling of LpCopAΔHMBD and C384S mutant.....                                      | 45        |
| 2.4.8.3    | Time-Correlated Single Photon Counting (TCSPC) measurements.....                                   | 45        |

**CHAPTER 3 EXPRESSION, PURIFICATION AND FUNCTIONAL CHARACTERIZATION OF  
COPPER-TRANSPORTING ATPASE AND ITS CYTOSOLIC DOMAINS FROM *L. PNEUMOPHILA*... 47**

**INTRODUCTION.....47**

**RESULTS AND DISCUSSION.....48**

|            |                                                                        |           |
|------------|------------------------------------------------------------------------|-----------|
| <b>3.1</b> | <b>EXPRESSION AND PURIFICATION OF CYTOSOLIC DOMAINS OF LpCOPA.....</b> | <b>48</b> |
| 3.1.1      | DNA CLONING OF CYTOSOLIC DOMAINS .....                                 | 50        |
| 3.1.2      | EXPRESSION AND PURIFICATION OF CYTOSOLIC DOMAINS .....                 | 52        |
| 3.1.2.1    | The purification of HMBD .....                                         | 52        |
| 3.1.2.2    | Actuator domain purification .....                                     | 54        |
| 3.1.2.3    | Phosphorylation-/Nucleotide-binding domain purification .....          | 55        |

|            |                                                                                                                               |           |
|------------|-------------------------------------------------------------------------------------------------------------------------------|-----------|
| <b>3.2</b> | <b>EXPRESSION OF MEMBRANE PROTEINS .....</b>                                                                                  | <b>59</b> |
| <b>3.3</b> | <b>SOLUBILIZATION AND PURIFICATION MEMBRANE PROTEIN .....</b>                                                                 | <b>62</b> |
| 3.3.1      | CLASSICAL SOLUBILIZATION PROTOCOL .....                                                                                       | 63        |
| 3.3.2      | SARKOSYL-MEDIATED SOLUBILIZATION OF MEMBRANE PROTEINS .....                                                                   | 65        |
| 3.3.3      | DIRECT SOLUBILIZATION .....                                                                                                   | 67        |
| <b>3.4</b> | <b>MEASUREMENTS OF THE CATALYTIC ACTIVITY OF LpCOP<sub>A</sub> AND THE ISOLATED CYTOSOLIC PN DOMAIN <i>IN VITRO</i> .....</b> | <b>69</b> |
| 3.4.1      | USE OF THE LANZETTA ASSAY .....                                                                                               | 69        |
| 3.4.2      | FLUOROMETRIC REAL-TIME MONITOR FOR THE ATPASE ACTIVITY OF LpCOP <sub>A</sub> AND THE PN DOMAIN ..                             | 71        |
| 3.4.2.1    | Cytosolic domain activity .....                                                                                               | 72        |
| 3.4.2.2    | Optimization of the fluorometric ATPase assay for LpCop <sub>A</sub> .....                                                    | 73        |
| 3.4.2.2.1  | The effect of SO <sub>4</sub> <sup>2-</sup> ions on assay performance .....                                                   | 74        |
| 3.4.2.2.2  | The effect of metal ions on assay performance .....                                                                           | 75        |
| 3.4.2.2.3  | The effect of pH on assay performance.....                                                                                    | 75        |
| 3.4.2.3    | Fluorometric ATPase assay of LpCop <sub>A</sub> .....                                                                         | 77        |
|            | <b>SUMMARY AND DISCUSSION.....</b>                                                                                            | <b>78</b> |

**CHAPTER 4 STRUCTURAL AND BIOPHYSICAL CHARACTERIZATION OF THE EXPRESSED CYTOSOLIC DOMAINS FROM *LEGIONELLA PNEUMOPHILA COPA*.....80**

**INTRODUCTION.....80**

**RESULTS AND DISCUSSION.....81**

**4.1 CIRCULAR DICHROISM ANALYSIS OF CYTOSOLIC DOMAINS WITH LIGANDS.....81**

4.1.1 SECONDARY STRUCTURE OF THE EXPRESSED CYTOSOLIC DOMAINS .....

4.1.2 THE CHANGES IN THE STRUCTURAL CONFORMATION OF CYTOSOLIC DOMAIN WITH LIGANDS .....

**4.2 LIGAND BINDING ASSAY OF CYTOSOLIC ASSAY .....**

4.2.1 TNP-NUCLEOTIDES AFFINITY OF PN DOMAIN .....

4.2.2 COPPER(I) AFFINITY OF THE HMBD .....

4.2.3 THERMAL STABILITY OF CYTOSOLIC DOMAINS.....

**SUMMARY AND DISCUSSION .....**

**CHAPTER 5 THE LIGAND-DEPENDENT INTERACTIONS AMONG CYTOSOLIC DOMAINS OF *LEGIONELLA PNEUMOPHILA COPA*.....94**

**INTRODUCTION.....95**

**RESULTS AND DISCUSSION.....96**

**5.1 CO-PURIFICATION ASSAY OF CYTOSOLIC DOMAIN INTERACTIONS .....**

5.1.1 THE HMBD INTERACTS WITH A-DOMAIN IN A COPPER-DEPENDENT MANNER .....

5.1.2 THE HMBD DOES NOT BIND TO THE PN DOMAIN .....

5.1.3 THE CONTROLS FOR THE HMBD CO-PURIFICATION ASSAY.....

5.1.4 CO-PURIFICATION OF PN DOMAIN WITH A-DOMAIN.....

**5.2 FLUOROMETRIC ASSAY OF Cu (I) DEPENDENT INTERACTION OF HMBD WITH A-DOMAIN .....**

5.2.1 THE FLUORESCENT CPM LABELING MONITORED THE DOMAIN-DOMAIN INTERACTION .....

5.2.2 THE FLUORESCENT BADAN LABELING MONITORED THE DOMAIN-DOMAIN INTERACTION .....

|                                                                                                                                                                                     |            |
|-------------------------------------------------------------------------------------------------------------------------------------------------------------------------------------|------------|
| <b>SUMMARY AND DISCUSSION.....</b>                                                                                                                                                  | <b>113</b> |
| <br>                                                                                                                                                                                |            |
| <b>CHAPTER 6 THE STRUCTURAL IMPACT OF MODEL PEPTIDES DERIVED FROM ACTUATOR DOMAIN ON THE CYTOSOLIC HEADPIECE AND THE CPC-MOTIF CONFORMATIONS IN <i>L. PNEUMOPHILA</i> COPA.....</b> | <b>116</b> |
| <br>                                                                                                                                                                                |            |
| <b>INTRODUCTION.....</b>                                                                                                                                                            | <b>116</b> |
| <br>                                                                                                                                                                                |            |
| <b>RESULTS AND DISCUSSION.....</b>                                                                                                                                                  | <b>117</b> |
| <br>                                                                                                                                                                                |            |
| <b>6.1 SYNTHESIS OF ACTUATOR-DERIVED PEPTIDES .....</b>                                                                                                                             | <b>117</b> |
| <b>6.2 THERMAL STABILIZATION OF PN DOMAIN .....</b>                                                                                                                                 | <b>119</b> |
| <b>6.3 FLUOROMETRIC BINDING ASSAY OF PEPTIDE ACT-2 TO PN DOMAIN .....</b>                                                                                                           | <b>122</b> |
| <b>6.4 STOPPED-FLOW KINETICS OF ACT-2 INTERACTION WITH PN DOMAIN .....</b>                                                                                                          | <b>123</b> |
| <b>6.5 THERMODYNAMICS PARAMETERS OF ACT-2/PN DOMAIN INTERACTION .....</b>                                                                                                           | <b>126</b> |
| <b>6.6 THE EFFECT OF ACTUATOR PEPTIDES ON TRANSMEMBRANE HELICES STRUCTURE.....</b>                                                                                                  | <b>128</b> |
| 6.6.1 INHIBITORY EFFECT OF ACTUATOR-DERIVED PEPTIDES ON ATPASE ACTIVITY .....                                                                                                       | 128        |
| 6.6.2 STRUCTURAL IMPACT OF PEPTIDE ACT-1 ON THE CYS384 RESIDUE IN THE CPC MOTIF .....                                                                                               | 130        |
| 6.6.2.1 Fluorometric assay.....                                                                                                                                                     | 130        |
| 6.6.2.2 Colorimetric assay.....                                                                                                                                                     | 134        |
| <br>                                                                                                                                                                                |            |
| <b>SUMMARY AND DISCUSSION.....</b>                                                                                                                                                  | <b>135</b> |
| <br>                                                                                                                                                                                |            |
| <b>CHAPTER 7 TIME-RESOLVED STRUCTURAL DYNAMICS OF THE TRANSMEMBRANE CPC MOTIF IN LPCOPA: TIME-CORRELATED SINGLE-PHOTON COUNTING TECHNIQUE (TCSPC) ..</b>                            | <b>136</b> |
| <br>                                                                                                                                                                                |            |
| <b>INTRODUCTION.....</b>                                                                                                                                                            | <b>136</b> |
| <br>                                                                                                                                                                                |            |
| <b>RESULTS AND DISCUSSION.....</b>                                                                                                                                                  | <b>137</b> |
| <br>                                                                                                                                                                                |            |
| <b>7.1 FLUORESCENCE PROPERTIES OF BADAN DYE: FOR LIFETIME MEASUREMENTS.....</b>                                                                                                     | <b>137</b> |
| <b>7.2 SITE-DIRECTED LABELING OF TRANSMEMBRANE METAL-BINDING SITE .....</b>                                                                                                         | <b>139</b> |
| 7.2.1 BADAN LABELING ASSAY OF LPCOPA MUTANTS.....                                                                                                                                   | 140        |
| 7.2.2 ON-COLUMN BADAN LABELING .....                                                                                                                                                | 142        |
| <b>7.3 RECONSTITUTION OF BADAN-LABELED MEMBRANE PROTEINS .....</b>                                                                                                                  | <b>144</b> |
| <b>7.4 TIME-RESOLVED FLUORESCENCE MEASUREMENTS .....</b>                                                                                                                            | <b>147</b> |
| 7.4.1 THE PRINCIPLE OF TIME-CORRELATED SINGLE PHOTON COUNTING (TCSPC) FLUORESCENCE DECAY LIFETIME .....                                                                             | 147        |
| 7.4.2 SOLVENT RELAXATION AROUND THE CPC MOTIF MEASURED BY TIME CORRELATED SINGLE PHOTON COUNTING .....                                                                              | 149        |
| 7.4.2.1 Time-Resolved Fluorescence measurements of the CPC motif in mixed micelles and liposomes.....                                                                               | 151        |
| 7.4.2.2 Modulation of the water relaxation by functionally relevant ligands.....                                                                                                    | 154        |
| <br>                                                                                                                                                                                |            |
| <b>SUMMARY AND DISCUSSION.....</b>                                                                                                                                                  | <b>160</b> |
| <br>                                                                                                                                                                                |            |
| <b>CHAPTER 8 CONCLUSION AND OUTLOOK .....</b>                                                                                                                                       | <b>162</b> |
| <br>                                                                                                                                                                                |            |
| <b>REFERENCES.....</b>                                                                                                                                                              | <b>166</b> |



## List of Figures

|                                                                                                                                          |    |
|------------------------------------------------------------------------------------------------------------------------------------------|----|
| <b>Figure 1.1.</b> Schematic diagram illustrating the three major types of membrane transport proteins. ....                             | 3  |
| <b>Figure 1.2.</b> Copper homeostasis mechanisms in <i>E. coli</i> . ....                                                                | 4  |
| <b>Figure 1.3.</b> Phylogenetic tree of the P-type-ATPase family. ....                                                                   | 5  |
| <b>Figure 1.4.</b> Topology diagram of LpCopA and SERCA. ....                                                                            | 7  |
| <b>Figure 1.5.</b> Crystal structural model of CopA from <i>Legionella pneumophila</i> . ....                                            | 8  |
| <b>Figure 1.6.</b> Structures of isolated metal-binding domains and Cu-chaperone. ....                                                   | 10 |
| <b>Figure 1.7.</b> Superimposition of HMBD and CopZ from <i>Bacillus subtilis</i> . ....                                                 | 11 |
| <b>Figure 1.8.</b> Proposed mechanism of copper ion transfer to Menkes and Wilson protein. ....                                          | 11 |
| <b>Figure 1.9.</b> A schematic model of CopZ/HMBD interaction mediates the allosteric Cu <sup>+</sup> -ATPase regulation. ....           | 12 |
| <b>Figure 1.10.</b> Crystal structure of PN domain derived from LpCopA structure. ....                                                   | 13 |
| <b>Figure 1.11.</b> Partial sequence alignment of P-/N- domains from archaeal CPx-ATPases. ....                                          | 15 |
| <b>Figure 1.12.</b> Partial sequence alignment of A-domains from archaeal CPx-ATPases. ..                                                | 16 |
| <b>Figure 1.13.</b> Cartoon representation of A-domain of crystal LpCopA structure. ....                                                 | 17 |
| <b>Figure 1.14.</b> A cartoon illustrating the cytosolic domain arrangement in SERCA1 during the reaction cycle. ....                    | 19 |
| <b>Figure 1.15.</b> Post-Albers cycle of P-type ATPases. ....                                                                            | 21 |
| <b>Figure 1.16.</b> Proposed catalytic and transport cycle of Cu <sup>+</sup> -ATPases. ....                                             | 22 |
| <b>Figure 2.1.</b> DNA constructs used for expression of LpCopA and its cytosolic domains. ....                                          | 27 |
| <b>Figure 2.2.</b> Strategy used to introduce mutations via overlap extension PCR. ....                                                  | 32 |
| <b>Figure 2.3.</b> Reaction mechanism of 7-methylguanosine (m <sup>7</sup> Guo) phosphorylation by phosphate liberated from ATPase. .... | 38 |
| <b>Figure 2.4.</b> Structure of TNP-ATP at neutral or basic pH values. ....                                                              | 43 |
| <b>Figure 3.1.</b> The overview of the expressed cytosolic domains. ....                                                                 | 49 |
| <b>Figure 3.2.</b> DNA gel Electrophoresis of the isolated DNA encoding cytosolic LpCopA domains. ....                                   | 51 |
| <b>Figure 3.3.</b> DNA gel Electrophoresis of digested pET28a plasmid. ....                                                              | 51 |
| <b>Figure 3.4.</b> Schematic diagram of 11 kDa Strep-tagged HMBD protein. ....                                                           | 52 |
| <b>Figure 3.5.</b> SDS-PAGE analysis of HMBD expression in 2xYT medium. ....                                                             | 53 |
| <b>Figure 3.6.</b> Schematic diagram of N-terminal 6xHis-tagged A-domain proteins were used in this study. ....                          | 54 |
| <b>Figure 3.7.</b> SDS-PAGE analysis of purified A-domain. ....                                                                          | 54 |
| <b>Figure 3.8.</b> SDS-PAGE analysis of N-terminal His-tagged PN domain purification. ....                                               | 55 |
| <b>Figure 3.9.</b> SDS-PAGE analysis of PN domain stabilization in 6 M urea. ....                                                        | 56 |
| <b>Figure 3.10.</b> Schematic diagram of all recombinant PN domain proteins produced for this study. ....                                | 57 |
| <b>Figure 3.11.</b> SDS-PAGE analysis of C-terminal His-tagged PN domain purification. ....                                              | 58 |
| <b>Figure 3.12.</b> Chromatographic purification of PN domain. ....                                                                      | 59 |
| <b>Figure 3.13.</b> SDS-PAGE analysis of LpCopA expression in different hosts using two induction methods. ....                          | 61 |
| <b>Figure 3.14.</b> SDS-PAGE analysis of LpCopA expression screening with various IPTG concentrations. ....                              | 61 |
| <b>Figure 3.15.</b> A schematic representation of membrane proteins solubilization by detergents. ....                                   | 62 |

---

|                                                                                                                                                 |     |
|-------------------------------------------------------------------------------------------------------------------------------------------------|-----|
| <b>Figure 3.16.</b> SDS-PAGE analysis of N-terminal 6xHis-tagged LpCopA solubilized by typical protocol. ....                                   | 63  |
| <b>Figure 3.17.</b> Western blot analysis of 6x His-tagged LpCopA. ....                                                                         | 64  |
| <b>Figure 3.18.</b> Size-exclusion chromatographic profile of LpCopA purification. ....                                                         | 65  |
| <b>Figure 3.19.</b> SDS-PAGE analysis of Sarkosyl-mediated LpCopA purification. ....                                                            | 66  |
| <b>Figure 3.20.</b> Circular dichroism spectrum of Sarkosyl-solubilized LpCopA. ....                                                            | 67  |
| <b>Figure 3.21.</b> SDS-PAGE analysis of purified membrane proteins prepared using the "direct solubilization" method. ....                     | 68  |
| <b>Figure 3.22.</b> Standard curve of inorganic phosphate measured by Lanzetta assay. ....                                                      | 69  |
| <b>Figure 3.23.</b> Estimated ATPase activity of LpCopA and expressed cytosolic domains. ....                                                   | 70  |
| <b>Figure 3.24.</b> Concentration-dependent calibration of the fluorometric assay using $\text{KH}_2\text{PO}_4$ as a $\text{P}_i$ source. .... | 72  |
| <b>Figure 3.25.</b> Fluorometric ATPase activity of the PN domain. ....                                                                         | 73  |
| <b>Figure 3.26.</b> Comparison of conversion rate of $m^7\text{Guo}$ to $m^7\text{Gua}$ by PNP in chloride and sulfate buffer. ....             | 74  |
| <b>Figure 3.27.</b> Copper ion reduces the bacterial PNP enzyme activity. ....                                                                  | 75  |
| <b>Figure 3.28.</b> pH-dependence of fluorescence spectra of $m^7\text{Guo}$ . ....                                                             | 76  |
| <b>Figure 3.29.</b> pH-dependence of the bacterial PNP enzyme activity. ....                                                                    | 76  |
| <b>Figure 3.30.</b> ATPase activity of LpCopA monitored by the time-dependent fluorometric ATPase assay. ....                                   | 77  |
| <b>Figure 4.1.</b> Secondary structure characterization of LpCopA cytosolic domains. ....                                                       | 82  |
| <b>Figure 4.2.</b> Effect of nucleotides on the CD spectrum of the PN domain. ....                                                              | 83  |
| <b>Figure 4.3.</b> CD spectral changes of the HMBD upon $\text{Cu}^+$ ion binding. ....                                                         | 84  |
| <b>Figure 4.4.</b> Fluorescence change of TNP-nucleotide ( $\lambda_{\text{ex}}$ 408 nm) upon binding to PN domain. ....                        | 86  |
| <b>Figure 4.5.</b> Titration of TNP-nucleotides to $3\mu\text{M}$ PN domain. ....                                                               | 87  |
| <b>Figure 4.6.</b> The BCA competition assay of HMBD copper complex formation. ....                                                             | 88  |
| <b>Figure 4.7.</b> Thermal Denaturation of PN domain was determined by circular dichroism. ....                                                 | 90  |
| <b>Figure 4.8.</b> Thermal denaturation of A-domain. ....                                                                                       | 91  |
| <b>Figure 4.9.</b> PN domain is thermally stabilized by $\text{MgSO}_4$ . ....                                                                  | 92  |
| <b>Figure 5.1.</b> A schematic diagram represents domain-domain co-purification assay. ....                                                     | 96  |
| <b>Figure 5.2.</b> SDS-PAGE analysis of co-purification assay of $\text{Cu}^+$ -free HMBD with A-domain. ....                                   | 98  |
| <b>Figure 5.3.</b> SDS-PAGE analysis of co-purification assay of $\text{Cu}^+$ -loaded HMBD with A-domain. ....                                 | 99  |
| <b>Figure 5.4.</b> SDS-PAGE analysis of PN domain co-purification with HMBD. ....                                                               | 100 |
| <b>Figure 5.5.</b> SDS-PAGE analysis of N-term 6xHis TEV protease co-purified with HMBD as negative control. ....                               | 101 |
| <b>Figure 5.6.</b> SDS-PAGE gel indicates the specificity of Strep-Tactin resin for co-purification assay. ....                                 | 102 |
| <b>Figure 5.7.</b> SDS-PAGE analysis of co-purification of PN domain with A-domain. ....                                                        | 103 |
| <b>Figure 5.8.</b> Superimposition of LpCopA and $\text{Ca}^{2+}$ -ATPase with modulatory nucleotide. ....                                      | 105 |
| <b>Figure 5.9.</b> Cartoon representation shows the orientation of cysteine residues of HMBD in <i>Bacillus subtilis</i> CopA. ....             | 107 |
| <b>Figure 5.10.</b> The emission spectrum of CPM-labeled HMBD is quenched by $\text{Cu}^+$ . ....                                               | 108 |
| <b>Figure 5.11.</b> Fluorometric assay of copper-dependent binding of the CPM-labeled HMBD to the A-domain. ....                                | 109 |

---

---

|                                                                                                                                                                     |     |
|---------------------------------------------------------------------------------------------------------------------------------------------------------------------|-----|
| <b>Figure 5.12.</b> Normalized fluorescence emission spectra of CPM-labeled HMBD with A-domain. ....                                                                | 110 |
| <b>Figure 5.13.</b> Emission spectra of BADAN-labeled HMBD domain binding to Cu <sup>+</sup> and the A-domain. ....                                                 | 111 |
| <b>Figure 5.14.</b> Fluorometric binding assay of Cu <sup>+</sup> -loaded HMBD/BADAN domain with A-domain. ....                                                     | 112 |
| <b>Figure 5.15</b> A schematic diagram shows the difference in the putative HMBD rearrangement in LpCopA and AfCopA upon Cu <sup>+</sup> binding. ....              | 114 |
| <b>Figure 5.16.</b> Schematic diagram shows the classical P-type-ATPase reaction cycle including the interaction among LpCopA cytosolic domains in this study. .... | 115 |
| <b>Figure 6.1.</b> Design of synthetic peptide models derived from Actuator domain. ....                                                                            | 117 |
| <b>Figure 6.2.</b> CD spectrum of Act1 peptide in Phosphate buffer. ....                                                                                            | 118 |
| <b>Figure 6.3.</b> Thermal stabilization of the PN domain by peptide Act-1. ....                                                                                    | 119 |
| <b>Figure 6.4.</b> Trp emission spectra of Act-2 peptide with decreasing in concentration of PN domain. ....                                                        | 122 |
| <b>Figure 6.5.</b> Stopped-flow fluorescence kinetics of peptide Act-2/ PN domain interaction. ....                                                                 | 124 |
| <b>Figure 6.6.</b> The effect of ATP analog on the kinetics of the Act-2/PN domain interaction. ....                                                                | 124 |
| <b>Figure 6.7.</b> Isothermal titration calorimetry (ITC) of peptide Act-2 with 50 μM PN domain. ....                                                               | 127 |
| <b>Figure 6.8.</b> ATPase activity of LpCopA as a function of Act1 peptide. ....                                                                                    | 129 |
| <b>Figure 6.9.</b> ATPase activity of LpCopA with different actuator-driven peptides. ....                                                                          | 129 |
| <b>Figure 6.10.</b> Fluorometric assay of cysteine(s) reactivity of the conserved CPC motif of LpCopAΔHMBD. ....                                                    | 131 |
| <b>Figure 6.11.</b> Fluorescence spectra of thiol reactivity of cysteine at 382 in the C384S mutant. ....                                                           | 132 |
| <b>Figure 6.12.</b> Time course of the peak intensity of the CPM-Cys adduct for LpCopAΔHMBD. ....                                                                   | 133 |
| <b>Figure 6.13.</b> Time course of the peak intensity of the CPM-Cys adduct for the C384S mutant. ....                                                              | 133 |
| <b>Figure 6.14.</b> Time course of thiol reactivity of LpCopAΔHMBD with 4-DPS. ....                                                                                 | 134 |
| <b>Figure 7.1.</b> Previous MD simulations suggest the <i>E2~Pi</i> and <i>E2P</i> states to be open in LpCopA. ....                                                | 136 |
| <b>Figure 7.2.</b> Covalent chemical reaction of thiol residue of a protein with Fluorescent BADAN. ....                                                            | 137 |
| <b>Figure 7.3.</b> Fluorescence emission spectrum of BADAN. ....                                                                                                    | 138 |
| <b>Figure 7.4.</b> Schematic excited level diagram of BADAN. ....                                                                                                   | 139 |
| <b>Figure 7.5.</b> Kinetic assay of BADAN-labeling LpCopAΔHMBD. ....                                                                                                | 140 |
| <b>Figure 7.6.</b> Kinetics of BADAN-labeling C384S mutant. ....                                                                                                    | 141 |
| <b>Figure 7.7.</b> Removal of excess BADAN dye from Ni-NTA column. ....                                                                                             | 142 |
| <b>Figure 7.8.</b> SDS-PAGE analysis of purified BADAN-labeled membrane proteins. ....                                                                              | 143 |
| <b>Figure 7.9.</b> Fluorescence emission spectra of on-column BADAN-labeled C384S mutant and LpCopAΔHMBD. ....                                                      | 144 |
| <b>Figure 7.10.</b> SDS-PAGE analysis of the reconstituted BADAN-labeled LpCopAΔHMBD and C384S mutant. ....                                                         | 145 |
| <b>Figure 7.11.</b> Scheme for proposed Cu <sup>+</sup> -ATPase orientation in liposome. ....                                                                       | 146 |
| <b>Figure 7.12</b> Fluorescence lifetime decay of a fluorophore in the solvent relaxation process. ....                                                             | 148 |
| <b>Figure 7.13.</b> Dipole moment generated upon BADAN excitation. ....                                                                                             | 149 |

---

---

|                                                                                                                                                                       |     |
|-----------------------------------------------------------------------------------------------------------------------------------------------------------------------|-----|
| <b>Figure 7.14.</b> Cartoon diagram represents a proposed location of BADAN in CPC motif. ....                                                                        | 150 |
| <b>Figure 7.15</b> Time-resolved emission spectra (TRES) of LpCopA $\Delta$ HMBD and C384S mutant in detergent micelles solution. ....                                | 151 |
| <b>Figure 7.16</b> TRES comparison between LpCopA $\Delta$ HMBD in liposome and detergent micelles solution .....                                                     | 152 |
| <b>Figure 7.17</b> TRES analysis of BADAN-labeled LpCopA $\Delta$ HMBD with ligands in mixed micelles. ....                                                           | 155 |
| <b>Figure 7.18</b> Fluorescence emission spectra of BADAN-labeled LpCopA $\Delta$ HMBD in mixed micelles. ....                                                        | 156 |
| <b>Figure 7.19</b> TRES analysis of BADAN-labeled C384S mutant with ligands in mixed micelles. ....                                                                   | 157 |
| <b>Figure 7.20</b> TRES analysis of lipid reconstituted BADAN-labeled LpCopA $\Delta$ HMBD with ligands. ....                                                         | 158 |
| <b>Figure 7.21</b> Fluorescence emission spectra of BADAN-labeled LpCopA $\Delta$ HMBD in liposomes. ....                                                             | 159 |
| <b>Figure 7.22.</b> Schematic diagram illustrates the putative BADAN labeling mechanism of the CPC motif and its environments impact on the water distributions. .... | 161 |
| <b>Figure 8.1.</b> Model of cytosolic domain interactions and their influence on membrane domain accessibility for copper and solvent.....                            | 164 |

**List of Tables**

|                                                                                                                 |     |
|-----------------------------------------------------------------------------------------------------------------|-----|
| <b>Table 1.1.</b> Structural characteristics of each subgroup in the P1B-ATPase subfamily...                    | 18  |
| <b>Table 2.1.</b> List of PCR primers, vectors and the fusion tags.....                                         | 25  |
| <b>Table 2.2.</b> The components of PCR reaction. ....                                                          | 29  |
| <b>Table 2.3.</b> Touch-up PCR protocol .....                                                                   | 30  |
| <b>Table 2.4.</b> Preparation of SDS-PAGE gels. ....                                                            | 37  |
| <b>Table.3.1.</b> List of protease inhibitors were used to prevent PN domain degradation. ....                  | 56  |
| <b>Table 4.1.</b> Secondary structure composition of cytosolic domains.....                                     | 85  |
| <b>Table 7.1.</b> Comparison of the membrane proteins orientation in Triton X-100-mediated proteoliposomes..... | 147 |

## Preface

I am pleased to give a short overview of my doctoral research study supported by the Dresden International Graduate School for Biomedicine and Bioengineering (DIGS-BB). The dissertation focuses on the study of the mechanistic properties and structural aspects of P<sub>1B</sub>-type Cu<sup>+</sup>-ATPase from *Legionella pneumophila* (LpCopA) using Molecular biological and spectroscopic techniques. Understanding the molecular function of the bacterial Cu<sup>+</sup>-ATPases (as models) could support in finding therapy for human diseases caused by malfunction of this enzyme. Therefore, I focused on studying the interactions between the cytosolic domains of LpCopA and their implications on opening and closing the ion gate. During this study, I was trying to bring a novel ideology and to use new methodologies. Here, this study utilized a synthetic peptide approach and employed TCSPC method for investigating the cytosolic domains rearrangement in the Albers-Post cycle and the structural aspects of P-type ATPase.

The outcome of this study is divided into five Chapters (3-7). In Chapter 3, the expression and purification of the LpCopA and its cytosolic domains were described with showing the obstacles and the solutions accompanying their production. Also, the functional characterization of proteins is shown. In Chapter 4, the structural aspects and ligand affinity of cytosolic domains were determined. In addition, the Chapter shows how to study the protein stability with ligands using circular dichroism. Chapter 5 shows the interaction between the expressed cytosolic domains, namely heavy metal-binding domain, actuator domain and phosphorylation/nucleotide-binding domains, using the co-purification and fluorometric assays. The data obtained from this study elucidate how cytosolic ligands stimulate the interactions among the cytosolic domains, suggesting new aspects in the classical ATPase cycle of Cu-ATPases.

In Chapter 6, a synthetic peptide derived from a conserved site of actuator domain was designed to investigate the impact of this motif on the structure and function of the LpCopA. The stopped flow fluorescence measurement was carried out Dr. Yixin Zhang's lab in BCUBE–Center for Molecular Bioengineering. In chapter 7, the water distribution around the metal-binding site in transmembrane core of LpCopA was studied by time-correlated single photon counting method. The measurements and data analysis were carried out in our collaborator's lab, Prof. Hof, in the Jaroslav Heyrovsky Institute of Physical Chemistry.

## Acknowledgement

First of all, I am very much indebted to my first supervisor Prof. Karim Fahmy for his excellent guidance throughout the whole process of this work and shared his extensive knowledge with me. Again, I would like to thank him for giving me the opportunity to work in his group and for putting his trust in me. Thanks for many fruitful discussions and enthusiasm.

I would also like to express my thanks for Prof. Martin Hof (the Jaroslav Heyrovsky Institute of Physical Chemistry, Prague) for putting his facilities at my disposal and thanks for his PhD student, Mr. Petr Pospisil, for his efforts in the TCSPC data analysis. Thanks to Dr. Yixin Zhang (BCUBE–Center for Molecular Bioengineering, Dresden) for allowing me to use the stopped flow fluorescence spectrometer in his lab. Special thanks go to Prof. Marc Solioz for supplying us with *E. hirae* CopB and for fruitful discussions during his visits to our lab.

I wish to thank everyone in the DIGS-BB program for supporting my doctoral study, helping me in residence requirements, offering helpful supervision and instructive courses during my PhD study. I appreciate the financial support from DIGS-BB program which contributed to the completion of my project work. Special thanks to Mrs. Carolyn Fritzsche and Mrs. Anja Glenk from international office MPI-CBG, for their unlimited helps to facilitate my staying in Dresden without troubles.

All my gratitude goes to the members of my thesis advisory committee, Prof. Gerhard Rödel, Prof. Petra Schwille and Dr. Mayte Pisabarro for their ideas and suggestions that contributed to the success of this study.

I would like to extend my sincerest thanks to my colleagues and lab mates in Helmholtz-Zentrum Dresden-Rossendorf (HZDR): Prof. Satoru Tsushima, Dr. Jana Oertel, Mrs. Sawsan Abu Sharkh, Ms. Elisabeth Fischermeier, Mrs. Enas Attia, Mrs. Jenny Philipp, Ms. Gisela Gabernet Garriga and my friend, Mr. Mohammed Hassan for existing times and exchanging ideas.

Finally, and not last, I bear a huge gratefulness and love to my dear mom and to my little family for supporting and encouraging me. Special thanks to my wife, Iman El-Balasy, for accompanying me to Dresden and for sharing my life and my scientific journey.

## Abbreviations

|                         |                                                                                            |
|-------------------------|--------------------------------------------------------------------------------------------|
| OD                      | optical density                                                                            |
| 4-DPS                   | 4,4-dithiodipyridine                                                                       |
| 4-TP                    | 4- thiopyridone                                                                            |
| a.u.                    | absorption unit                                                                            |
| A-domain                | actuator domain                                                                            |
| ADP                     | adenosine 5'-diphosphate                                                                   |
| AfCopA                  | Cu <sup>+</sup> -transporting ATPase from <i>Archeoglobusfulgidus</i>                      |
| AppCp                   | β γmethyleneadenosine 5' triphosphate                                                      |
| AppNp                   | adenosine 5'(β, γ imido)triphosphate                                                       |
| ATP                     | adenosine 5'-triphosphate                                                                  |
| ATPγS                   | adenosine 5'-O-(3-thio)triphosphate                                                        |
| BADAN                   | 6-Bromoacetyl-2-Dimethylaminonaphthalene                                                   |
| BCA                     | bicinchonic acid                                                                           |
| BSA                     | bovine serum albumine                                                                      |
| C-MBD                   | C-terminus metal binding domain                                                            |
| CPM                     | 7-Diethylamino-3-(4'-Maleimidylphenyl)-4-Methylcoumarin                                    |
| C-term                  | carboxyl terminus                                                                          |
| Cu <sup>+</sup> -ATPase | Cu <sup>+</sup> -transporting ATPase                                                       |
| CV                      | column volume                                                                              |
| DDM                     | n-Dodecyl β-D-maltoside                                                                    |
| dH2O                    | distilled water                                                                            |
| DMSO                    | dimethylsulfoxide                                                                          |
| DNA                     | deoxyribonucleic acid                                                                      |
| DTT                     | dithiothreitol                                                                             |
| <i>E2</i>               | low-affinity ion binding state                                                             |
| <i>E2~P</i>             | product state of dephosphorylation                                                         |
| <i>E2P</i>              | phosphorylated state                                                                       |
| EDTA                    | ethylenediaminetetraacetic acid                                                            |
| EGTA                    | ethylenebis(oxyethylenenitrilo)tetraacetic acid                                            |
| <i>E1</i>               | high-affinity ion binding state                                                            |
| <i>E1-ADP~P</i>         | transition state of phosphorylation                                                        |
| FPLC                    | fast protein liquid chromatography                                                         |
| HEPES                   | 4-(2-hydroxyethyl)piperazine-1- ethanesulfonic acid                                        |
| HMBD                    | N-terminal heavy metal binding domain                                                      |
| HPLC                    | high performance liquid chromatography                                                     |
| IPTG                    | isopropyl β-D-thiogalactopyranoside                                                        |
| LpCopA                  | <i>legionellapneumophila</i> Cu <sup>+</sup> -ATPase                                       |
| LpCopAΔHMBD             | <i>legionellapneumophila</i> (Heavy-metal biding domain)-truncated Cu <sup>+</sup> -ATPase |
| MD                      | molecular dynamics                                                                         |
| MES                     | 2-(N-morpholino)ethanesulfonic acid                                                        |
| MOPS                    | 3-(N-morpholino)propanesulfonic acid                                                       |
| N-domain                | nucleotide binding domain                                                                  |
| Ni-NTA                  | nickel nitrilotriacetic acid                                                               |
| N-MBD                   | N-terminal metal binding domain                                                            |



|                          |                                                            |
|--------------------------|------------------------------------------------------------|
| N-term                   | amino terminus                                             |
| P <sub>1B</sub> -ATPases | P <sub>1B</sub> -type ATPases                              |
| PAGE                     | polyacrylamide gel electrophoresis                         |
| P-domain                 | phosphorylation domain                                     |
| Pi                       | inorganic phosphate                                        |
| PMSF                     | phenylmethanesulfonyl fluoride                             |
| RT                       | room temperature                                           |
| SDS                      | sodium dodecyl sulfate                                     |
| SERCA                    | sarco(endo)plasmic reticulum Ca <sup>2+</sup> ATPase       |
| TM                       | transmembrane segment                                      |
| TM-MBSs                  | transmembrane metal binding sites                          |
| TNP-AMP                  | 2',3'-O-(2, 4, 6-trinitrophenyl)adenosine 5'-monophosphate |
| TNP-ATP                  | 2', 3'-O-(2, 4, 6-trinitrophenyl)adenosine 5'-triphosphate |
| Tris                     | Tris(hydroxymethyl)aminomethane                            |
| TTM                      | ammonium tetrathiomolybdate                                |
| UV-Vis                   | ultraviolet-visible spectroscopy                           |
| Wt                       | wild type                                                  |
| β-ME                     | beta-mercaptoethanol                                       |



## Chapter 1 Introduction and Background

### 1.1 Copper and Life

Living cells require essential transition metals such as Cu, Fe, Co, Zn, Mn and Mo ions to carry out biological functions. Heavy metals act as cofactors for enzymatic reactions including group transfer, redox and hydrolysis. It has been reported that more than a quarter of the known enzymes require a particular metal ion for full catalytic activity[1]. These enzymes can be classified into metalloenzymes and metal-activated enzymes. The latter require the metal ions to become stimulated; the metals are loosely bound to the enzymes. For instance, heavy metals-transporting ATPase is activated in presence of the metal ions and consumes ATP molecule for metal transportation across the cell membrane. In metalloproteins, the metals have several structural or catalytic roles such as: 1) constituting enzyme active sites; 2) stabilizing enzyme geometry structure; 3) forming weak-bonds with substrates contributing to their orientation to support chemical reactions; and 4) stabilizing charged transition states [2]. In this case, the metal ion is firmly bound to the enzyme and is frequently recycled after protein degradation, for example Heme groups in hemoglobin or cytochromes tightly bind a  $\text{Fe}^{2+}$  ion. Cations of transition metal (such as Cu, Fe) have unpaired electrons that allow their participation in redox reactions involving mostly one electron loss (oxidation) or gain (reduction). Thus, they are essential micronutrients required for diverse essential cellular functions such as electron transfer, dioxygen utilization and osmotic balance.

Copper is an essential trace element with key physiological and biochemical functions. It became biologically important to organisms most likely over 300 million years ago when the Earth's atmosphere became aerobic due to the evolution of photosynthesis by cyanobacteria. While enzymes involved in anaerobic metabolism needed to work in the lower portion of the redox spectrum, the presence of dioxygen created the need for a redox-active metal such as the redox potential  $\text{Cu(II)/Cu(I)}$  of copper which has 200 to 800 mV depending on its coordination with protein [3, 4]. Divalent copper has the highest affinity of the divalent essential metals for binding to metalloproteins according to the Irving–Williams series of the order of stability of metal complexes:  $\text{Ca(II)} < \text{Mg(II)} < \text{Mn(II)} < \text{Fe(II)} < \text{Co(II)} < \text{Ni(II)} < \text{Cu(II)} > \text{Zn(II)}$  [5].

Copper (I) is a soft Lewis acid, which prefers coordination to S and N groups, such as cysteine sulfhydryl (SH) groups and histidine nitrogen in proteins, as well as to oxygen groups in other biological molecules while Cu (II) is a moderate strength Lewis acid preferring coordination to harder nitrogen ligands such as nitrite [6, 7]. Both nitrogen and sulfur ligands can bind to Cu(I) and Cu (II), however ligands with sulfur donor groups bind Cu(I) stronger than they bind Cu (II) [8]. Cu associates with numerous proteins involved in biological processes in the cell; such as superoxide dismutase (SOD) for antioxidant activity, cytochrome C oxidase for oxidative phosphorylation, ceruloplasmin for iron metabolism, lysyl oxidase for connective tissue formation, tyrosinase/laccase for innate immune system [9-11]. However, the excess of copper ions is extremely toxic. The transition between a stably oxidized-Cu<sup>2+</sup> and unstable reduced-Cu<sup>+</sup> can generate free radicals such as superoxide radical and hydroxyl radical which in turn cause damages to many biomolecules such as nucleic acids and membrane lipids and eventually lead to cell death [12]. Therefore, cell needs highly regulated mechanisms for Cu homeostasis.

## 1.2 Ion transport in cell

Most molecules and ions enter or leave the cell aided by transporter proteins. There are three major classes of membrane transport proteins, depicted in Fig. 1.1, they are integral transmembrane proteins and exhibit a high specificity for the transported substance. First, ion channel proteins play a key role in the functioning of nerve cells by transporting ions and water molecules down their concentration gradient and electric potential gradients. They form an open gate across the membrane through which multiple water molecules or ions move simultaneously at a very rapid rate — up to 10<sup>8</sup> per second without consuming ATP molecules. Many other types of channel proteins are usually closed, and open only in response to specific signals. A second class of membrane proteins is the Transporters, which move a wide variety of molecules and ions across the cell membrane. In contrast to channel proteins, transporters undergo conformational changes in their structures to move one (or a few) substrate molecules at a time, with relatively slow rate of 10<sup>2</sup> – 10<sup>4</sup> molecules per second. Thirdly, ATP-powered pumps are enzymes known as ATPases which harness the energy released from the hydrolysis of ATP to pump ions across the membrane against a chemical concentration gradient or electric potential in a process known as active transport. Such pumps mediate, for example, the metal homeostasis inside virtually all animal cells, and

generate the low pH inside animal-cell lysosomes, plant-cell vacuoles, and the lumen of the stomach.

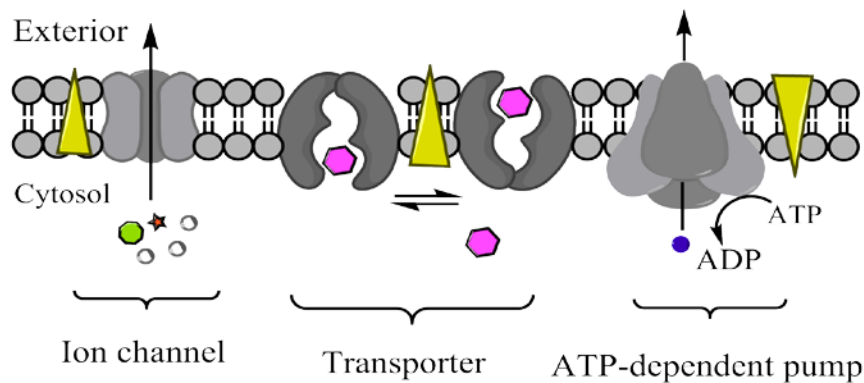


**Figure 1.1. Schematic diagram illustrating the three major types of membrane transport proteins.**

Channels catalyze the movement of specific ions (or water) down their electrochemical gradient. Electrochemical potential-driven transporters facilitate movement of specific small molecules such as amino acids and glucose. Pumps utilize the energy released by ATP hydrolysis to power movement of specific ions (red circles) or small molecules against their electrochemical gradient. Gradients are indicated by triangles with the tip pointing toward lower concentration, electrical potential, or both.

### 1.3 Copper homeostasis in *E.coli* bacteria

In bacteria, Cu enters the periplasm by an unknown mechanism, possibly through the porins, OmpC and OmpF [13, 14]. After entering the cell, Cu is bound to the Cu chaperones, therefore there are almost no free Cu ions in the cytosol [15, 16]. The Cu chaperones, for example CopZ in *Enterococcus hirae*, are small cytosolic proteins which deliver Cu ion to Cu-transporting ATPases, and to Cu-dependent enzymes. Cu chaperones will be discussed in details in section 1.5.1. In *E. coli*, the CusCFBA system is exclusively found in Gram-negative bacteria that could export Cu<sup>+</sup> outside the cell via the proton gradient across the inner membrane as an energy source [13]. The CusCFBA system includes four proteins, which are CusA, CusB, CusC and CusF. These proteins are members of the RND1 (resistance, nodulation, division) or CBA type of efflux systems. Delivery of copper to the CusCFBA system may occur via the periplasm, the cytoplasm or the copper-binding chaperone CusF from the periplasm [17]. Also, it is well known that CopA and CopB, which belong to the P<sub>1B</sub>- type ATPases, are exported

out of the cells by energy produced by ATP hydrolysis [18, 19]. No intracellular copper chaperone has yet been identified in *E. coli* [13].

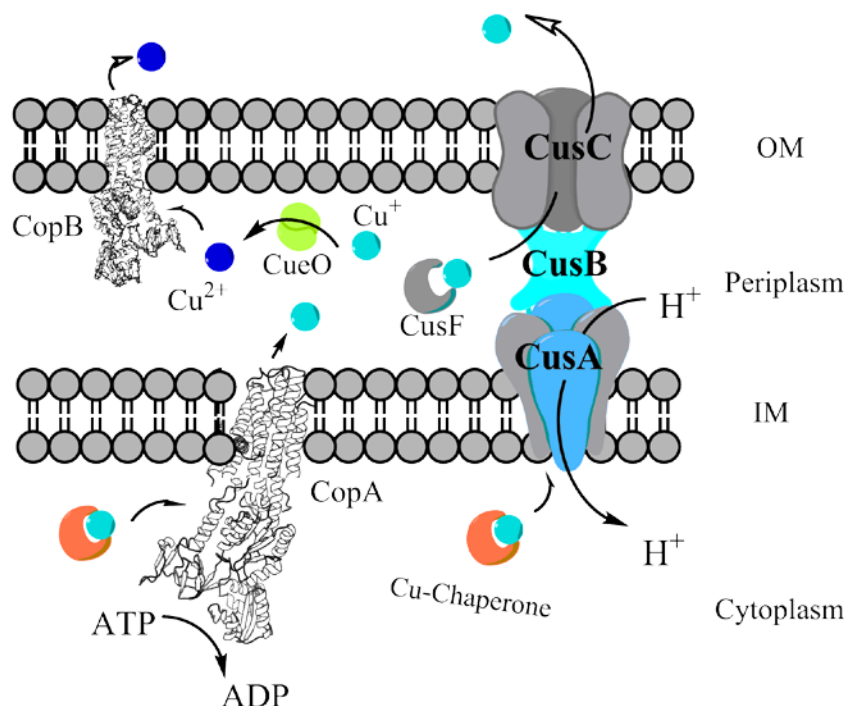


**Figure 1.2. Copper homeostasis mechanisms in *E. coli*.**

Copper enters the bacterial cell through an unknown importer. The CusCBA system, RND-driven tripartite complex, exports  $\text{Cu}^+$  from both the cytoplasm and the periplasm (via CusF) to the extracellular space. The CopA ATPase exports cytosolic copper across the inner membrane. CopB (or PcoB) has a putative function of exporting  $\text{Cu}^{2+}$  across the outer membrane [19, 20]. CueO, multicopper oxidase, oxidize periplasmic Cu (I); CusF, Cu(I)-binding metallochaperone.

#### 1.4 P-type ATPase superfamily

The P-type ATPase superfamily is a group of proteins that is involved in the transport of a variety of ions ( $\text{H}^+$ ,  $\text{Na}^+$ ,  $\text{K}^+$ ,  $\text{Cu}^+$ ,  $\text{Ca}^{2+}$ ,  $\text{Mg}^{2+}$ ,  $\text{Cd}^{2+}$ ,  $\text{Cu}^{2+}$ ,  $\text{Zn}^{2+}$ , etc.) across biological membranes by the energy produced from ATP hydrolysis. The key feature of pump, to be classified as a putative P-type ATPase, is the phosphorylation of an aspartate (D) residue found in the amino acid sequence DKTGT motif [21]. All P-type ATPases are multi-domain membrane proteins with molecular masses of 70–150 kDa [22]. Both their carboxyl and amino termini face the cytoplasmic side of the membrane, so they all have an even number of transmembrane segments. Based on sequence homology, the phylogenetic tree of conserved core sequences in 159 P-type ATPases classifies the proteins, independent of the organism from which they are isolated, into five major branches denoted type I-V ATPases (Fig. 1.3.). Each subtype is specific for a particular

substrate ion [23]. The PI group is divided into: PIA: bacterial Kdp-like ATPases and PIB or CPx-ATPases: soft transition metal ions transporters. The PII group includes: Na<sup>+</sup>/K<sup>+</sup> ATPases, H<sup>+</sup>/K<sup>+</sup>- ATPases sarcoplasmic reticulum (SR) Ca<sup>2+</sup>-ATPases, and plasma membrane Ca<sup>2+</sup>-ATPases, Group PIII are: H<sup>+</sup> and Mg<sup>2+</sup> transporters. Group PIV are eukaryotic enzymes that are involved in the transport of aminophospholipids lipid transporters. PV is a group with unknown substrate specificity.

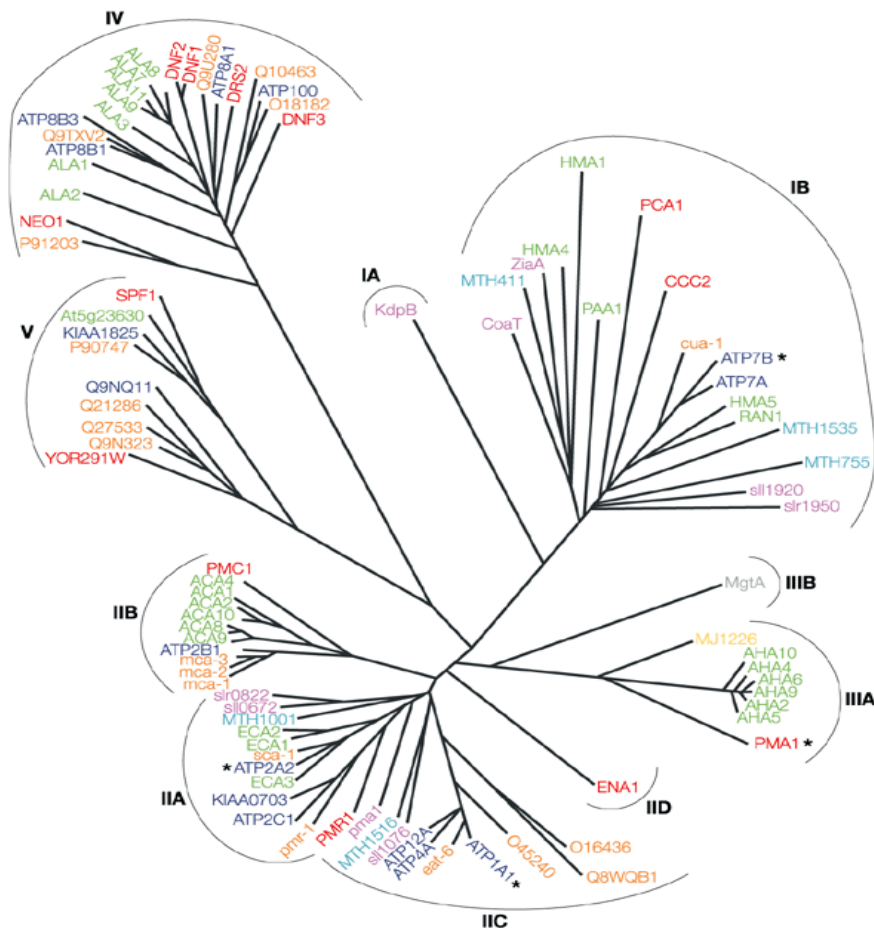


**Figure 1.3. Phylogenetic tree of the P-type-ATPase family.**

Subfamilies cluster according to their ion specificities: type IA, bacterial Kdp-like K<sup>+</sup>-ATPases; type IB, soft-transition-metal-translocating ATPases; type IIA, sarcoplasmic-reticulum (SR) Ca<sup>2+</sup>-ATPases; type IIB, plasma-membrane Ca<sup>2+</sup>-ATPases; type IIC, Na<sup>+</sup>/K<sup>+</sup>-ATPases and H<sup>+</sup>/K<sup>+</sup>-ATPases; type IID, eukaryotic Na<sup>+</sup>-ATPases; type IIIA, H<sup>+</sup>-ATPases; type IIIB, bacterial Mg<sup>2+</sup>-ATPases; type IV, 'lipid flippases'; and type V, eukaryotic P-type ATPases of unknown substrate specificity. Representative gene products are color coded by species: green, genes from *Arabidopsis thaliana*; orange, *Caenorhabditis elegans*; grey, *E. coli*; dark blue, *Homo sapiens*; light blue, *Methanobacterium thermoautotrophicum*; yellow, *Methanococcus jannaschii*; purple, *Synechocystis PCC6803*; and red, *Saccharomyces cerevisiae*. The figure is adapted from [22], and the classification is according to Axelsen and Palmgren [23].

## 1.5 Structural aspects of P1B-ATPases

P1B-ATPases are a subgroup of P-type ATPases that plays an important role in metal homeostasis in organisms including archaea, bacteria, fungi, and Eukaryotes by selective transport of heavy metals such as Cu (I), Cu (II), Pb (I), and Co (II) across biological membranes. They are differentiated into at several subgroups with distinct metal selectivity: (P1B-1:  $\text{Cu}^+$ , P1B-2:  $\text{Zn}^{2+}$ , P1B-3:  $\text{Cu}^{2+}$ , P1B-4:  $\text{Co}^{2+}$ ) based on their signature sequences which give the enzymes their characteristic metal selectivity [24]. In eukaryotes they play a role in metal micronutrient absorption, distribution and clearance.

The two human P1B-ATPases, called Menkes (ATP7A; MNK) and Wilson (ATP7B; WND), exhibit around 60% amino acid sequence identity, and are both localized primarily in a *trans*-Golgi compartment. In bacteria, the genes encoding copper-transporting ATPases are named CopA and CopB, since disruption of the genes rendered the cells copper-dependent and copper-sensitive, respectively [25]. CopA and CopB from *Enterococcus hirae* share 35–40% sequence identity with the human Menkes and Wilson copper ATPases, respectively[26].

The P1B-ATPases consist of eight transmembrane (TM) helices, of which three (TM6, TM7, and TM8) form the transmembrane metal-binding site, and four cytosolic domains: a heavy-metal binding domain (HMBD) at the N-terminus, an actuator domain (A-domain) between TM4 and TM5, phosphorylation and nucleotide-binding domains (PN-domain) linking TM6 and TM7. Some other P1B-ATPases have additional C-terminal metal binding domain (C-MBD) such as CopB of the archaeon *Archaeoglobus fulgidus* [27, 28]. In contrast, the  $\text{Ca}^{2+}$ -ATPases have ten transmembrane helices of which the last four helices are missing in the CPx-ATPase, while two extra helices are found in the N-terminal part of CPx-ATPase. Therefore, the 4<sup>th</sup>-8<sup>th</sup> TMs of CPx-ATPase correspond to 2<sup>nd</sup>- 6<sup>th</sup> TMs of  $\text{Ca}^{2+}$ -ATPase [29, 30]. Contrary to  $\text{Ca}^{2+}$ -ATPase in which transmembrane aspartate and glutamate residues mediate  $\text{Ca}^{2+}$  ion translocation [31], the P1B-ATPases have a putative transmembrane metal binding CPx motif: C (cysteine), P (proline) and x (cysteine, serine, or histidine) in the 6<sup>th</sup> TM [24]. Another feature of P1B-type ATPases is the presence of N-terminal heavy metal binding domain (HMBD) which is missing in  $\text{Ca}^{2+}$ -ATPase.



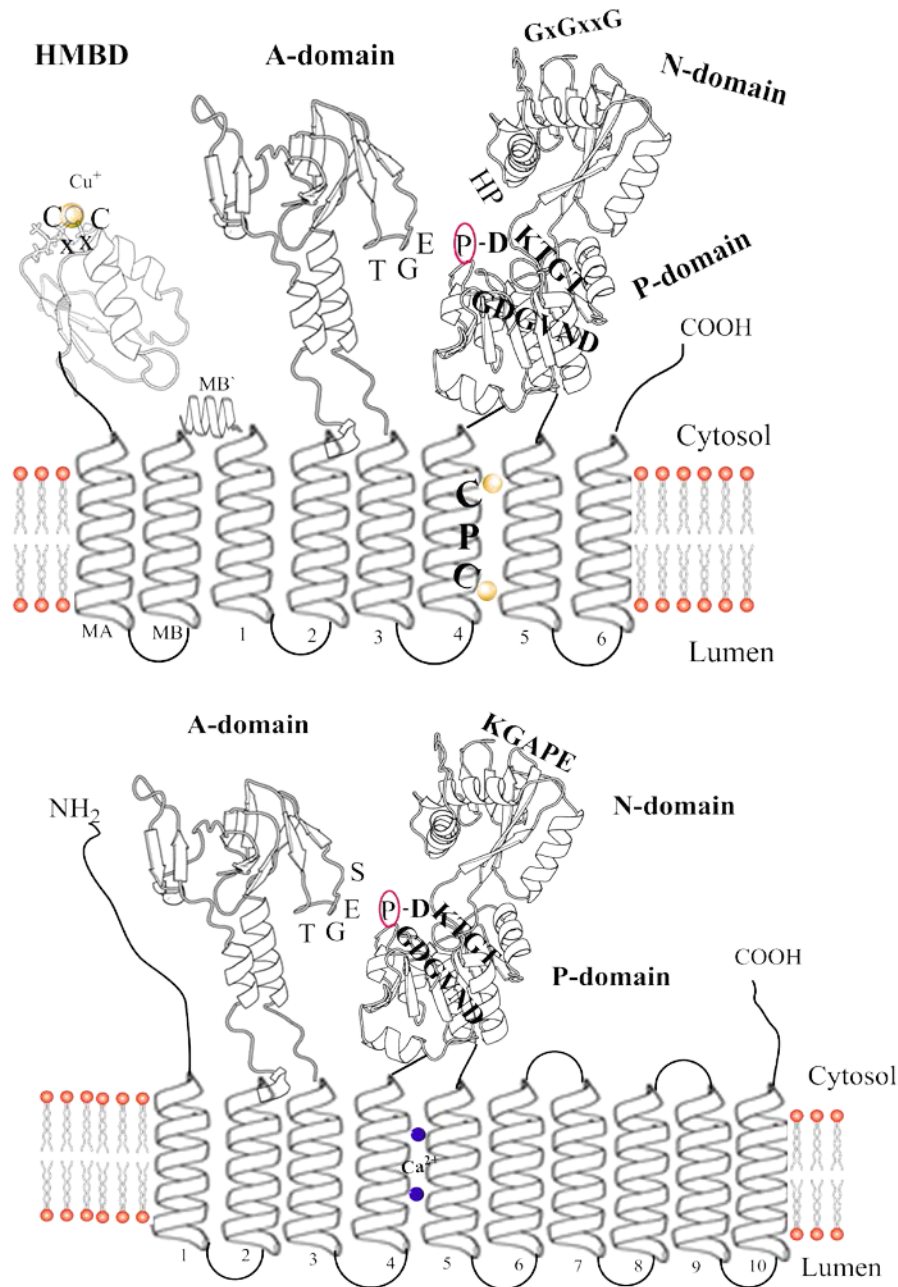


**Figure 1.4. Topology diagram of LpCopA and SERCA.**

Both ATPases consist of three similar domains architecture facing to the cytoplasm: actuator (A)-, phosphorylation (P)- and nucleotide binding (N) – domain. LpCopA consists of eight putative transmembrane segments (according to LpCopA numbering from N-terminus : MA, MB/MB' and 1-6 ) [32]. Conserved motifs are highlighted. SR Ca<sup>2+</sup>-ATPase consists of 10 transmembrane helices (numbered) [33]. The transmembrane copper-binding CPC motif of LpCopA located in TM4. The HMBD which is exclusively located in the N-terminus of LpCopA is replaced by a long tail in SR Ca<sup>2+</sup>-ATPase. The P-domain includes a conserved aspartate residue responsible for phosphorylation in phosphoenzyme intermediates.

The crystal structure of CPx- ATPases has been solved excluding the metal-binding domain due to weak or absent electron density for the region [32], for instance copper-transporting ATPase LpCopA from *Legionella pneumophila* (PDB ID: 3RFU;  $E2\sim P$  and 3B9R;  $E2P$  states) [32, 34], AfcopA from *A. fulgidus* (3J08 and 3J09)[35], zinc-transporting ATPase zntA from *S. sonnei* (PDB ID: 4UMW for  $E2\sim P$  and 4UMW for  $E2P$  states) [36]. LpCopA exhibits a significant level of sequence identity with ATP7A/ATP7B reach 35.4 and 36.3% [37]. The Wilson and Menkes ATPases contain six CxxC motif sequences in the N terminus, while LpCopA has only one CxxC motif.

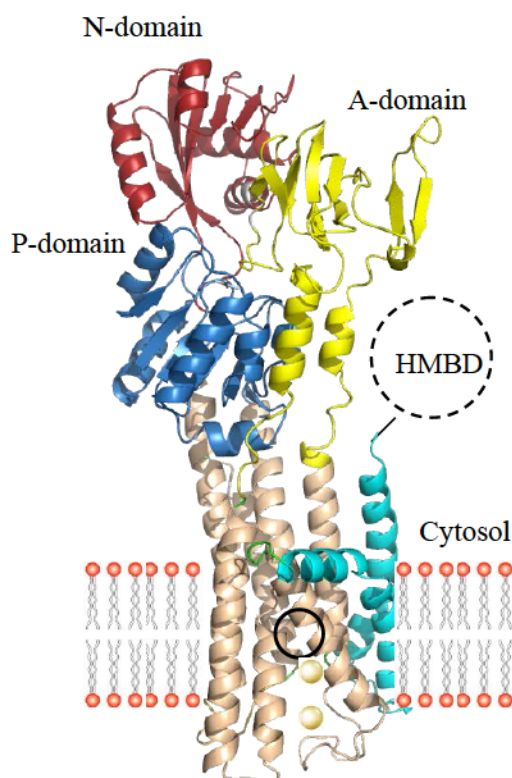


**Figure 1.5. Crystal structural model of CopA from *Legionella pneumophila*.**

The cartoon representation shows the P-, N-, A- domains in blue, red and yellow colors, respectively. The crystal structure captures the LpCopA in  $E2\sim P$  (PDB ID: 3RFU). The HMBD location is denoted by the dotted circle. The solid circle demonstrates the location of CPC motif, metal binding site within the transmembrane helices in wheat color. MA, MB and MB' are in cyan color.

### 1.5.1 Metal-binding domain and Cu-Chaperones

Almost all P1B-type ATPases have a regulatory cytoplasmic metal binding domains in the N-terminus (N-HMBDs), C-terminus (C-HMBDs), or both. These domains, which are of much smaller size in comparison with other cytoplasmic domains, have the ferredoxin-like fold with metal binding-motifs which give them their characteristic metal-binding selectivity. HMBDs could be found with either His-rich sequence, such as in *A. fulgidus* CopB and *E. hirae* CopB or MxCxxC motif (x= amino acid residues) in CopA proteins.

The number increases from one or two copper-binding domains in bacteria[25], yeast [38] and plants [39] to three in *C. elegans* [40], four in *Drosophila* [41], five in rat [42], and finally six in ATP7A and ATP7B of humans [43, 44]. Although the current structural information provides a good model for the transfer of copper between a copper chaperone and copper-binding domains of a target ATPase, but still actual function of this domain is conclusive. The biochemical data on HMBD function show that an impaired activity is typically observed when the HMBD is removed or the metal-binding (CxxC) motif is mutated [45]. It is thought that it may play a regulatory role [46] a pseudo-atomic mode suggests that the N-terminal MBD may be auto-inhibitory in the Cu-free state, leading to Cu-dependent regulation of CopA activity [47].

The copper chaperones, such as CopZ of *B. subtilis* and *E. hirae*, Atx1 of *S. cerevisiae* and Hah1 or Atox1 of mammals, bind and deliver copper ions to intracellular compartments and insert the copper ion into Copper-transporting ATPases [48, 49]; they have a ferredoxin-like fold ( $\beta\alpha\beta\beta\alpha\beta$ ) typical of proteins that bind inorganic ions or clusters, such as ferredoxins (Fe-S cluster proteins), nickel-responsive transcriptional factor (NikR), and bacterial mercury resistance protein (MerP) [50-52]. Bacterial cytosolic copper chaperone CopZ is a small protein (approximately 70 residues) containing a metal binding MxCxxC motif, while both Atx1 and Atox1 have MxCxGC motif [53]. CopZ delivers copper to CopA for copper exporting and to CopY repressor protein in *E. hirae* for protein regulation [54].

Several HMBD structures have been solved separately from the integrated Cu (I)-transporting ATPase (Fig. 1.6). Strikingly, C-MBD monomers of *A. fulgidus* form a domain-swapped dimer structure, which has not been observed previously for similar domains [55].

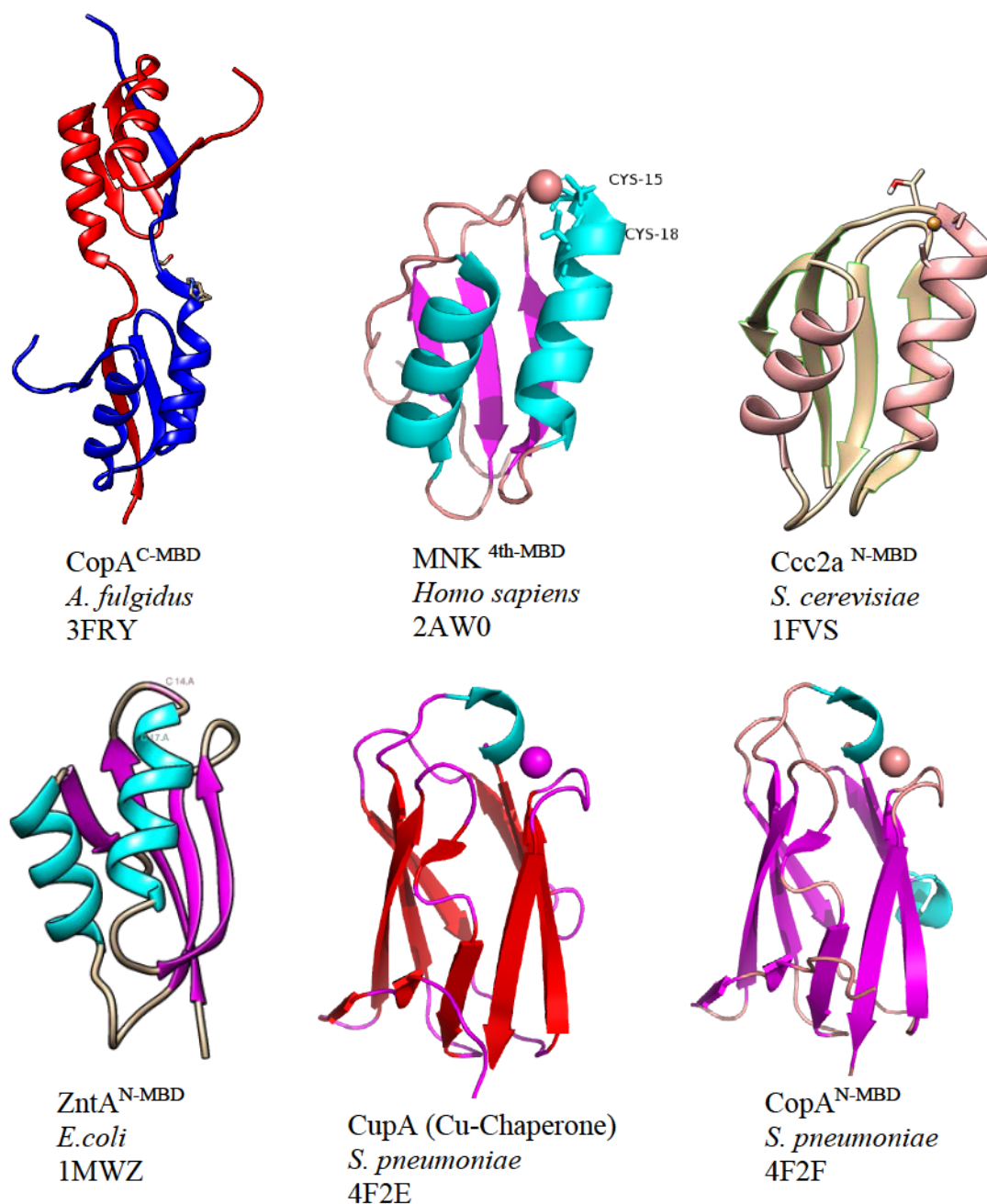


**Figure 1.6. Structures of isolated metal-binding domains and Cu-chaperone.**

The cartoon is represented by Pymol and UCSF Chimera software. The structures are retrieved from PDB webpage. The spheres are denoted to copper ion.

The mechanism of copper transfer between copper chaperones and CopA is unknown, but it is proposed to involve conserved MxCxxC sequence motifs in both the chaperone and N-MBD of Cu-ATPases. For instance, the structure similarity between BsCopA and BsCopZ of *B. subtilis*, suggests that the two proteins could interact one with the other as shown in Fig. 1.7. The conformation variability of N-terminal cysteine of the CxxC

motif in many copper transporting proteins suggests that this may be the cysteine which binds first to the copper (I) [56].

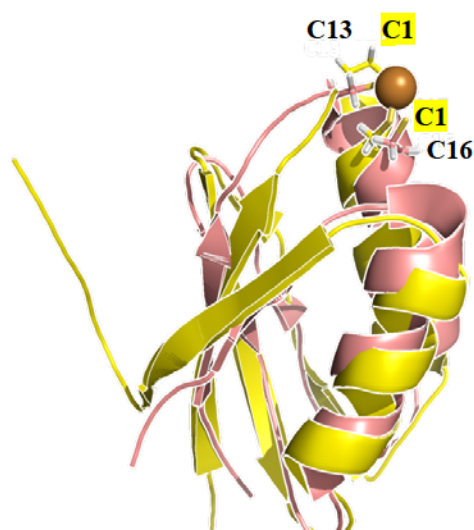


**Figure 1.7. Superimposition of HMBD and CopZ from *Bacillus subtilis*.**

Protein structures were retrieved from PDB. The HMBD (PDB ID: 1KQK) and CopZ (PDB ID: 1K0V) are in yellow and salmon colors, respectively. The cysteine residues of C14xxC17 and C13xxC16 motif belong to the HMBD and CopZ structures, respectively. Both sequences are copper loaded, but one copper ion was eliminated for simplifying.

According to biochemical and spectroscopic data, both chaperone and target proteins bind Cu (I), which is coordinated by the two Cys residues in the MxCxxC sequence motif. Figure 1.8 shows a proposed mechanism of copper transferring between copper chaperone (e.g. Hah 1) and copper-binding site of a partner.

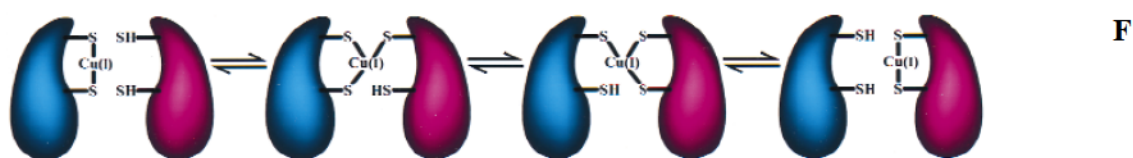


**Figure 1.8. Proposed mechanism of copper ion transfer to Menkes and Wilson protein.**

Hah1 is in blue color, and the partner protein is in magenta. Figure is adapted from [57].

The crystal structure of LpCopA, illustrated a putative Cu transfer mechanism from cytosolic Cu-chaperone to the entry site of LpCopA. The MB` segment is kinked and forms an electropositive platform at the cytoplasm/membrane interphase. Therefore, it is suggested, based on electrostatic potential of cytosolic domains, that the positively charged platform in LpCopA serves as the docking site for both the Cu-loaded chaperone and HMBD in different manner as shown in Fig. 1.9. The chaperone in turn releases the Cu ion to the transiently ligating conserved Met and Glu of CopA, which form the entrance of the metal permeation path [30].

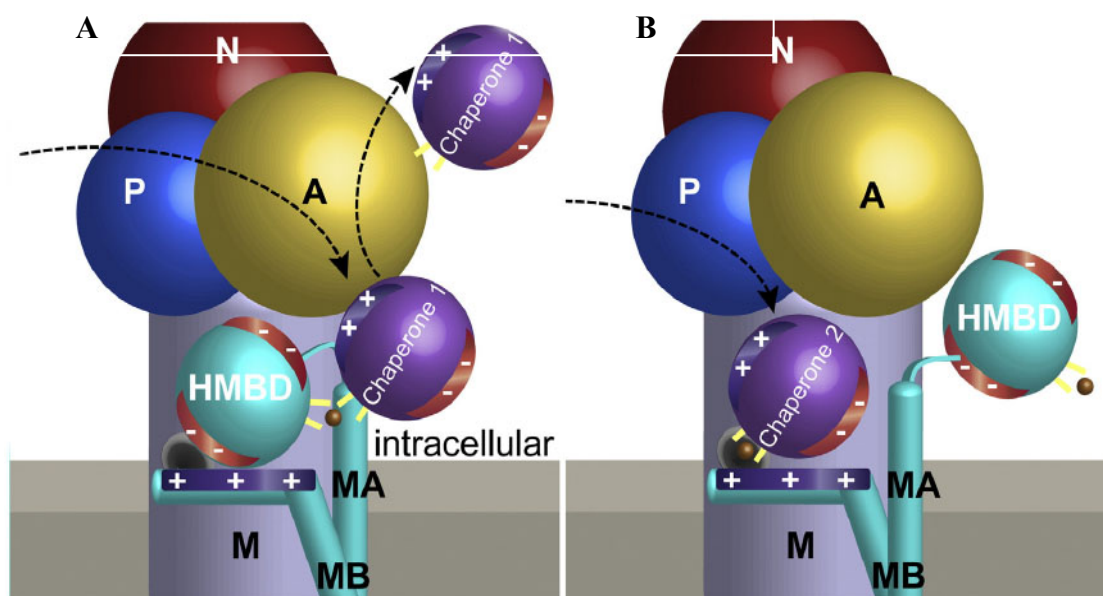


**Figure 1.9. A schematic model of CopZ/HMBD interaction mediates the allosteric Cu<sup>+</sup>-ATPase regulation.**

**A)** the first Cu<sup>+</sup> ion delivery from CopZ-like chaperones to the HMBD may facilitate opening the entry gate for the second Cu<sup>+</sup> ion by oppositely charged areas (red, negative; blue, positive), and HMBD dissociation from the docking platform. **B)** When the HMBD is Cu<sup>+</sup> occupied, copper chaperone may donate the second Cu<sup>+</sup> to entry site to trigger the catalytic cycle. The figure is adapted from [30].

### 1.5.2 Phosphorylation-/Nucleotide-binding domains

P-type ATPases transport metal ions across membranes in an ATP-dependent fashion. In solution, the enthalpy of the ATP decomposition into hydrated ADP and inorganic phosphate is  $-20.5$ - $31$  kJ/mol, with a change in free energy  $3.4$  kJ/mol, at standard temperature and pressure [58, 59]; 40-60% of this enthalpy produces heat and the rest is used for other biological processes. The total quantity of ATP in the human body at any one time is about  $0.1$  mol. It cannot be stored and so it has to be recycled 2000 to 3000 times during the day [60].

The distinctive feature of P-type ATPases is the nucleotide-binding domain (N-domain) that carries the ATP-binding pocket and the phosphorylation domain (P-domain) where a covalent phosphate bond intermediate with an aspartate residue is formed [47, 48]. These domains are located between TM helices 6 & 7 of P1B-ATPases. The N-domain has two sequence motifs characteristic only to members of CPx-ATPase; the HP motif is present 34-43 residues from the phosphorylated aspartate and a protein kinase-like GxGxxG/A motif is found downstream in the same domain[29, 32].

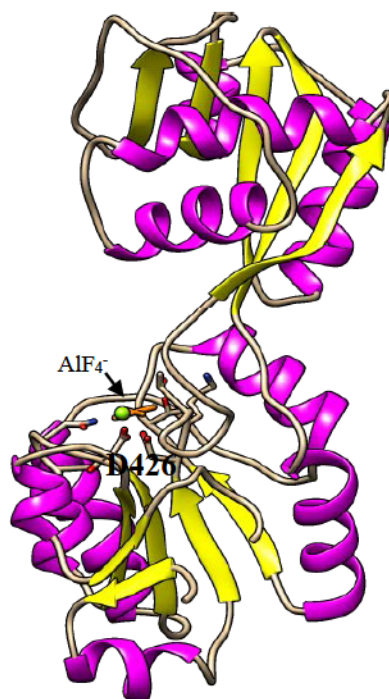


**Figure 1.10.** Crystal structure of PN domain derived from LpCopA structure.

The secondary structure is shaded by magenta for  $\alpha$ -helix and yellow for  $\beta$ -sheet. The  $\text{AlF}_4^-$  is denoted as phosphate analog near to the conserved D426 residue in E2~P state of LpCopA (PDB ID: 3RFU). The cartoon structure is displayed by UCSF Chimera software.

The role of the histidine in HP motif is ambiguous, the mutagenesis studies have reported that mutations of the residue affect ATP binding, retain significant ATPase activity in vitro [61, 62] and impair the phosphorylation, which suggests that the residue might participate in steps of the catalytic cycle other than ATP binding [61]. It is believed that the HP motif plays a role in the interaction of the N-domain with other cytosolic domains. The interaction between the HMBD with the PN domain is already reported to occur in a Cu (I)-dependent manner [47, 63, 64]. The GxGxxG/A motif has been demonstrated to interact with ATP in the nucleotide-binding pocket of protein kinases [65] and perhaps participates in the nucleotide binding in P1B-ATPases as well [66].

The P-domain, belonging to the haloacid dehalogenase superfamily [67, 68], contains signature motifs for the auto(de)phosphorylation of a P-type ATPase. The conserved aspartate side chain of the DKTG motif is covalently phosphorylated by  $\gamma$ -phosphate of ATP during the catalytic cycle [42]. The orientation of the attached phosphate is provided by a magnesium ion in the P-domain that interacts with the DKTG motif and the MXGDGXNDXP (Asp-703 and Asp-707 of Ca<sup>2+</sup>-ATPase) motif. This magnesium ion plays a key role for the energy transduction during the reaction cycle [69]. The sequence MXGDGXNDXP motif, found in the hinge region that connects the P- domain to N-domain might be responsible for the large rigid body movements during catalysis.



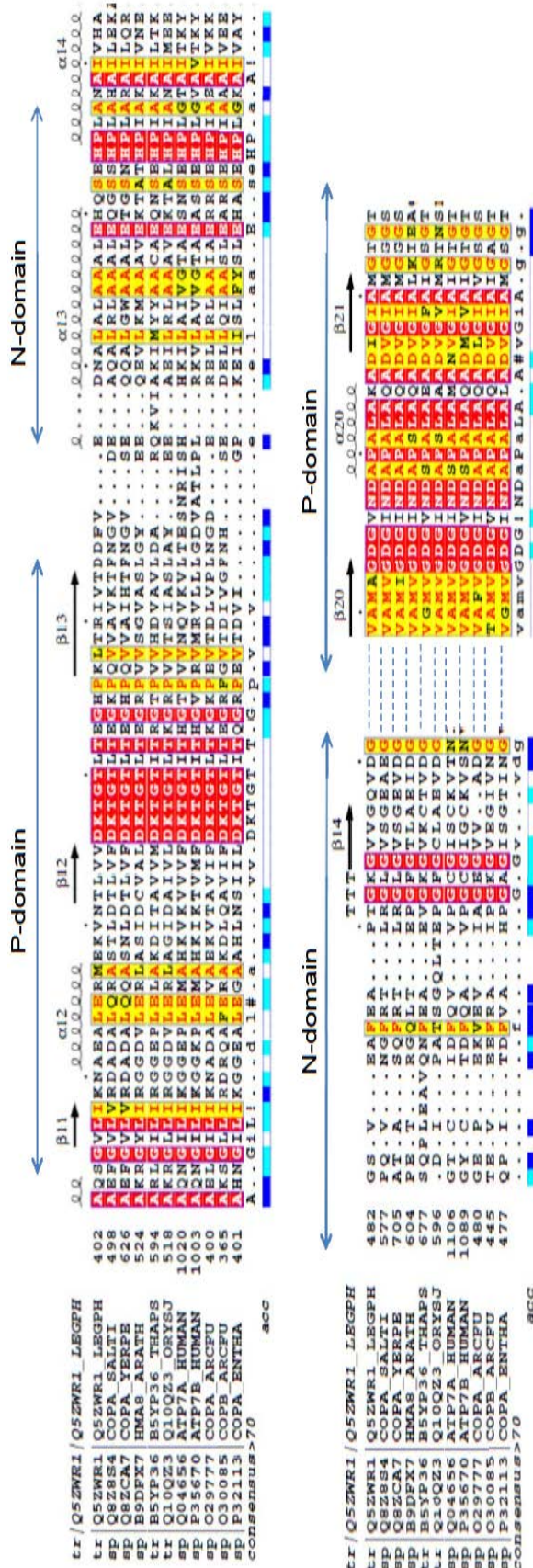


**Figure 1.11. Partial sequence alignment of P-/N-domains from archaeal CPx-ATPases.**

The sequences of Cu-Transporting ATPase are retrieved from uniprot database: Q5ZWR1 (LpCOPa, *Legionella pneumophila*), Q8ZS4 (CopA, *Salmonella typhi*), Q8ZCA7 (CopA, *Yersinia pestis*), B9DFX7 (*chloroplastic Arabidopsis thaliana*), B5YP36 (*Thalassiosira pseudonana*), Q10QZ3 (CopA, *Oryza sativa*), Q04656 (ATP7A, *Homo sapiens*), P35670 (ATP7B, *Homo sapiens*), O29777 (CopA, *Archaeoglobus fulgidus*), O30085 (CopB, *Archaeoglobus fulgidus*) and P32113 (CopA, *Enterococcus hirae*). The multiple sequence alignment is carried out using T-Coffee server (<http://tcoffee.org.cat/>). The red and yellow colors indicate the highly conserved and semi-conserved sequences, respectively. The secondary structure, based on the crystal structure of LpCOPa (PDB code: 3rfu), is displayed with arrows and helix symbols using the ESPript program (<http://esprict.ibcp.fr/ESPript/ESPript/>).

### 1.5.3 Actuator domain

The A-domain is highly conserved among all members of the P- type ATPases (45% sequence similarity and 23% sequence identity, determined by averaging between Ca<sup>2+</sup>-ATPase and archaeal CPX-ATPases) [70]. The actuator domain exists as a smaller loop (compared to the PN domain) between 4<sup>th</sup> & 5<sup>th</sup> TM helices of P<sub>IB</sub>-type ATPases and separates from N-terminal HMBD by two transmembrane helices. In Ca<sup>2+</sup>-ATPase also a small portion of the N-terminal peptide adds to the A-domain which places in 2<sup>nd</sup> & 3<sup>rd</sup> TM helices.

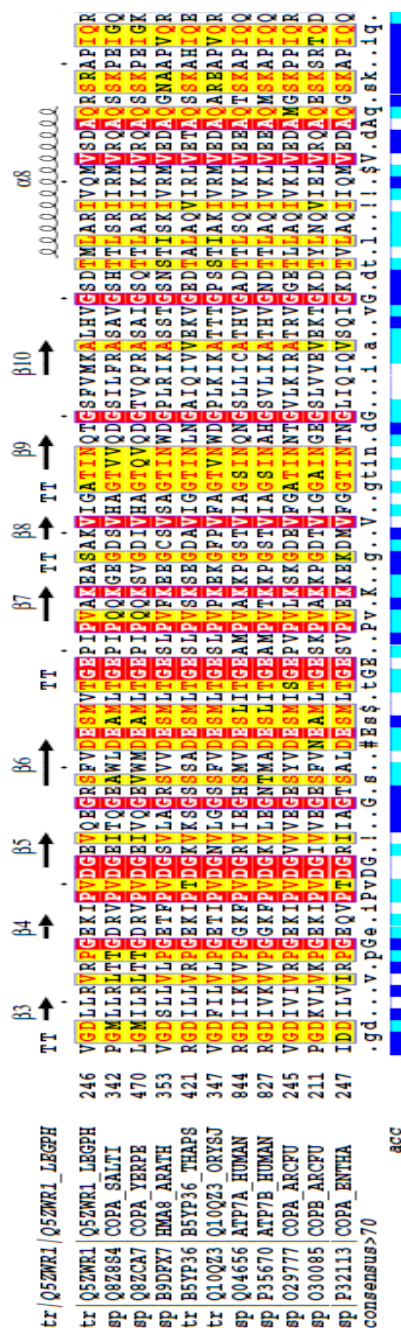


**Figure 1.12. Partial sequence alignment of A-domains from archaeal CPx-ATPases.**

The sequences of Cu-Transporting ATPase are retrieved from uniprot database: Q5ZWR1 (LpCopA, *Legionella pneumophila*), Q8Z8S4 (CopA, *Salmonella typhi*), Q8ZCA7 (CopA, *Yersinia pestis*), B9DFX7 (*chloroplastic Arabidopsis thaliana*), B5YYP36 (*Thalassiosira pseudonana*), Q10QZ3 (CopA, *Oryza sativa*), Q04656 (ATP7A, *Homo sapiens*), P35670 (ATP7B, *Homo sapiens*), O29777 (CopA, *Archaeoglobus fulgidus*), O30085 (CopB, *Archaeoglobus fulgidus*) and P32113 (CopA, *Enterococcus hirae*). The multiple sequence alignment is carried out using T-Coffee server. The red and yellow colors indicate the highly conserved and semi-conserved sequences, respectively. The secondary structure, based on the crystal structure of LpCopA (PDB ID: 3RFU), is displayed with arrows and helix symbols using the ESPript program.

The common signature sequences of A-domains in all P-type ATPases are the conserved sequence motif (S/T)GE(P/S) as shown in Fig. 1.12. This sequence makes a loop, located at the tip of a solvent accessible loop on the side of the A-domain (Figure 1.13). Several structural and biochemical studies revealed that the A-domain interacts with the P-domain during enzyme phosphorylation/de-phosphorylation [32, 71], with the N-domain upon ATP binding [72, 73] and associates with the HMBD [47, 74, 75].

The entire A-domain, highly mobile, undergoes a significant rigid body movement with subsequent rearrangement of TMs during the catalytic cycle. This arrangement regulates the binding and release of metal ions [71, 76]. The A-domain comes very close to the phosphorylation site of the DKTG motif in the *E2* and *E2P* states.

In the *E2P* state, this loop appears to be very important for shielding the aspartyl phosphate from bulk water and meanwhile localizing the Glu residue of this loop in close contact to the bound  $Mg^{2+}$  next to the phosphorylation site of the DKTG motif [32, 77], facilitating a particular water molecule to attack the acylphosphate bond [32, 78, 79].

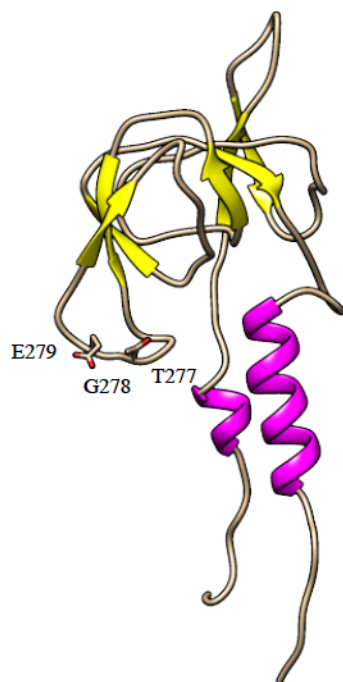


**Figure 1.13. Cartoon representation of A-domain of crystal LpCopA structure.**

The secondary structure is shaded by magenta for  $\alpha$ -helix and yellow for  $\beta$ -sheet. The A-domain consists of a 7  $\beta$ -strand cores with 2  $\alpha$ -helices connecting the TMs. The structure (PDB code: 3RFU) is displayed by UCSF Chimera software.

### 1.5.4 Transmembrane helices domain

The transmembrane segments (TM helical segments) are connected to the cytosolic domains through five linker regions. The transmembrane domain of CP<sub>x</sub>-ATPases consists of eight hydrophobic putative helices. The structure of LpCopA shows that the six core helices share a principal organization as the first six helices of other P-type ATPases, in addition to the two P<sub>IB</sub>-specific helices (MA and MB) at the N-terminus. The MA interacts with TM2 and TM6, while the MB interacts with TM1 and TM2. The MB segment consists of two helices separated by a highly conserved glycine; membrane-spanning helix (MB) and a perpendicular amphipathic helix at the cytoplasmic interface, MB' (Fig. 1.4). Because of its positively charged residues toward the cytoplasmic environment, MB' can form a putative docking platform for copper chaperones and HMBD. Cytosolic copper chaperones interact with a structural platform in CopA and deliver copper into the ion permeation path; the putative Cu<sup>+</sup> entry of LpCopA is formed by the three highly conserved residues, Met148 (M1), Glu205 (M2) and Asp337 (M4). The TM helical segments are connected to the cytosolic soluble domains “headpiece” through five linker regions. The TM4 harbors the CP<sub>x</sub> motif, which forms a transient ion binding site by providing the amino acid side chain ligands for heavy metals as shown in Table 1.1.

**Table 1.1. Structural characteristics of each subgroup in the P<sub>IB</sub>-ATPase subfamily.**

Metal specificity of subgroup is shown in addition to the signature conserved sequences in transmembrane regions TM6-TM8 and N-MBD. Transmembrane signature motifs are shown as defined in [80].

| Subgroup | Metal specificity                                    | N-MBD                      | TM6                           | TM7                                                         | TM8                                                          |
|----------|------------------------------------------------------|----------------------------|-------------------------------|-------------------------------------------------------------|--------------------------------------------------------------|
| IB-1     | Cu <sup>+</sup> /Ag <sup>+</sup>                     | CxxC                       | CPC-x <sub>6</sub> -P         | N-x <sub>6</sub> -YN-x <sub>4</sub> -P                      | P-x <sub>6</sub> -M-x <sub>2</sub> -SS-x <sub>5</sub> -[N/S] |
| IB-2     | Zn <sup>2+</sup> /Cd <sup>2+</sup> /Pb <sup>2+</sup> | CxxC+<br>(Hx) <sub>n</sub> | CPC-x <sub>4</sub> -<br>S-x-P | N-x <sub>7</sub> -K                                         | D-x-G-x <sub>7</sub> -N                                      |
| IB-3     | Cu <sup>+</sup> /Cu <sup>2+</sup> /Ag <sup>+</sup>   | H-rich                     | CPH                           | N-x <sub>5</sub> -GY-N-<br>x <sub>4</sub> -P                | P-x <sub>6</sub> -MS-x-ST-<br>x <sub>5</sub> -N              |
| IB-4     | Co <sup>2+</sup>                                     | --                         | SPC-x <sub>6,7</sub> -P       | N<br>at the cytoplasmic<br>end                              | HEG-[G/S]-T-<br>x <sub>5</sub> -[N/S]-<br>[G/S/A]            |
| IB-5     | unidentified                                         | --                         | TPCP-x <sub>5</sub> -P        | Q-x <sub>4</sub> -G-x <sub>3</sub> -<br>S-x <sub>3</sub> -M | P-x <sub>6</sub> -QE-x <sub>2</sub> -D-<br>x <sub>5</sub> -N |

## 1.6 Catalytic Mechanism of P-type ATPases

All P-type ATPases, including CPx-ATPases, undergo similar conformational changes during *E1-E2* states based on experimental evidence [81, 82]. SERCA is the best characterized P-type ATPase up to date, used as a representative example for a P-type ATPase. Figure 1.14 depicts an overview of all available crystal structures in the classical *E1/E2* cycle of SERCA ATPase. The transport process is made up of a series of steps: ion binding, ATP hydrolysis, conformational changes in the protein, and ion release to the extracellular domain. Recently, the proposed copper transporting mechanism has been illustrated as well for LpCopA based on crystallographic data and MD simulation [30, 34].

The  $\text{Ca}^{2+}$ -ATPase in the *E1* state has a high affinity for  $\text{Ca}^{2+}$  from the cytoplasmic side to form *E1.2Ca<sup>2+</sup>* state and the enzyme undergoes a conformational change. In contrast, an enzyme in the *E2* state has a low affinity for  $\text{Ca}^{2+}$  and the binding sites face the opposite side of the membrane.

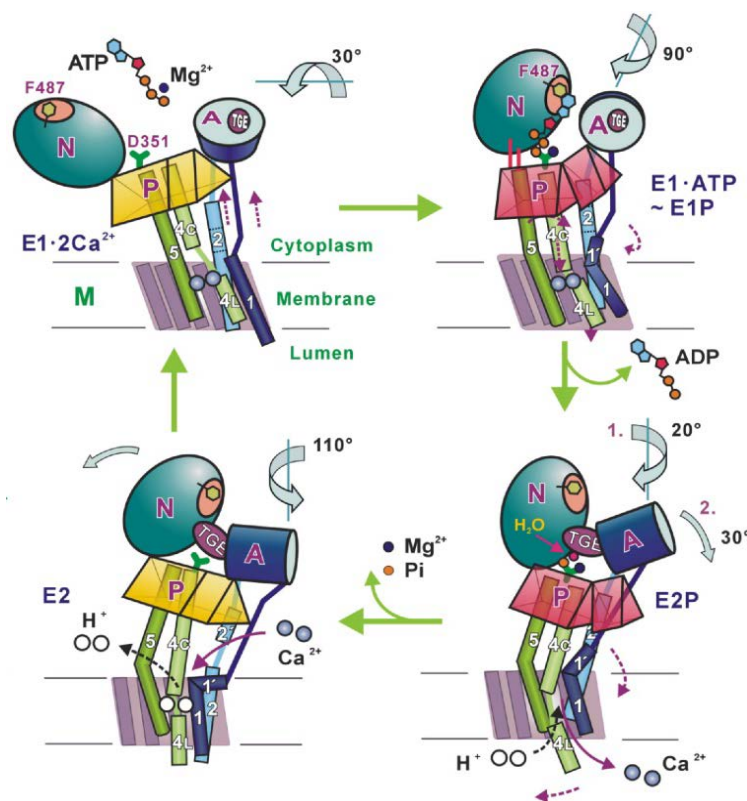


**Figure 1.14** A cartoon illustrating the cytosolic domain arrangement in SERCA1 during the reaction cycle.

P-, N- and A-domains stand for phosphorylation, nucleotide-binding and actuator domains. The diagram shows the rotation of the A-domain during the catalytic cycle. The figure is adapted from [83].

ATP binds to the N-domain and occlusion of the ions occurs through conformational changes of the P-type ATPase ( $\text{Ca}^{2+}$ -E1-ATP). ATP binds near the hinge between the P- and N-domains and penetrates P-domain, so that the  $\gamma$ -phosphate of ATP and  $\text{Mg}^{2+}$  (or  $\text{Ca}^{2+}$ ) bind to the P-domain [83]. The N-domain tilts towards the P-domain to initiate the hydrolysis of ATP and formation of phosphoenzyme intermediate, “ADP-sensitive phosphoenzyme” or “ $\text{Ca}^{2+}$  E1-ADP~P”. The covalent phosphate binding triggers the opening of the membrane domain towards the extracellular/luminal side (E2P) and the A-domain rotates so that the conserved TGE loop is positioned close to the phospho-aspartate of the DKTG group which is exposed to a water molecule attack and dephosphorylate [79]. In  $E1 \cdot 2\text{Ca}^{2+} \rightarrow E2P$  transition, the rotation of A-domain occurs in subsequent steps; first rotation is by  $\sim 30^\circ$  due to ATP binding and bending of the P-domain, followed by  $90^\circ$  upon the  $E1P \rightarrow E2P$  transition [83]. The two  $\text{Ca}^{2+}$  ions are delivered to the lumen in exchange for 2–3 luminal protons. The counter ions “protons” are released on the cytoplasmic side concluding a fully-functional cycle and ready for a new substrate export cycle (E2) [84]. Strikingly, Crystal structures of SERCA1a in several key catalytic states reveal that this enzyme can bind a nucleotide throughout the entire reaction cycle, either in a catalytic (E1) or a modulatory (E2) mode [85-87]. The two modes of ATP binding, catalytic or modulatory, can take place in the same pocket, but differ slightly [88-90]; the  $\gamma$ -phosphate of modulatory ATP is 9 Å away from the phosphorylation site. The modulatory ATP with low affinity accelerates the E2-E1 transition [82].

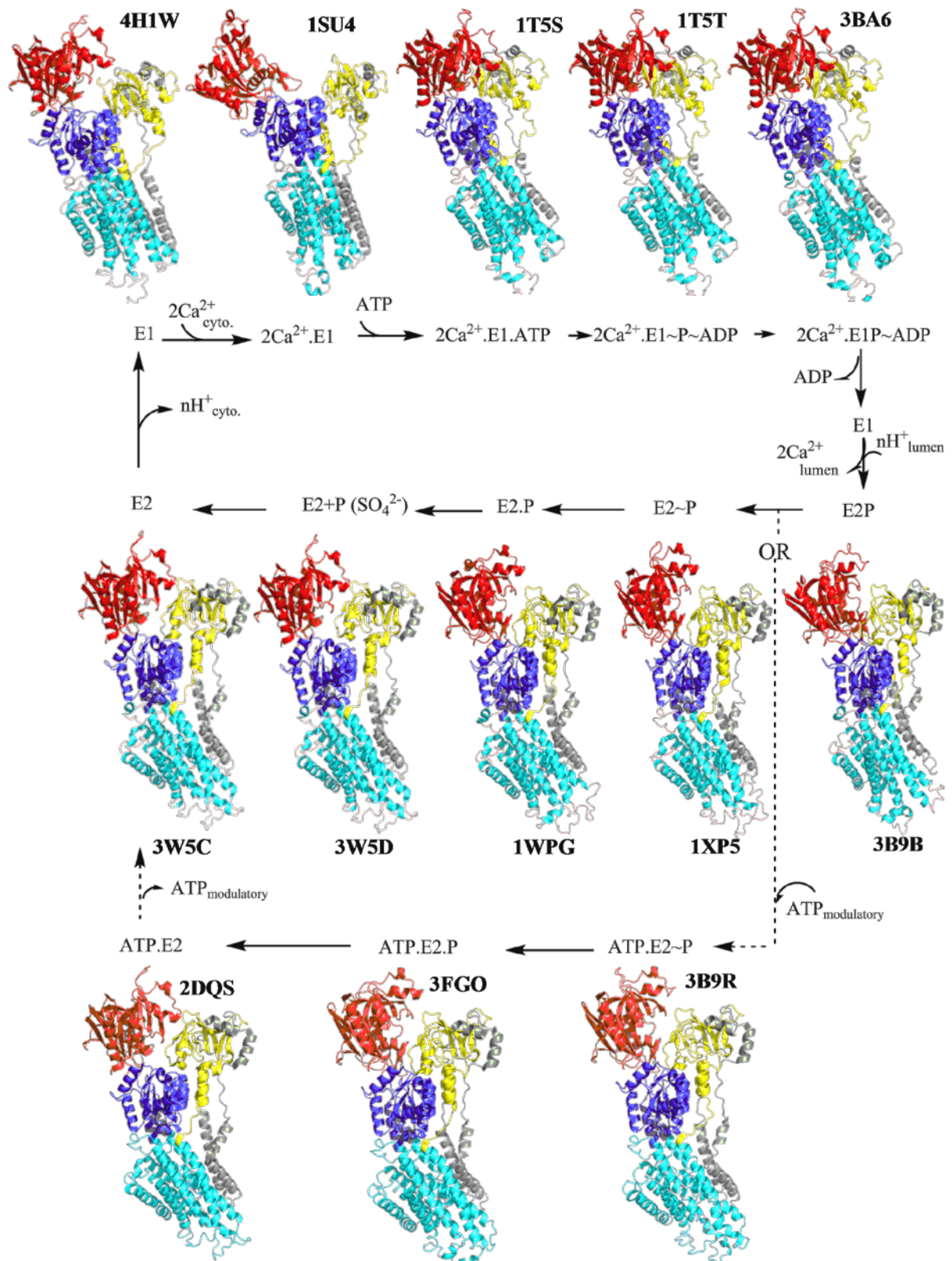


**Figure 1.15. Post-Albers cycle of P-type ATPases.**

The transport cycle is exemplified from structural models of SR  $\text{Ca}^{2+}$ -ATPase. The catalytic cycle starts with binding of  $\text{Ca}^{2+}$  to the E1 state of the ATPase. ATP binds to the N-domain to form the  $\text{Ca}_2.\text{E1}.\text{ATP}$  state and occludes the  $\text{Ca}^{2+}$  ion. Upon ATP hydrolysis, the  $\gamma$ -phosphate of ATP is transferred to the aspartate of the DKTG motif to form  $\text{Ca}_2\text{E1P}$ , an ADP-sensitive phosphoenzyme intermediate. The A-domain rotates toward the P-domain,

causing rearrangement of TMs in  $E2P$  state, an ADP-insensitive phosphoenzyme intermediate. Thereby,  $Ca^{2+}$  ions are excluded and protons are involved in the  $E2P$  state. The A-domain dephosphorylates the aspartate residue and protons get released to the cytoplasm in the  $E2$  state. Alternatively, the modulatory ATP binds to the N-domain from  $E2P$  to  $E2$  states according to [88-90]. The corresponding PDB-IDs of the different conformational states are identified by **bold** font. All structures are aligned to each other and displayed by PyMol program. The N-terminal loop, A-, P-, N-, TM domains are in wheat, yellow, blue, red and cyan, respectively.  $E2+SO_4^{2-}$  state represents likely a phosphate ion before release into the bulk medium [72].

In LpCopA, the copper chaperones deliver the first copper ion to the HMBD, thereby the interaction between the PN-domain and the HMBD is diminished to allow ATP binding to the N-domain. Next, the second Cu ion is delivered to the transmembrane metal-binding site in  $Cu^+-E1-P\sim ADP$  to trigger the catalytic cycle [63, 82].

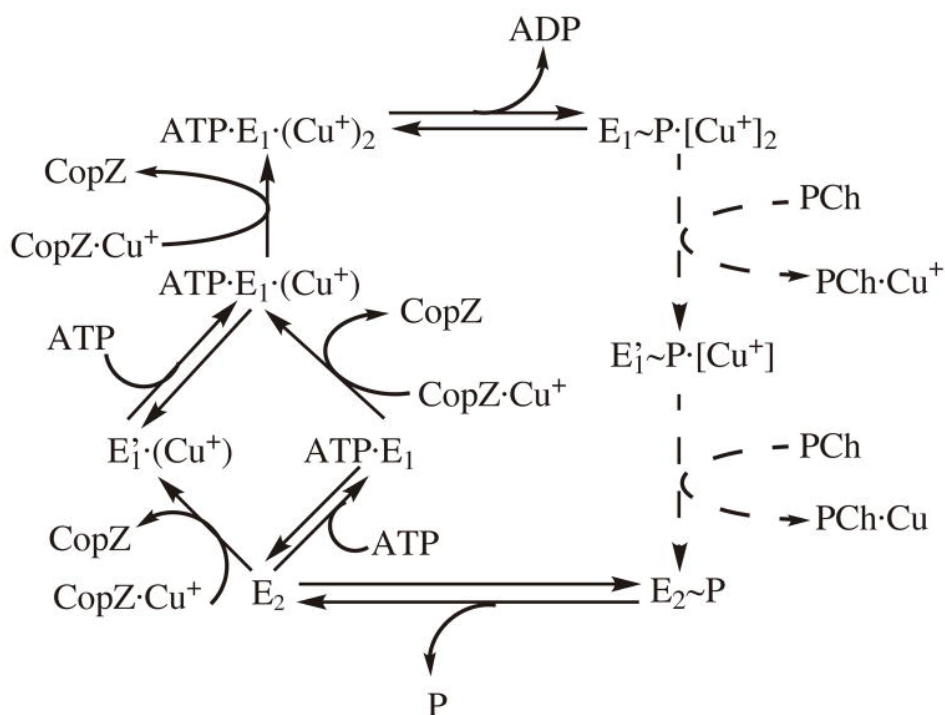


**Figure 1.16. Proposed catalytic and transport cycle of  $Cu^+$ -ATPases.**

CopZ chaperone delivers cytoplasmic  $Cu^+$  ion binding to trigger the copper-transporting cycle. Discontinued lines indicate proposed steps in the cycle. PCh indicates a hypothetical periplasmic  $Cu^+$ -chaperone/acceptor. The figure is adapted from [82].



## Aim of this study

The Cu (I)-transporting ATPase (CopA) plays a key role in cellular copper homeostasis and its malfunction causes severe diseases such as Wilson and Menkes diseases in human. Copper pumps consume ATP molecule as an energy source through its cytosolic domains interaction for transporting copper across cell membranes. Till nowadays, the entire structure of Cu-ATPase (including the cytosolic heavy-metal binding domain (HMBD)) is not available and the function role of HMBD in the catalytic ATPase cycle is still unknown. Recently, the crystal structure of HMBD-truncated CopA from *Legionella pneumophila* (LpCopA) was determined in transition *E2~P* and *E2P* states. The Molecular Dynamic (MD) simulation on the same protein shows a unique ion pathway in which the water molecules penetrate the transmembrane metal-binding site in *E2~P*.

This study aims at:

- 1- Improving our understanding of the cytosolic domain interactions in Cu<sup>+</sup>-ATPase, driving ATP binding, hydrolysis, phosphorylation, and copper transport.
- 2- Studying the structural and functional properties of LpCopA and its cytosolic domains and providing structural insights into the transmembrane helical domain.
- 3- Investigating the role of HMBD in the catalytic turnover and addressing the question of whether the HMBD plays an inhibitory role, an activating role or both.
- 4- Studying the domain-domain interactions using synthetic model peptides combining with circular dichroism and time-resolved fluorescence spectroscopy.
- 5- Investigating the water accessibility and mobility of the transmembrane metal-binding site using time-resolved fluorescence spectroscopy. Examining the validity of MD study of LpCopA using site-directed mutagenesis and site-specific fluorescent labeling in combination with Time-Correlated Single Photon Counting (TCSPC) technique.

## Chapter 2 Materials and Methods

### 2.1 Materials

#### 2.1.1 Culture Media and Antibiotics

##### **Luria Bertani Medium (LB) medium:**

- 20 g/l bacto-tryptone
- 5 g/l yeast extract
- 5 g/l NaCl

##### **SOB medium**

- 20 g/l bacto-tryptone
- 5 g/l yeast extract
- 0.5 g/l NaCl
- 0.186 g/l KCl
- 10 mM MgCl<sub>2</sub>
- 10 mM MgSO<sub>4</sub>

Heat sterilize the medium and add sterile MgCl<sub>2</sub> and MgSO<sub>4</sub> just before use.

##### **2x YT medium**

- 16 g/l Bacto-Tryptone.
- 10 g/l Bacto Yeast Extract.
- 5 g/l NaCl.

Adjust pH to 7.0 with 5N NaOH.

##### **Antibiotics**

If not otherwise noted antibiotics were applied at the following concentrations:

- 100 µg/ml Ampicillin
- 500 µg/ml Kanamycin
- 500 µg/ml Chloramphenicol

##### **LB-plates**

1 liter of LB medium supplemented with 15 g agar were autoclaved, and cooled to 50 °C under stirring. If desired, antibiotics were added from a stock solution. Finally the mixture was poured into petri-dishes and allowed to harden at RT.

## 2.1.2 Oligonucleotides and Vectors

Table 2.1. List of PCR primers, vectors and the fusion tags.

| Domains                                                                             | Purification tag    | Vector                                                             | Primers                                                                                                                                                                        |
|-------------------------------------------------------------------------------------|---------------------|--------------------------------------------------------------------|--------------------------------------------------------------------------------------------------------------------------------------------------------------------------------|
| Phosphorylation and Nucleotide binding domains (PN domain; residue no. 403-664 a.a) | N-term 6x His       | pProExHTa                                                          | <i>Fw_Eco_PN</i><br>5' ATTGAA TTCATGGCACAGAGC GGTGTTCTG                                                                                                                        |
|                                                                                     |                     | pET28a                                                             | <i>Rev_xho_PN</i><br>5' ATT CTC GAG TTA GCT CAG ACG ACG TGC TT                                                                                                                 |
|                                                                                     | N-term Strep-tag II | pET-51b Ek-LIC                                                     | <i>Fw_lic_PN</i><br>5' ACGACGACAAGATGGCACAGAGCGGTGTTCTGA                                                                                                                       |
|                                                                                     |                     |                                                                    | <i>Rev_lic_PN</i><br>5' GAGGAGAAGCCCGGTTAGCTCAGACGACGTGCTTT                                                                                                                    |
| N-term Strep-tag & C-term 10x His tag                                               | Mod_pET-51b         | <i>Fw_lic_PN</i><br>5' ACGACGACAAGATGGCACAGAGCGGTGTTCTGA           |                                                                                                                                                                                |
|                                                                                     |                     | <i>Rev_lic_noStop_PN</i><br>5' GAGGAGAAGCCCGGTGCGCTCAGACGACGTGCTTT |                                                                                                                                                                                |
| PN mut. L466Y                                                                       |                     |                                                                    | The codon-optimized DNA sequence of PN domain inserted in Mod_pET-51b was synthesized by GeneArt®<br><i>Fw_PN_L466Y</i><br>5' GGAACATCAGAGCGAACATCCGTATGCAAATGCAATTGTTTCATGCAG |
| Actuator domain (A; residue no. 207-334 a.a)                                        | N-term 6x His       | pET28a                                                             | <i>Fw_Eco_A-domain</i><br>5' ATTGAATTCATGAAAGCTCGCGAACAAACG                                                                                                                    |
|                                                                                     |                     |                                                                    | <i>Rev_xho_A-domain</i><br>5' TATCCTCGAGTTATCGCTGAATCGGCGCAC                                                                                                                   |
|                                                                                     | N-term Strep-tag II | pET-51b Ek-LIC                                                     | <i>Fw_Lic_A-domain</i><br>5' GACGACGACAAGATGAAAGCTCGCGAACAAACG                                                                                                                 |
|                                                                                     |                     |                                                                    | <i>Rev_Lic_A-domain</i><br>5' GAGGAGAAGCCCGGTTATCGCTGAATCGGCGCA                                                                                                                |
| I281W mutant (Ile281 in A-domain is substituted with Trp)                           | N-term 6x His       | pET28a                                                             | <i>Fw_I281W_A-dom</i><br>5' TTACCGGTGAACCGTGGCCGGTTGCAAAA                                                                                                                      |
|                                                                                     |                     |                                                                    | <i>Rev_I281W_A-dom</i><br>5' TTT TGC AAC CGG CCA CGG TTC ACC GGT AA                                                                                                            |
| Heavy metal-binding domain (HMBD; residue no. 1-79 a.a)                             | N-term Strep-tag II | pET-51b Ek-LIC                                                     | <i>Fw_Lic_MBD</i><br>5' GACGACGACAAGATGAAACACGACCACCA                                                                                                                          |
|                                                                                     |                     |                                                                    | <i>Rev_Lic_MBD</i><br>5' GAGGAGAAGCCCGGTTAATCAAGATATTCA GG                                                                                                                     |

Table 2.1. (Cont.).

| Proteins                                                                                     | Purification tag      | Vector                                                                                                                                                                                                                                      | Primers                                                                                                                                |
|----------------------------------------------------------------------------------------------|-----------------------|---------------------------------------------------------------------------------------------------------------------------------------------------------------------------------------------------------------------------------------------|----------------------------------------------------------------------------------------------------------------------------------------|
| <b>LpCopA</b>                                                                                | N-term<br>6x His tag  | pProExHTa                                                                                                                                                                                                                                   | <b>Fw_CopA</b><br>5' ATC <u>GAA TTC</u> ATG AAA CAC GAC CAC<br>CAT CAA GGA<br><b>Rev_CopA</b><br>5'ATTCTCGAGTTACAGGGTCCACACGTTTC<br>AG |
| <b>LpCopAΔHMBD</b><br>(HMBD-truncated<br>LpCopA)                                             |                       |                                                                                                                                                                                                                                             | <b>Fw_CopAΔMBD</b><br>5'ATG <u>GAA TTC</u> ATG GTT AGT CCG GAA<br>TAT CTG                                                              |
| <b>LpCopAΔHMBD</b><br>(HMBD-truncated<br>LpCopA)                                             | C-term<br>10x His tag | mod pET-<br>51b<br><br>(the DNA<br>sequences of<br>Strep-tag and<br>EK in pET-51b<br>Ek-LIC vector<br>are replaced<br>with EcoRI<br>recognition site<br>while XhoI<br>recognition site<br>is inserted<br>prior to 5'-end<br>of 10x His-tag) | <b>Fw_CopAΔMBD</b><br>5'ATG <u>GAA TTC</u> ATG GTT AGT CCG GAA<br>TAT CTG<br><b>Rev_CopA</b><br>5'ATTCTCGAGTTACAGGGTCCACACGTTTC<br>AG  |
| <b>C384S mutant</b><br>(Cys384 side chain<br>of LpCopAΔHMBD<br>are substituted by<br>Serine) |                       |                                                                                                                                                                                                                                             | <b>Fw_C384S</b><br>5'TGATTATTGCATGTCCGAGCGCACTGGG<br>TCTGGCAAC<br><b>Rev_CopA</b><br>5'ATTCTCGAGTTACAGGGTCCACACGTTTC<br>AG             |

## 2.1.3 DNA constructs

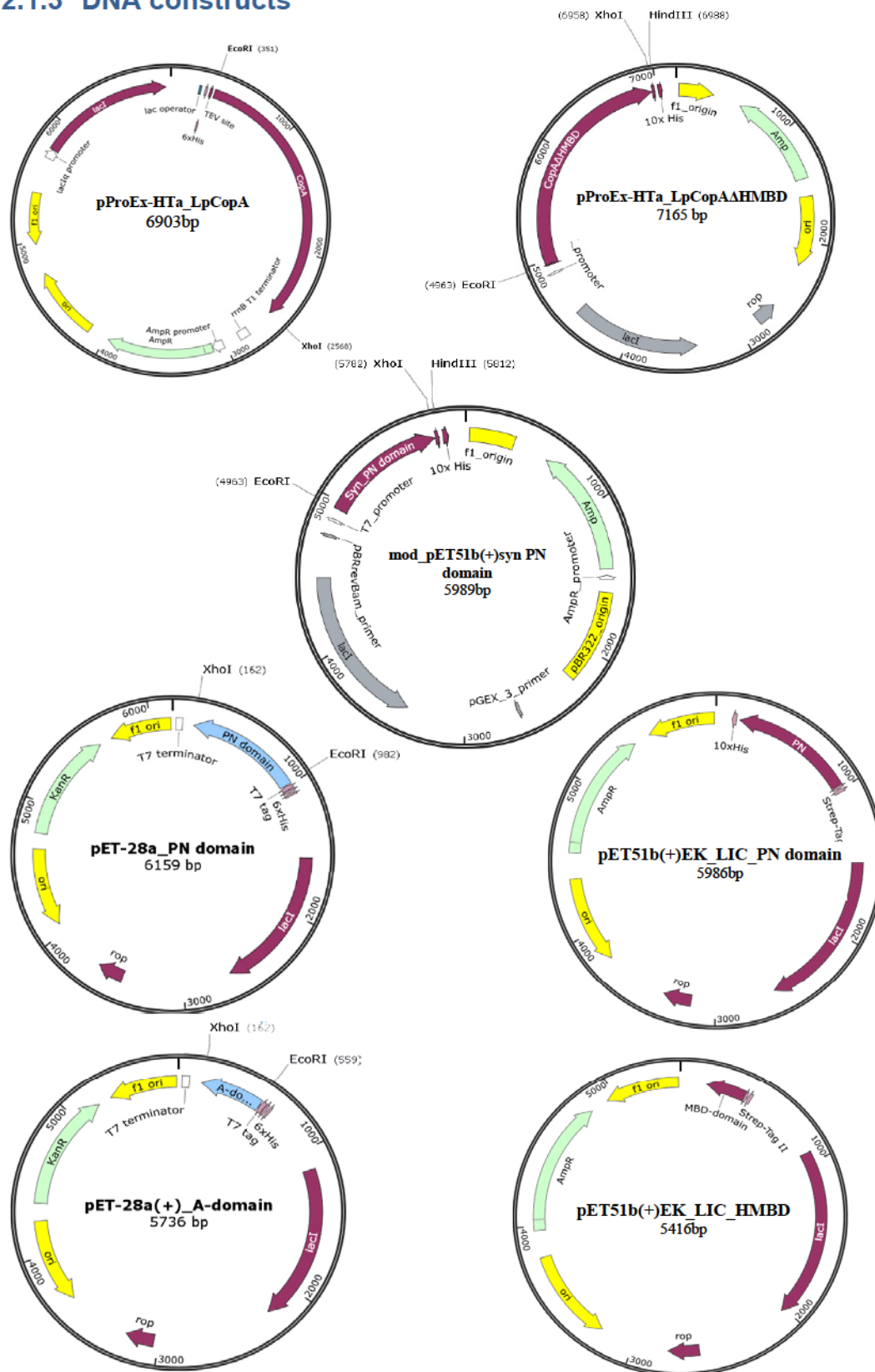


**Figure 2.1.** DNA constructs used for expression of LpCopA and its cytosolic domains. The labels indicate the names of plasmids and the inserts.

### 2.1.4 Common buffers

The most common buffers are listed here:

**PBS buffer**

50 mM NaH<sub>2</sub>PO<sub>4</sub> pH 7.4  
100 mM NaCl  
1 mM EDTA

**Buffer A**

50 mM Tris-HCl pH 7.5,  
200 mM NaCl  
1mM MgCl<sub>2</sub>  
30 mM Imidazole  
10% glycerol

**Buffer B**

50 mM HEPES-NaOH pH7.4  
200 mM Na<sub>2</sub>SO<sub>4</sub>  
50 mM K<sub>2</sub>SO<sub>4</sub>  
3 mM MgSO<sub>4</sub>  
20 % glycerol  
0.05 %DDM  
50 mM imidazole

**Buffer C**

50 mM Tris-HCl pH 7.4  
50 mM NaCl  
1 mM MgCl<sub>2</sub>

**Buffer W**

100 mM Tris-HCl pH 8.0  
150 mM NaCl  
1 mM DTT  
1 mM EDTA

**Buffer E**

100 mM Tris-HCl pH 8.0  
150 mM NaCl  
1 mM DTT  
1 mM EDTA  
2.5 mM D-desthiobiotin

**Assay buffer A**

30 mM Tris-HCl pH 7.5  
100 mM NaCl  
5 mM MgCl<sub>2</sub>

**Assay buffer B**

30 mM HEPES-KOH pH7.4  
100 mM KCl  
3 mM MgCl<sub>2</sub>  
1 mM β-mercaptoethanol  
0,05 % DDM  
1 mg/ml Asolectin  
100 μM CuSO<sub>4</sub>

**Assay buffer C**

50 mM Tris-HCl pH 7.4  
100 mM KCl  
1 mM MgCl<sub>2</sub>  
10% glycerol

## 2.2 Molecular cloning methods

### 2.2.1 Oligonucleotides design

Polymerase chain reaction (PCR) primers were designed with the aid of online software e.g. ([http://www.bioinformatics.org/sms2/pcr\\_primer\\_stats.html](http://www.bioinformatics.org/sms2/pcr_primer_stats.html) and <http://www.basic.northwestern.edu/biotools/OligoCalc.html>). The primers that were selected satisfied the General Guidelines for Standard PCR Primers outlined in the *Taq* PCR Handbook. Primers were synthesized by Eurofins MWG Operon, Germany. Lyophilized primers were dissolved in a small volume of autoclaved MilliQ water to make a 100 pmol/ $\mu$ l stock solution. Aliquots of working solutions containing 10 pmol/ $\mu$ l were prepared to avoid repeated thawing and freezing. Store all primer solutions at  $-20\text{ }^{\circ}\text{C}$ .

### 2.2.2 Polymerase chain reactions

Unless stated otherwise, the following conditions were constant for all PCRs and the solutions were from the QIAGEN *Phusion*<sup>®</sup> *High-Fidelity* DNA Polymerase Kit (Catalog number M0530S). The reaction was set up as described in the following:

**Table 2.2. The components of PCR reaction.**

| COMPONENT                 | 50 $\mu$ l<br>REACTION | FINAL<br>CONCENTRATION   |
|---------------------------|------------------------|--------------------------|
| Nuclease-free water       | to 50 $\mu$ l          |                          |
| 5X Phusion HF Buffer      | 10 $\mu$ l             | 1X                       |
| 10 mM dNTPs               | 1 $\mu$ l              | 200 $\mu$ M              |
| 10 $\mu$ M Forward Primer | 2.5 $\mu$ l            | 0.5 $\mu$ M              |
| 10 $\mu$ M Reverse Primer | 2.5 $\mu$ l            | 0.5 $\mu$ M              |
| Template DNA              | variable               | < 250 ng                 |
| Phusion DNA Polymerase    | 0.5 $\mu$ l            | 1.0 units/50 $\mu$ l PCR |

Precautions were taken to limit the PCR contamination or to detect any contamination that may occur. All PCR components were divided into smaller aliquots in fresh sterile tubes. The master mixes were prepared in a DNA-free environment using aerosol resistant tips and pipettors dedicated only to setting up PCR master mixes. All microfuge tubes were also from a sterile stock dedicated to making PCR master mixes. A negative control that contained no template was included in every set of reactions. When

appropriate, an additional negative control containing a template, such as an empty vector, was included to check the specificity of primers.

Polymerase chain reactions (PCRs) were carried out using a T1 Thermocycler (Biometra, Göttingen). An initial annealing temperature of  $T_1=55-65$  °C was increased 1 °C per cycle over 10 cycles, followed by 20 cycles at a constant annealing temperature of  $T_2=60-70$  °C depending on the primers used.

**Table 2.3. Touch-up PCR protocol**

|                      | <b>Temperature</b>          | <b>Time</b> | <b>Cycle No.</b> |
|----------------------|-----------------------------|-------------|------------------|
| Initial denaturation | 94 °C                       | 5 min       | 1                |
| Denaturation         | 94 °C                       | 30 s        | 10               |
| Annealing            | $T_1 \pm 55$<br>+1 °C/cycle | 45 s        |                  |
| Elongation           | 72 °C                       | 90 s        |                  |
| Denaturation         | 94 °C                       | 30 s        | 20               |
| Annealing            | $T_2$                       | 45 s        |                  |
| Elongation           | 72 °C                       | 90 s        |                  |
| Final Elongation     | 72 °C                       | 10 min      | 1                |
| Store                | 4 °C                        | $\infty$    | 1                |

### 2.2.3 Agarose gels

Agarose gel electrophoresis was used for the analysis of restriction and PCR products, and the preparative purification of DNA fragments. Agarose gels were made with 1x TBE and contained between 0.8 and 2.0% agarose. The percentage of agarose used in each gel varied with the expected size and desired resolution of the nucleic acid product(s); generally the concentration of agarose was increased as the expected size of the product(s) decreased. The agarose gels were all run in freshly diluted 0.5x TBE at 130 V ( Voltage). Before loading, DNA samples were mixed with 6x loading dye.  $\lambda$ -DNA/Eco130I was used as DNA marker. DNA was visualized using a standard ultraviolet transilluminator.

### 2.2.4 Gel extraction

The amplified PCR products were purified from agarose gels using the Wizard® SV Gel and PCR Clean-Up System Kit (Promega Catalog number A9281). The gel extraction carried out according to manufacturer's protocol.



### 2.2.5 DNA Cloning

All DNA constructs were prepared using restriction enzyme cloning except pET51b-Ek/LIC vector prepared by Ligation independent cloning (LIC).

#### 2.2.5.1 Restriction enzyme digestion

Purified PCR products and the target vector were digested by EcoRI/XhoI restriction enzymes. In a sterile 500- $\mu$ l microfuge tube, 5-7  $\mu$ g DNA was mixed with 2.5  $\mu$ l of each restriction enzyme (NEB), 5  $\mu$ l of 10X restriction enzyme buffer, 0.5  $\mu$ l of 100X BSA and sterile water to 50  $\mu$ l at 37 °C for 2-4 h. The reaction was stopped by heat inactivation at 65 °C for 20 min. Desired fragments were separated by standard agarose electrophoresis and eluted as described above.

#### 2.2.5.2 Ligation

Vector and fragment (1:2 molar ratio) were mixed with 2  $\mu$ l of 10X ligation buffer and 20U T4 DNA ligase (NEB) in a final volume of 20  $\mu$ l and incubated overnight at 18 °C.

#### 2.2.5.3 Ligation independent cloning (LIC)

PCR products were ligated into pET-51b Ek/LIC according to the manufacturer's protocol (Novagen Ek/LIC Cloning kit, catalog number 71570-3)

### 2.2.6 Site-directed mutagenesis

Site-directed mutagenesis was performed either by a mutagenesis kit or overlap extension PCR method. The QuikChange Lightning Multi Site-Directed Mutagenesis Kit was used according to the manufacturers' instructions. Site-directed mutagenesis by overlap-extension PCR has been described in [91]. The two separated PCR reactions produced two overlapping fragments of the original template, both containing the mutation within the overlap region. These fragments then needed to be purified from template DNA by agarose gel electrophoresis and subsequent extraction from the gel. At the second stage, these two PCR products were annealed to generate the entire fragment with the mutation. The flanking primers contain the restriction sites for ligating the fragment into the desired vector.

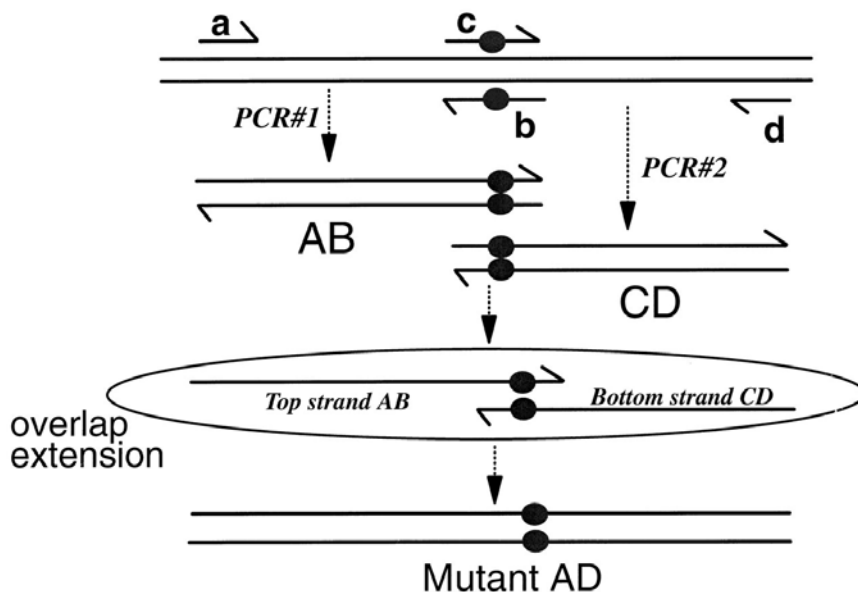


**Figure 2.2. Strategy used to introduce mutations via overlap extension PCR.**  
The diagram was taken from [91].

### 2.2.7 The production of competent *Escherichia coli* cells

Competent cells were produced according to Inoue et al. [92]. An LB plate was streaked from a *E. coli* strains glycerol stock and incubated overnight at 37 °C. An isolated colony from this plate was used to inoculate 5 ml of LB liquid medium that was then incubated overnight at 37 °C and 250 RPM. One hundred µl of this overnight culture was used to inoculate 125 ml of SOB liquid medium in a 500 ml flask. The inoculated SOB was then grown at 25 °C and 200 RPM until it reached an OD<sub>600</sub> of 0.4-0.6. The culture was rapidly cooled on ice for at least 10 min, then cells were collected by centrifugation for 10 min at 3000 x g and 4° C.

The pellets were resuspended in a total of 25 ml of fresh TB and chilled on ice for 10 min, then centrifuged for 10 min at 3000 x g and 4 °C. The pellets were then resuspended in a total of 4.7 ml of TB and pooled. The pooled mixture was swirled as 350 µl of DMSO was added. This mixture was divided into 50 µl aliquots that were shock-frozen in liquid nitrogen and stored at -80 °C. A number of precautions were taken to help produce highly competent cells. All glassware was washed, rinsed thoroughly, and sterilized before use. All reagents and medium were prepared immediately before use. When appropriate, all solutions and tubes were chilled before use. Whenever possible, manipulations were performed in the laminar flow hood.

### 2.2.8 Transformation of competent *Escherichia coli* DH5 $\alpha$ cells

Both ligation mixtures or intact plasmids were transformed into competent *E. coli* cells, DH5 $\alpha$  for DNA cloning and BL21(DE3) (Invitrogen) for overexpression. Competent cells were thawed on ice and 5-10  $\mu$ l of the ligation mixture or 5 ng of intact plasmid was added to the cells that were then left on ice for 15 minutes. The cells were exposed to a 42 °C heat shock for 45 seconds and then transferred on ice for at least 5 min. 200  $\mu$ l of LB broth was added to the cells and they were incubated with shaking at 37 °C for 1 hour. Microcentrifuge tubes were centrifuged for 1 min at 5,000 rpm in a microfuge centrifuge, and then 150  $\mu$ l of the supernatant were removed and the cells resuspend in the remaining medium. The cell suspension was plated out on a LB agar plate containing the appropriate antibiotic and incubated overnight at 37 °C. Negative controls containing only competent cells and ligation control were always setup.

#### 2.2.8.1 Glycerol stocks

Glycerol stocks were created to maintain each *E. coli* strain that had been transformed with a vector of interest. All glycerol stocks were made by mixing 0.5 ml of a sterile glycerol/LB liquid medium solution (1:1) with 0.5 ml of an overnight culture made of a single colony. The mixture was partitioned into sterile microcentrifuge tubes, frozen with liquid nitrogen, and stored at -80 °C.

## 2.3 Molecular biological methods

### 2.3.1 Expression of recombinant proteins

Recombinant proteins were commonly expressed either in *E. coli* BL21 (DE3) Gold or OverExpress C43(DE3)*pLysS* (lucigen). The cells were grown in 2x YT media with 50-100  $\mu$ g/ml appropriate antibiotics at 37 °C until they reached an OD<sub>600</sub> of 0.6 for the expression of cytosolic LpCopA domains and an OD of 1 for membrane protein expression. The expression started by the addition of IPTG at a final concentration of 0.5 mM (overnight at 18 °C). Cells were harvested at 10,000 xg, resuspended in PBS buffer (50 mM NaH<sub>2</sub>PO<sub>4</sub>, 100 mM NaCl and 1 mM EDTA) and again harvested at 10,000 xg. The cell pellet was frozen at -20 °C.

### 2.3.2 Purification of His-tagged Cytosolic domains

All procedures were performed at 4 °C unless stated otherwise. Frozen cells from 2l culture were suspended in 40 ml of buffer A (with 20 µg/ml DNaseI, 1 mM phenylmethylsulphonyl fluoride and 1x protease inhibitor cocktails (Sigma)) using a homogenizer. The cells were disrupted by 5 pass cycles through Microfluidizer M-110L at 16,000-18,000 p.s.i. The total cell lysates were centrifuged at 20,000 xg for 30 min, and the supernatant was filtered through 0.2 µm nitrocellulose filters to remove large aggregates before applying it to 2 ml of Ni-NTA Superflow resin slurry (Qiagen), pre-equilibrated with buffer A. The column was washed with 20 CV (column volumes) of buffer A, followed by vertical mixing with 5 CV of wash buffer A plus 10 mM MgCl<sub>2</sub> and 5 mM ATP for 20 min to remove DnaK. Finally, the column was washed with 3 CV of wash buffer A with 100 mM imidazole for C-terminal 10x His tagged protein and 30 mM imidazole for N-terminal 6x His tagged protein. The bound proteins were eluted in buffer A with 0.3 M imidazole.

To remove metal traces, 1 mM EDTA was added to the eluate before it was concentrated and exchanged for 50 mM Tris-HCl pH 7.4, 200 mM NaCl, 1 mM MgCl<sub>2</sub> and 10% glycerol using PD-10 desalting columns (GE Healthcare). The protein samples were divided into aliquots, flash-frozen in liquid nitrogen and stored in -80 °C. The protein purity was analyzed on 13% or 15% SDS-PAGE.

### 2.3.3 Purification of Strep-tagged cytosolic domains

The Strep-tagged cytosolic domains were purified in 1 ml Strep-Tactin Superflow slurry (IBA GmbH, Göttingen, Germany) according to manufacture's protocol [93]. The cleared lysates in buffer W were applied to the column equilibrated previously with the same buffer. The column was washed with 5 CV of buffer W to remove unbound proteins before the bound protein was eluted 6 times with 0.5 ml of buffer E (buffer W with 2.5 mM D-desthiobiotin). In the HMBD purification, mixtures of chelating agents (50 mM EDTA and 10 mM EGTA) and reducing agents (20 mM DDT and 5 mM TCEP) were added to the cell lysate.

### 2.3.4 Anion-Exchange Chromatography

The anion exchange purification was carried out only for the PN domain. The protein was dialyzed twice for overnight against buffer C (50 mM Tris-HCl pH 7.4, 50 mM NaCl, 1 mM MgCl<sub>2</sub>). The eluate was applied to a (CV= 1 ml) monoQ HR10/10 anion exchange column (GE-healthcare, Hamburg), pre-equilibrated with the buffer C. After a 10 CV washing step, the protein was eluted by applying a linear salt gradient from 0.05-1 M NaCl over 20 CV (flow rate 1 ml/min) and fractionated to 1ml.

### 2.3.5 The solubilization of membrane proteins

The protein expression and cell disruption of membrane proteins (LpCopA, LpCopAΔHMBD and C384S mutant) were carried out as described above in sections 2.3.1 and 2.3.2 except the buffer B with 20 µg/ml DNaseI, 1 mM phenylmethylsulphonyl fluoride and 1x protease inhibitor cocktails (Sigma) was used instead. 5 mM β-mercaptoethanol (β-ME) was added for LpCopA purification only. The total cell lysates were centrifuged at 10,000 xg for 15 min.

The solubilization was done either by addition of DDM to membrane pellet or directly to clear lysate as described below. In the solubilization protocol established in our lab, the lysate supernatant was centrifuged at 200,000 xg at 4 °C in a T647.5 rotor (Sorvall ultracentrifuge) for 1h, the membrane pellet was suspended in buffer B and solubilized by addition of solid DDM at 1% final concentration with gentle stirring for 60 minutes. Unsolubilized material was removed by ultracentrifugation at ~165,000 xg for 1 h at 4 °C. While, in the direct solubilization protocol, the supernatant of cell lysate was gradually titrated with 5% DDM solution till obtaining relatively clear solution (up to ~0.5% DDM, final concentration) and finally filtered by 0.2 µm nitrocellulose filter.

### 2.3.6 Purification of membrane proteins

The solubilized membrane proteins were applied to a pre-equilibrated 1 ml HisTrap HP column (GE Healthcare) at a rate of 1 ml/min and subsequently washed with 5 CV of buffer B with 0.5% DDM, 20 CV buffer B and finally 5 CV of buffer B plus 50 mM imidazole. Bound proteins were eluted with 400 mM imidazole and the buffer was exchanged with buffer B without imidazole before freezing as 300 µl aliquots in liquid nitrogen for storage at -80 °C.

### 2.3.7 Reconstitution of membrane protein in lipid

Proteoliposomes of LpCopA $\Delta$ HMBD and C384S mutant were prepared with modifications as indicated in [94]. 50 mg Asolectin lipid was dissolved in Chloroform/Methanol (2:1) and dried under N<sub>2</sub> gas stream for 2 h to remove organic solvent traces. The lipid was resuspended in pre-heated buffer of 50 mM HEPES pH 7.4 above the phase transition temperature (60 °C) to a final concentration of 25 mg/ml. MLVs were prepared by 11 freezing/thawing cycles and followed by extruding 20 times through 0.1  $\mu$ m polycarbonate membrane (Avanti Polar Lipids, Inc.) to form LUVs. LUVs solution was diluted in 50 mM HEPES pH 7.4 and 20% glycerol to a final concentration of 2.5 mg/ml and supplemented with 10% Triton X-100 at a detergent/lipid ratio of 3:5 (wt/wt). Purified BADAN-labeled LpCopA $\Delta$ HMBD and C384S mutant were added to lipid at a ratio of 1:50 (wt/wt; protein: lipid) at a final concentration of 0.05 mg/ml of protein. Bio-Beads SM2 was added as indicated, and the proteoliposomes were harvested at 42'000 rpm for 30 min at 4 °C. The pellets were resuspended in 50 mM HEPES pH 7.4 and 20% glycerol and stored at -80 °C. Incorporation of BADAN-labeled proteins was checked by SDS PAGE gel.

### 2.3.8 SDS polyacrylamide gel electrophoresis (SDS-PAGE)

One-dimensional SDS polyacrylamide gel electrophoresis (SDS-PAGE) of proteins was carried out essentially as described in [95]. Buffers were prepared as follows:

#### Separating gel buffer

1.5 M Tris-Cl pH 8.8  
0.4 % (w/v) SDS

#### 10x Running buffer

0.25 M Tris-base  
2 M glycine  
1% (w/v) SDS

#### Staining solution

0.025% (w/v) Coomassie brilliant blue G250  
50% (w/v) methanol  
10 % (w/v) acetic acid

#### Stacking gel buffer

0.5 M Tris-Cl pH 6.8  
0.4 % SDS

#### 3 x Sample buffer \*

150 mM Tris-HCl pH 6.8  
30% (v/v) glycerol  
10% (w/v) SDS  
0,05% (w/v) bromophenol blue  
10 mM DTT or  $\beta$ -mercaptoethanol

#### Destaining solution

30% (v/v) methanol  
10% (v/v) acetic acid

\*stored at -20 °C and rest at room temperature.

**Table 2.4. Preparation of SDS-PAGE gels.**

|                              | Separating Gel |            |            | Stacking Gel |
|------------------------------|----------------|------------|------------|--------------|
|                              | 11%            | 13%        | 15%        | 5%           |
| % Acrylamide                 | 11%            | 13%        | 15%        | 5%           |
| 30% Acryl/0.8%Bisacryl-amide | 7.3 ml         | 8.5 ml     | 10 ml      | 1.3 ml       |
| Separating gel buffer        | 5 ml           | 5 ml       | 5 ml       | -            |
| Stacking gel buffer          | -              | -          | -          | 2.5 ml       |
| ddH <sub>2</sub> O           | 10.3 ml        | 9.1 ml     | 7.6 ml     | 6.1 ml       |
| TEMED*                       | 13 $\mu$ l     | 13 $\mu$ l | 13 $\mu$ l | 10 $\mu$ l   |
| 10% Ammoniumpersulfate       | 67 $\mu$ l     | 67 $\mu$ l | 67 $\mu$ l | 50 $\mu$ l   |

\*: N,N,N',N'-tetramethylethylenediamine (TEMED)

Gels were composed as shown in Table 2.4. The proteins were separated using the BioRad Mini Protean 3 system. The gel was cast using two different layers of acrylamide concentrations. First, the components of the separating gel were poured into the space between two glass plates to a height of about 4 cm from the top of the glass plates and then covered by isopropanol to avoid contact with air until polymerization was complete. Isopropanol was then discarded and the stacking gel was poured over the separating gel up to the top of the glass plates. A comb was placed into the stacking gel which was left to polymerize. The gel cassette sandwich was covered with a wetted tissue and kept at 4 °C until use.

Samples were diluted with 3x concentrated sample buffer and incubated for 5 min at 90 °C prior to loading of the gels. Electrophoresis was carried out at voltage (200 V) in 1x running buffer. After SDS-PAGE, gels were stained using a staining solution for around 1 h and destained by incubation in destain solution.

### 2.3.9 Protein concentration determination

Protein concentration was determined as described by Bradford (1976) [96]. Bradford reagent (BioRad) was mixed with the protein sample, incubated at RT for 5 min and absorbance was determined at 595 nm using a spectrophotometer. Samples containing known concentrations of bovine serum albumin (BSA) were used to generate a standard curve. The absorption is proportional to the amount of protein present in the sample. Also, protein concentration was spectroscopically measured using the extinction coefficient calculated from with the Expsy website (<http://web.expsy.org/protparam/>).

## 2.4 Biophysical and Biochemical analysis

### 2.4.1 ATPase assay

#### 2.4.1.1 Fluorimetric enzyme-coupled ATPase assay

In the presence of inorganic phosphate, the enzyme purine nucleoside phosphorylase (PNP, EC 2.4.2.1) can phosphorylate the fluorescent substrate 7-methylguanosine ( $m^7\text{Guo}$ ) to 7-methylguanine ( $m^7\text{Gua}$ ) which has a much lower fluorescent quantum yield. Therefore, the PNP-catalyzed reaction can be coupled to an ATPase and phosphate production evaluated from a fluorescent decreasing in the following manner[97]:

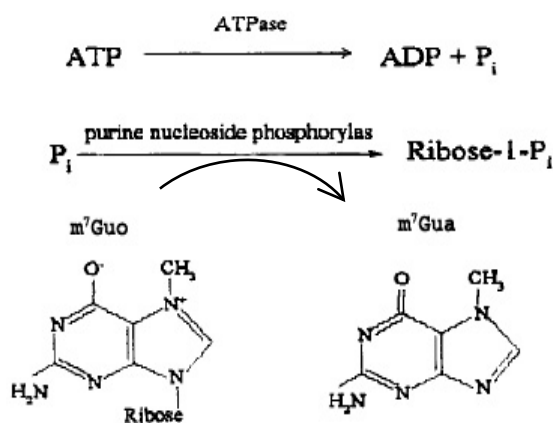


**Figure 2.3. Reaction mechanism of 7-methylguanosine ( $m^7\text{Guo}$ ) phosphorylation by phosphate liberated from ATPase.**

PNP enzyme (Sigma) was diluted to 30 U/ml and dialyzed overnight against 20 mM Tris-HCl pH 7.4 to remove additives from the enzyme. The PNP enzyme concentration was calculated by measuring absorbance at  $\lambda_{276\text{nm}}$  using a millimolar extinction coefficient  $42.3 \text{ mM}^{-1} \text{ cm}^{-1}$ , while  $m^7\text{Guo}$  substrate conc. was measured at  $\lambda_{257\text{nm}}$  and  $\lambda_{281\text{nm}}$  with millimolar extinction coefficient 81 and  $7.7 \text{ mM}^{-1} \text{ cm}^{-1}$  [98].

The assay was performed with a Perkin–Elmer LS-55 Luminescence Spectrometer. An assay mixture contained  $100 \mu\text{M}$   $m^7\text{Guo}$ ,  $0.5 \mu\text{M}$  nucleoside phosphorylase, 1 mM ATP in assay buffer A (30 mM Tris-HCl pH 7.5, 100 mM NaCl, 5 mM  $\text{MgCl}_2$ ). The buffer was equilibrated for 10 min until a constant fluorescence spectrum was obtained, symbolized as ( $F_0$ ). Then, PN domain was added in at a final concentration of  $120 \mu\text{g} / 0.5 \text{ ml}$  to initiate the reaction. The decrease in fluorescence was recorded per 1 min at



380 nm ( $\lambda_{\text{ex}} \sim 300$  nm) over 20 min and the final spectrum denoted as (F). Finally, 1 mM  $\text{KH}_2\text{PO}_4$  was added to convert the rest of  $\text{m}^7\text{Guo}$  to  $\text{m}^7\text{Gua}$ , and the fluorescence value of  $\text{m}^7\text{Gua}$  measured as ( $F_\infty$ ) and subtracted from all fluorescence values. A standard curve of 1, 5, 10, 26 and 65  $\mu\text{M}$  ATP concentrations was prepared as previous. The rate of fluorescence decay of  $\text{m}^7\text{Guo}$  was calculated as following:

$$\Delta F = \frac{(F_0 - F)}{F_0} \quad \text{Rate} = \frac{\Delta F}{\text{time}(\text{min})}$$

#### 2.4.1.2 Malachite green assay

Alternatively, the malachite green assay was used as a classical ATPase assay described by Lanzetta *et.al* [93]. This method is based on the complex formation between malachite green, ammonium molybdate, and free orthophosphate (inorganic phosphate,  $\text{P}_i$ ) under acidic conditions. Orthophosphate, liberated by an ATPase, forms a complex with ammonium molybdate in a solution of hydrochloric acid. The formation of the malachite green phosphomolybdate complex, measured at 620-650 nm, is directly related to the free  $\text{P}_i$  concentration. The malachite green assay is rapid and very sensitive to nanomolar  $\text{P}_i$  concentrations, but the color development is influenced by some assay components (such as glycerol, SDS and DMSO) and pH change. The malachite green/ammonium molybdate reagent was prepared by addition of 3 volumes 0.045% malachite green hydrochloride, 1 volume of ammonium molybdate (4.2% in 4 M HCl), and 1/50 volume of 1% Triton X-100 and left stand in dark for 1 hour before filtration through Whatman #2 paper.

The reaction mixture (150  $\mu\text{l}$ ) contained 10–20  $\mu\text{g}$  full length LpCopA in assay buffer B and 50-100  $\mu\text{g}$  PN or actuator domains in assay buffer A. The reaction was initiated by 2 mM ATP for 20 min at 37°C and stopped by 20 mM EDTA. The inhibitory effect of actuator-derived peptides was measured by addition of various conc. of Act-1 (0, 25, 50, 100 and 200  $\mu\text{M}$ ) to assay buffer B. 100  $\mu\text{l}$  reaction mixture was mixed with 800  $\mu\text{l}$  malachite green/ammonium molybdate reagent. After 1 min at RT, 100  $\mu\text{l}$  34% sodium citrate was added to stop the color development. Absorbance at 630 nm was measured, and phosphate release was quantified by comparison to inorganic phosphate standards.

## 2.4.2 BCA Cu<sup>+</sup> Assay

### 2.4.2.1 Cu<sup>+</sup> Loading to Proteins

Cu<sup>+</sup> loading of the HMBD was performed by incubating the protein in the presence of a 5-fold molar excess of CuCl<sub>2</sub>, 25 mM HEPES-NaOH pH 8.0 and 10 mM ascorbic acid for 10 min at room temperature with gentle agitation. The unbound Cu<sup>+</sup> was removed by passing through a PD-10 column. The blank was prepared as the following: the same amount of CuCl<sub>2</sub> was added to the buffer instead of HMBD and loaded to PD-10 column to use the eluted CuCl<sub>2</sub> traces as a blank. The amount of Cu<sup>+</sup> bound was determined by the BCA method [99]. CuCl<sub>2</sub> solutions were used as standards.

### 2.4.2.2 Cu<sup>+</sup>-Binding Affinity

The K<sub>D</sub> value of HMBD·Cu<sup>+</sup> was determined by using a competition assay with BCA (Pierce) followed by colorimetric determination of the BCA<sub>2</sub>·Cu<sup>+</sup> complex at 356 nm [93]. 2 μl of 1mM CuCl<sub>2</sub> was titrated into a 400 μl solution of 5 μM HMBD in 30 mM HEPES pH 7.3, 50 μM BCA and 1 mM ascorbic acid at RT. The color development was monitored at 356 nm. The standard curve of BCA<sub>2</sub>·Cu<sup>+</sup> complex was prepared under the same conditions.

## 2.4.3 Co-purification assay for domain-domain interaction study

Using Micro-spin column (23 mm length x 4 mm diameter, Pierce), the Strep-tagged HMBD (2 nmol) in 30 mM HEPES-NaOH pH 8, 100 mM NaCl, 1 mM DTT and 1 mM ascorbic acid buffer was mixed with 10 μM Ammonium tetrathiomolybdate (TTM) or with 30 μM CuCl<sub>2</sub> and loaded onto 50 μl Strep-Tactin resin, and washed with 4 CVs buffer to remove unbound HMBD and free Cu<sup>+</sup>. Afterwards, 2 nmol of A-domain or C-term 10xHis-tag PN domain (±100 μM AppNp) were added to the column containing Cu<sup>+</sup>-loaded or Cu<sup>+</sup>-free HMBD, and followed by washing with 8 CVs buffer. Finally, the HMBD was eluted with two consecutive 50 μl of elution buffer (containing the washing buffer plus 5 mM D-desthiobiotin). Because of the close proximity in size between the HMBD (which forms a dimer) and the A-domain, all SDS samples obtained from co-purification were labeled with 0.5 mM BADAN (thiol-reactive dye) to distinguish between the A-domain (cysteine-free) and the HMBD (containing 4 cysteines) bands under UV light. Thus the A-domain is visible only after Coomassie-

blue staining but not under UV light. Each SDS-PAGE gel was exposed to the UV light prior to staining with Coomassie blue dye.

The co-purification assay of the PN domain with the A-domain was also performed under the same conditions with some modifications. 6 nmol A-domain was loaded into 2 nmol of the dual tagged PN domain with N-term Strep and C-term 10xHis tags while it is bound to 100  $\mu$ l Strep-Tactin resin. The column was washed twice with 4CV of 50 mM Tris-HCl pH 8, 100 mM NaCl, 1 mM DTT, 1% glycerol. 0.1 mM ATP $\gamma$ S/5mM MgCl<sub>2</sub> was added to PN domain during binding to the column. The bound PN domain was eluted by adding 100  $\mu$ l elution buffer (washing buffer with 5 mM D-desthiobiotin).

## **2.4.4 Circular Dichroism measurements**

### **2.4.4.1 Secondary structure determination of cytosolic domains**

The PN and actuator domains (final concentration, 5  $\mu$ M) were dialyzed twice against 7 mM KH<sub>2</sub>PO<sub>4</sub> pH 7.4 buffer for overnight and filtrated using dialysis membrane (MW cut off 10kDa). The far-UV CD spectra of PN and A domains (260-178 nm) were measured at 25 °C in a 1 mm path-length cell using a Jasco J-815 Circular Dichroism Spectrometer. 400  $\mu$ l proteins were supplemented with 2  $\mu$ l of 1M MgSO<sub>4</sub>, 5 mM AMPPNP or ATP, 5 mM ADP, 10 mM Act1 and 20 mM VO<sub>4</sub>. The measurement parameters were 50 nm/min scanning Speed, 3nm bandwidth, baseline correction and 3 accumulations.

### **2.4.4.2 Thermal stability of cytosolic domains with additives**

CD measurements of 5  $\mu$ M PN domain, dissolved in 1ml of 10 mM KH<sub>2</sub>PO<sub>4</sub> pH 7.4 and 3 mM MgSO<sub>4</sub> buffer containing of 100  $\mu$ M ATP $\gamma$ S, 50  $\mu$ M Act-1 or both, were performed on a Jasco J-815 Circular Dichroism Spectrometer equipped with a temperature-controlling unit, using a 1 cm path-length cell with a magnetic stirrer.

To monitor thermal denaturation, CD spectra at 195-300 nm range were recorded at 2 °C steps, with increasing temperature from 20-91 °C at 2 °C/min with 1 nm bandwidth and 2s response time. Blank spectra of buffer solutions were subtracted from the PN domain spectra. At 222 nm, ellipticity was taken as a measure of the alpha-helical content of the protein and plotted against temperature.

### 2.4.5 Isothermal titration calorimetry (ITC)

An isothermal titration MicroCalorimeter (VP-ITC, from Microcal Inc., Northampton, MA) was used to measure the enthalpy changes resulting from the association of the PN domain with ligands. A typical titration involved 16 injections of 1.2 mM Act-2 (first 5  $\mu$ l/10 s and the rest 10  $\mu$ l aliquots / 20 s), at 3 min intervals, into the sample cell (volume of 1.4359 ml) containing 50  $\mu$ M PN domain in buffer C. All solutions were degassed prior to loading into the cell or syringe. The temperature of the solution in the titration cell was 25 °C and the solution was stirred at 307 rpm throughout the experiments. The resultant enthalpy changes were then analyzed using the inbuilt MicroCal Origin Version 7.0 to obtain the apparent dissociation constant,  $K_{app}$ , and other thermodynamic parameters ( $\Delta H$  and  $\Delta S$ ).

### 2.4.6 Cysteine accessibility assay of a CPC motif

#### 2.4.6.1 Fluorescent CPM Assay

N-[4-(7-diethylamino-4-methyl-3-coumarinyl)phenyl]maleimide (CPM from Setareh biotech), a fluorescent thiol reactive dye, was dissolved in DMSO (Sigma) at 4 mg/ml as the stock solution. The stock solution was diluted to 250  $\mu$ M in dye dilution solution (50 mM Tris-HCl pH 7.4, 150 mM NaCl, 3 mM MgCl<sub>2</sub> and 0.1% DDM) before use. The thiol reactivity assay was performed with total volume of 130  $\mu$ l of 10  $\mu$ M LpCopA $\Delta$ HMBD or C384S samples in 50 mM Tris-HCl pH 7.4, 150 mM NaCl, 3 mM MgCl<sub>2</sub>, 5% glycerol 0.1% DDM, 1mg/ml asolectin and  $\pm$  50  $\mu$ M Act-1 in a 1 cm path-length quartz micro-cuvette (Hellma). The reaction started by addition of 7.5 of the diluted dye to the protein solution and it was incubated for 20 min at room temperature. The mixed solution was excited at 387 nm and emission spectra in range of 400-550 nm was recorded every 1 min using a Perkin–Elmer LS-55 Luminescence Spectrometer.

### 2.4.6.2 Colorimetric 4-DPS assay

Another experiment was used to investigate the cysteine accessibility of LpCopA $\Delta$ HMBD using 4,4'-Dithiodipyridine (4-DPS from Sigma). When 4-DPS is reduced by thiols, it forms 4-thiopyridone (4-TP), which absorbs strongly at 324 nm. 13 mM 4-DPS was dissolved in 95% ethanol and diluted to 2.5 mM in assay buffer before use. 50  $\mu$ M 4-DPS was added to 5  $\mu$ M LpCopA $\Delta$ HMBD in 250  $\mu$ l of 50 mM Tris-HCl pH 7.4, 150 mM NaCl, 3mM MgCl<sub>2</sub>, 0.1% DDM, 1mg/ml Asolectin and  $\pm$  50  $\mu$ M Act-1 in a 1 cm path-length cell (Hellma). The time course of 4-TP formation was monitored at 324 nm using Perkin Elmer Lambda 35 UV-VIS spectrometer.

### 2.4.7 Steady-state Fluorescence measurements

#### 2.4.7.1 TNP-nucleotides affinity of PN domain

Trinitrophenyl (TNP) nucleotides, i.e., fluorescent analogues of nucleotides, have been utilized as a valuable probe for examining the nucleotide affinity of the PN domain in other P-type ATPases. Here, 3  $\mu$ M of PN domain in 500  $\mu$ l of assay buffer C was titrated with 400  $\mu$ M TNP-ATP (Jena Bioscience) or TNP-AMP at room temperature. The concentration of TNP-nucleotides was determined spectrophotometrically using an extinction coefficient of 25.0 and 18.5 mM<sup>-1</sup> cm<sup>-1</sup> at  $\lambda_{\text{max}}$  259 and 470 nm, respectively. Binding of TNP-nucleotides was observed by measuring the increases in fluorescence from 480-600 nm at excitation wavelength 405 nm. The same experiment procedure was used with assay buffer C without protein as a control and the result subtracted from all measurements. All titrations were carried out in 1.0 cm path length quartz cuvette.

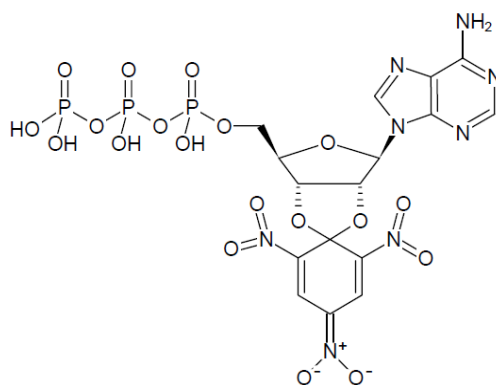


**Figure 2.4. Structure of TNP-ATP at neutral or basic pH values.**

### 2.4.7.2 Interaction of actuator-derived peptides with the PN domain

The titration was carried out by measuring changes in Trp emission of Act-2 upon binding to the PN domain. The measurement was made using quartz cuvette containing 130  $\mu$ l of buffer C (50 mM Tris-HCl pH 7.5, 200 mM KCl, 1 mM MgCl<sub>2</sub>, and 10% glycerol) and constant concentration of Act-2 at 25  $\mu$ M throughout titration. Fluorescence changes were monitored by recording emission spectra between 300 -400 nm with excitation at 285 nm.

The titration started by addition of equal volumes of PN domain and Act-2 to reach at 130  $\mu$ l of 55  $\mu$ M and 25  $\mu$ M final concentrations, respectively. Secondly, 50  $\mu$ l of 25  $\mu$ M Act-2 was added to dilute the PN domain to 40  $\mu$ M. Sequentially, 50  $\mu$ l of reaction mixture was replaced by 50  $\mu$ l of 25  $\mu$ M Act-2. The concentration of PN domain was calculated throughout the titration. The same experimental scheme was repeated in the presence of 100  $\mu$ M AppNp.

### 2.4.7.3 Binding kinetics of actuator-derived peptides to the PN domain: Stopped-Flow Fluorescence

The kinetics of the association of Act-2 with the PN domain was monitored by changes in the tryptophan emission intensity of Act-2 over the time. A tryptophan residue has been introduced in the actuator-derived sequence specifically for this purpose (see Chapter 6). The time course of Act-2 emission was measured using a Perkin–Elmer LS-55 Luminescence Spectrometer equipped with a SFA-20 rapid kinetic accessory from Hi-Tech Scientific. Equal volumes of Act-2 and PN domain were rapidly mixed with a dead time  $\sim$  8ms to make final concentrations of 25  $\mu$ M and 20  $\mu$ M, respectively. The sample was constantly excited at 285 nm and the emission recorded at 335 nm with integration time and time interval of 20 ms. To measure the association in the presence of a non-hydrolyzable ATP analog, 200  $\mu$ M AppNp was added to the PN domain prior to rapid-mixing with peptide Act-2. Three to four injections were averaged to generate the final traces.

### 2.4.8 Fluorescence lifetime measurements

The local environment around the conserved CPC motif in the TM-MBS of LpCopA was investigated by covalently labeling the thiol residues of the conserved motif with BADAN probe and measuring the time-resolved fluorescence of the bound dye using

TCSPC method. The labeling assay was carried out by two protocols as described below for LpCopA $\Delta$ HMBD and C384S mutant.

#### **2.4.8.1 Labeling of LpCopA $\Delta$ HMBD and C384S mutant with BADAN**

Initially, the kinetics of LpCopA $\Delta$ HMBD and C384S mutant reactivity with the Cys-reactive fluorophore BADAN was measured by addition of equivalent volumes of 10  $\mu$ M LpCopA $\Delta$ HMBD or C384S mutant and 27  $\mu$ M BADAN (Molecular Probes), pre-incubated in buffer (50 mM Tris-HCl pH 7.4, 150 mM NaCl, 3 mM MgCl<sub>2</sub> and 0.3% DDM) for at least 1hr prior to the reaction. The reactivity was monitored by measuring emission spectra of BADAN between 410-700 nm at excitation wavelength 390 nm for 20 min.

#### **2.4.8.2 On-column BADAN labeling of LpCopA $\Delta$ HMBD and C384S mutant**

As described in section 2.3.6 and before elution, the LpCopA $\Delta$ HMBD and the C384S mutant bound to the Ni-NTA column were washed with 10 CV of 20  $\mu$ M BADAN in buffer B at 0.5 ml/min followed by 50 CV of buffer B to remove excess BADAN. The BADAN removal was checked by measuring emission spectra between 410-700 nm ( $\lambda_{3exc} = 390$  nm) in the washing fractions. Bound proteins were eluted with 400 mM imidazole and concentrated using Vivaspin 500 membrane 10,000 MWCO (Sartorius AG, Germany) before loading them on a disposable PD-10 desalting column (GE Healthcare) to remove imidazole. Protein were frozen in 300  $\mu$ l aliquots in liquid nitrogen and stored in -80 °C. The BADAN-labeled proteins were reconstituted into lipid bilayer of Asolectin as described in section 2.3.7.

#### **2.4.8.3 Time-Correlated Single Photon Counting (TCSPC) measurements**

TCSPC measurements and analyses were carried out by Mr. Petr Pospisil, at Prof. Martin Hof's lab. Stationary emission spectra were obtained on Fluorolog-3 spectrofluorometer (model FL3-11; HORIBA Jobin Yvon) equipped with a Xenon-arc lamp. All spectra were collected in 1 nm steps (2 nm bandwidths were typically chosen for both the excitation and emission monochromators). Time-resolved fluorescence decays were measured using the time-correlated single photon counting technique on an IBH 5000 U SPC instrument equipped with a cooled Hamamatsu R3809U-50

microchannel plate photomultiplier with 40 ps time resolution and time setting of 14 ps per channel. Bandwidths for both the excitation and emission monochromators were set to 16 nm for the DDM measurements and for the proteoliposomes measurement bandwidths were set to 32 nm and 16 nm for excitation and emission monochromators respectively. In order to eliminate scattered light, a 399 nm cut-off filter was used. Samples were excited at 373 nm with an IBH NanoLED-11 diode laser (80 ps fwhm) with a repetition frequency of 1 MHz. The detected signal was kept below 20 000 counts per second in order to avoid shortening of the recorded lifetime due to the pile-up effect. Measurements were performed under magic angle in order to avoid anisotropy effect. Fluorescence decays were fitted (using the iterative reconvolution procedure with IBH DAS6 software) to a multiexponential function (eq. 1) convoluted with the experimental response function IRF ("prompt"), yielding sets of lifetimes  $\tau_i$  and corresponding amplitudes  $A_i$ .

$$I(t) = \sum_i A_i e^{-t/\tau_i} \otimes IRF \quad (1)$$

The effect of hydration and mobility of the environment can be estimated from the dynamic Stokes shift. Stokes shift is usually manifested as a time evolution of the maxima of the time resolved emission spectra (TRES). TRES is calculated from the intensity decays  $D(t, \lambda)$  and steady state emission spectra  $S_0(\lambda)$  (eq. 2).

$$S(\lambda, t) = \frac{D(t, \lambda) \times S_0(\lambda)}{\int_0^{\infty} D(t, \lambda) dt} \quad (2)$$



## Chapter 3

### **Expression, Purification and Functional characterization of Copper-Transporting ATPase and its Cytosolic domains from *L. pneumophila***

#### Introduction

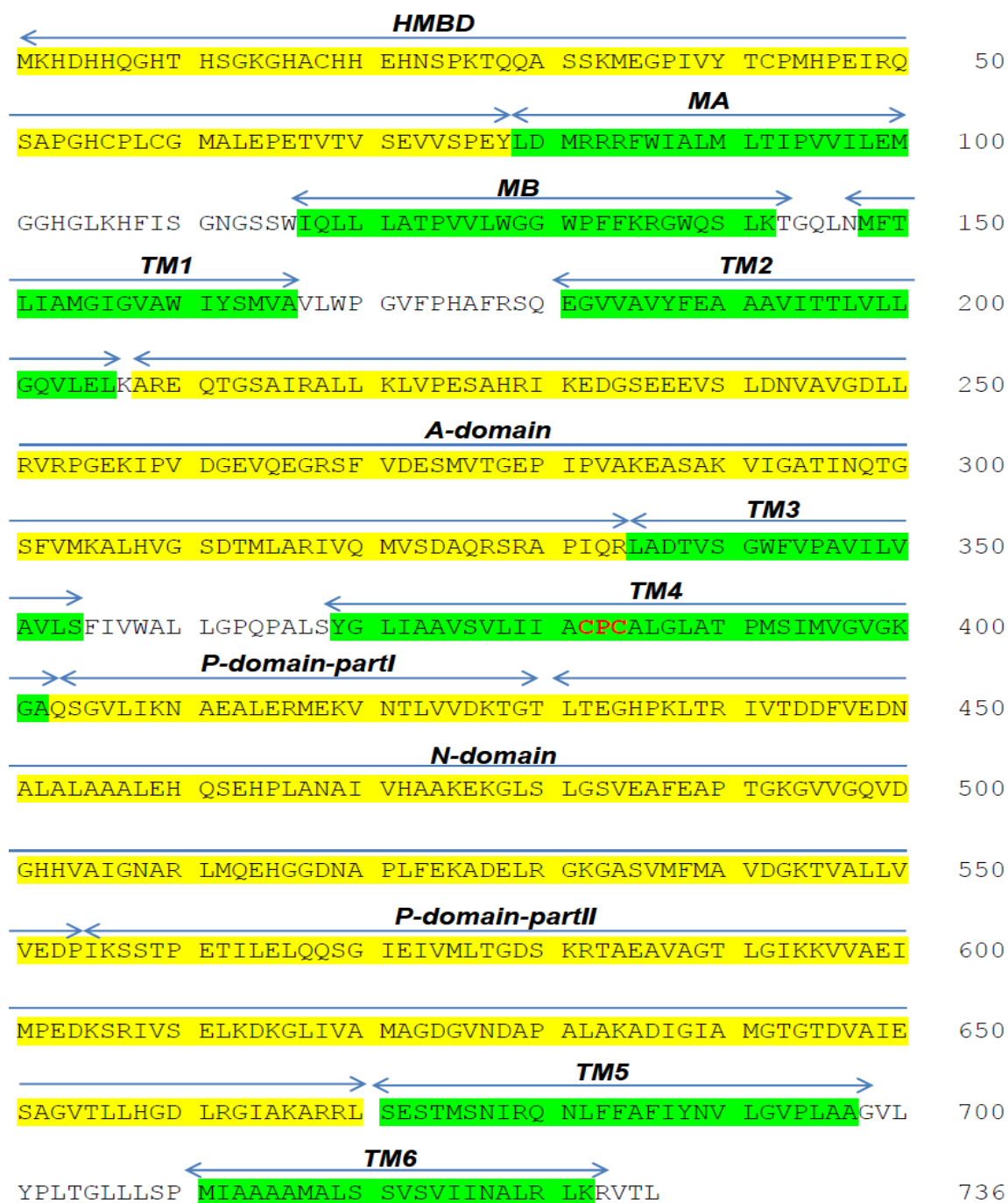
P<sub>1B</sub>-type ATPases transport heavy metal ions against the electrochemical gradient across membranes using energy liberated from ATP hydrolysis. It consists of 4 cytosolic domains termed the HMBD (N-terminal heavy metal-binding domain), the A- (actuator), the P- (phosphorylation), the N- (nucleotide-binding) domains and 8 transmembrane (TM) helices with a CPX or SPC motif at the 6<sup>th</sup> TM. The rearrangement of the cytosolic domains induces open–close movements of the TM helices. Several studies have used the isolated catalytic fragments of the copper-transporting CPX-ATPase for studying their functional characterization and for determining their crystal structures due to the difficulties in crystallization of integral membrane proteins. Recently, the crystal structure of HMBD-truncated Copper-transporting ATPase from *L. pneumophila* (LpCopA) has been determined in *E2~P* and *E2P* states [32, 100].

Here, we expressed functionally the LpCopA and its cytosolic domains for further structural, biochemical and biophysical characterizations as it will be discussed later in Chapters 4-7. Moreover, we developed and optimized a fluorometric ATPase assay for suiting the harsh assay conditions of heavy-metal transporting ATPases.

## Results and discussion

### 3.1 Expression and Purification of Cytosolic domains of LpCopA

A)



B)

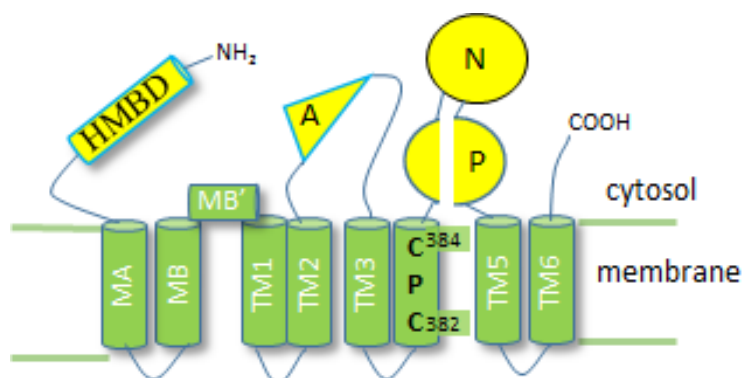


**Figure 3.1. The overview of the expressed cytosolic domains.**

**A)** The amino acid sequence of LpCopA. **B)** A schematic diagram of LpCopA structure. The cytosolic HMBD, A-, P- and N-domains in yellow denote to the heavy metal-binding domain, the actuator, the phosphorylation and the nucleotide-binding domains, respectively. Transmembrane helices (MA, MB and TM1-TM6) are in green. Both cysteines 384 and 382 of TM-MBS locate at TM4. The amino acid sequence of LpCopA retrieved from uniprot (Q8RNP6). The TM segments determined by DAS-TMfilter server and according to LpCopA crystal structure [32].

The cytosolic domains of P-type ATPases play a key role in the modulation of ion transport. The expression and biophysical characterization of the isolated cytosolic domains contribute to the understanding of their functionality as modules in the conformational transitions of the full length protein. During the Post-Albers cycle, the cytosolic domains rearrange in a specific manner to mediate the metal ion (de)occlusion, ATP hydrolysis and (de)phosphorylation steps. The experiments described in this part aim at over-expression and purification of these domains.

The constructs will then be used to investigate their structure and possible autonomous interactions independently of the transmembrane part of the ATPase. This approach can give insight into the role of different domain interactions during the Post-Albers- cycle. Furthermore, the expression and functional analysis of the isolated cytosolic domains are of conceptual importance for peptide interference studies performed in this work (see Chapter 6), where the synthetic peptides from an interdomain-binding epitope are used to disrupt interaction during the catalytic cycle. Obviously, the binding of such peptides would have to be demonstrated for the isolated cytosolic domain in the first place.

The cloning and purification will be described as well as the establishment of a fluorometric ATPase assay. The latter was chosen and optimized to allow measuring the ATPase activity in aqueous solution in both the absence and the presence of detergent, such that data could be obtained under identical conditions for the isolated cytosolic domains and the full length constructs of LpCopA.

### 3.1.1 DNA cloning of cytosolic domains.

Using touch-up PCR (TU-PCR) protocol in which PCR begins with an initial annealing temperature increasing by one degree with each cycle, the DNA sequences of the cytosolic domains, i.e. HMBD (250 kb), A-domain (390 kb) and PN domain (819 kb) were isolated from the codon-optimized DNA sequence of LpCopA synthesized by GeneArt (Invitrogen) as shown in Fig. 3.2. Afterward, the PCR products were extracted from DNA gel using the Wizard SV Gel and PCR Clean-Up System kit and the purified DNA fragments of HMBD and A-domain were cloned into pET-51b(+) Ek/LIC, pET28a plasmids, respectively. While the DNA fragment of the PN domain was ligated initially into pET28a plasmid and latter re-cloned into several plasmids, such as pET-51b(+) Ek/LIC, modified pET-51b(+), pPR-IBA1 and pProEX-HTa plasmids to optimize the expression and the stability of the protein as it will be discussed in the next sections. Both of the PCR fragments of PN-domain and desired vector were digested with EcoRI/XhoI restriction enzymes and purified using the same method mentioned above. Figure 3.3 shows the DNA gel electrophoresis of digested pET28a plasmid with EcoRI/XhoI restriction enzymes.

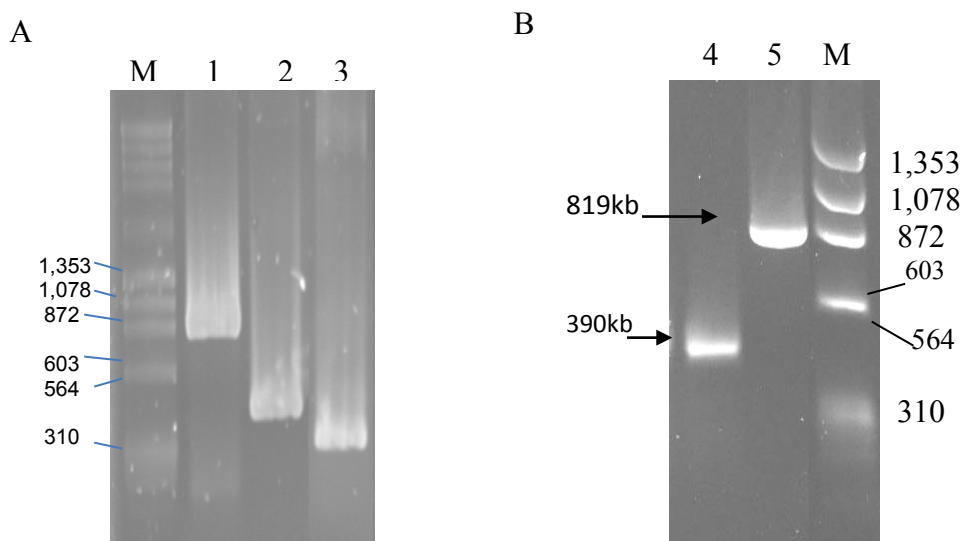


**Figure 3.2. DNA gel Electrophoresis of the isolated DNA encoding cytosolic LpCopA domains.**

The DNA sequences of cytosolic domains were isolated from the codon-optimized DNA sequence of LpCopA protein (GeneArt) by PCR technique and purified using the Wizard SV Gel and PCR Clean-Up System (Promega). **A)** The PCR products of the cytosolic domains. **B)** The purification of PCR products. M, 1 Kb molecular weight DNA Ladder; lanes 1&5, PCR product encoding PN domain; lanes 2&4, PCR product encoding Actuator domain and lane 3, PCR product encoding HMBD domain. The samples were run in 1% agarose gel.

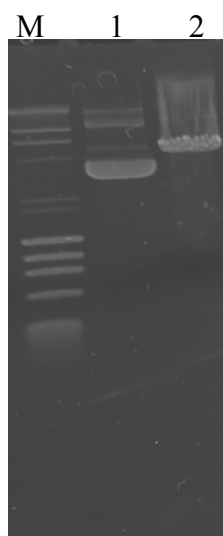


**Figure 3.3. DNA gel Electrophoresis of digested pET28a plasmid.**

The pET28a plasmid was digested with EcoRI/XhoI restriction enzymes and loaded into 0.8% agarose gel. The digest pET28a was extracted according to manufacture's protocol of the Wizard SV Gel and PCR Clean-Up System (Promega). Lane M, 1 Kb molecular weight DNA Ladder; lane 1, undigested pET28a plasmid, lane 2, digested pET28a plasmid.

### 3.1.2 Expression and purification of cytosolic domains

The two contiguous cytosolic regions, responsible for transient phosphorylation and nucleotide binding (i.e. the PN domain) on the one hand and for dephosphorylation (i.e. the A-domain) on the other hand, were initially expressed in *BL21-Gold(DE3)* harboring pET28a with an N-terminal 6x His tag in 2xYT medium at 18 °C. Additionally, the heavy metal-binding domain (HMBD) was expressed with N-terminal Strep-tag in *BL21-Gold(DE3)* /pET51b in the same expression conditions as mentioned above. These domains are easily soluble in cell lysis buffer and can be separated from insoluble materials by centrifugation at 10,000 xg.

#### 3.1.2.1 The purification of HMBD

The N-terminal heavy metal-binding domain (HMBD), containing around 75 amino acid residues, is suggested to play a regulatory role during the catalytic ATPase cycle. The crystal structures of the most CPx-ATPases are solved without including the HMBD; the independent expression of the HMBD could therefore allow understanding its functional role in the catalytic cycle by studying its interaction with other cytosolic domains. Such a study is particular of interest for the putative autoinhibitory role of the HMBD in the Cu-free state as will be further discussed in Chapter 5. The DNA sequence encoding the HMBD was isolated from the whole DNA sequence of LpCopA via PCR and ligated into pET51b vector using a ligation-independent cloning (LIC) method. The insertion of the HMBD-encoding DNA sequence was confirmed by DNA sequencing. The HMBD, tagged with an N-terminal Strep tag II, was expressed overnight in *BL21-Gold(DE3)* by 0.5 mM IPTG.



**Figure 3.4. Schematic diagram of 11 kDa Strep-tagged HMBD protein.**

The SDS-PAGE gel of the expressed host shows a dimer formation of HMBD as shown in Fig. 3.5. This anomalous band does not change in the presence of strong reducing agents added to the SDS-loading buffer, so that a disulfide-induced dimer formation is unlikely. The reason for this dimerization is unknown as it has not been

observed previously [63, 64], except in the case of the C-HMBD from *A. fulgidus* [55] where a domain-swapped dimer forms in crystals as well as in solution due to salt bridges and hydrogen bonding between monomers [55]. Another possibility could be that the HMBD, which contains a ferredoxin-like fold, exhibits copper-mediated dimerization such as several CopZ(s) [53, 101-105].

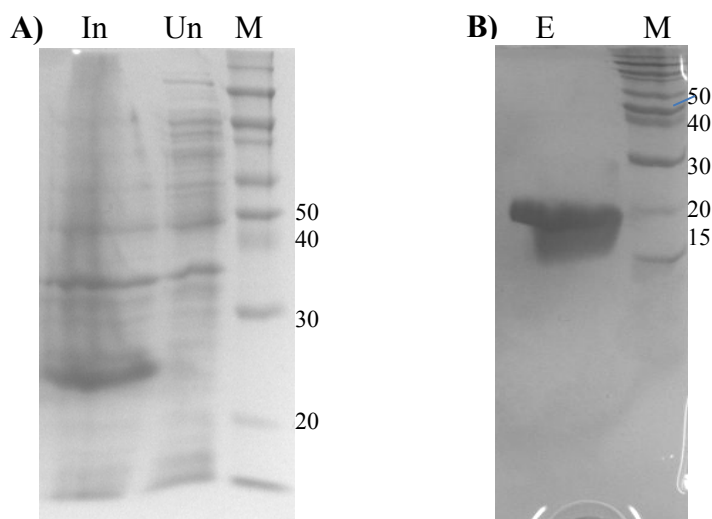


**Figure 3.5. SDS-PAGE analysis of HMBD expression in 2xYT medium**

**A)** The HMBD domain is expressed in *BL21 Gold* strain carrying pET51b vector. **B)** The elution of Strep-tagged HMBD from Strep-Tactin column. The HMBD always appears in dimeric form. Lane M, molecular mass standard (kDa); lane Un, uninduced cells; lane In, induced cells; lane E, the purified HMBD from Strep-Tactin column. The lane In exhibits a smear due to addition of excess of  $\beta$ -ME.

Attempting to break down the interaction between HMBD monomers, mixtures of metal chelators, such as 50 mM EDTA, 10 mM EGTA and 20  $\mu$ M TTM (in some preparations), and reducing agents, such as 20 mM DDT and 5 mM TCEP, were added to the cell lysate prior to loading into Strep-Tactin resin to chelate the metal ions and break down the disulfide bonds. The HMBD bound to Strep-Tactin column was washed with 4CVs with the same buffer as above and the concentration of reducing agents and metal chelator gradually reduced to 1 mM DTT and 1 mM EDTA in the elution buffer. In other preparations, EDTA was omitted from the elution buffer for further metal affinity assay. The SDS-gel of purified HMBD shows the persistence of domain dimerization despite the harsh chelating and reducing condition; this reveals that the dimerization is caused by another process than metal binding or disulfide bond formation.

### 3.1.2.2 Actuator domain purification

The Actuator domain (A-domain), containing 124 amino acid residues (~18 kDa), was expressed in *BL21-Gold(DE3)* strain at 18 °C in 2xYT medium (Fig. 3.7). The I281 side chain of A-domain was replaced with tryptophan, according to the instructions of Stratagene Site-Directed Mutagenesis Kit, for further spectroscopic experiments discussed in the Chapters 2.

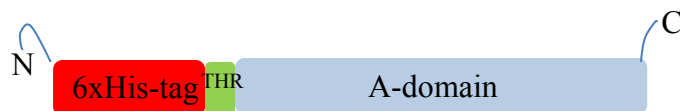


**Figure 3.6. Schematic diagram of N-terminal 6xHis-tagged A-domain proteins were used in this study.**

The supernatant of the cell lysate was filtrated before loading onto Ni-NTA slurry. The purification of the A-domain was unproblematic and the protein was often purified in a single-step thoroughly >95% purity as shown in Fig. 3.7A. The 6xHis-tag of A-domain was cleaved off by Thrombin protease (Fig. 3.7B) for further interaction assay of A-domain with HMBD (see Chapter 5).

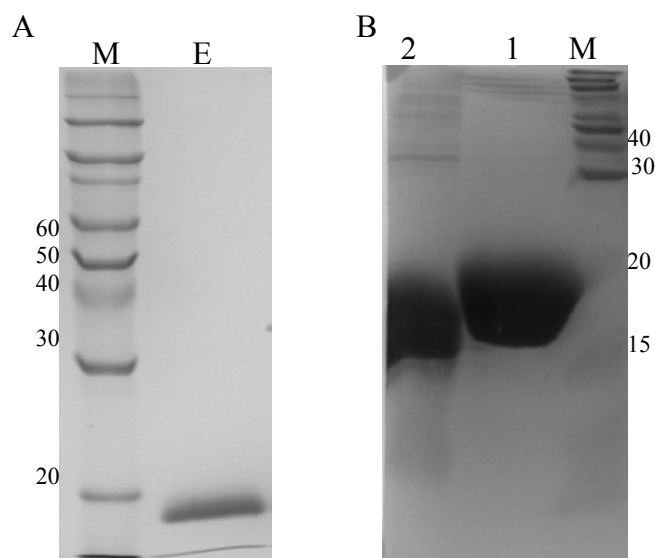


**Figure 3.7. SDS-PAGE analysis of purified A-domain.**

**A)** The A-domain protein, tagged with N-term 6xHis-tag, was purified using Ni-NTA resin. Lane M, molecular mass standard (kDa) and lane E, the eluted A-domain from the Ni-NTA column (12% acrylamide gel used), while **B)** the 6xHis-tag was removed by treatment A-domain with 0.1 Unit Thrombin. Lane 1: before and lane 2: after the His-tag cleaved from A-domain (15% acrylamide gel used).



### 3.1.2.3 Phosphorylation-/Nucleotide-binding domain purification

As the phosphorylation domain forms many intramolecular contacts with the nucleotide-binding domain in the structure of P-type ATPases, we expressed both domains as a single domain named “PN domain”. Initially, the PN domain was expressed in pET28a vector with an N-terminal 6xHis-tag and purified by Ni-NTA resin. Unfortunately, the PN domain was found to be prone to partial degradation upon cell lysis as shown in Fig. 3.8.

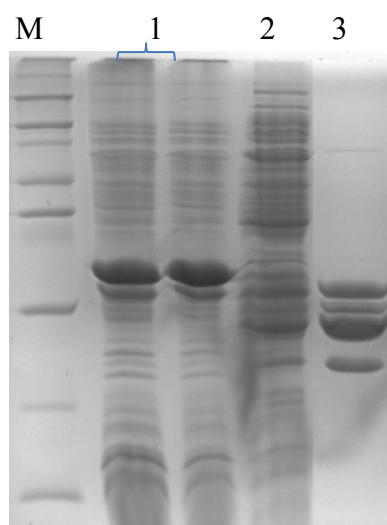


**Figure 3.8. SDS-PAGE analysis of N-terminal His-tagged PN domain purification.**

The PN domain expressed in *BL21-Gold(DE3)* harboring pET28a plasmid at 18°C in 2xYT medium. PN domain was purified using Ni-NTA chromatography. PN domain exposed to degradation upon cell lysis. Lane M, molecular mass standard (kDa); lane 1, cell induced PN domain; lane 2, soluble fraction of cell extracts; while lane 3, degraded fragments of PN domain. 13% acrylamide gel was used.

Despite using a wide spectrum of protease inhibitors (Table 3.1) and performing all purification steps on ice, the degradation of PN domain was not suppressed even though the protease inhibitors were added to the lysis buffer before cell disruption.

**Table.3.1. List of protease inhibitors were used to prevent PN domain degradation.**

| <b>Protease inhibitors</b>                                      |
|-----------------------------------------------------------------|
| Complete protease inhibitor cocktail (EDTA-free, Roche)         |
| SIGMAFAST™ Protease inhibitor cocktail (EDTA-free)              |
| Home protease inhibitor mix ( <i>provided by Prof. Soloiz</i> ) |
| o-Phenanthroline                                                |
| TPCK (Tosyl-Phenylalaninechloromethylketone)                    |
| p-Aminobenzamidin-HCl                                           |
| TLCK (Tosyl-Lysinechloromethylketone)                           |
| PMSF (Phenylmethylsulfonylfluoride)                             |
| 1mM EDTA                                                        |

Therefore, we tried to change the purification strategy by unfold the protein during the purification and refold it afterwards.



**Figure 3.9. SDS-PAGE analysis of of PN domain stabilization in 6 M urea.**

N-terminal His-tagged PN domain was purified using Ni-NTA chromatography under denaturation conditions using 6M urea. Lane M, molecular mass standard (kDa); lane 1, unfold PN domain eluted from Ni-NTA column.

Thus, the PN domain was purified under denaturing condition; the protein degradation was inhibited using urea concentration above 3 M as shown in Fig. 3.9. This protocol increased protein stability, but the ATPase assay of refolded PN domain did not show any activity. However, we did not push much more efforts in improving refolding conditions. Instead, different expression systems and conditions were examined to stabilize the N-terminally fusion tagged PN domain, such as varying incubation temperatures (25, 30 and 37 °C instead of 18 °C), short induction period (4 h instead of

overnight), various IPTG concentrations (0.1-1 mM) and finally using different expression vectors, e.g. pProEX-HTa vector with a weak *trc* promoter for slowing protein synthesis and pET51b EK/LIC vector with N-terminal Strep-tag (Fig. 3.10).

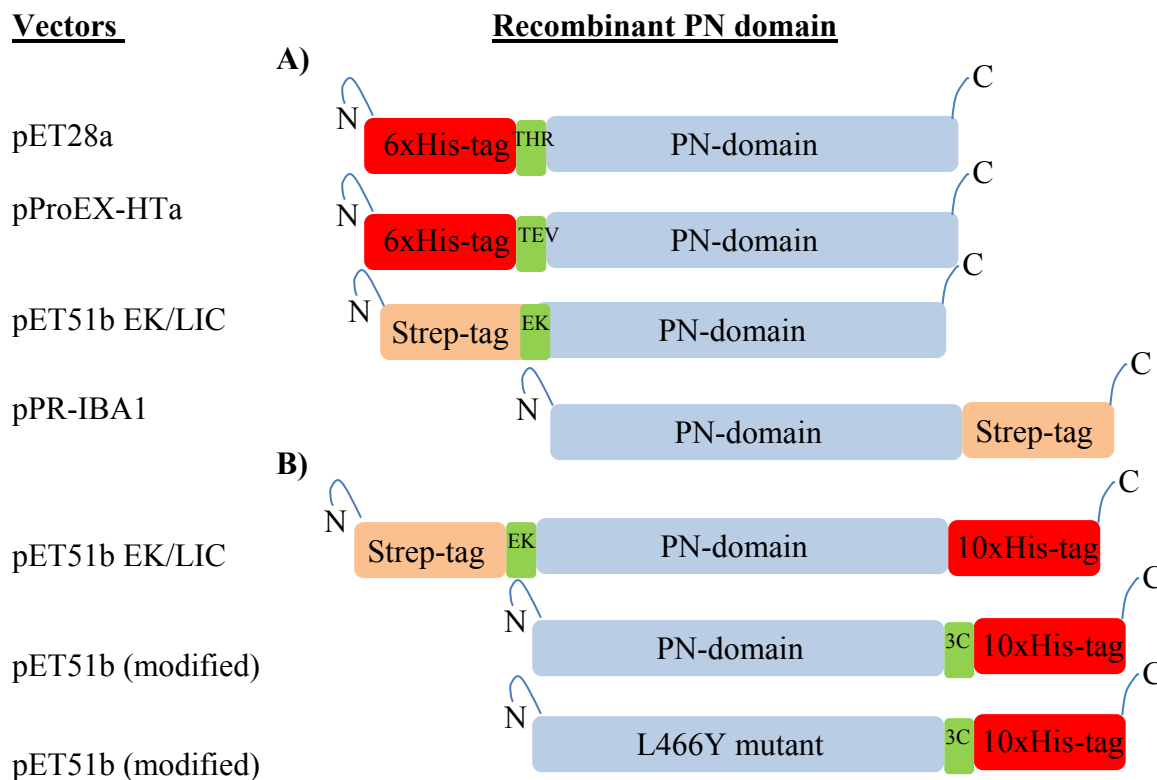


**Figure 3.10. Schematic diagram of all recombinant PN domain proteins produced for this study.**

The recombinant PN domain proteins produced in this study are listed in: **A)** recombinant PN-domain proteins were unsuccessfully purified due to degradation effect while **B)** the recombinants were successful purified by Ni-NTA column. L466Y mutant refers to replacement of L466 side chain of PN domain with Tyr. The EK, 3C, THR and TEV symbols stand for the recognition site of enterokinase, 3C protease, thrombin and TEV protease, respectively.

Unfortunately, none of these attempts produced catalytically active PN domains. Therefore alternative expression vectors with C-terminal fusion tag were examined (Fig 3.10 B). A C-terminal Strep-tagged PN domain was produced but did not bind to the resin. Finally, the protein was successfully purified with a C-terminal 10xHis tag; the PN domain was expressed in either pET51b vector with dual N-Strep and C-10xHis tag or mod\_ pET51b vector with only C-terminal 10xHis tag (Fig. 3.10 B).

The dual-tagged PN domain was utilized in co-purification assay (see chapter 5) while the PN domain with a single C-term 10xHis-tag was used for spectroscopic measurements (see Chapter 4). The purity of C-term 10xHis-tagged PN exceeded 95% as shown in Fig. 3.11 when 5 mM ATP was supplied in the washing buffer. Additionally, the PN domain was purified by Ion-exchange chromatography (Fig. 3.12).

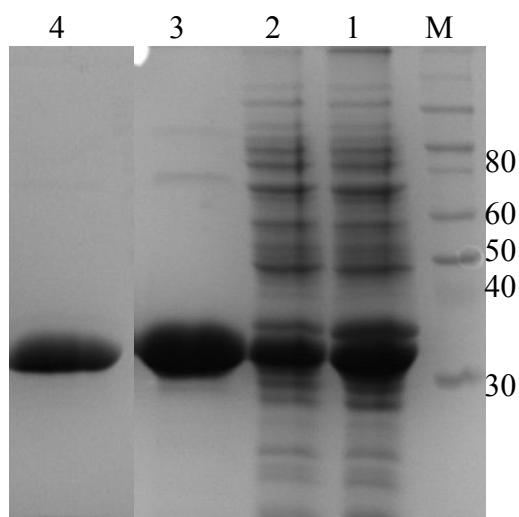


**Figure 3.11. SDS-PAGE analysis of C-terminal His-tagged PN domain purification.**

The PN domain was expressed in pET51b vector with C-terminal 10xHis-tag in 2xYT medium at 18 °C. PN domain was purified using both Ni-NTA and Ion-exchange chromatography. PN domain exposed to degradation upon cell lysis. Lane M, molecular mass standard (kDa); lane 1, induced cell PN domain; lane 2, soluble fraction of cell extracts; lane 3, eluted PN domain from Ni-NTA; lane 4, purified PN domain from Ion-exchange chromatography.

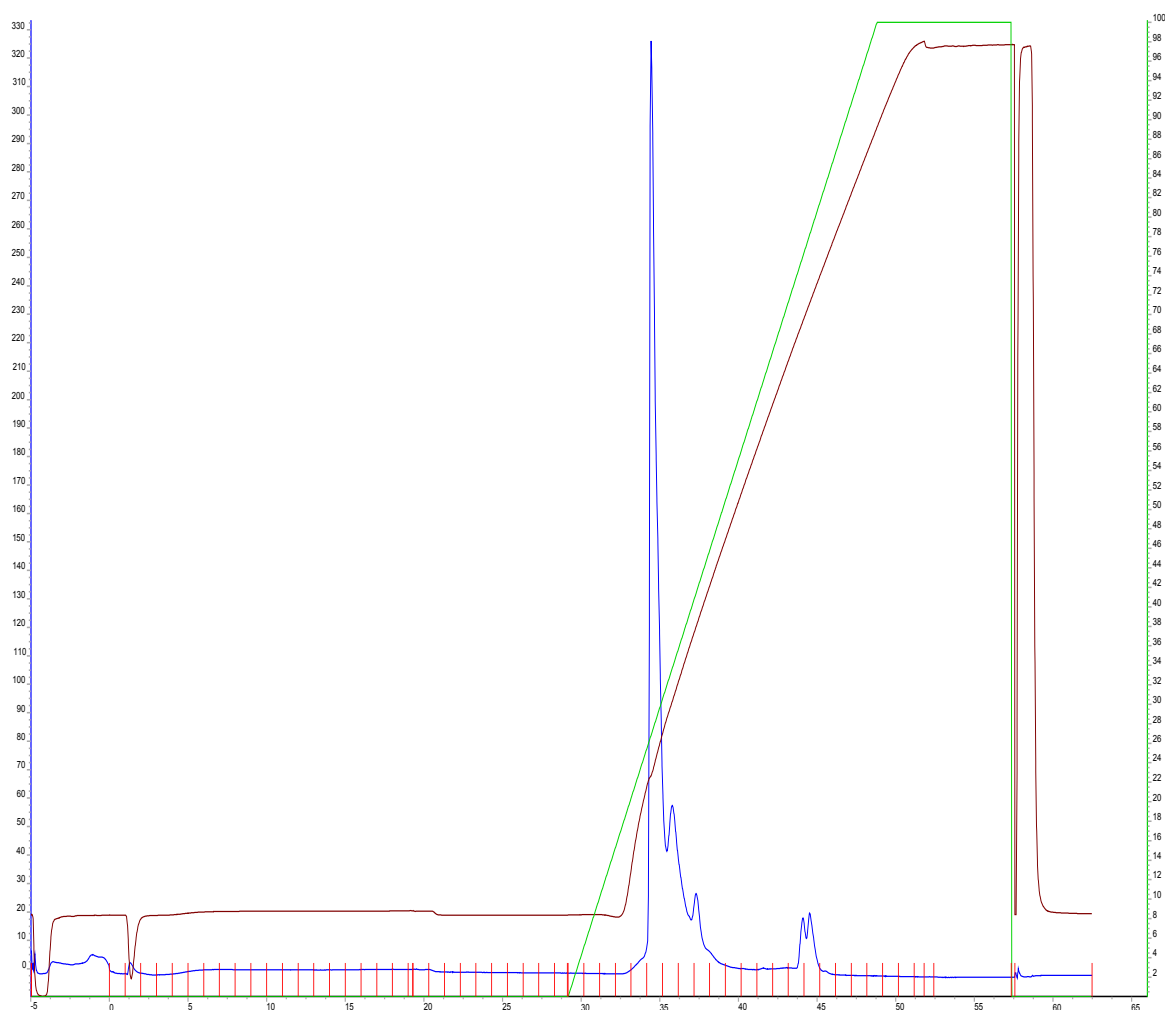


**Figure 3.12. Chromatographic purification of PN domain.**

500  $\mu$ l protein sample (8 mg/ml) was loaded on a Mono-Q anion-exchange chromatography column and eluted with a gradient from 0.05-1 M NaCl at a flow rate of 1 ml/min.

### 3.2 Expression of membrane proteins

Escherichia coli, the main heterologous expression host, is employed for recombinant protein over-expression. However, the over-expression of a foreign membrane protein usually leads to inclusion body formation, improperly folded proteins, or toxicity for bacterial cells. Several factors can play critical roles for minimizing those effects such as the cell growth conditions, type of the bacterial strain, expression vector, and induction rate.

Therefore, we tried to improve the expression of LpCopA by reducing the rate of protein synthesis. The protein expression rate can be slowed down by cultivating the host cells at 18 °C, examining different bacterial hosts, using expression vector with weak promoter or lowering the inducer concentration. The codon-optimized nucleotide sequence of LpCopA was provided into pET28a plasmid by GeneArt (Invitrogen); the DNA sequence was re-cloned into pProEX-HTa plasmid. The latter contains a T7-promoter, a weak promoter that is advantageous for improving the solubility of recombinant membrane proteins inside the bacterial cell. Both expression vectors encode an N-terminally 6xHis-tagged LpCopA. The expression test for both vectors in *BL21-Gold(DE3)* growing in LB medium shows no expression of LpCopA in the pET28a-bearing host in contrast to the pProEX-HTa-bearing host. Therefore, the pProEX-HTa plasmid encoding LpCopA is commonly used.

We further examined the expression level of LpCopA using the standard inducer (IPTG) and an alternative induction method called “auto-induction” which has been established for the expression of toxic membrane proteins in several bacterial hosts, such as *C41(DE3)* and *C43(DE3)*, as well as *Gold(DE3)*, *Rosetta(DE3)* and *CodonPlus-RIL(DE3)* strains. The pLysS strains were also used for suppressing the basal expression of T7 RNA polymerase. The auto-induction protocol, in which protein production is induced by 0.5% (v/v) glycerol, 0.05% (w/v) glucose and 0.02% (w/v)  $\alpha$ -lactose, was designed to enhance the overproduction efficiency of the membrane proteins [106]. As shown in Fig. 3.13 and 3.14 (lane5), the protein expression level of LpCopA in *C41(DE3) pLysS*, *C43(DE3) pLysS* and *Gold (DE3)* is higher than in others strains. Furthermore, the auto-induction protocol did not properly work for LpCopA over-expression (Fig. 3.13). We saw no obvious advantage of *C41(DE3) pLysS* and *C43(DE3)pLysS* strains over *Gold (DE3)* strain in expression level and stability of LpCopA. Therefore, *Gold(DE3)* strain was routinely used for LpCopA expression throughout this study.

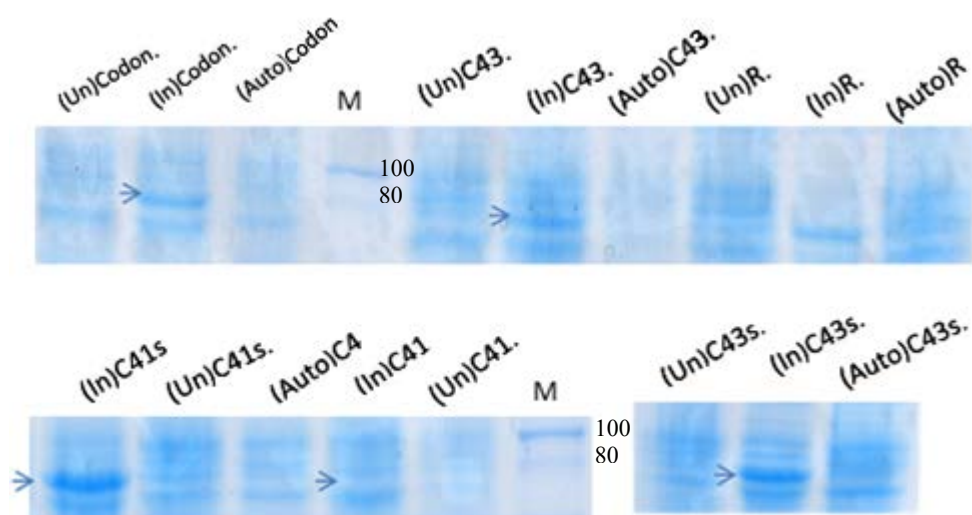


**Figure 3.13. SDS-PAGE analysis of LpCopA expression in different hosts using two induction methods.**

All cells were induced by 0.5 mM IPTG except those symbolized by “Auto” were induced according to the auto-induction protocol. The normalized OD of bacterial cells was loaded into the lanes. The C41, C41s, C43, C43s, Codon and R symbols stand for *C41(DE3)*, *C41(DE3)pLysS*, *C43(DE3)*, *C43(DE3)pLysS*, *BL21(DE3) CodonPlus-RIL* and *Rosetta(DE3)* strains, respectively. The symbols of “Un” and “In” denote to the uninduced and induced cells. The arrow refers to the expressed LpCopA band.

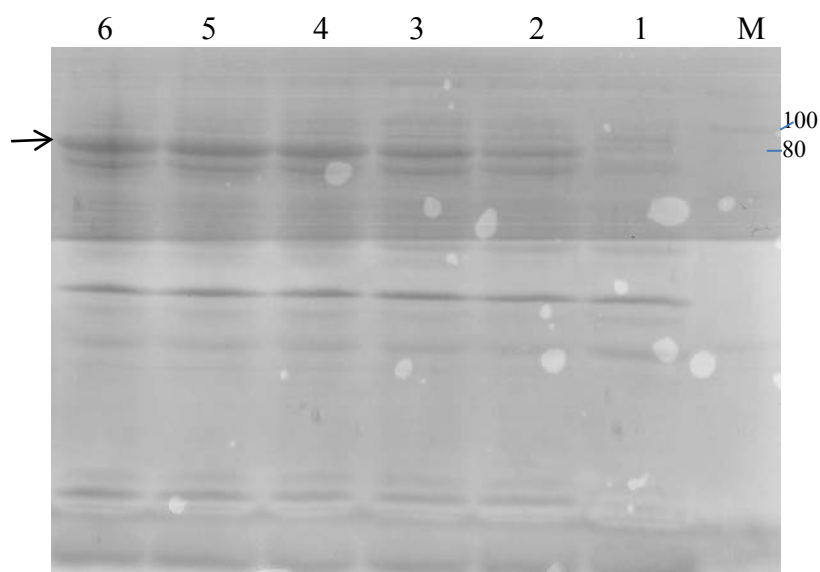


**Figure 3.14. SDS-PAGE analysis of LpCopA expression screening with various IPTG concentrations.**

The *E. coli Gold* cells harboring pProEX-HTa plasmid were induced by the concentration range of 0.05-1 mM IPTG. The OD of bacterial cells was normalized before loading into the lanes. Lane M, molecular weight markers; lane 1, uninduced cells; lane 2, induced cells with 0.01 mM IPTG; lane 3, induced cells with 0.12 mM IPTG; lane 4, induced cells with 0.25 mM IPTG; lane 5, induced cells with 0.5 mM IPTG; lane 6, induced cells with 1mM IPTG. The arrow refers to the expressed LpCopA band. Unfortunately not all the marker bands are appeared.

Another factor, affecting the protein solubility, is the IPTG concentration; the higher IPTG concentration may become toxic to the cells while the lower concentration may not be enough for appropriate expression. Therefore, we investigated the threshold IPTG concentration for appropriate expression of LpCopA. Figure 3.14 shows the expression level of LpCopA in *E. coli Gold(DE3)* induced overnight by variable IPTG concentrations from 0.05-1 mM. It is clear to the naked eye that the concentrations between 0.25-0.5 mM IPTG are quite similar in the protein expression level and thereby we can conclude that the 0.25 mM IPTG is quite sufficient concentration for LpCopA expression in *E. coli Gold(DE3)*.

In summary, the optimal expression conditions of LpCopA and its mutants, namely LpCopA $\Delta$ HMBD and a C384S mutant used for site-directed fluorescence labeling (see Chapter 7), were obtained from *E. coli Gold(DE3)* carrying the pProEX-HTa plasmid induced overnight by 0.25 mM IPTG at 18 °C in 2xYT medium.

### 3.3 Solubilization and purification Membrane protein

The solubilization of integral membrane proteins is a process in which the proteins and membrane lipids are suitably dissociated in a detergent solution. The solubilization is one of the most critical steps for protein extraction from lipid membrane in active form; it depends on several factors such as the type and concentration of detergent used, temperature and buffer compositions.

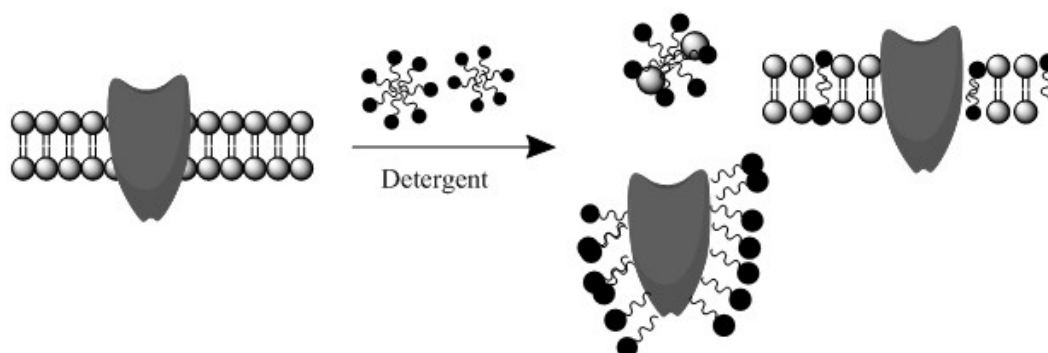


**Figure 3.15.** A schematic representation of membrane proteins solubilization by detergents.

The detergent micelles penetrate the membrane to dissociate the protein and lipids into the solution. As the concentration of detergent increases, the membrane bilayer is disrupted and protein totally delipidated to form mixed micelles of lipid and detergent and that of protein and detergent.



We tried to balance between retaining the ATPase activity of the protein and getting an appropriate yield. We used n-Dodecyl- $\beta$ -maltoside (DDM, CMC of 0.17 mM) as the most versatile detergent used in membrane protein extraction and purification [107]. In addition, we used Sarkosyl detergent coupled with DDM in the purification of LpCopA as it will be discussed in the next section. In this study, there are three solubilization protocols to be considered: 1) the well-established protocol in our lab, 2) the dual-detergent method and 3) the direct solubilization protocol.

### 3.3.1 Classical solubilization protocol

Initially, both LpCopA and LpCopA $\Delta$ HMBD were solubilized according to an established protocol in our lab for membrane protein solubilization. In this protocol, the membrane fraction, obtained from the cell lysis was collected by ultracentrifugation and the pellet re-solubilized by adding DDM in a ratio of protein/detergent (1:4, wt/wt). The solubilized proteins were applied to Ni-NTA resin, washed and eluted with imidazole gradient.

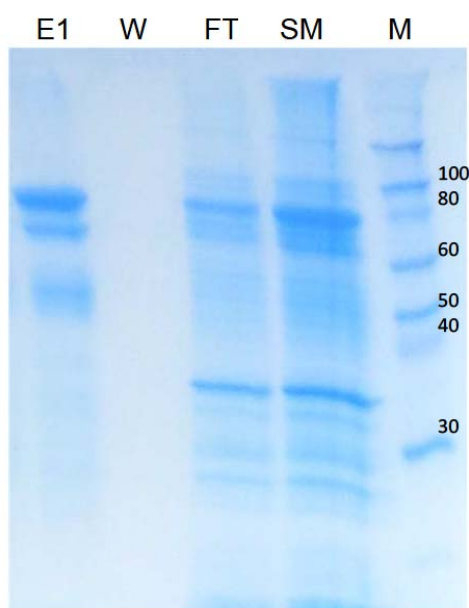


**Figure 3.16. SDS-PAGE analysis of N-terminal 6xHis-tagged LpCopA solubilized by typical protocol.**

The membrane pellet was solubilized by DDM and the soluble fractions were loaded to Ni-NTA column. Lane M, molecular mass standard (kDa); lane SM, solubilized membrane proteins; lane FT, flow-through from Ni-NTA affinity column; lane W, washing with 50mM Imidazole; lane E1, eluted LpCopA protein with 400mM Imidazole from Ni-NTA affinity column.

The SDS gel of purified 6xHis tagged LpCopA shows a band at 80 kDa, corresponding to LpCopA, and two additional bands at around 70 kDa and 50 kDa. These bands were frequently associated with LpCopA purification, however many attempts to remove them by intensive washing and by gradient elution did not work. Most likely, these bands are caused by His-tagged proteins (i.e. byproducts of LpCopA degradation) or protein chaperones.

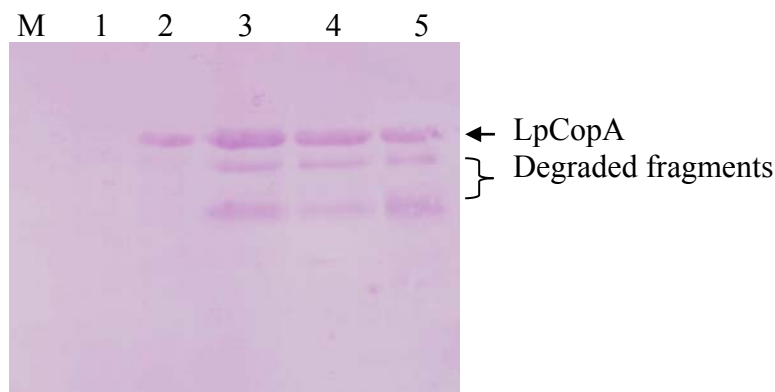


**Figure 3.17. Western blot analysis of 6x His-tagged LpCopA.**

The degraded fragments of LpCopA protein were detected by blotting with Rabbit anti-6x His tag antibody. Lane M, molecular mass standard (used as negative control); lane 1, uninduced cells; lane 2, induced cells; lane 3, solubilized membrane proteins; lane 4, flow-through from Ni-NTA affinity column; lane 5, eluted LpCopA protein from Ni-NTA affinity column. *This gel is a part of joint project in our lab.*

The bands were blotted with the Rabbit anti-6x His tag antibody revealing the recognition of the anti-6x his tag antibody in these bands, which therefore are assigned to degraded LpCopA fragments (Fig. 3.17). Further purification by gel-filtration was not successful (Fig. 3.18). The protein yield obtained after purification was low at ~1-2 mg of LpCopA/2L of cell culture.

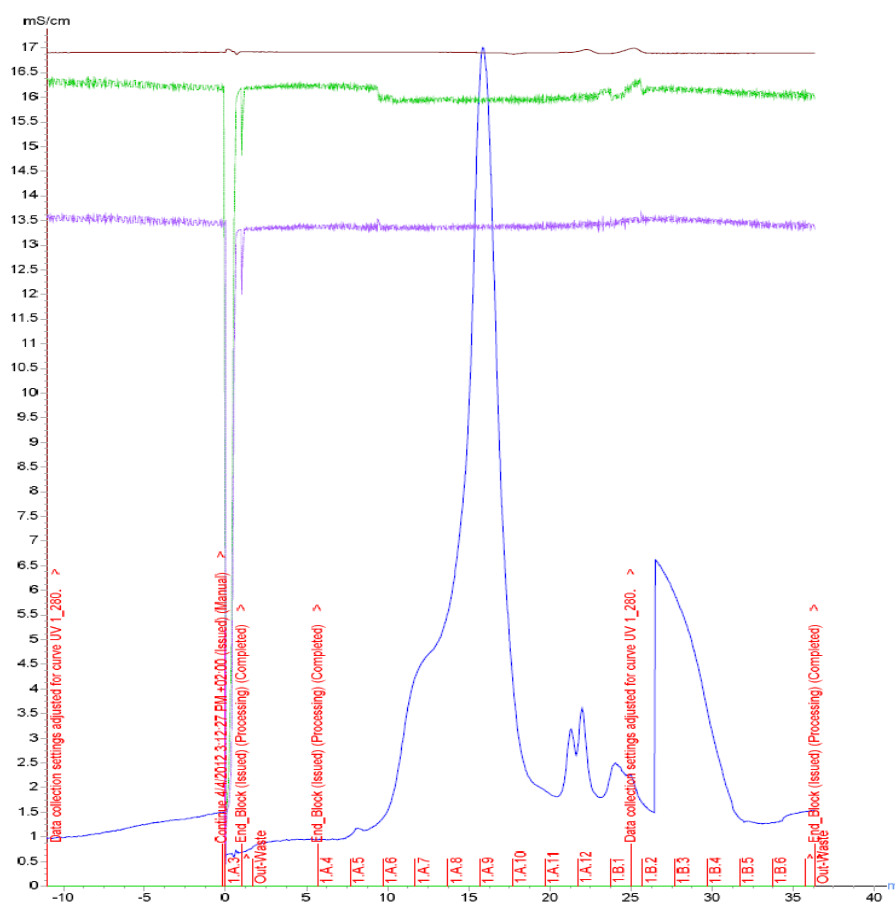


**Figure 3.18. Size-exclusion chromatographic profile of LpCopA purification.**  
*This chromatography is a part of joint project in our lab.*

### 3.3.2 Sarkosyl-mediated solubilization of membrane proteins

As described above, the quality and quantity of LpCopA from previous purification protocols was not sufficient. Therefore, we tried to improve the solubilization step by using an alternative detergent. N-lauroylsarcosine (Sarkosyl), a mild anionic detergent, is often used for solubilization of cytoplasmic membrane only (inner membrane) [108-110] and aggregated proteins [111, 112]. It has been used previously for ATPases [113-117]. Here, we combined two detergents in the solubilization and purification processes for LpCopA. In the solubilization step, 0.5% Sarkosyl detergent was initially added to the membrane pellet which was then gently agitated for 1 hour. It was obvious that the membrane solubilization was enhanced in this step, but the residual Sarkosyl can

interfere with protein reconstitution and with the further spectroscopic measurements because of its large background signal in circular dichroism spectroscopy [118].

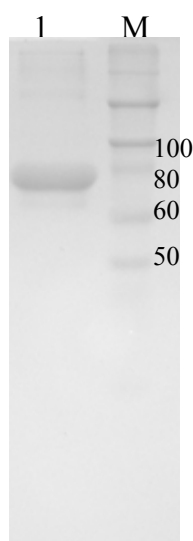


**Figure 3.19. SDS-PAGE analysis of Sarkosyl-mediated LpCopA purification**

The membrane pellet was solubilized by 0.5% Sarkosyl detergent that is exchanged with 0.1% DDM detergent while the protein was bound to the column. Lane M, Molecular weight markers and lane 1, Purified LpCopA eluted from Ni-NTA column. 11% polyacrylamide gel was used.

Therefore, the Sarkosyl detergent was exchanged gradually with 0.1% DDM while the protein was bound to the resin. As shown in Fig. 3.19, the purified LpCopA in the SDS gel appears as a single band. The total LpCopA yield obtained by this method is around 10 mg/1L of cell culture. Moreover, The CD spectrum of LpCopA exhibits two negative bands at 208 nm and 222 nm corresponding to  $\alpha$ -helix spectrum (Fig. 3.20). The secondary structure analysis of these data agrees with spectroscopic and crystallographic results for LpCopA. Whereas the secondary structure content of crystal LpCopA structure (PDB code: 3RFU) is calculated according to DSSP method (available at <http://2struc.cryst.bbk.ac.uk>) as 49%  $\alpha$ -helix, 14%  $\beta$ -sheet (37% others), the CD analysis (CDSSTR method) estimates the secondary structure of Sarkosyl-solubilized LpCopA as 56 %  $\alpha$ -helix, 18%  $\beta$ -sheet (26% others). Although LpCopA appears well-folded, its ATPase activity was diminished or negligible. It seems that Sarkosyl detergent deactivates the LpCopA by complete delipidation of protein from essential lipids. Therefore, an alternative solubilization method was established as described in the following.

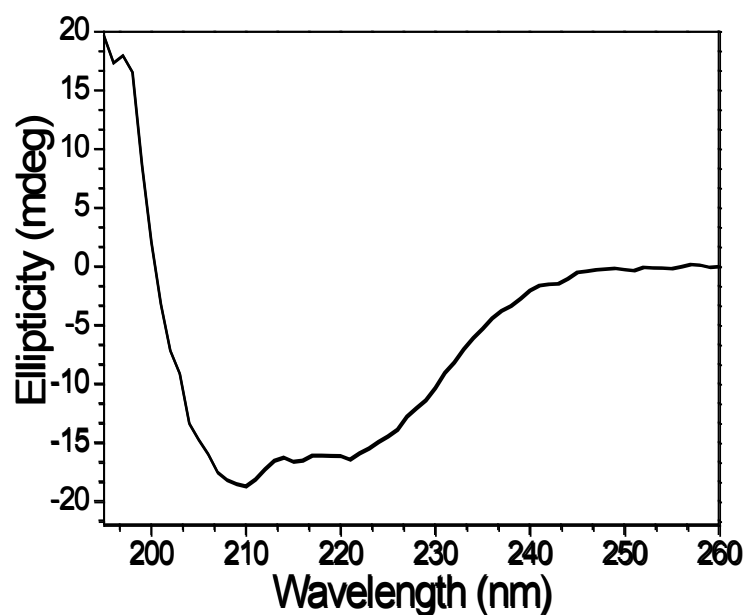


**Figure 3.20. Circular dichroism spectrum of Sarkosyl-solubilized LpCopA.**

The secondary structure is estimated as 56%  $\alpha$ -helix, 18%  $\beta$ -sheet and 26% others using CDSSTR method (at <http://dichroweb.cryst.bbk.ac.uk>)

### 3.3.3 Direct solubilization

The third and eventually more effective method was “direct solubilization”. In this method, the detergent is added while the membrane lipids are suspended in the supernatant of cell lysate[119]. This method, however it is not commonly used for CPx-ATPase solubilization. However, it is described in several handbooks of membrane protein purification such as GE-Healthcare handbook of *Purifying Challenging Proteins: Principles and Methods* [119], *Laboratory Methods in Enzymology: Protein part C* [120] and others[121, 122] and has been used for several transporters[123] including SR  $\text{Ca}^{2+}$ -ATPase [124]. We employed this method with some modifications. Briefly, after removing the large aggregates, a concentrated DDM solution was titrated into the supernatant of the cell lysate of 8 g cell wet weight unit the solution became less turbid, nearly up to 0.5% DDM final concentration. Then the insoluble fragments were removed by centrifugation and filtration before loading the solubilized fraction on a Ni-NTA slurry. This method produces a higher LpCopA yield of 3-4 mg/L of cell culture as compared to purification from membrane pellets. Figure 3.21 shows the purified LpCopA (with either N-term 6x His or C-term 10x His) and LpCopA $\Delta$ HMBD. There

was no detectable ATPase activity of C-term 10x His-tagged LpCopA, in contrast to that tagged with N-term 6xHis. Therefore, N-term 6xHis tagged LpCopA is commonly used for functional study.

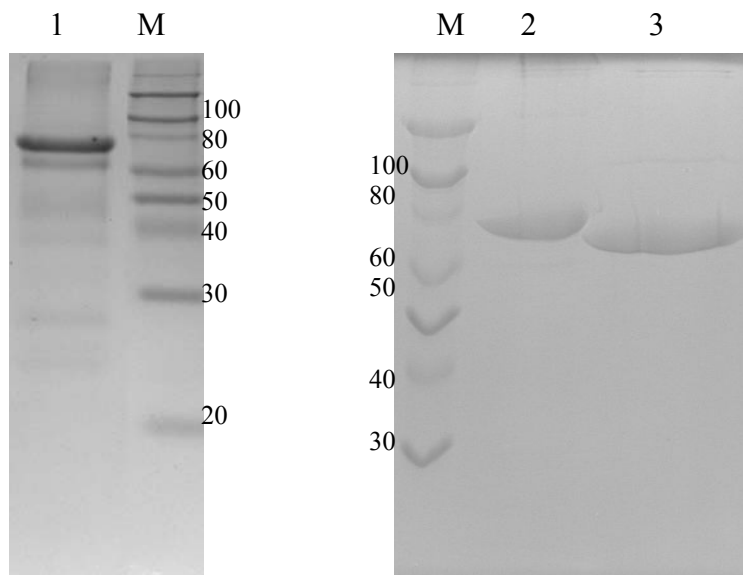


**Figure 3.21. SDS-PAGE analysis of purified membrane proteins prepared using the "direct solubilization" method.**

The membrane suspensions of N-terminal and C-terminal His-tagged LpCopA and C-terminal His-tagged LpCopA $\Delta$ HMBD were directly solubilized by DDM detergent below the total membrane solubilization. The proteins were purified via Ni-NTA chromatography. Lane M, Molecular weight markers and lane 1, purified N-term. His-tag LpCopA; lane 2, purified C-term. 10xHis-tag LpCopA; lane 3, purified C-term. 10xHis-tag LpCopA $\Delta$ HMBD. The proteins were run on 11% acrylamide gel.

### 3.4 Measurements of the catalytic activity of LpCopA and the isolated cytosolic PN domain *in vitro*

#### 3.4.1 Use of the Lanzetta assay

The Lanzetta or malachite green assay is calorimetric assay for determination of nanomole amounts of inorganic phosphate produced by ATPases [93]. It is a classical ATPase assay commonly used for most P-type ATPases.

In the Lanzetta method, the inorganic phosphate forms a complex with molybdate salt which in turn associates with the malachite green to produce a strong absorbance peak near 640 nm as shown in Fig. 3.22B. The color development of the phospho-molybdate complex needs at least 20 minutes to stabilize.

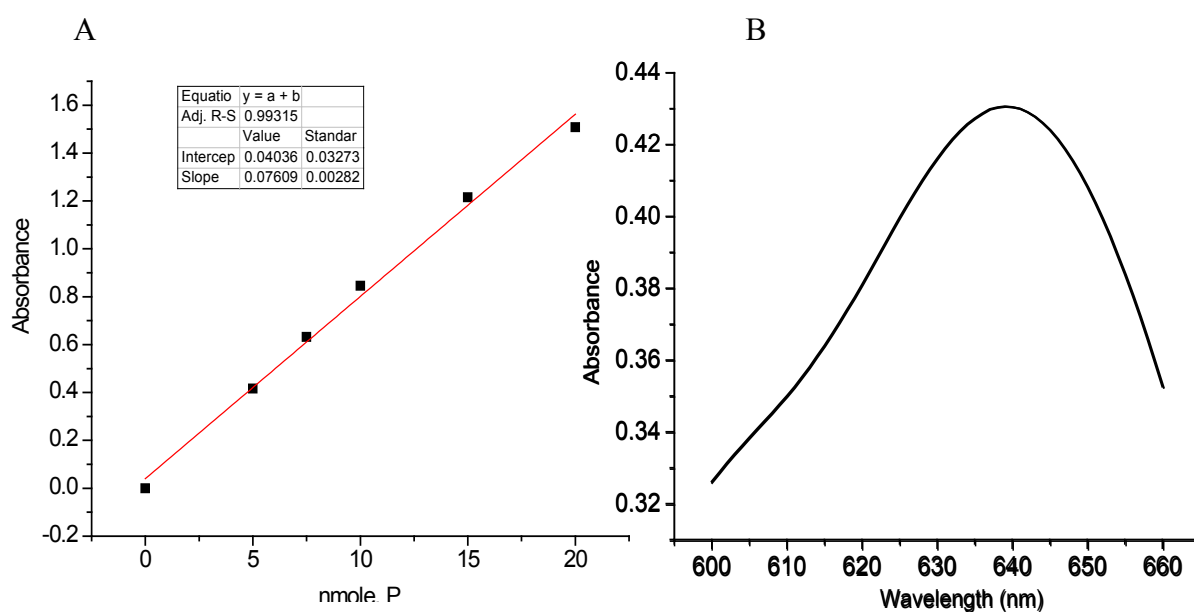


**Figure 3.22. Standard curve of inorganic phosphate measured by Lanzetta assay.**

Various concentrations of  $\text{KH}_2\text{PO}_4$  (5-20nmol) were mixed with Malachite green reagent. **A)** Standard curve of  $\text{KH}_2\text{PO}_4$  at 630 nm. **B)** Absorbance spectrum of a 5 nmol phospho-molybdate complex was monitored from 600-660 nm.

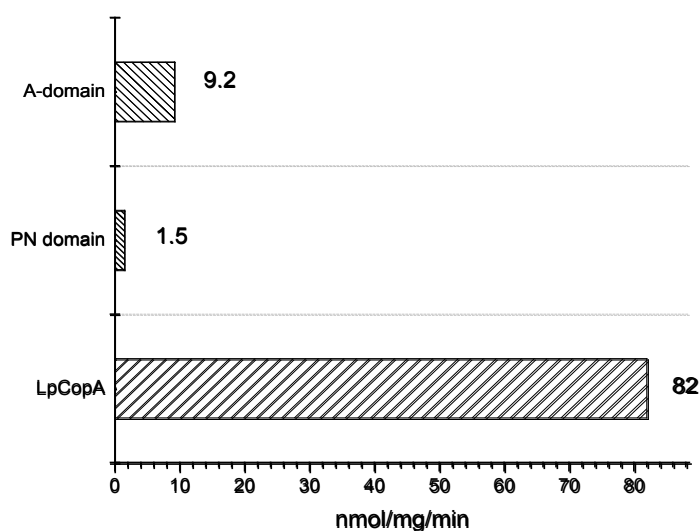


**Figure 3.23. Estimated ATPase activity of LpCopA and expressed cytosolic domains.**

The of LpCopA was estimated in presence of 100  $\mu\text{M}$  Cu(I) while ATPase activity of cytosolic domains was measured without heavy metal including in the assay buffer. See the assay conditions in Chapter 2.

Preserving and measuring the *in vitro* ATPase activity of the purified LpCopA was the largest biochemical challenge encountered in this work. Correspondingly much effort was invested in trying and adapting different ATPase assays to the specific needs of a metal-dependent membrane protein. The trials, optimizations and finally the standardized application of two assays will be described in the following. One assay, a modified Lanzetta assay allows assessing inorganic phosphate at certain time intervals during catalysis, whereas another assay based on substrate fluorescence enables real-time monitoring of the enzyme activity. Among several protein preparations, we were finally able to detect remarkable ATPase activity of LpCopA prepared by the "direct solubilization" method. The maximum activity was found at 100  $\mu\text{M}$   $\text{CuSO}_4$  around 80 nmol/mg/min as shown in Fig. 3.23; above of this copper concentration, the ATPase activity was inhibited. The reaction was carried out in 30 mM HEPES-KOH pH 7.4, 100 mM KCl, 3 mM  $\text{MgCl}_2$ , 1 mM  $\beta\text{-ME}$ , 0.05 % DDM and 1 mg/ml Asolectin buffer at 37  $^\circ\text{C}$ .

The ATPase activity of the PN domain was very low (1.5 nmol/mg/min) similar to the ATPase activity of the same domain in *S. solfataricus* CopB [125]. Interestingly, we detected an ATPase activity also for the A-domain of ( $\sim 10$  nmol/mg/min) under the same assay conditions used for the PN domain. This was not expected because the A-domain does not contain a nucleotide binding site. A possible explanation could be that

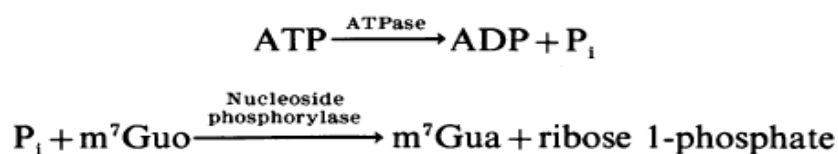


that the A-domain, which is a phosphatase domain, has some diffusive access to ATP molecules in solution and stimulated their hydrolysis at a low rate.

### 3.4.2 Fluorometric real-time monitor for the ATPase activity of LpCopA and the PN domain

Besides the thorough optimization of the conditions for complete expression and purification of LpCopA and the cytosolic PN domain, as shown above, the demonstration of its catalytic activity is crucial for further experiments. In addition to the time interval-based Lanzetta assay, we were interested in a real-time assay of ATPase hydrolysis, as it is potentially more sensitive, non-hazardous material and simple. Therefore, we have optimized a continuous fluorometric ATPase assay which is not commonly used for P-type ATPases; It has been used for monitoring the ATPase activity of Na<sup>+</sup>/K<sup>+</sup> ATPase [126] and myosin [97].

It is an enzyme-coupled assay based on the decrease in fluorescence intensity of N7-methylguanosine (m<sup>7</sup>Guo) upon phosphorylation by utilizing free inorganic phosphate liberated from the ATPase. The m<sup>7</sup>Guo phosphorylation is catalyzed by a bacterial purine nucleoside phosphorylase (PNP) to produce non-fluorescent 7-methylguanine [97, 98]. Commercially, the PNP enzyme coupled with alternative substrate, named MESG in EnzChek® Phosphate Assay kit (molecular probes), is used for colorimetric ATPase assay [127]. Here, we used an alternative low-cost method, in which the fluorescent m<sup>7</sup>Guo is substrate in the following reaction:



### 3.4.2.1 Cytosolic domain activity

The PN domain exhibited low enzymatic ATPase activity (Fig.3.25) which was determined by both the  $m^7$ -Guo-based real-time fluorometry and the malachite green-based colorimetry malachite with activities of 3.4 and 1.5 nmol/mg/min, respectively. The standard curve of  $\text{KH}_2\text{PO}_4$  was run at the same condition (Fig 3.24). In the same context, it had been reported a comparable ATPase activity value of the similar isolated domain from *S. solfataricus* CopB [125]. This low enzymatic activity of the isolated PN domain was expected because of the absence of the A-domain which catalyzes the hydrolysis of the aspartyl phosphate intermediate during the ATP turnover. The ATPase assays of the isolated PN domain indicate that the aspartyl-426 phosphate bond is exposed slowly to water attack causing dephosphorylation. Such basal turnover has been observed in another isolated PN domain [125].

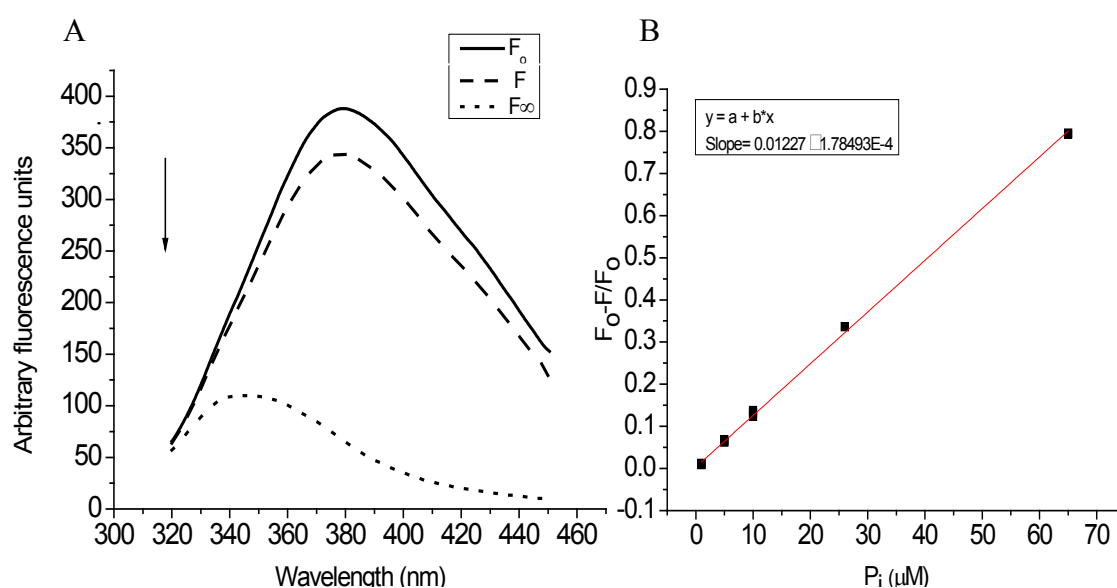


**Figure 3.24. Concentration-dependent calibration of the fluorometric assay using  $\text{KH}_2\text{PO}_4$  as a  $\text{Pi}$  source.**

**A)** Emission spectra of  $m^7\text{Guo}/m^7\text{Gua}$  at free phosphate ( $F_0$ ), at 10  $\mu\text{M}$   $\text{Pi}$  ( $F$ ) and at saturated Phosphate ( $F_\infty$ ). **B)** Standard curve at 1, 5, 10, 26, 65  $\mu\text{M}$   $\text{KH}_2\text{PO}_4$  averaged from triplicates. The assay mixture contained 0.5  $\mu\text{M}$  bacterial purine nucleoside phosphorylase (PNP), 100  $\mu\text{M}$   $m^7\text{Guo}$  in 30 mM Tris-HCl pH 7.4, 100 mM NaCl, 5 mM  $\text{MgCl}_2$ , was initiated by  $\text{KH}_2\text{PO}_4$ . The decrease in fluorescence ( $\lambda_{\text{ex}}$  300 nm) was recorded after a stable intensity was achieved ( $F$ ) which corresponds to the  $\text{Pi}$  concentration. Then,  $\text{KH}_2\text{PO}_4$  was added at a final concentration of 1 mM to convert the rest of  $m^7\text{Guo}$  to  $m^7\text{Gua}$  whose background signal subtracted from all spectra.

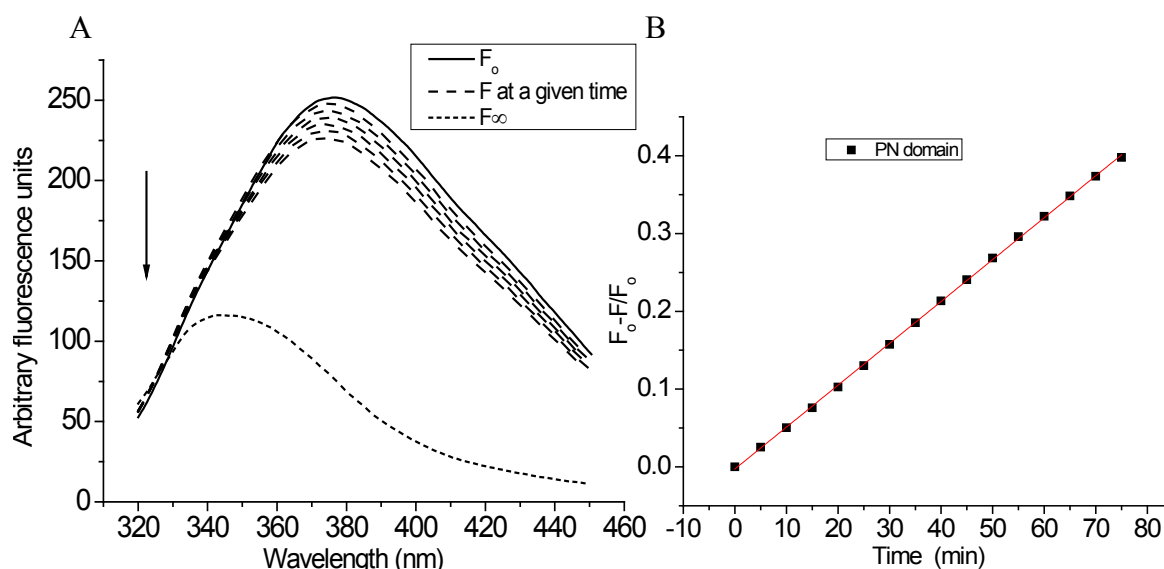


**Figure 3.25. Fluorometric ATPase activity of the PN domain.**

**A)** Fluorescence spectra of  $m^7\text{Guo}$  decrease as function in PN ATPase activity. Each spectrum was taken every 5 min. **B)** Kinetic rate of ATPase activity of PN domain. The assay mixture containing  $0.5 \mu\text{M}$  bacterial PNP,  $100 \mu\text{M}$   $m^7\text{Guo}$  and  $1 \text{mM}$  ATP in  $30 \text{mM}$  Tris-HCl pH 7.4,  $100 \text{mM}$  NaCl,  $5 \text{mM}$   $\text{MgCl}_2$ , was initiated by addition of  $120 \mu\text{g}$  PN domain. The arrow indicates the decreasing rate of fluorescence intensity.

$F_0$ ,  $F$  and  $F_\infty$  symbols are denoted to the initial  $m^7\text{Guo}$  fluorescence, the change in emission spectrum at a given time after adding PN domain and the fluorescence after completely converting  $m^7\text{Guo}$  with addition of  $1 \text{mM}$  Pi, respectively.

### 3.4.2.2 Optimization of the fluorometric ATPase assay for LpCopa

Although the fluorometric assay was successful in measuring the ATPase activity of the soluble cytosolic PN domain, it was not clear whether it is also compatible with the ATPase activity conditions of the full-length LpCopa, i.e. in the presence of copper ion, detergent and lipid. Therefore, the fluorometric assay was tested in the presence of metal ions and mixed detergent lipid micelles.

### 3.4.2.2.1 The effect of $\text{SO}_4^{2-}$ ions on assay performance

In some ATPase assays, sulfate salts were used instead of chloride when silver ions were present to avoid the formation of AgCl precipitation. We examined the activity of PNP enzyme in both buffers under the same conditions of pH and substrates concentrations and found that the conversion rate of  $180 \mu\text{M m}^7\text{Guo}$  was reduced to  $0.70 \pm 0.03 \text{ s}^{-1}$  in the presence of  $30 \text{ mM SO}_4^{2-}$  ions, i.e., the reaction was 7 fold times slower than in chloride buffer ( $0.103 \pm 0.0007 \text{ s}^{-1}$ ) as shown in Fig. 3.26. This indicates that  $\text{SO}_4^{2-}$  ions may act as phosphate competitors. Therefore, the sulfate buffer is not recommended in this ATPase assay.

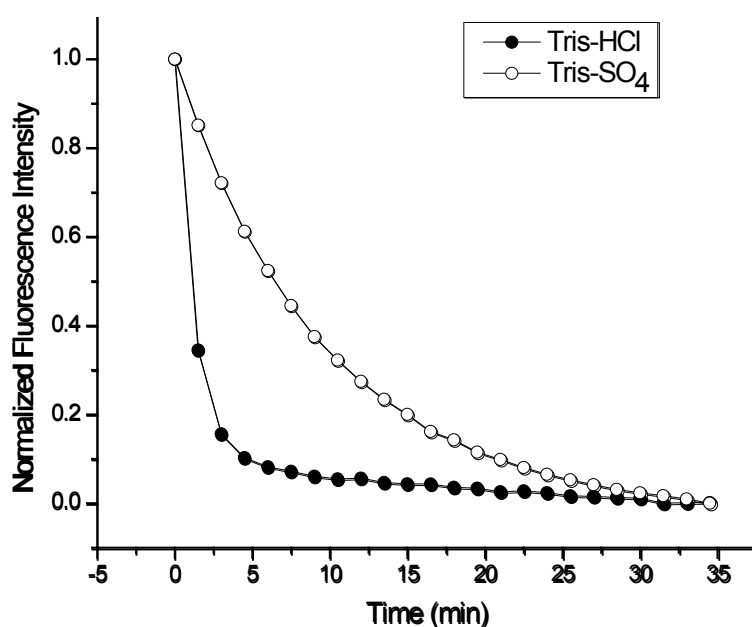


**Figure 3.26. Comparison of conversion rate of  $\text{m}^7\text{Guo}$  to  $\text{m}^7\text{Gua}$  by PNP in chloride and sulfate buffer.**

$150 \mu\text{M K}_2\text{HPO}_4$  was added to  $0.5 \mu\text{M}$  bacterial PNP enzyme and  $180 \mu\text{M m}^7\text{Guo}$  in buffer of  $30 \text{ mM Tris-HCl pH } 7.4$  (●) and  $30 \text{ mM Tris-H}_2\text{SO}_4 \text{ pH } 7.4$  (○). The rate constants of  $\text{m}^7\text{Gua}$  formation were  $0.70 \pm 0.03 \text{ s}^{-1}$  and  $0.103 \pm 0.0007 \text{ s}^{-1}$ , respectively.

### 3.4.2.2.2 The effect of metal ions on assay performance

Another crucial factor for CopA ATPase activity is the cation concentration and redox state. For instance, CopB exhibits a high ATPase activity with few micromoles of  $\text{Cu}^{2+}$  while CopA shows a maximum ATPase activity at sub-millimolar concentrations of  $\text{Cu}^+$  [21, 128]. We examined the effect of both  $\text{Cu}^+$  and of  $\text{Ag}^+$  ions on the PNP enzyme activity. Up to 10  $\mu\text{M}$  metal ions, there is no significant effect, but above this concentration the activity of the PNP was dramatically reduced as shown in Fig. 3.27. In addition, a reducing agent (DTT) is essential in the presence of copper above 10  $\mu\text{M}$ . Therefore the divalent copper can be used in this assay up to 10  $\mu\text{M}$ .

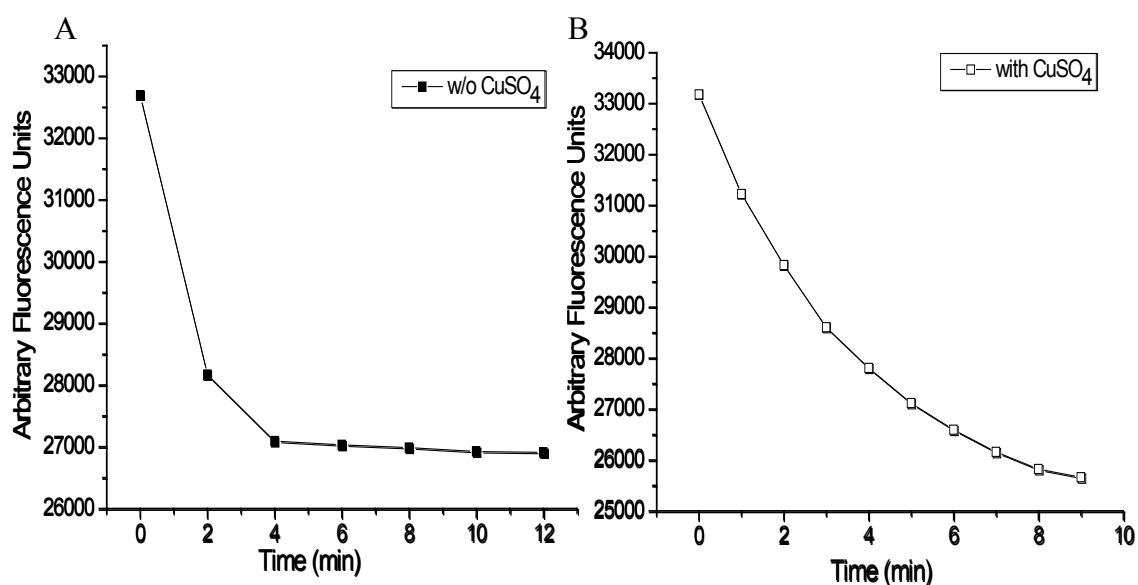


**Figure 3.27. Copper ion reduces the bacterial PNP enzyme activity.**

Activity of 0.5  $\mu\text{M}$  bacterial PNP in buffer containing 30 mM Tris-HCl pH 7.4, 100  $\mu\text{M}$   $\text{m}^7\text{Guo}$ , 20  $\mu\text{M}$   $\text{K}_2\text{HPO}_4$  and 1 mM  $\beta\text{-ME}$  was measured in **A**) absence and **B**) presence of 60  $\mu\text{M}$   $\text{CuSO}_4$ .

### 3.4.2.2.3 The effect of pH on assay performance

As the most ATPase assays of P-type ATPases are carried out at slightly acidic pH [32, 63, 129, 130], the validity of the fluorometric assay was examined at different pHs. The spectral profile of fluorescence emission from  $\text{m}^7\text{Guo}$  changes with pH forming a sharp and intense peak at lower pH, and a very broad and less intense peak at higher pH as shown in Fig. 3.28. Also, the PNP activity decreased at pH 6.2 (Fig. 3.29).

Knowing these influential factors, the standard conditions of the fluorometric assay were fixed to pH 6.8-7.4.

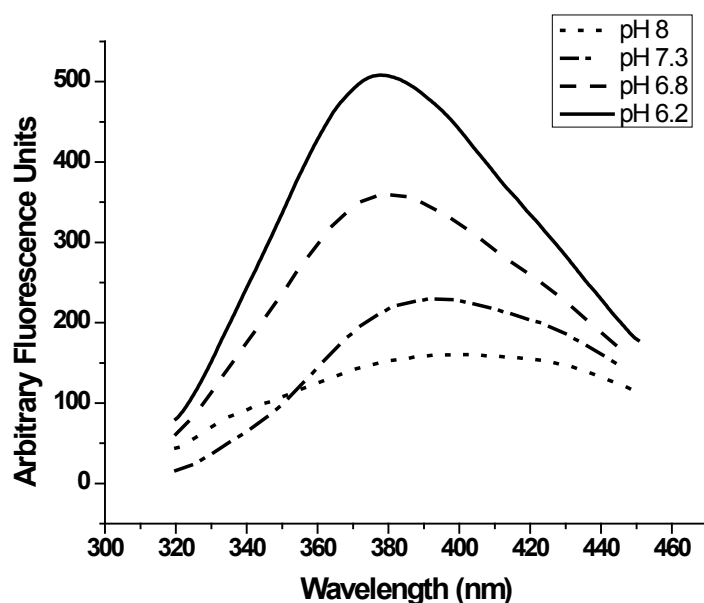


**Figure 3.28. pH-dependence of fluorescence spectra of  $m^7\text{Guo}$ .**

The emission spectra of 100  $\mu\text{M}$   $m^7\text{Guo}$  in 30 mM Tris-HCl were recorded at different pHs (from top to bottom) 6.2, 6.8, 7.3 and 8. The  $m^7\text{Guo}$  was excited at  $\lambda_{\text{ex}}$  300 nm

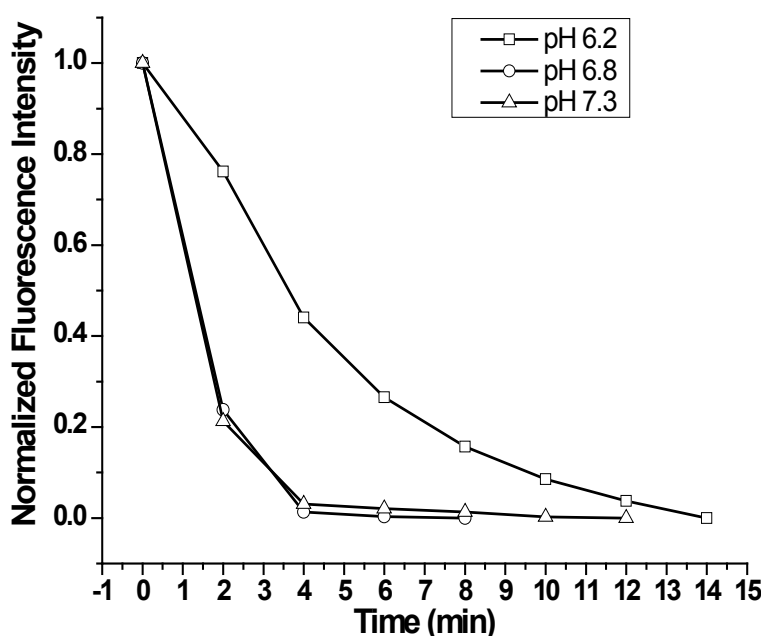


**Figure 3.29. pH-dependence of the bacterial PNP enzyme activity.**

The activity of 0.5  $\mu\text{M}$  bacterial PNP enzyme was measured in different pH buffers containing 30 mM Tris-HCl, 100  $\mu\text{M}$   $m^7\text{Guo}$ , 20  $\mu\text{M}$   $\text{K}_2\text{HPO}_4$ .

### 3.4.2.3 Fluorometric ATPase assay of LpCopA

Based on the optimizations described above, the ATPase activity of LpCopA was measured at room temperature in assay buffer of 30 mM Tris-HCl pH 7.3, 100  $\mu$ M  $m^7$ Guo, 100 mM NaCl, 2 mM ATP, 3 mM MgCl<sub>2</sub>, 60  $\mu$ M CuSO<sub>4</sub>, 1 mM  $\beta$ -ME, 0.1% DDM and 0.3 mg/ml Asolectin. The Asolectin lipid concentration was reduced in the assay buffer to 0.3 mg/ml to minimize the light scattering. The reaction started by adding 20  $\mu$ g LpCopA (final concentration) after a stable emission spectrum of  $m^7$ Guo had been recorded. Using the time-dependent change of  $m^7$ -Guo emission, the ATPase activity of LpCopA was calculated as 22.3 nmol/mg/min comparable to the 24 nmol/mg/min measured by the malachite green assay.

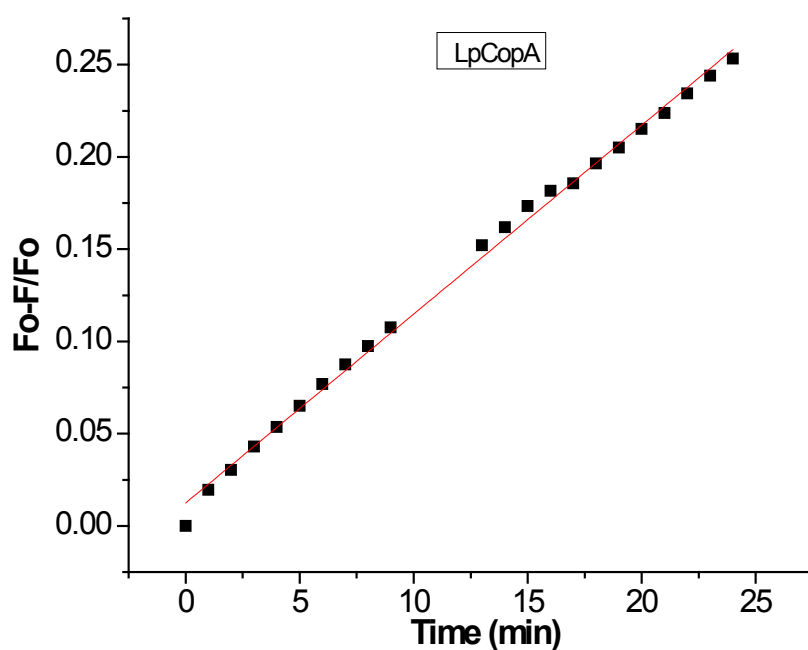


**Figure 3.30.** ATPase activity of LpCopA monitored by the time-dependent fluorometric ATPase assay.

The assay buffer contained 30 mM Tris-HCl pH 7.3, 100  $\mu$ M  $m^7$ Guo, 100 mM NaCl, 2 mM ATP, 3 mM MgCl<sub>2</sub>, 60  $\mu$ M CuSO<sub>4</sub>, 0.1% DDM and 0.3 mg/ml Asolectin was pre-incubated at 25 °C to obtain a stable fluorescence spectrum of  $m^7$ Guo ( $\lambda_{ex}$  300nm). Then, 20  $\mu$ g LpCopA was added to assay buffer. Each point was taken every 2 min.

## Summary and discussion

The Cu (I)-transporting ATPase (CopA), the most widespread among P<sub>1B</sub>-type ATPases, has received considerable attention during recent years from several groups of workers, including our own, because the defect in the human copper-translocating ATP7A and ATP7B is the direct cause of the severe Menkes and Wilson diseases, respectively.

The crystal structure of LpCopA was determined at 3.6 Å in a transition state of dephosphorylation (*E*<sub>2</sub>~P state) excluding the heavy-metal binding domain (HMBD) [32]. We employed the LpCopA as a model to better understand the mechanism of metal transport, and the accompanying structural changes. To do that, the entire LpCopA structure and its isolated cytosolic domains were expressed and purified, as described in this chapter, for further analyses in the next chapters. In term of retaining the enzymatic activity, the production of LpCopA protein was elusive using a traditional solubilization protocol which is established in our lab.

Alternatively, the direct solubilization method allowed obtaining the enzyme, solubilized by DDM detergent, in active form. The maximum ATPase activity of LpCopA was estimated as 82 nmol/mg/min at 100 μM Cu<sup>+</sup> ion, over this copper concentration the enzymatic activity was inhibited; we were unable to detect the highest activity of LpCopA in 1 mM Cu<sup>+</sup> ion as reported by Gourdon, P., *et al* 2011 [32]. In another hand, the soluble cytosolic domains of LpCopA were also produced with some difficulties. In general, the N-terminal fusion tag is preferable because sometimes addition of a C-terminal tag to a protein impairs its function, producing a growth defect if the protein activity is essential cell viability [131]. In the light of the foregoing, we expressed the cytosolic domain with N-terminal tag. Unfortunately, the purification of PN domain was also a big challenge; it was vulnerable to degradation during cell lysis and none of attempts succeeded to keep the protein in entire form with N-terminal fusion tag. Alternatively, the addition of fusion tag at the C-terminus of PN domain allows obtaining the protein un-degradable.



The ATP turnover activity of PN domain was remarkably slow (1.5 nmol/mg/min), this is consistent with an ATPase activity of the similar isolated domain from *S. solfataricus* CopB [125]. Interestingly, and for the first time, we report an ATPase activity of A-domain, the phosphatase domain, addressing a question of the real role of A-domain in the catalytic cycle. The third cytosolic domain, HMBD, expressed in a dimer form as such as the C-MBD of *A. fulgidus* CopA form a domain-swapped dimer [55]. Therefore, it is suggested that HMBD dimerization is due to a domain-swapped dimer which temporally dissociates by passing through the 10 kDa MWCO filter.

Finally, we developed a sensitive fluorescence assay for measuring ATPase activity of cytosolic domain and membrane protein with some limitations. In this assay, we coupled the bacterial purine nucleoside phosphorylase (PNP) with ATPase enzyme. The assay is sensitive to pH change, metal concentration, sulfate salts and lipid concentration.

## Chapter 4

### Structural and Biophysical Characterization of the expressed Cytosolic domains from *Legionella pneumophila* CopA

#### Introduction

The particular ligands binding to the cytosolic domains induce essential conformations of Cu-ATPase for ion transport. The binding affinity of ligand to corresponding domain can be affected by the domain-domain interactions. Therefore, the isolation of cytosolic domains from transmembrane segments can facilitate studying independently the structure and function of each domain. For instance, the isolated N-terminal metal-binding domains of human copper-ATPases were purified from *Escherichia coli* in a soluble form for characterizing their metal-binding properties [132]; these domains, binding to Cu (I) with stoichiometry of one copper per metal-binding domain, can protect the N-MNK and N-WND against labeling with the cysteine-directed probe.

Another example of ligands inducing structural changes in their domain is the sulfate anion; the crystal structures of isolated PN domain from *S. solfataricus* CopB and SERCA1 bound to  $\text{SO}_4^{2-}$  anion are assigned the proteins to  $E2\sim\text{P}$  state because the sulfate anion acts as phosphate analog, bound at the phosphate-binding location in P-domain [72, 133].

Here, we characterized the secondary structure and ligand affinity of each cytosolic domain has been purified in Chapter 3 using fluorescence and circular dichroism methods.

## Results and Discussion

### 4.1 Circular Dichroism analysis of cytosolic domains with ligands

#### 4.1.1 Secondary structure of the expressed cytosolic domains

The previous sections showed the functional expression of the PN domain. In the context of the catalytic cycle of full length LpCopA, conformational transitions in the cytosolic domains need to be transmitted to the transmembrane domain to modulate Cu-affinity and accessibility to either the intra or extracellular side. The secondary structure of the expressed cytosolic domains and possible structural transitions within the PN domain in response to nucleotide binding are addressed in the following based on circular dichroism spectra.

Figure 4.1 shows the CD spectra of the PN, HMBD and A domains of LpCopA. The percentage of helical, strand and random structure was estimated by the CD database provided by DICHROWEB server [134] as shown in Table II.1. Depending on the dataset used, the  $\alpha$ -helical content of the cytosolic domains in solution varies between 38-23%, while the  $\alpha$ -helical content of LpCopA from the crystal structure (PDB ID: 3RFU) is calculated as 49% using the DSSP method. Although the secondary structure composition varies with the use of the data set, the ratio of  $\alpha$ -helix to strand, i.e. the more reliable predictions, is well reproduced and in line with the crystal structure. Importantly, however, CD spectroscopy is used here to detect structural changes in response to nucleotides, copper ion or temperature, rather than to determine the absolute secondary structure composition (which is particularly error-prone for membrane proteins, because CD datasets are largely based on structure analyses of soluble proteins).

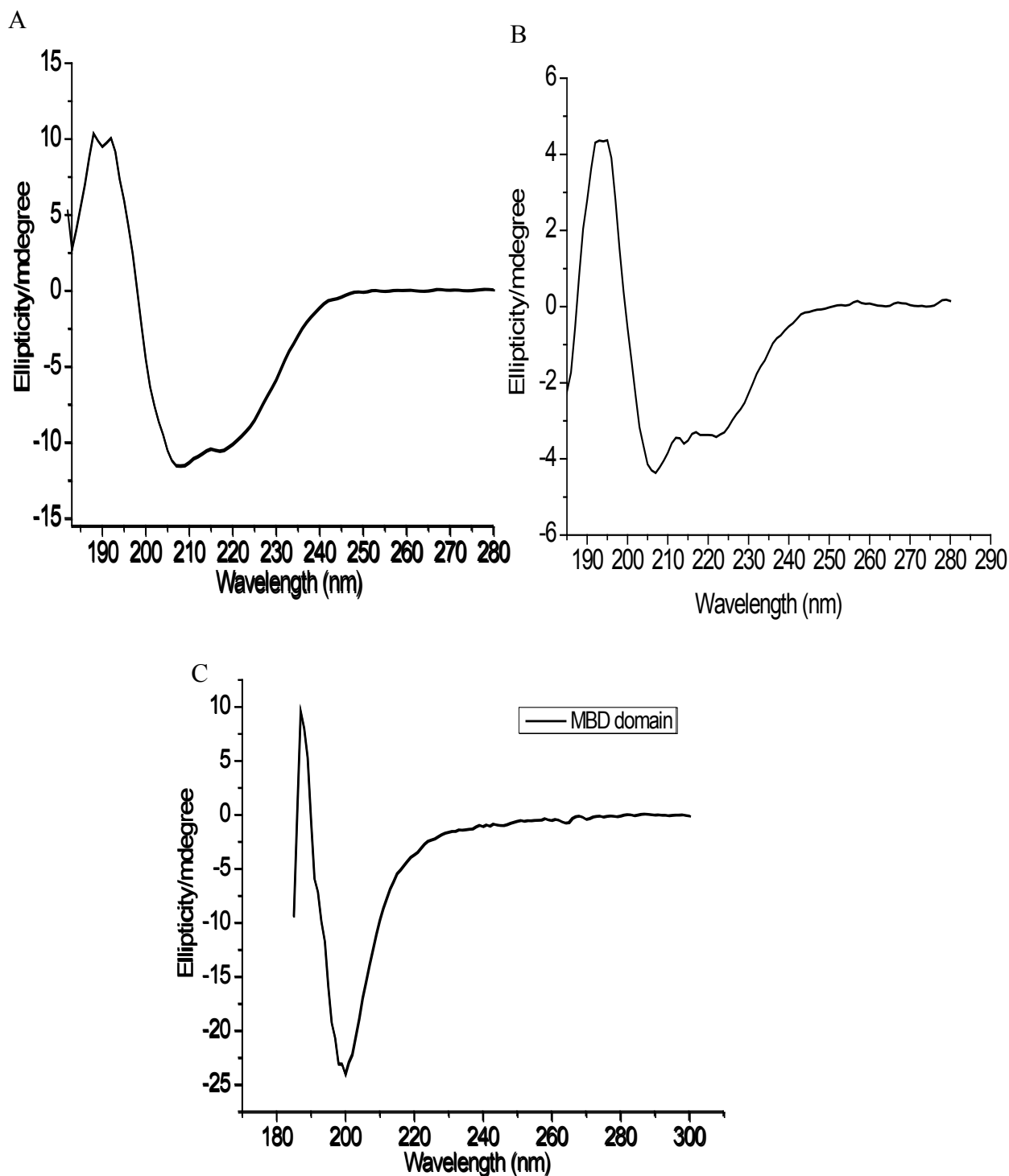
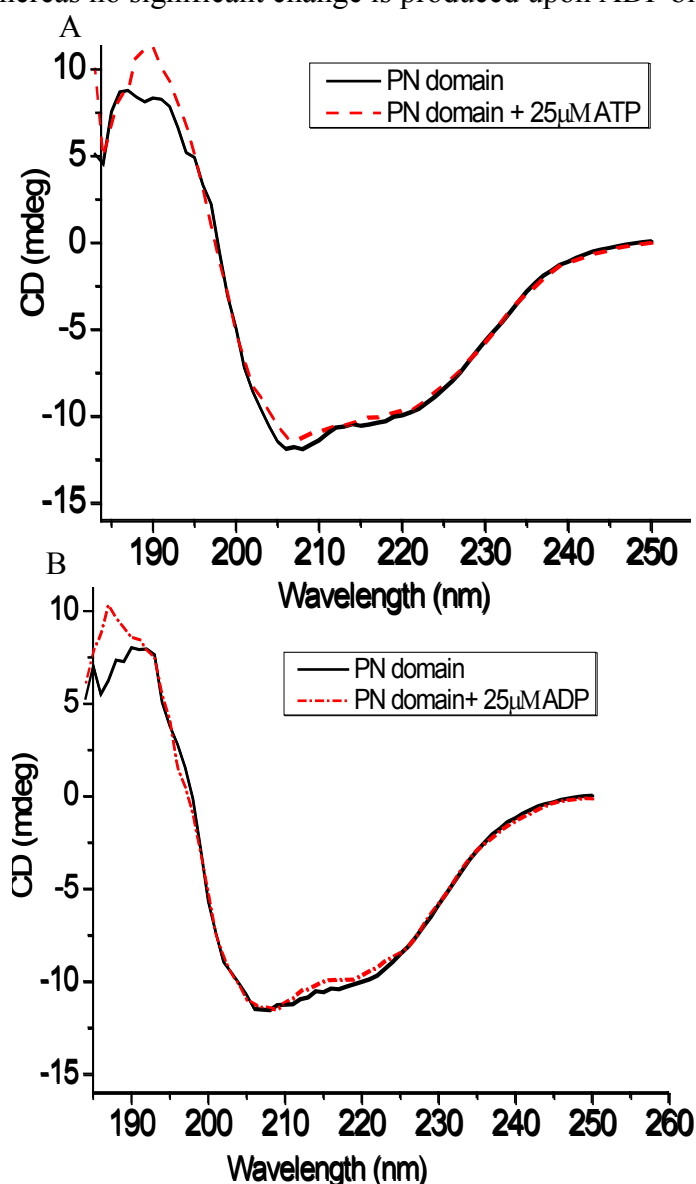


**Figure 4.1. Secondary structure characterization of LpCopA cytosolic domains.**

CD spectrum of 5  $\mu$ M C-terminal His-tagged PN domain (A) and 5  $\mu$ M N-terminal His-tagged Actuator domain (B) were measured in 7 mM  $\text{KH}_2\text{PO}_4$  pH 7.4 and 5 mM  $\text{MgSO}_4$  buffer, while 13  $\mu$ M Strep-tagged HMBD domain (C) was measured in 3 mM MOPS pH 7.6 and 1 mM ascorbic acid. All measurements were carried out using a 1 mm path length quartz cell (Hella) at 25  $^\circ\text{C}$ . Each spectrum was accumulated at least five times.

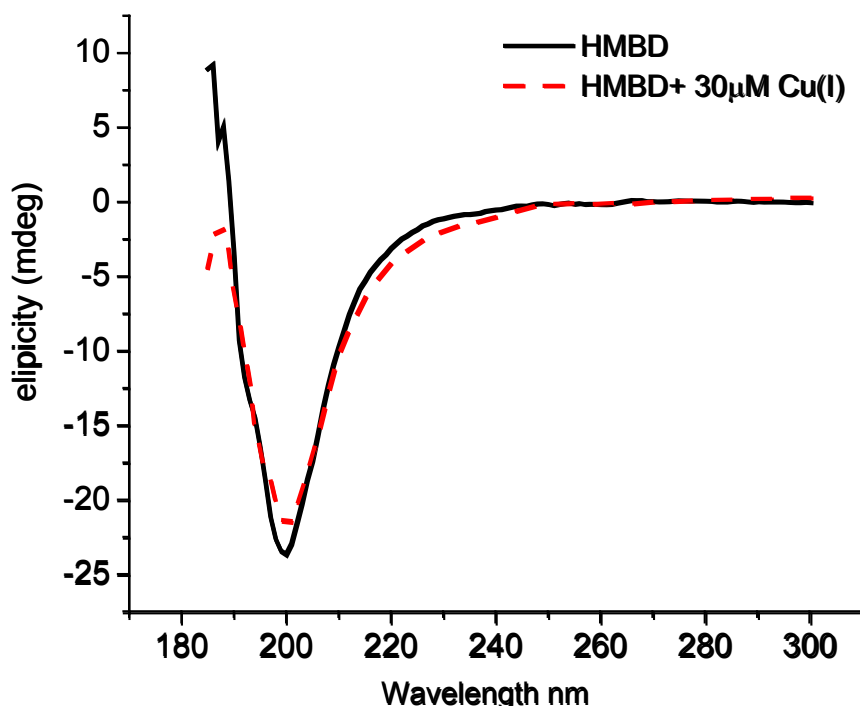
### 4.1.2 The changes in the structural conformation of cytosolic domain with ligands

Figure 4.2 shows the effect of nucleotides on the CD signature of the PN domain. The effect of nucleotides binding on PN domain is small and not accompanied by dramatic changes in secondary structure. This low but significant changes had also been observed in CD spectra with binding of ATP to Rad51 [135] and to GroEL [97]. The small changes are reproducible and indicate a 5-10% increase in helical structure upon ATP binding, whereas no significant change is produced upon ADP binding.



**Figure 4.2. Effect of nucleotides on the CD spectrum of the PN domain.**

25 μM nucleotides were added to 5 μM PN domain in 7 mM  $\text{KH}_2\text{PO}_4$  pH 7.4 at 25 °C. The CD spectrum change of PN domain upon binding to (A) ATP and to ADP nucleotides (B) was small but reproducible beyond experimental uncertainty. The blank (buffer only) was subtracted from the CD spectrum of each sample.



**Figure 4.3. CD spectral changes of the HMBD upon  $\text{Cu}^+$  ion binding.**

300  $\mu\text{l}$  of 13  $\mu\text{M}$  Strep-tagged HMBD  $\pm$ 30  $\mu\text{M}$   $\text{CuCl}_2$  was measured in 3 mM MOPS pH 7.6 and 1 mM ascorbic acid buffer using 1 mm path length quartz cell (Helma) at 25  $^\circ\text{C}$ . The buffer including copper was used as a blank before adding the HMBD.

In contrast, larger effects are observed for the isolated HMBD domain.  $\text{Cu}^+$  binding to the HMBD induced a change in the CD spectrum shown in Fig. 4.3. The  $\alpha$ -helical content increased at the expense of unordered structure (Table 4.1). The more pronounced spectral change agrees with the large copper-dependent modulation of the affinity of the HMBD to the actuator domain described in Chapter 5.

Table 4.1 summarizes the secondary structures of cytosolic domains estimated from their CD-spectra analysis using online SELCON3 program.

**Table 4.1. Secondary structure composition of cytosolic domains.**

The secondary structure contents were estimated using SELCON3 program from the online CD analysis site, DICHROWEB (<http://dichroweb.cryst.bbk.ac.uk>).

|                                                   | <b>Helix1</b><br>% | <b>Helix2</b><br>% | <b>Strand1</b><br>% | <b>Stran2</b><br>% | <b>Turns</b><br>% | <b>Unordered</b><br>% |
|---------------------------------------------------|--------------------|--------------------|---------------------|--------------------|-------------------|-----------------------|
| <b>PN domain</b>                                  | <b>11.8</b>        | <b>12.8</b>        | <b>1.2</b>          | <b>8.6</b>         | <b>44.6</b>       | <b>35.4</b>           |
| <b>PN domain+25 <math>\mu</math>M ATP</b>         | <b>17.3</b>        | <b>13.4</b>        | <b>5.4</b>          | <b>9.0</b>         | <b>34.1</b>       | <b>37.1</b>           |
| <b>PN domain+25 <math>\mu</math>M ADP</b>         | <b>12.7</b>        | <b>12.0</b>        | <b>2.5</b>          | <b>8.9</b>         | <b>44.6</b>       | <b>33.7</b>           |
| <b>A-domain</b>                                   | <b>19.1</b>        | <b>19.10</b>       | <b>1.9</b>          | <b>4.0</b>         | <b>17.8</b>       | <b>35.6</b>           |
| <b>HMBD</b>                                       | <b>14.0</b>        | <b>10.0</b>        | <b>17.0</b>         | <b>7.0</b>         | <b>18.0</b>       | <b>35.0</b>           |
| <b>HMBD + 30 <math>\mu</math>M Cu<sup>+</sup></b> | <b>33.0</b>        | <b>13.0</b>        | <b>14.0</b>         | <b>10.0</b>        | <b>9.0</b>        | <b>22.0</b>           |

Helix1, regular  $\alpha$ -helix; Helix2, distorted  $\alpha$ -helix; Strand1, regular  $\beta$ -strand; Strand2, distorted  $\beta$ -strand. The normalized root-mean-square deviation (NRMSD) values were  $<0.15$  indicating good fitting between the experimental spectrum and calculated secondary structure.

## 4.2 Ligand binding assay of cytosolic assay

### 4.2.1 TNP-nucleotides affinity of PN domain

Whereas the ATPase assays demonstrated the ATP-hydrolyzing functionality of the PN domain (Chapter 3), they do not allow determining the nucleotide affinity.

Therefore, ATP analogs were used that exhibit spectroscopic changes upon binding to ATP-binding sites which allows deducing estimates of the affinity.

Trinitrophenyl (TNP)-nucleotides are a fluorescently labeled nucleotides to examine the structural integrity of an ATP binding sites, since these nucleotide derivatives increase their fluorescence at 545 nm drastically upon binding to an appropriate binding site. It has been shown that TNP-nucleotides bind to members of the P-type ATPase family and have been used for structural studies [85, 136-141].

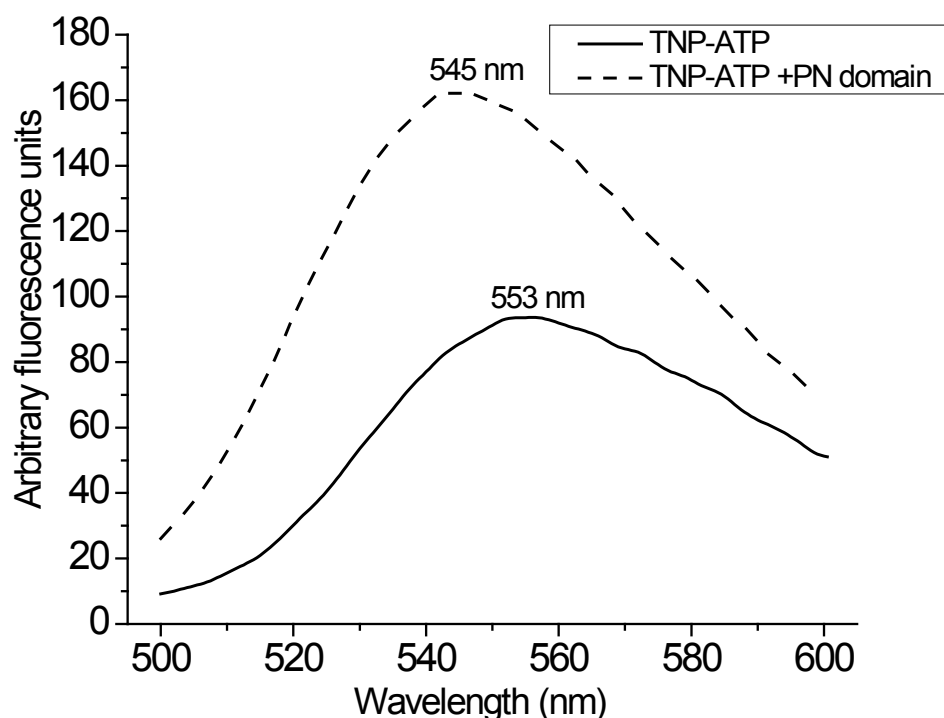


**Figure 4.4. Fluorescence change of TNP-nucleotide ( $\lambda_{\text{ex}}$  408 nm) upon binding to PN domain.**

10  $\mu\text{M}$  PN domain added to 20  $\mu\text{M}$  TNP-ATP in 50 mM Tris-HCl pH 7.4 and 200 mM KCl buffer results in intensity increasing and blue-shift of TNP-ATP fluorescence from 553 nm to 545 nm.

Figure 4.4 shows the increase of TNP-ATP upon binding to the PN domain. The increase is typically related to the restricted motion of the dye within the binding pocket as compared to the dissolved state, where more frequent collisions deactivate the excited state. The observed blue shift of the emission maximum is typical of the exposure to a more hydrophobic environment as expected for the binding site in comparison to the state in aqueous solution.

Using titration experiments, the  $K_D$  values were estimated from the concentration of the nucleotide analogs that evoked half of the maximal fluorescence change, when titrated to a solution of the PN domain as shown in Fig. 4.5. The TNP-nucleotides had a high affinity to the PN domain with an apparent binding constant ( $K_D$ ) in the 4-8  $\mu\text{M}$  range for both nucleotide analogs. These values are in the typical range of nucleotide binding domains [138, 142, 143]. Together with the catalytic assays, the data reveal that the recombinant PN domain is a well folded catalytically active protein and thus suitable for further structural and functional analysis.



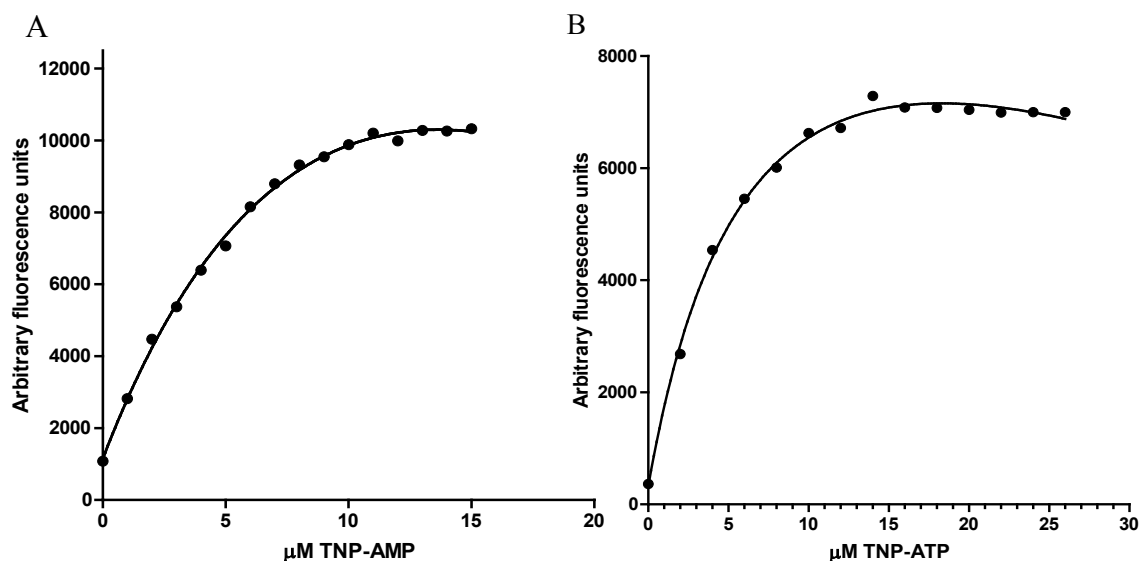


**Figure 4.5. Titration of TNP-nucleotides to 3  $\mu$ M PN domain.**

A) TNP-AMP and B) TNP-ATP were titrated to 3  $\mu$ M PN domain in 50 mM Tris-HCl pH 7.4 and 200 mM KCl buffer. TNP-nucleotides were excited at  $\lambda_{\text{ex}}$  408 nm and emission spectra recorded from 500-600 nm range. In parallel, the same titration system of TNP-nucleotides to buffer without protein were performed as control and subtracted from all data points. The dissociation constants ( $K_d$ ) of TNP-AMP and TNP-ATP were determined to be 4-8  $\mu$ M. Data were fitted to one site model using GraphPad Prism software.

#### 4.2.2 Copper(I) affinity of the HMBD

We studied the characteristic interaction of  $\text{Cu}^+$  with the LpCopA HMBD as a soluble cytosolic domain. The  $\text{Cu}^+$  binding to the HMBD was studied in the presence of the  $\text{Cu}^+$  indicator bicinchoninic acid (BCA). The BCA competition assay has been developed for the determination the copper affinity of metal binding domain as an alternative to other methods [144-146]. Two molecules of BCA bind to one  $\text{Cu}^+$  ion to form a colored  $[\text{BCA}_2\cdot\text{Cu}^+]$  complex with  $K_D = 1 \times 10^{-11} \text{ M}^2$  [147]. The color development can be monitored at 356 nm [99]. As shown in Fig. 4.6, 5  $\mu$ M HMBD almost completely displaced  $\text{Cu}^+$  from 50  $\mu$ M of the competing BCA at 5  $\mu$ M  $\text{CuCl}_2$  concentration, i.e. there was almost no absorbance of the  $\text{BCA}_2\cdot\text{Cu}^+$  complex at this copper concentration as compared to the control without the HMBD. Therefore,  $K_D$  of the HMBD $\cdot\text{Cu}^+$  complex must be significantly lower than a  $5 \times 10^{-6} \text{ M}$ . More specifically, the presence of the HMBD reduces the BCA-Cu complex concentration by a factor of 8, corresponding

to 0.63  $\mu\text{M}$ . The explicit use of the  $K_D$  of the  $\text{BCA}\cdot\text{Cu}^+$  complex yields a free copper concentration of 450 nM which together with the  $\text{BCA}$ -bound  $\text{Cu}^+$  adds up to 1.1  $\mu\text{M}$   $\text{Cu}^+$ . This leaves 3.9  $\mu\text{M}$   $\text{Cu}^+$  that is bound to the  $\text{HMBD}$  at 450 nM free  $\text{Cu}^+$ . From this we obtain the more realistic estimate of the  $K_D$  of the  $\text{Cu}^+$   $\text{HMBD}$  complex of 130 nM. On another hand, the  $\text{Cu}^+$  loading assay (as described in Chapter 2 section 2.4.2.1) indicates that the stoichiometry of copper binding by  $\text{HMBD}$  is 1:1.5 (protein : metal).

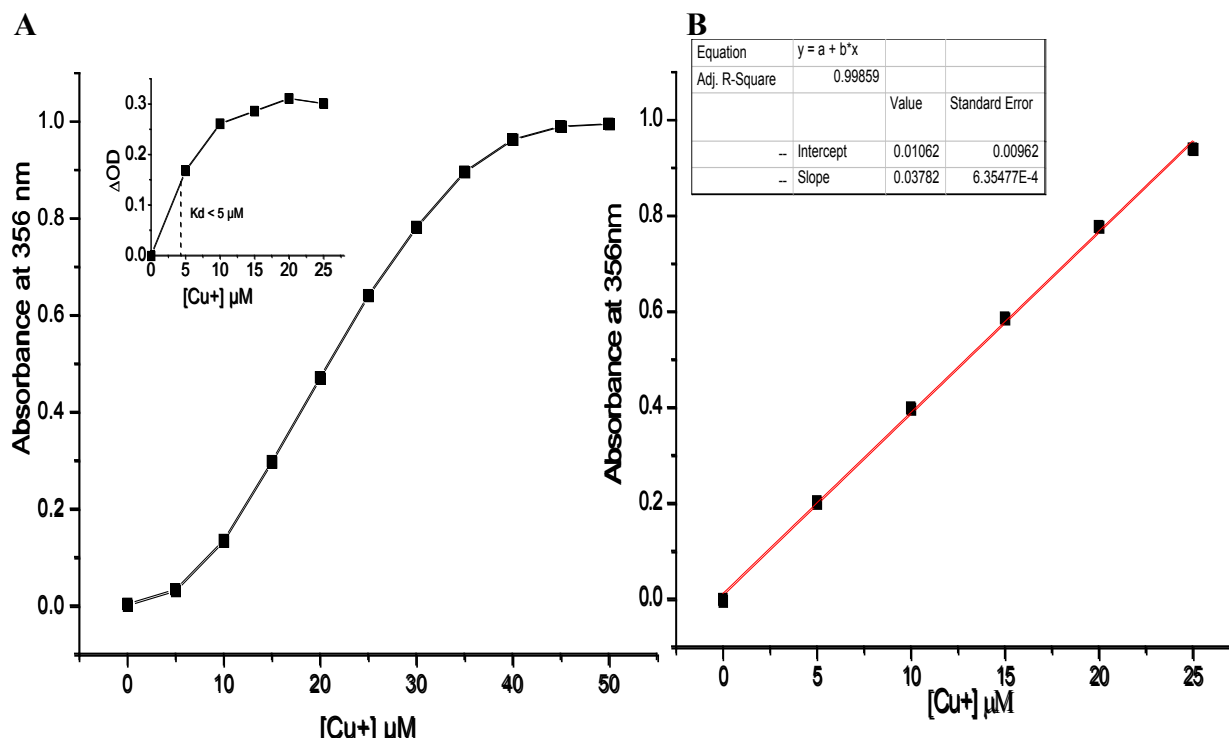


**Figure 4.6. The BCA competition assay of HMBD copper complex formation.**

In 400  $\mu\text{l}$  total assay volume, **A**) 5  $\mu\text{M}$   $\text{HMBD}$  and 50  $\mu\text{M}$  Pierce  $\text{BCA}$  mixture, in 30 mM  $\text{HEPES}$  pH 7.3 and 1 mM ascorbic acid buffer, was titrated with 1 mM  $\text{CuCl}_2$  with continuous stirring at room temperature. The bright purple color of  $[\text{BCA}_2\cdot\text{Cu}^+]$  complex is detected at  $\lambda = 356$  nm. **B**) Standard curve of the  $[\text{BCA}_2\cdot\text{Cu}^+]$  complex. The insert is the absorbance difference between  $\text{HMBD}+\text{BCA}$  mixture and  $\text{BCA}$  alone.

### 4.2.3 Thermal stability of cytosolic domains

Thermal unfolding monitored by spectroscopy is widely used to determine protein stability. Circular dichroism spectroscopy (CD) measurements taken at small temperature intervals were used to determine the melting temperature,  $T_m$ , of the expressed soluble proteins by following the changes in secondary structure in the entire far-UV CD region or at a specific wavelength over time (i.e. at different temperatures during constant heating). The measurement can be performed with micrograms of protein; therefore the technique is very effective for membrane proteins. Here, we have studied the thermal stability of the recombinant cytosolic domains as a function of a ligand using the CD spectroscopy.

The CD signal at 222 nm corresponding to the alpha-helical content can be used to distinguish folded and unfolded states of protein. We examined the thermal denaturation of the PN and actuator domains by recording the CD signal between 298 and 364 K. Data points of the 222 nm signal were collected every 2 K (Fig. 4.7 & 4.8). The  $T_m$  was determined by curve fitting according to the equation described in Chapter. . The  $T_m$  values were calculated from the midpoint of the transition curves between folded and unfolded states of the proteins. The  $T_m$  value for the denaturation of the PN domain was at 334.3 K. In the presence of 0.1 mM ATP $\gamma$ S, the PN domain exhibited two apparent melting temperatures, indicative of the nucleotide stabilizing only the N domain but not the P domain within the expressed PN domain (Fig. 4.7). In contrast, the actuator domain was less stable and melted at 315 K (Fig. 4.8).

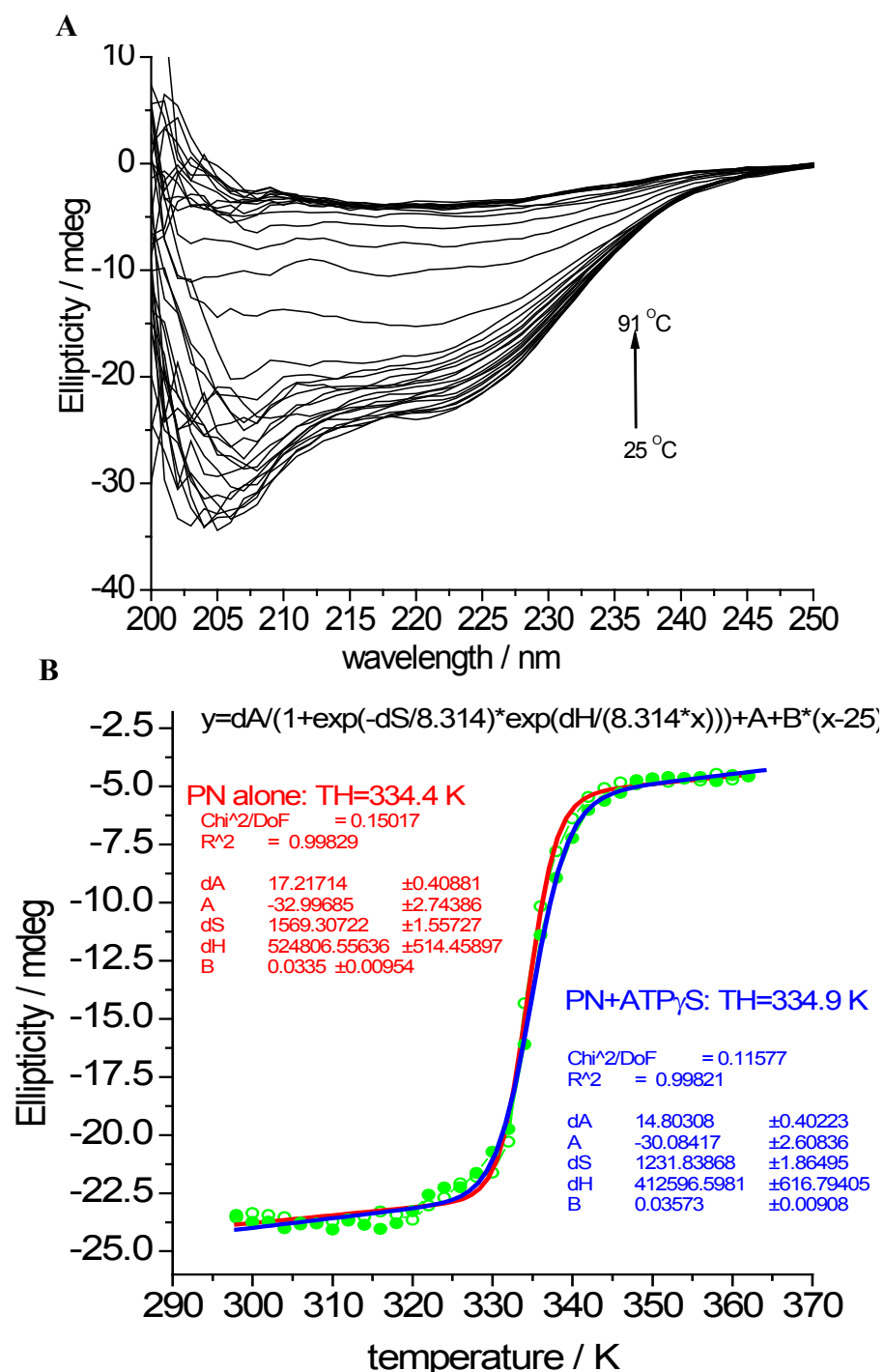


**Figure 4.7. Thermal Denaturation of PN domain was determined by circular dichroism.**

**A)** Far-UV circular dichroism (Far-UV CD) of 3  $\mu$ M PN domain in 10 mM KH<sub>2</sub>PO<sub>4</sub> pH 7.4 and 3 mM MgCl<sub>2</sub> using 1-cm cylindrical cuvette recorded at different temperatures (from 298 to 364 K). **B)** Unfolding of the PN domain in the absence (red line) and presence (blue line) of 0.1 mM ATP $\gamma$ S was monitored with the CD signal at 222 nm. The unfolding is identical within experimental error in the lower temperature half, assigned to unfolding of the N domain. The curves deviate in the higher temperature side by the shift to higher temperature of the curve recorded with ATP $\gamma$ S, indicating the independent folding properties of the two domains, i.e., there is no indication for a cooperative effect nucleotide-induced stabilization of both domains.

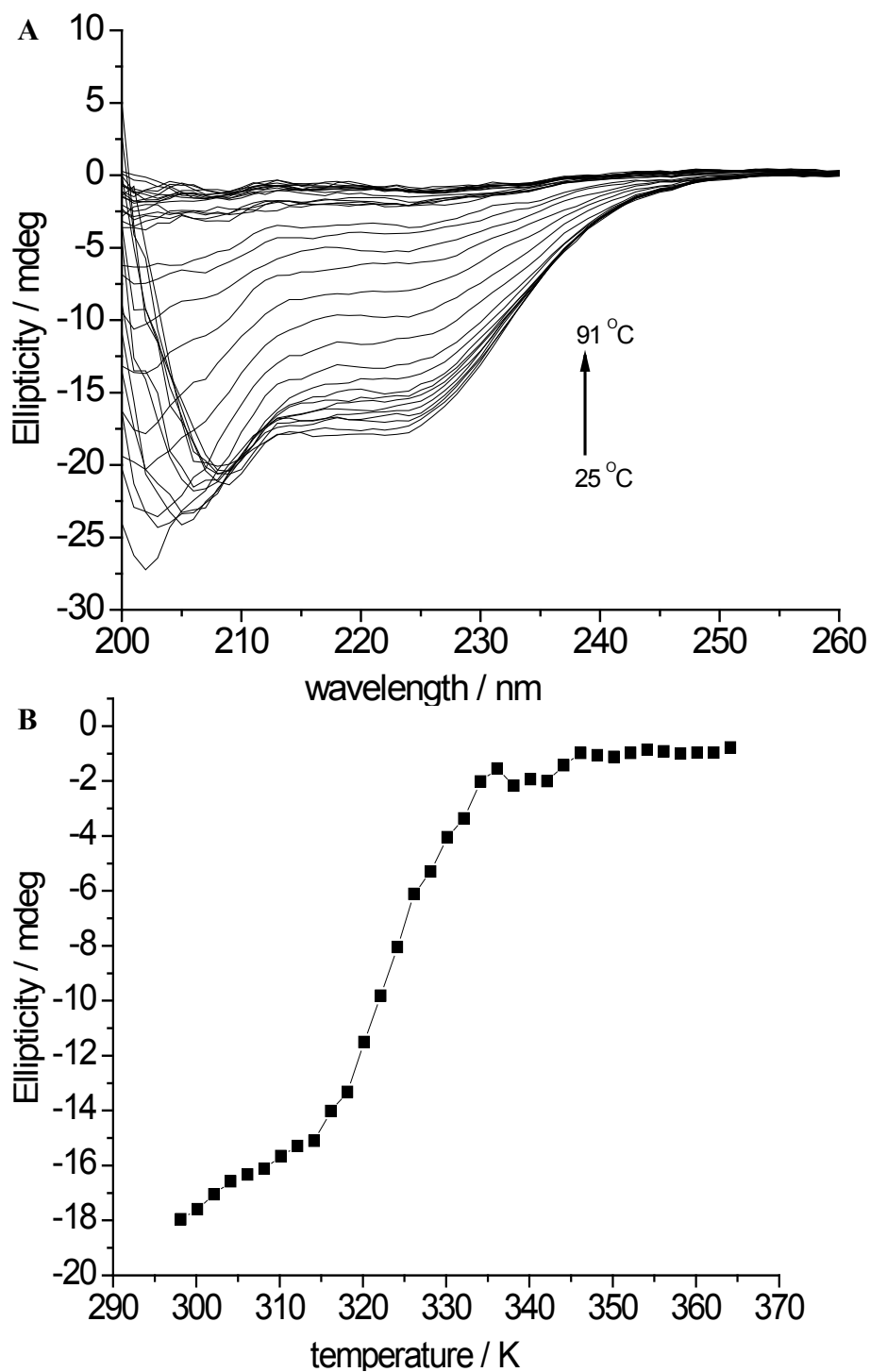


**Figure 4.8. Thermal denaturation of A-domain.**

**A)** Far-UV CD of 10  $\mu\text{M}$  A-domain in 10 mM  $\text{KH}_2\text{PO}_4$  pH 7.4 and 3 mM  $\text{MgCl}_2$  using 1-cm cylindrical cuvette was recorded. **B)** Thermal denaturation profile of A-domain was determined by tracing ellipticity at 222 nm at a 2 K/min heating rate from 298 to 364 K.

Interestingly 5 mM magnesium sulfate stabilized the PN domain by  $\sim 5$  K in comparison with 5 mM magnesium chloride as shown in Fig. 4.9. This anion-specific effect indicates that the sulfate anion may have bound to the P-domain as a phosphate surrogate at the crystallographically identified phosphate-binding location. It has been reported that sulfate ion acts as phosphate analog at P-domain of the *S. solfataricus* CopB [133] and SERCA1a [72]. Therefore, it is suggested that sulfate ion has a comparable impact on the P-domain stabilization.

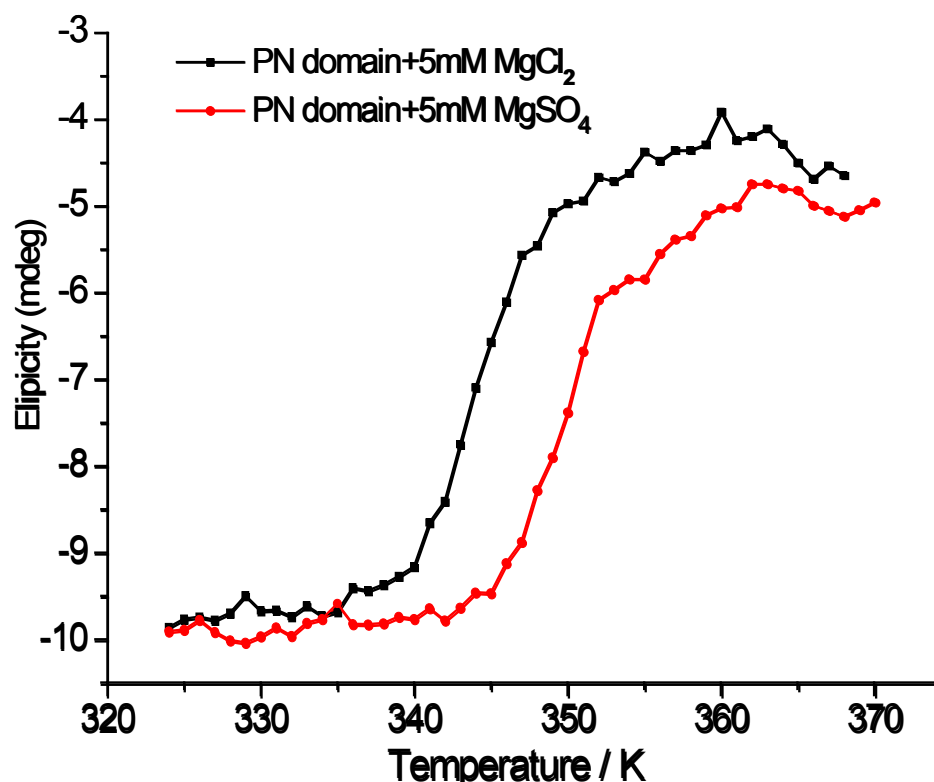


**Figure 4.9. PN domain is thermally stabilized by MgSO<sub>4</sub>.**

At 222 nm, the CD signals of 3  $\mu$ M PN domain, in 20 mM Tris-HCl pH 7.5 + 5 mM MgCl<sub>2</sub> buffer (black traces) and in 20 mM Tris-H<sub>2</sub>SO<sub>4</sub> pH 7.5 + 5 mM MgSO<sub>4</sub> buffer (red traces), were recorded at different temperatures from 324 to 370 K with ramp rate of 1  $^{\circ}$ C/min.

## Summary and discussion

Our data show that the expressed cytosolic domains are well-folded and capable of binding to the particular ligands. The secondary structure estimated from CD signals of cytosolic domains show that the alpha-helical content varies between 23 and 38% in line with the total secondary content of crystal structure of LpCopA (PDB ID: 3RFU) calculated by the DSSP method. Moreover, the data analysis of CD and fluorescence spectroscopy show that PN domain bind with the nucleotide with an apparent binding constant ( $K_d$ ) of the 4-8  $\mu\text{M}$  range, inducing a limited structural alteration, while Cu (I) binding to HMBD induce increasing in  $\alpha$ -helical content in high affinity ( $K_d < 5 \times 10^{-6}$  M). In another hand, the thermal stability profiles of PN domain show that sulfate-bound P-domain is considerably stabilized the entire PN domain by  $\sim 5$  K, while ATP $\gamma$ S weakly stabilized the N-domain merely. Finally, the biophysical characterizations of cytosolic domain demonstrated the structural integrity and proper function of expressed domains.

## Chapter 5

### The ligand-dependent Interactions among Cytosolic domains of *Legionella pneumophila* CopA

#### Introduction

The cytosolic domains interaction and rearrangement modulate the conformation of TM domain and regulate the metal binding and release. The structures of full Ca<sup>2+</sup>-ATPase are solved in all transition states, on contrast to the structure of Cu-ATPases which is failed to be entirely solved including the Heavy metal-binding domain (HMBD). Therefore, it remains unknown how the HMBD interacts with other cytosolic domain in the catalytic cycle. The exact role of HMBD in the enzymatic function of CopA is somewhat controversial. HMBD does not play a role in the direct metal transfer to the entry site of TM; however it can exchange the Cu<sup>+</sup> with soluble chaperones.

The biochemical studies on the function of HMBD are not conclusive; the truncation of HMBD in *A. fulgidus* CopA yielded a higher enzymatic turnover while alterations in the MxCxxC motif or HMBD truncation impaired the enzymatic activity of CopA in *T. maritima* and *L. pneumophila*. Argüello and his co-workers suggested that N-MBD plays a regulatory and self-inhibitory role for controlling the turnover rate of the enzyme [148]. This hypothesis is supported by electron microscopy and docking studies of Stokes et al that place the N-MBD of AfCopA in close contact with N- and A-domains to restrict the movement of these domains in Cu<sup>+</sup>-free state while displaced upon Cu<sup>+</sup> binding and thus, launch the catalytic motions of the domains [149]. However, the co-purification assay of AfCopA N-MBD with A-domain shows no interaction under any conditions.

In contrast, Hatori and his coworkers proposed that the HMBD is an integral part of enzyme headpiece and its Cu<sup>+</sup> loading is required to produce an active conformation and full activity of CopA [150]. Recently, our model study, *L. pneumophila* CopA (LpCopA), has been structurally solved in E2P and E2~P states (excluding HMBD) by X-ray crystallography [100] and its domain interaction have not been investigated yet.



Here, utilizing the functionally expressed cytosolic domains in Chapters 3 and 4, we investigate the interactions among cytosolic domains of LpCopA in function of appropriate ligands, and try to answer the question of whether the HMBD interacts with other cytosolic domain and play a catalytic role. Our data show Cu<sup>+</sup>-dependent interaction of HMBD with A-domain and suggest that HMBD of LpCopA has an activating role in presence of Cu<sup>+</sup> and an inhibitory role in absence of Cu<sup>+</sup> ion.

## Results and discussion

After proving the structural and functional integrity of the expressed cytosolic domains in previous sections, the interactions among the cytosolic domains were monitored by two different assays, co-purification and fluorometric assays.

In the latter, the cysteine side chains of HMBD were previously labeled with fluorescent dyes, CPM (7-Diethylamino-3-(4'-Maleimidylphenyl)-4-Methylcoumarin) and BADAN (6-Bromoacetyl-2-Dimethylaminonaphthalene), to monitor its interaction with A-domain.

### 5.1 Co-purification assay of cytosolic domain interactions

The proposed interactions among cytoplasmic domains of CPx-type ATPases had previously been studied by co-purifying the isolated cytosolic domains as function of ligands via batch affinity chromatography in order to mimic the different states of the catalytic cycle of P-type ATPases [55, 63, 64, 151, 152]. The assessment of domain-domain co-purification provides a remarkable insight into the way these domains interact during the catalytic cycle without providing affinity values. Here, we employed the column chromatography instead of batch affinity chromatography to investigate the interaction among the HMBD, PN- and A-domains of LpCopA. This method is characterized with: 1) simple mixing without disrupting the interaction, 2) easy ligand exchange, 3) partner domains stay in close contact, and 4) easy elimination of unbound protein.

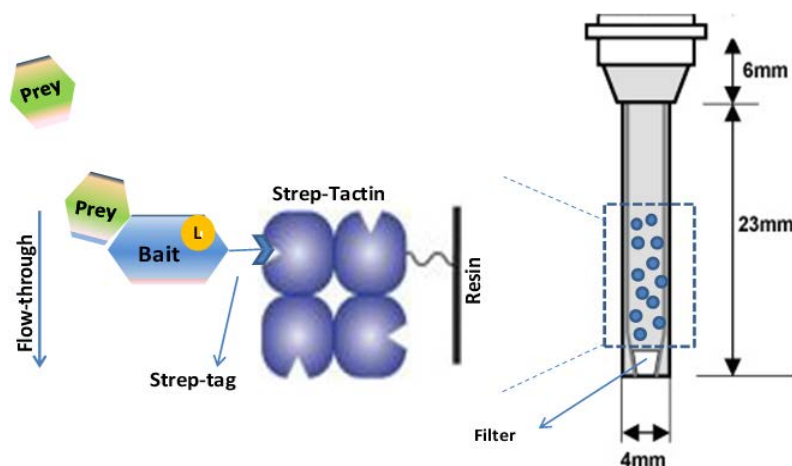


**Figure 5.1. A schematic diagram represents domain-domain co-purification assay.**

Micro-spin column (23 mm length x 4 mm diameter) was filled with 50-100  $\mu$ M Strep-Tactin, and buffer is exchanged either by centrifugation at the lowest speed or by gravity-flow. The strep-tagged protein acts as immobilized “bait” protein for the partner protein “prey” in function of ligand “L”. Unbound proteins are washed away, and the target protein complex is recovered by elution with desthiobiotin.

In all co-purification assays, Strep-Tactin resin was preferred over Ni-NTA resin due to its high specificity, and to prevent binding of the HMBD to Ni-NTA or interference of Ni<sup>2+</sup> ions with Cu<sup>+</sup> ions. The Strep-tagged protein bound to Strep-Tactin resin was used as a stationary phase for the partner protein in micro-spin column (Pierce) as shown in Fig. 5.1.

### 5.1.1 The HMBD interacts with A-domain in a copper-dependent manner

Under gravity flow, the HMBD (2 nmol) mixed with 10 μM TTM or with 30 μM Cu<sup>+</sup> ion (reduced by ascorbic acid) was loaded onto 50 μl Strep-Tactin resin, and washed to remove unbound HMBD and free Cu<sup>+</sup>. In this stage, most of the loaded HMBD protein was bound to the resin as shown in Fig. 5.2 & 5.3 (lane FT<sub>MBD</sub>). Afterwards, 2 nmol A-domain, previously digested with Thrombin protease to remove the 6x His-tag, was added to the column containing Cu<sup>+</sup>-loaded or Cu<sup>+</sup>-free HMBD, and the unbound protein was washed out before elution of the HMBD with 5 mM desthiobiotin. Because of the close proximity in size between the HMBD (which elutes forms a dimer) and the A-domain, all SDS samples obtained from co-purification were labeled with the thiol-reactive dye, BADAN, for detecting the HMBD band under UV light as opposed to the A-domain which has no thiols and is thus visible only after Coomassie-blue staining but not under UV light. Each SDS-PAGE gel was exposed to the UV light prior to staining with Coomassie blue dye.

In Fig. 5.2, The SDS-PAGE analysis of co-purification of the Cu<sup>+</sup>-free HMBD with the A-domain shows that the elution bands of the HMBD in both the control (lane E) and after loading the A-domain (lane E<sub>A</sub>) are alike. This suggests that the HMBD does not interact with the A-domain in absence of Cu<sup>+</sup> ion.

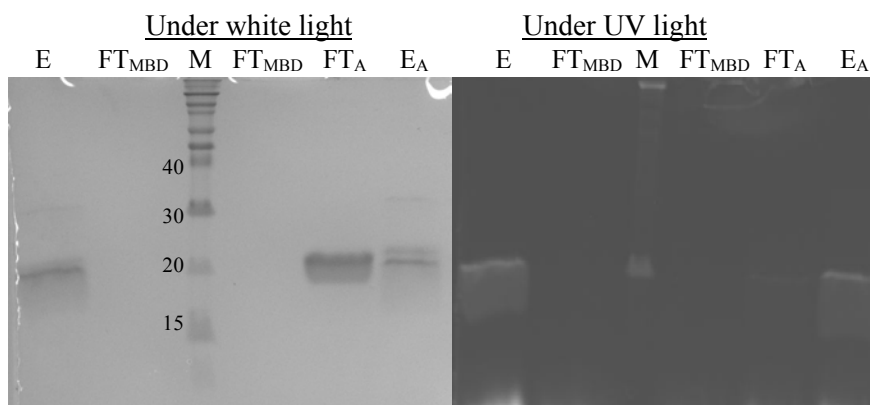


**Figure 5.2. SDS-PAGE analysis of co-purification assay of Cu<sup>+</sup>-free HMBD with A-domain.**

2nmole strep-tagged HMBD with 10  $\mu$ M TTM was loaded onto 50  $\mu$ l Strep-Tactin resin, followed by 4CVs washing buffer. 2 nmole A-domain was added to the bound HMBD. The samples were labeled with excess BADAN dye prior to gel loading. The gel was displayed first under UV light (Right panel) and then the stained gel under white light (Left panel). Lane M, protein molecular weight standards (kDa); lane FT<sub>MBD</sub>, flow-through of HMBD; lane FT<sub>A</sub>, flow-through of A domain; lane E, Elution of HMBD (control); lane E<sub>A</sub>, Elution of HMBD co-purified with A domain.

In contrast, the Cu<sup>+</sup>-loaded HMBD seems to interact with the A-domain as shown in Fig. 5.3 in the presence of 30  $\mu$ M Cu<sup>+</sup>. Comparing the equivalent SDS-PAGE gel of co-purification of Cu<sup>+</sup>-loaded HMBD with A-domain under white and UV light, it is obvious that most of the bound HMBD was now associated with the flow-through of the A-domain (Fig. 5.3, lane FT<sub>A</sub>). Furthermore, the elution band of HMBD appears now more intense under white light than under UV light (Fig. 5.3, lane E<sub>A1</sub>) which indicates that the A-domain is co-eluted with HMBD, thereby enhancing the Coomassie stain but not the fluorescence stain. The HMBD association with the flow-through of A-domain was unexpected and striking as the binding affinity of Strep-tag II to Strep-Tactin resin is strong ( $K_d \sim 1 \mu$ M) according to IBA manufacturer instructions[153]; however, a similar behavior has also been detected in the co-purification assay of the same domains from *A. fulgidus* CopB in presence of copper (Fig. 2.9c from [152]). These two observations suggest that the HMBD interacts with the A-domain in Cu<sup>+</sup>-dependent manner with an affinity that is higher than that between Strep-tag and Strep-Tactin resin.

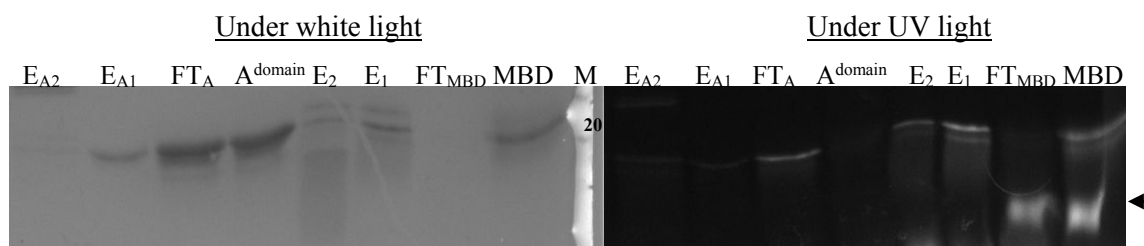


**Figure 5.3. SDS-PAGE analysis of co-purification assay of Cu<sup>+</sup>-loaded HMBD with A-domain.**

A mixture of 2 nmole strep-tagged HMBD and 30  $\mu$ M CuCl<sub>2</sub> was loaded into 50  $\mu$ l Strep-Tactin resin. 2 nmole untagged A-domain was added to the bound HMBD. The assay was carried out in buffer of 30 mM HEPES-NaOH pH 8, 100 mM NaCl, 1 mM DTT and 1 mM ascorbic acid. The gel was displayed under UV light (Right panel) and under white light (Left panel). Lane M; protein molecular weight standards (kDa); lane MBD, HMBD before loading onto the column; lane FT<sub>MBD</sub>, flow-through of Cu<sup>+</sup>-loaded HMBD; lanes E<sub>1</sub> and E<sub>2</sub>, two consecutive elutions of HMBD (control) with 50  $\mu$ l of 5 mM desthiobiotin; lane A<sup>domain</sup>, A-domain prior to loading; lane FT<sub>A</sub>, flow-through of A domain; lanes E<sub>A1</sub> and E<sub>A2</sub>, two consecutive elutions of HMBD co-purified with A domain. The arrow indicates a fluorescence artifact under UV light, which is not due to protein bands (no corresponding Coomassie stained band under white light) but to excess BADAN.

This assay provides the first experimental finding that supports the interaction between the HMBD and the A-domain in a Cu-specific manner. For instance, the co-purification of C-MBD from *A. fulgidus* CopA [55] and N-MBD from *A. fulgidus* CopB [152] with the A-domain showed always interaction in a Cu<sup>+</sup>-independent manner, while the N-MBD from *A. fulgidus* CopA did not show any interaction at any state [63]. Nevertheless in the latter study there was an indication of an interaction between these domains according to the SDS gel of the A-domain/Cu<sup>+</sup>-loaded N-MBD co-purification (Fig. 5.3), but the authors ignored it [63].

Moreover, the assay provides additional experimental support for the pseudoatomic model of *A. fulgidus* CopA [47, 149], the biochemical study of domain organization of *T. maritima* copA [74], the structural model of *E. hirae* CopA based on chemical cross-linking[154], and crystallographic and NMR studies of *S. pneumoniae* CopA HMBD [75]; in which the association of the HMBD with the A-domain is suggested even in a Cu<sup>+</sup>-free state.

The proposed interaction between the HMBD and the A-domain can be understood on the basis of electrostatic surface potential analysis of these domains from *S. pneumoniae* [75] and *E. hirae* CopA[154] suggesting that the positively charged HMBD could preferentially dock against the negatively charged A-domain. This electrostatic contact is likely to be strengthened when  $\text{Cu}^+$  binds to the HMBD. In LpCopA, the electrostatic surface of the HMBD cannot be determined because the LpCopA structure does not resolve the HMBD. The electrostatic surface of the resolved A-domain is indeed negatively charged at the close proximity to the proposed site of the HMBD.

### 5.1.2 The HMBD does not bind to the PN domain

The co-purification of the HMBD with the C-terminal 10xHis tagged PN domain was examined as well. The tag of the PN domain was left uncleaved as the tag was not exposed to the corresponding protease enzyme. In this assay, the PN domain with and without AppNp (as a non-hydrolyzable trinucleotide analog) was co-purified with  $\text{Cu}^+$ -free and  $\text{Cu}^+$ -loaded states of the HMBD as described above. We were unable to detect any interaction between these domains under these experimental conditions as shown in Fig. 5.4.

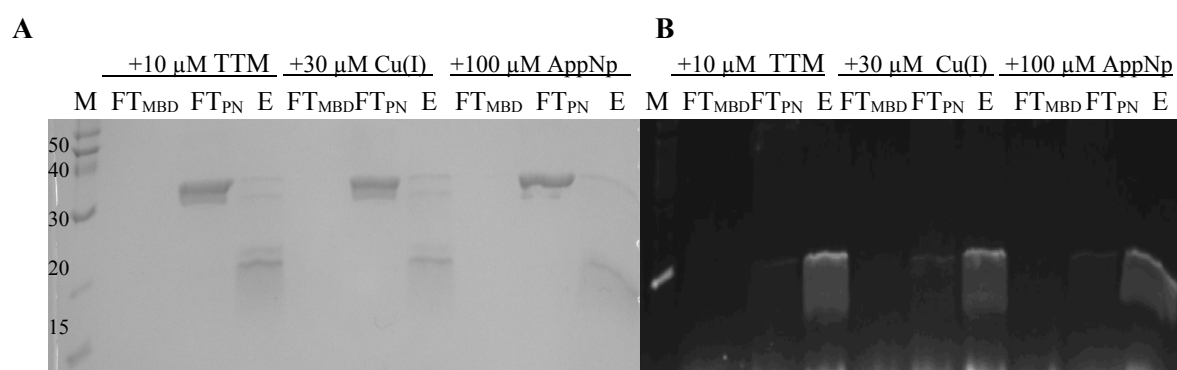


**Figure 5.4. SDS-PAGE analysis of PN domain co-purification with HMBD.**

2 nmole PN-domain was co-purified with 2 nmole HMBD bound to the column in function of 10  $\mu\text{M}$  TTM (Cu-chelator), 30  $\mu\text{M}$   $\text{CuCl}_2$  (6 nmol) or 100  $\mu\text{M}$  AppNp. The assay buffer contains of 30mM HEPES-NaOH pH 8, 100 mM NaCl, 1 mM DTT, 1% glycerol and 1mM ascorbic acid. The protein samples were labeled with fluorescent BADAN dye and detected in the gel under **A**) white and **B**) UV light. Lane M, protein molecular weight standards (kDa); lane  $\text{FT}_{\text{MBD}}$ , flow-through of HMBD; lane  $\text{FT}_{\text{PN}}$ , flow-through of PN domain; lane E, Elution of HMBD co-purified with PN domain.

This result, however, does not agree with previously equivalent assays of the same domains from human ATP7B [64] and *A. fulgidus* CopA [63] in which those domains interact with each other in a specific manner. Also, cryo-EM study of CopA from *A. fulgidus* suggests that the HMBD interacts with the A- and N-domains [149].

### 5.1.3 The controls for the HMBD co-purification assay

As a control, the His-tagged TEV protease was used for examining the specificity of the assay. The Cu (I)-loaded HMBD was co-purified with His-tagged TEV protease under the identical conditions. The recombinant TEV protease is rich in cysteines which can be labeled and monitored on the gel under UV light. As shown in Fig. 5.5, there was no detection of TEV protein band in HMBD elution. On another hand, no band of HMBD was detected in the flow-through (FT) of TEV protease. The last observation indicates, therefore, that the HMBD eluted with the FT of A-domain in Fig. 5.3 perhaps occurred in a specific manner due to strong interaction between these domains.

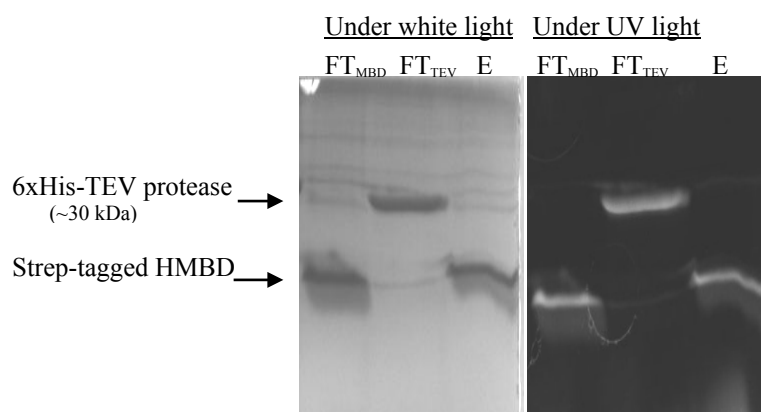


**Figure 5.5. SDS-PAGE analysis of N-term 6xHis TEV protease co-purified with HMBD as negative control.**

The recombinant TEV protease rich in cysteine residues can be also labeled with BADAN and monitored under UV light. 2 nmole HMBD with 6 nmole  $\text{CuCl}_2$  was loaded onto 50  $\mu\text{l}$  Strep-Tactin resin. Then, 2 nmole 6xHis TEV was added to the bound HMBD. The gel was displayed under UV light (Right panel) and under white light (Left panel). Lane  $\text{FT}_{\text{MBD}}$ , Flow-through of HMBD; lane  $\text{FT}_{\text{TEV}}$ , Flow-through of 6xHis-TEV protease and lane E, Elution of HMBD.

Moreover, the specificity of Strep-Tactin was examined by using Strep-tag-free PN or A-domains instead of HMBD. The SDS-PAGE gel shows no detection of 6xHis-tagged PN domain or A-domain in the elution fraction as shown in Fig. 5.6.

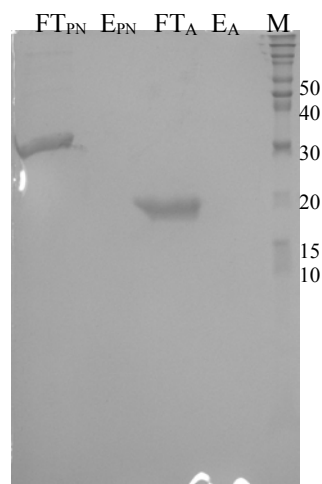


**Figure 5.6. SDS-PAGE gel indicates the specificity of Strep-Tactin resin for co-purification assay.**

2 nmole 6xHis-tagged PN or A domains were loaded in free Strep-Tactin resin to check the specificity of the column. M; protein Marker (kDa), FT<sub>A</sub>; Flow-through of A domain loading, E<sub>A</sub>; Elution of A-domain; FT<sub>PN</sub>; Flow-through of PN domain loading, E<sub>PN</sub>; Elution of PN-domain.

#### 5.1.4 Co-purification of PN domain with A-domain

It has been established that the A-domain is associated with P-domain in phosphoenzyme (*EP*) conformations in all P-type ATPases. In the *E1.ATP* state of the  $\text{Ca}^{2+}$ -ATPase, the N-domain is more inclined towards the P-domain [72, 155], causing gathering of the cytosolic domains to form a compact headpiece after widely separating in the *E1.2Ca<sup>2+</sup>* state. This in turn causes a tilt of the A-domain by 30° around an axis to make contact with the N-domain with a different interface compared to the *E2(TG)* [72, 83, 155].

Therefore, the interaction between the PN- and the A- domains has been investigated by a co-purification assay as a function of nucleotide. Unfortunately, the designated FRET measurement between L466Y mutant of PN domain and I281W mutant of A-domain was cancelled due to anomalous emission spectrum of tyrosine in L466Y mutant (data not shown). In co-purification assay, 10  $\mu\text{M}$  dual-tagged PN domain (N-Strep and C-10xHis tags) was co-purified with 30  $\mu\text{M}$  6xHis-tagged A-domain on a Strep-Tactin resin in the presence of 100  $\mu\text{M}$  ATP $\gamma$ S/5 mM MgCl<sub>2</sub>, a non-hydrolyzable analogue of ATP. The column was washed twice with 4 CV of washing buffer, and then eluted with 5 mM desthiobiotin.



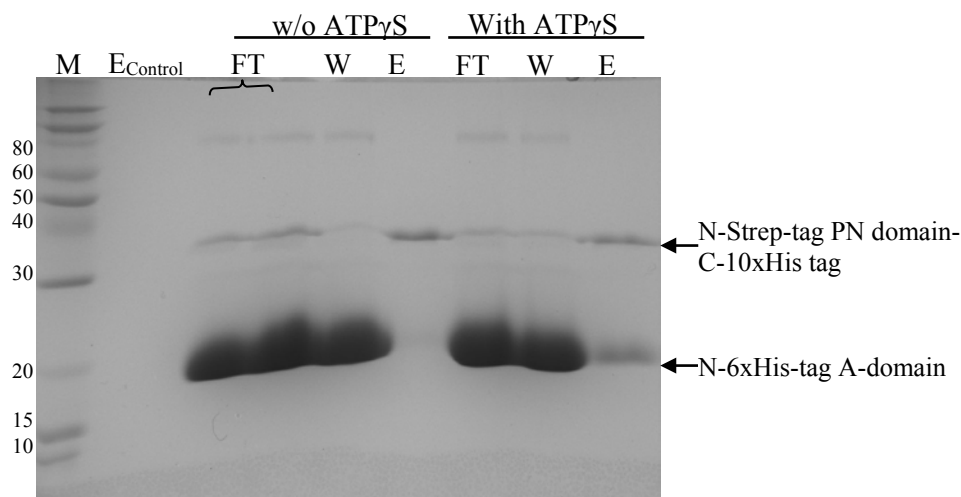


**Figure 5.7. SDS-PAGE analysis of co-purification of PN domain with A-domain.**

6 nmol A-domain was loaded into 2nmol dual tagged PN domain ( $\pm 0.1$  mM ATP $\gamma$ S/5 mM MgCl<sub>2</sub>) bound to 100  $\mu$ l Strep-Tactin resin. The column washed twice with 4CV of 50 mM Tris-HCl pH 8, 100 mM NaCl, 1 mM DTT, 1% glycerol  $\pm 0.1$  mM ATP $\gamma$ S/5 mM MgCl<sub>2</sub>. Lane M, Molecular weight marker (kDa); lane E<sub>Control</sub>, Elution of A-domain loaded to Strep-Tactin resin (control); lane FT, Flow-through of A-domain; W, first washing aliquot; E: Elution of PN domain. Arch refers to duplicated lane of The FT of A-domain.

In Fig. 5.7, The SDS-PAGE gel of these domains co-purification indicates that A-domain co-eluted merely with ATP $\gamma$ S-bound PN domain and did not bind to the nucleotide-free PN domain. The same result has been obtained when ATP $\gamma$ S was replaced by 100  $\mu$ M ADP/5 mM MgCl<sub>2</sub> (data not shown). This indicates that the binding between these domains probably involves directly the nucleotide pocket of the N-domain rather than the P domain.

There are two possible explanations for this affinity; first the bound nucleotide induces conformational changes at the nucleotide pocket of the N-domain, thereby exposing side chain residues for interaction. A key feature of CPx-ATPase is the conserved HP motif located on the outermost surface of the N-domain which is involved in ATP binding and perhaps in interaction of the N-domain with other domains [156].

The second explanation is that the A-domain interacts directly with the bound nucleotide. This hypothesis is supported by an unexpected ATPase activity of the A-domain in solution as discussed in Chapter 3, section 3.4.1. However, further experiments are required to substantiate this hypothesis.

Moreover, it is worth mentioning that the crystal structure of the  $\text{Ca}^{2+}$ -ATPase (PDB ID: 3B9R) in  $E2\text{.AlF}_4\text{.AppCp}$  conformation indicates that the A-domain interacts with a modulatory ATP bound to the N-domain. Specifically the Arg174, Ile188, and Lys205 side chains of the A-domain in the  $\text{Ca}^{2+}$ -ATPase are closely associated with the bound nucleotide to modulate the phosphoenzyme processing [73]. Also, the Ser186 side chain of the A-domain and the Glu439 side chain of the N-domain are closely located to the modulatory ATP binding site for the  $EP$  isomerization and their hydrogen bond stabilizes the  $E2P$  ground state structure [157]. Knowing that the Copper-ATPase also shows the two modes of ATP binding, catalytic and modulatory, in the same pocket, but slightly separated as well as the other P-type ATPases [37, 63, 90], and the crystal structure of LpCopA bound with either catalytic or modulatory ATP has not been solved yet. Taken together, it is suggested that A-domain in LpCopA has a close contact with modulatory ATP-bound N-domain through relevant residues to those in  $\text{Ca}^{2+}$ -ATPase, Figure 5.8 shows the comparative position of residues in the A-domain of LpCopA to those bound to modulatory ATP in  $\text{Ca}^{2+}$ -ATPase have interaction with.

In Fig. 5.8, the superposition of the  $\text{Ca}^{2+}$ -ATPase bound with modulator nucleotide in  $E2\sim\text{P}\text{-AppCp}$  state (PDB ID: 3B9R) and LpCopA in  $E2\sim\text{P}$  state (PDB ID: 3RFU) demonstrates that the LpCopA structure shares a basic architecture with the  $\text{Ca}^{2+}$ -ATPase despite of a low degree of sequence identity. Considering the crystal structure of LpCopA has no AppCp nucleotide (in Fig. 5.8), the Arg268, Ala284 and Lys290 residues of LpCopA are in a close proximity to the Arg174, Ile188, and Lys205 residues of  $\text{Ca}^{2+}$ -ATPase which interact with the modulatory ATP bound in N-domain.

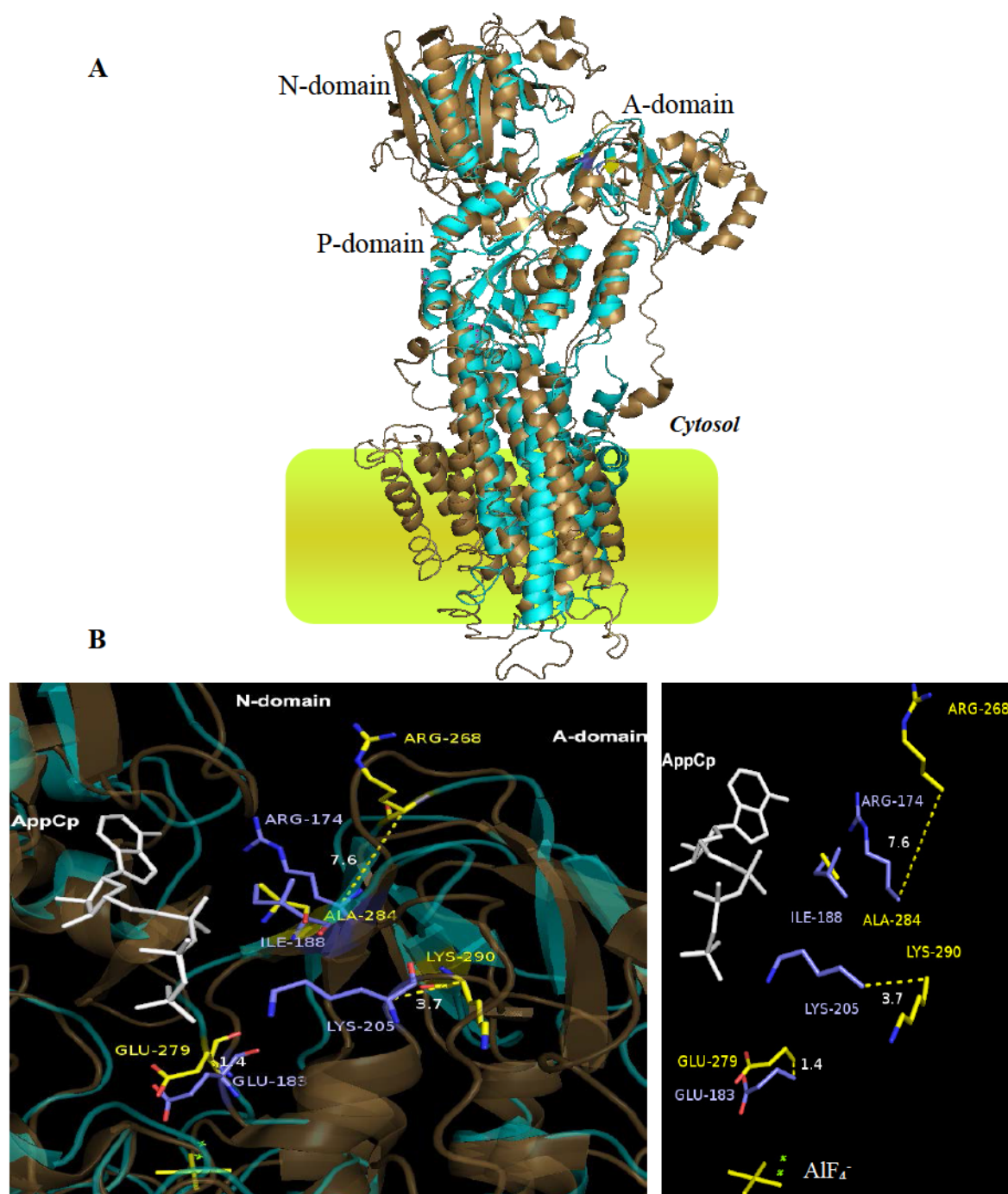


**Figure 5.8. Superimposition of LpCopA and  $\text{Ca}^{2+}$ -ATPase with modulatory nucleotide.**

The cartoon represents the superimposed  $\text{Ca}^{2+}$ -ATPase in  $E2.\text{AlF}_4^-.\text{AppCp}$  state (PDB ID: 3B9R) with LpCopA in  $E2.\text{AlF}_4^-$  state (PDB ID: 3RFU). The LpCopA structure is in cyan color and  $\text{Ca}^{2+}$ -ATPase structure in forest color. **A)** The overall structure of both superimposed ATPases shows similarity in a basic architecture. Nucleotide-binding, Phosphorylation and Actuator domains were denoted as N-, P- and A-domains, respectively. **B)** Close-view of the binding interface between N-domain and A-domain, proposed by Clausen et al.[73], shows the exist of Arg268, Ala284 and Lys290 residues of LpCopA (in yellow color) in relatively close position to the Arg174, Ile188, and Lys205 residues of  $\text{Ca}^{2+}$ -ATPase (in light-blue color).the distance in Å is measured between  $\alpha$ -carbons of comparative residues.

## 5.2 Fluorometric assay of Cu (I) dependent interaction of HMBD with A-domain

As described in the co-purification assay, the A-domain exhibited a specific interaction with Cu (I)-bound HMBD. This interaction needed further proof by another assay. Here, we benefit from the naturally occurring cysteines in the sequence of the HMBD as compared to the Cys-free A-domain for detecting their interaction using Fluorometric assay. The amino acid sequence of HMBD contains of four cysteines and many histidine residues. Two of these cysteines are in the conserved MxCxxC motif and the others at the N-terminal MxCxxC motif of the HMBD. Labeling these cysteines with a fluorescent thiol-reactive dye will assist to monitor the proposed interaction.

The cysteine residues of HMBD were randomly labeled with either the fluorescent CPM or BADAN dyes in solution. In this labeling method, the HMBD was reacted with excess concentrations of CPM or BADAN dye (1:6, molar ratio of protein: dye) in solution to label the largest possible number of cysteines, and then the excess of un-reacted dye was removed by a PD-10 Desalting column followed by dialysis against the assay buffer for 4 hours with adjustment of the pH. The untagged A-domain (6xHis tag was cleaved off as described in Chapter 3 in section 3.1.2.2) was also dialyzed in the same assay buffer of 30 mM HEPES-NaOH pH 8, 100 mM NaCl and 1% glycerol. 1 mM ascorbic acid was added later to the assay buffer prior to launching the assay.

To examine whether the dye-labeled HMBD still has a metal affinity to Cu<sup>+</sup> ion, the BCA assay was performed by titration of CuCl<sub>2</sub> to 10 μM of dye-labeled HMBD (CPM or BADAN) as described in the materials and methods chapter. The assay detected the capability of the CPM-labeled HMBD to bind Cu<sup>+</sup> in stoichiometry 2:1 (protein : copper ion), suggesting at least one cysteine at the MxCxxC motif is still available after labeling of the other cysteine of the MxCxxC motif with the fluorescent dye. Knowing, the stoichiometry of copper binding by the HMBD is estimated at 1:1.5 (protein: metal; see Chapter 4).

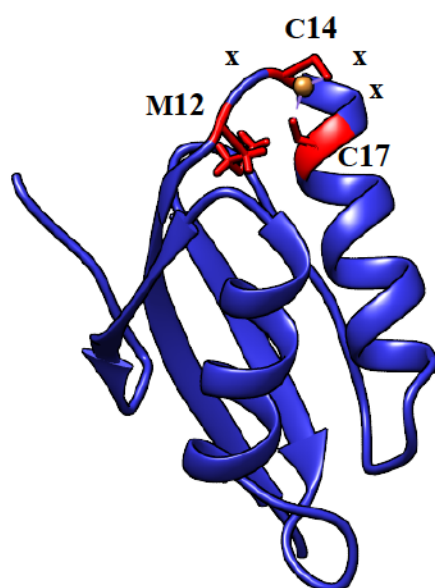


**Figure 5.9.** Cartoon representation shows the orientation of cysteine residues of HMBD in *Bacillus subtilis* CopA.

Protein structure was retrieved from PDB ID:1KQK. The copper binding residues of MxCxxC motif are displayed in red color

### 5.2.1 The fluorescent CPM labeling monitored the domain-domain interaction

The fluorometric assay was started by adding first either 30  $\mu\text{M}$   $\text{CuCl}_2$  or 5  $\mu\text{M}$  of A-domain to 10  $\mu\text{M}$  CPM-labeled HMBD. After measuring the induced spectral changes of the CPM dye ( $\lambda_{\text{ex}} = 387 \text{ nm}$ ), the second constituent was added. The copper ion quenches the fluorescence spectrum of CPM and causes a small peak shift from 478 nm to 477 nm as shown in Fig. 5.10.

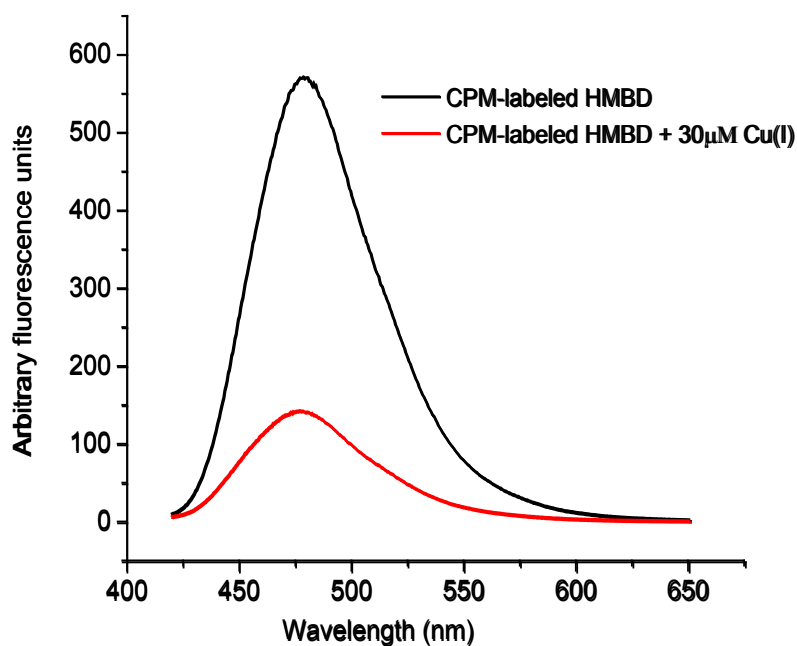


**Figure 5.10. The emission spectrum of CPM-labeled HMBD is quenched by  $\text{Cu}^+$ .**

30  $\mu\text{M}$   $\text{CuCl}_2$  was added to 10  $\mu\text{M}$  HMBD in buffer assay containing 1 mM ascorbic acid. The dye was excited at 387nm.

The addition of the A-domain to the HMBD in the absence of copper did not cause a substantial change in the fluorescence spectrum of CPM as shown in Fig. 5.11A. The time-resolved emission spectra of CPM-labeled HMBD were slightly shifted from 478 nm to 477 nm, indicating perhaps that the A-domain weakly interacts with the HMBD in absence of  $\text{Cu}^+$  ion (Fig 5.11A).

This interaction is strongly increased in the presence of  $\text{Cu}^+$  as shown in Fig. 5.11B. The 5  $\mu\text{M}$  A-domain induced a time-dependent increase of the emission intensity of 10  $\mu\text{M}$  CPM-labeled HMBD with 30  $\mu\text{M}$   $\text{Cu}^+$  ion, in addition to blue-shifting the emission maximum from 477 nm to 474 nm (Fig. 5.11B). The latter result had been again obtained when 30  $\mu\text{M}$   $\text{CuCl}_2$  was added to a mixture of 5  $\mu\text{M}$  A-domain and 10  $\mu\text{M}$  CPM-labeled HMBD (Fig.5.12). Titration of  $\text{Cu}^+$  ion to CPM-labeled HMBD with caused slightly peak shift from 478 nm to 477 nm (Fig. 5.12).

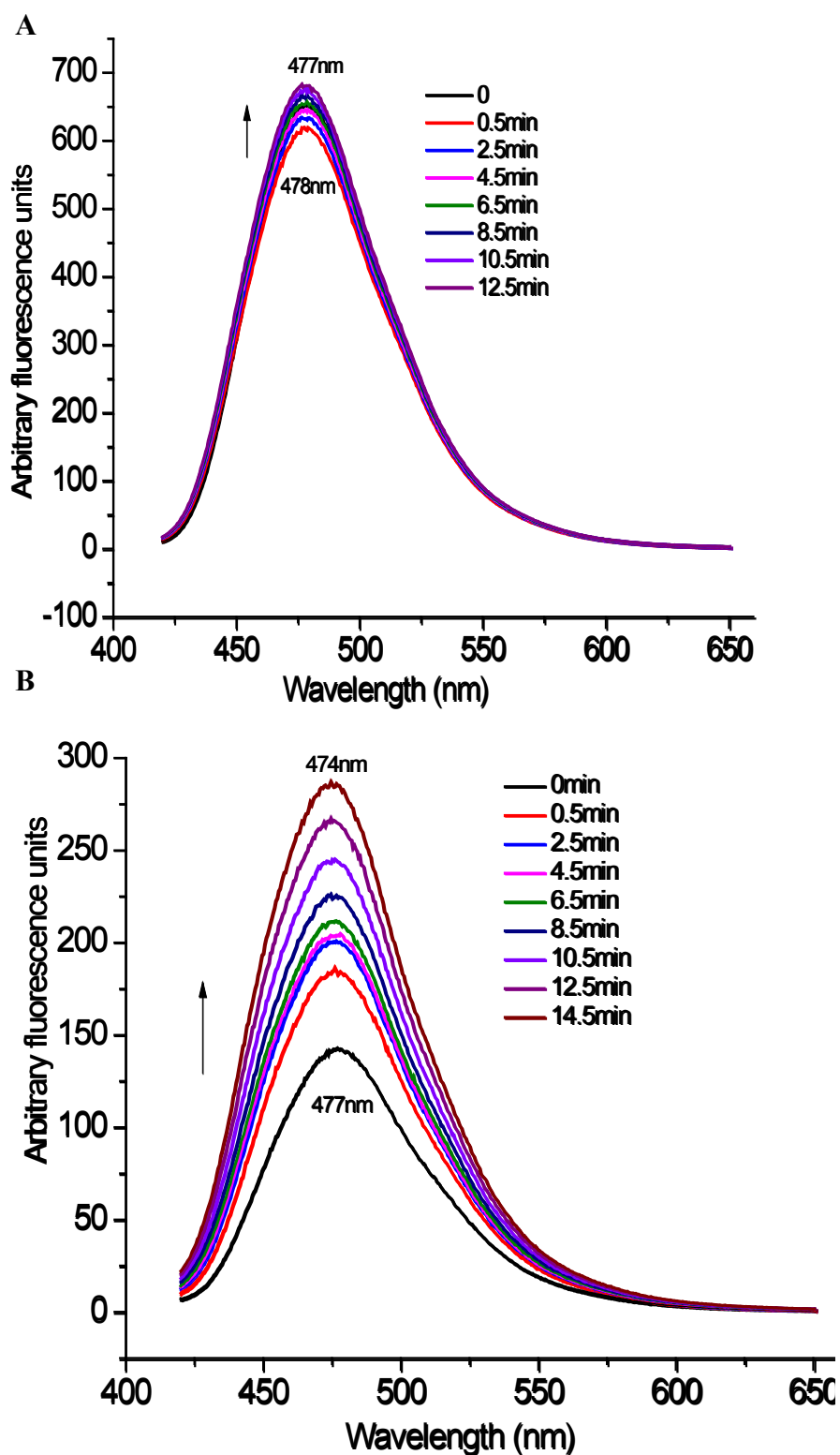


**Figure 5.11. Fluorometric assay of copper-dependent binding of the CPM-labeled HMBD to the A-domain.**

A) In the absence and B) in the presence of 30 μM CuCl<sub>2</sub>, the emission spectra of 10 μM CPM-labeled HMBD interaction with 5 μM A-domain were recorded every 2 min at  $\lambda_{\text{ex}} \sim 387$  nm. The initial spectrum in B, i.e., in the presence of Cu<sup>+</sup> but before addition of the A domain, is identical with the one in Fig. 5.10 after Cu<sup>+</sup> addition (red trace).

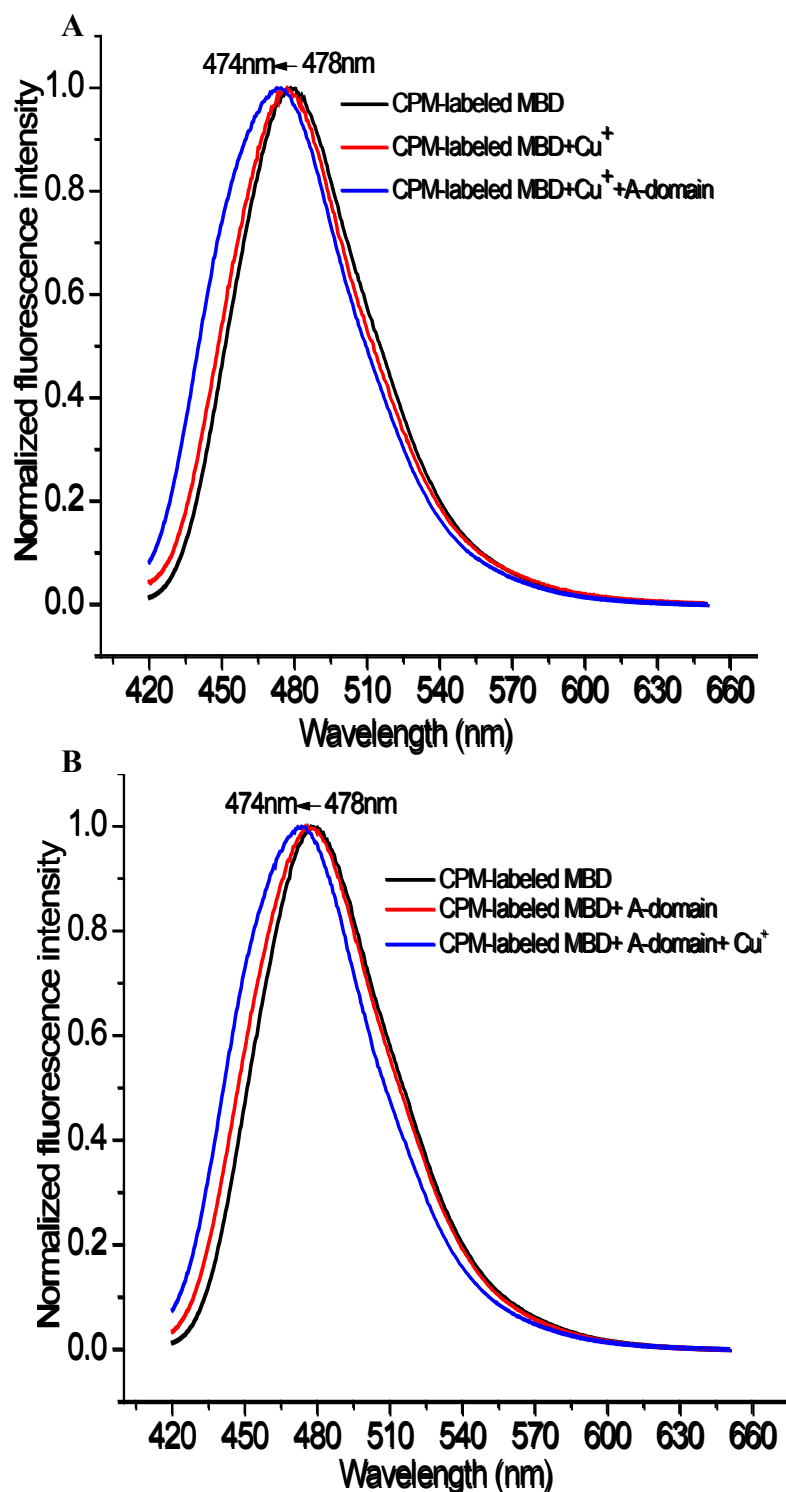


**Figure 5.12. Normalized fluorescence emission spectra of CPM-labeled HMBD with A-domain.**

The interaction between HMBD with A-domain was initiated by adding either **A)** 10  $\mu\text{M}$  A-domain to the mixture of 10  $\mu\text{M}$   $\text{Cu}^+$ -loaded HMBD or **B)** 30  $\mu\text{M}$   $\text{CuCl}_2$  to 10  $\mu\text{M}$  HMBD + 5  $\mu\text{M}$  A-domain mixture. The legend order (top to bottom) indicates the sequence of titration and measurements.



### 5.2.2 The fluorescent BADAN labeling monitored the domain-domain interaction

Likewise, the interaction between HMBD and A-domain was monitored by labeling the HMBD with BADAN, an excellent environment-sensitive probe. Interestingly, the spectrum of BADAN-labeled HMBD was changed upon  $\text{Cu}^+$  ion binding to the protein (Fig. 13.A).  $30 \mu\text{M}$   $\text{Cu}^+$  induced a time-dependent emission decrease of BADAN-labeled HMBD. The emission decay was decreased in the presence of  $5 \mu\text{M}$  A-domain and new peaks appeared at 481 and 443 nm as shown in Fig. 5.13.B.

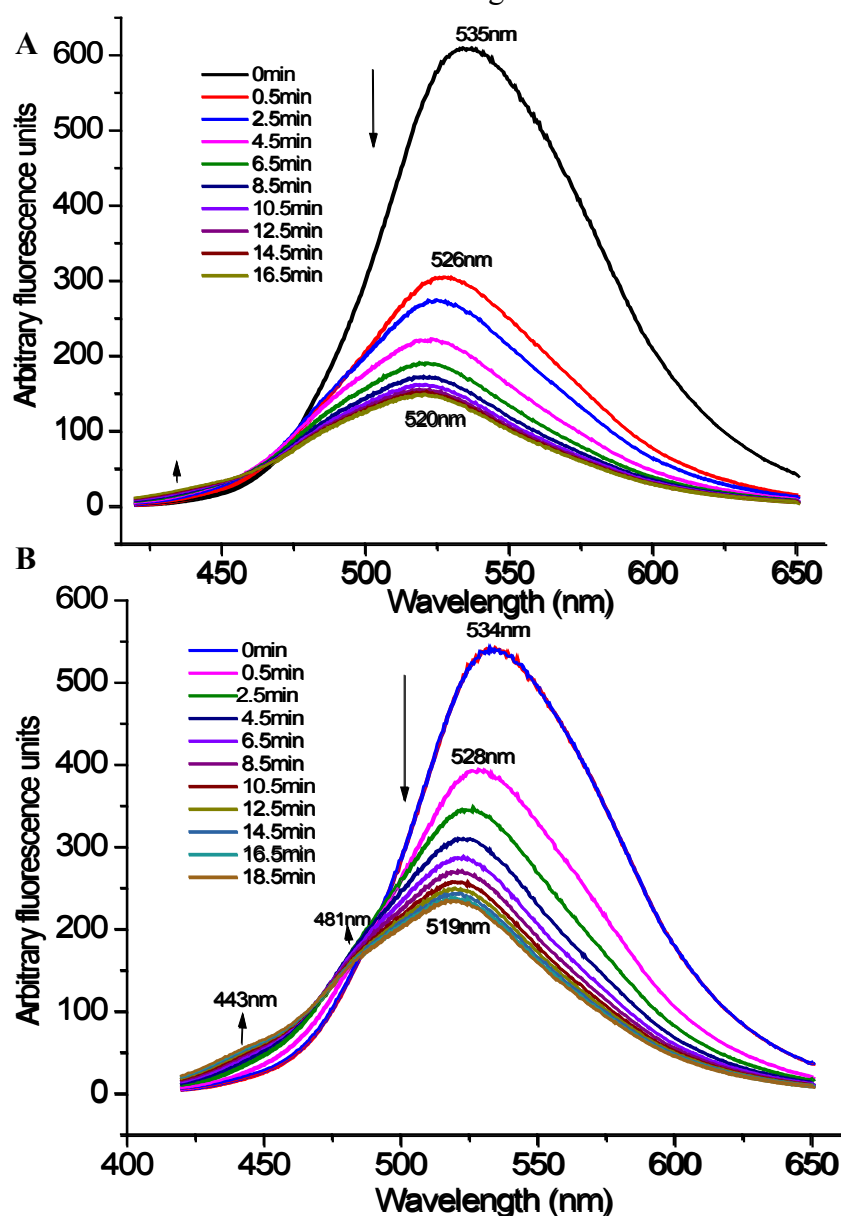


**Figure 5.13. Emission spectra of BADAN-labeled HMBD domain binding to  $\text{Cu}^+$  and the A-domain.**

Binding rate of  $10 \mu\text{M}$  BADAN-labeled HMBD with  $30 \mu\text{M}$   $\text{Cu}^+$  ion was monitored by measuring the changes in emission spectra of BADAN-labeled HMBD ( $\lambda_{\text{ex}}=387 \text{ nm}$ ) every 2 min in the absence **A)** and presence **B)** of  $5 \mu\text{M}$  A-domain.

In a complementary experiment, the addition of 5  $\mu\text{M}$  A-domain to 10  $\mu\text{M}$  BADAN-labeled HMBD, pre-equilibrated with 30  $\mu\text{M}$   $\text{Cu}^+$ , induced the increase of the emission spectrum of BADAN and a blue-shift from 520 nm to 518 nm as shown in Fig. 5.14.

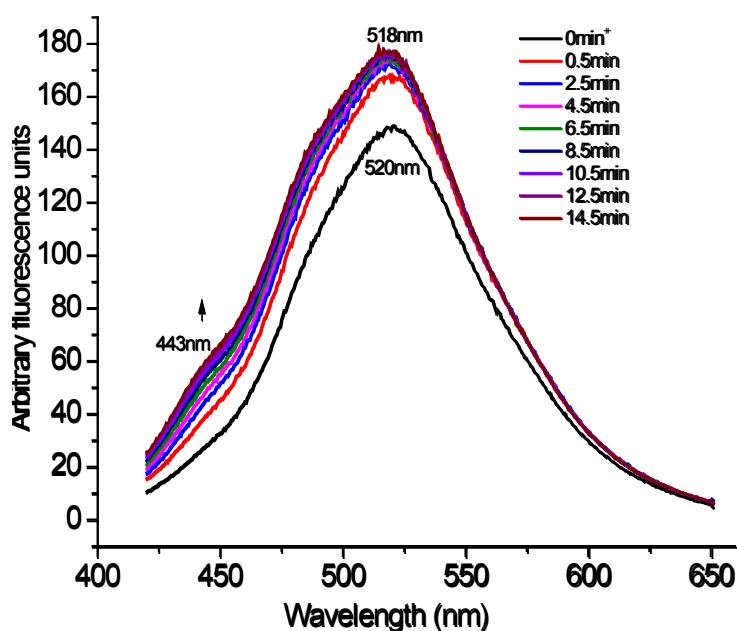


**Figure 5.14. Fluorometric binding assay of  $\text{Cu}^+$ -loaded HMBD/BADAN domain with A-domain.**

Emission spectral changes of 10  $\mu\text{M}$  BADAN-labeled HMBD domain loaded with 30  $\mu\text{M}$   $\text{Cu}^+$  ion were recorded every 2 min after adding 5  $\mu\text{M}$  A-domain in the assay buffer containing 30 mM HEPES-NaOH pH 8, 100 mM NaCl and 1% glycerol and 1mM ascorbic acid. The BADAN was also excited at 387 nm.

All these results are consistent with the results of the co-purification assay of these domains and underscore the interaction of the A-domain with HMBD in a copper-dependent manner. We suggest that the copper binding to the HMBD initiates the molecular recognition between the HMBD and the A-domain which together are required for the proper interaction of these cytosolic domains during catalytic turnover.

Finally, and most importantly, this study provides for the first time, direct experimental proof for the proposed cytosolic domain organization during the copper-transporting mechanism as it can explain the discussed copper-dependent inhibitory or activating role of the HMBDs in P-type ATPases by its direct interaction with the A-domain. More specifically, our data supports the view of Hatori and co-workers who suggest that copper binding to the N-terminal HMBD is required to obtain the active conformation that sustains catalytic and transport cycles [150].

## Summary and discussion

The rearrangements of cytosolic domains during the catalytic turnover induce conformational changes in the transmembrane domain, leading to metal transport. We assumed that the cytosolic ligands ( $\text{Cu}^+$  and nucleotide) modulate the interactions among cytosolic domains in catalytic cycle. To prove this hypothesis, the interactions among isolated cytosolic domains were examined in function of appropriate ligands by co-purification and fluorometric assays. Through the co-purification assays, we try to answer the question of what the role of HMBD in the enzymatic function of CopA. In AfCopA, The co-purification assay demonstrated that N-MBD interacts with PN domain only in the absence of  $\text{Cu}^+$  or ADP while it does not interact with A-domain. On another hand, the electron microscopy and docking studies of  $\Delta\text{C}$ -AfCopA place the N-MBD in close contact with the N- and the A- domains in  $\text{Cu}^+$ -free state. All these findings lead Argüello and Stokes to the assumption that N-MBD plays auto-inhibitory role in absence of  $\text{Cu}^+$  while it dissociates from the catalytic domains upon  $\text{Cu}^+$  binding, allowing the enzymatic cycle starts (Fig. 5.15) [148].

Here, our data on the cytosolic domains of LpCopA show a different interaction pattern of HMBD from LpCopA with the other domains than that of N-MBD from AfCopA. The HMBD of LpCopA undergoes a  $\text{Cu}^+$ -dependent interaction with the A-domain and does not interact with the PN domain regardless of a ligand. On the other hand, the A-domain does interact with the PN domain in the presence of either ATP or ADP. In agreement with previous studies of Hatori et al. 2008 [74, 150] on another, we postulate that the A-domain interaction with the  $\text{Cu}^+$ -loaded HMBD is required for forming a catalytically compact headpiece with other cytosolic domains for launching the catalytic turnover and copper transport. Perhaps the A-domain is associated with the HMBD in the  $E1\text{P}\sim\text{ADP}$  and  $E2\text{P}$  intermediates [74]. It has been reported that the two TM-MBSs are independently loaded with  $\text{Cu}^+$ . However, their simultaneous occupation is associated with ATP binding to the N-domain.

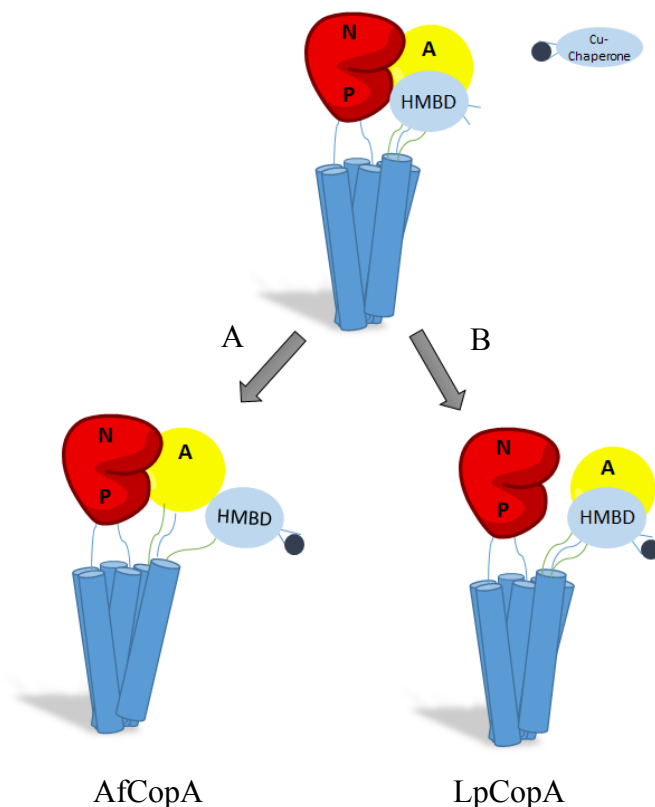


**Figure 5.15** A schematic diagram shows the difference in the putative HMBD rearrangement in LpCopA and AfCopA upon  $\text{Cu}^+$  binding.

The copper chaperone delivers the first  $\text{Cu}^+$  ion to the cytosolic metal binding domain of CopA, causing rearrangement of the cytosolic headpiece. There are two proposed mechanisms of HMBD rearrangement upon  $\text{Cu}^+$  binding: **A)** The N-MBD of AfCopA dissociates from other cytosolic domain, suggesting auto-inhibitory role for N-MBD. **B)** In our model, the HMBD of LpCopA may play a catalytic role by association with A-domain upon  $\text{Cu}^+$  binding for leaving room for ATP binding to form an active conformation for launching the catalytic cycle. The HMBD, A-, P- and N- domains stand for Heavy metal binding domain, actuator domain, phosphorylation- and nucleotide-binding domain, respectively.

In the light of our recent data, and besides our knowledge about mechanistic characteristics of P-type ATPases, we can suggest a copper transport mechanism of LpCopA (Fig 5.16). In *E1* state, a copper chaperone delivers the first copper ion to HMBD, causing dissociation of HMBD from the interfacial platform helix (MB') and thereby leading to opening of the transmembrane entry site of the ion transport pathway for occupying the first TM-MBS with second copper delivered directly by a copper chaperone. In line with the previous step, the copper-occupied HMBD does interact with A-domain allowing the N-domain to receive one ATP molecule. Upon ATP binding,

both of N- and P- domains incline to each other and the A-domain, the latter linked with the HMBD as shown in this study, rotates with a small angle (by  $\sim 30^\circ$  parallel to the membrane) to make a contact with N-domain [83]. At this stage, the compact headpiece forms the higher energetic state,  $(\text{Cu}^+).E1\text{P}\sim\text{ADP}$ , in which the second TM-MBS is occupied, perhaps, by the copper bound HMBD [146, 158]. In the  $E1\text{P}\rightarrow E2\text{P}$  state transition, the A-domain rotates toward the high-energy aspartyl-phosphate intermediate at P-domain, causing a drastic rearrangement of the transmembrane helices leading to the opening of the luminal gate and releasing the  $\text{Cu}^+$  ions into the lumen (extracellular space). Finally the P-domain is dephosphorylated by the A-domain and the conformation recycles to  $E1$  state.

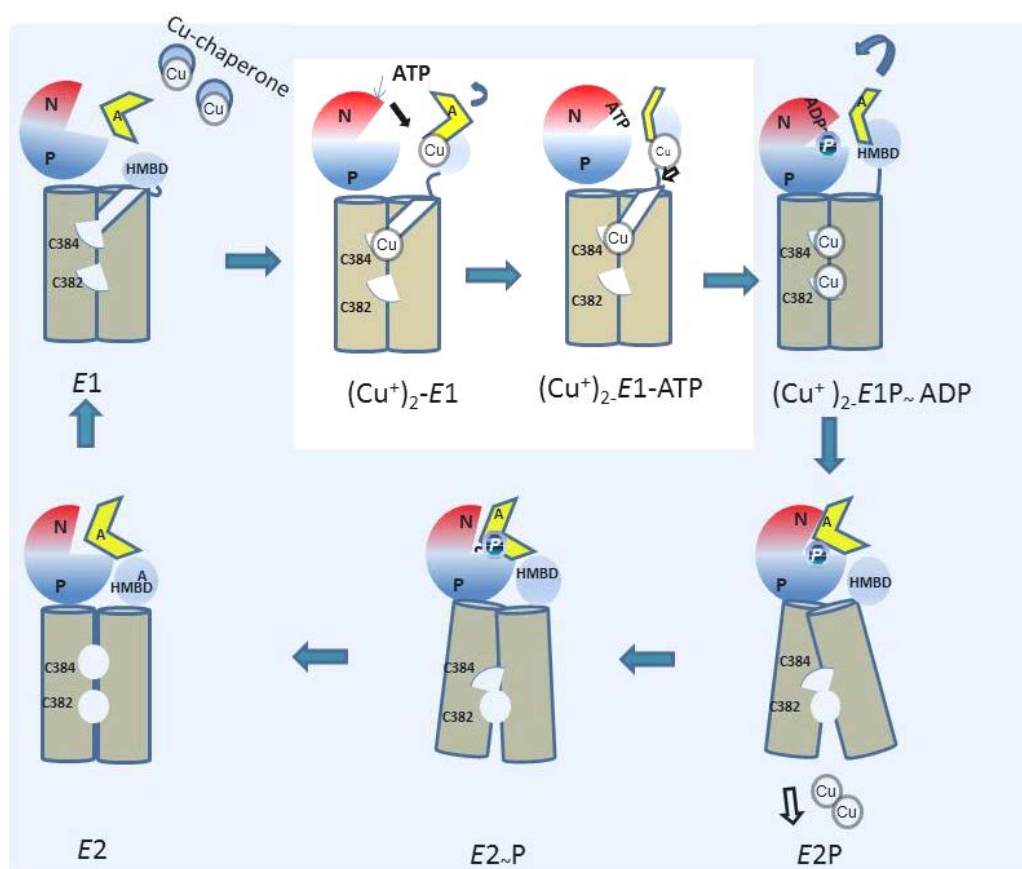


**Figure 5.16. Schematic diagram shows the classical P-type-ATPase reaction cycle including the interaction among LpCopA cytosolic domains in this study.**

The cytosolic HMBD, A-, P- and N- domains are colored in light-blue, yellow, red and blue, respectively, and the TM domain is gray. The box with white ground indicates on the proposed mechanism based on the cytosolic domains interaction concluded from this study. According to our hypothesis, the A-domain associates with copper-loaded HMBD leaving room for ATP binding, subsequently the A-domain-linked HMBD makes contact with N-domain to form compact headpiece for catalytic turnover. The HMBD, A-, P- and N-domains stand for Heavy metal binding domain, actuator domain, phosphorylation- and nucleotide-binding domain, respectively.

## Chapter 6

### **The Structural impact of Model peptides derived from Actuator domain on the Cytosolic Headpiece and the CPC-motif conformations in *L. pneumophila* CopA**

#### Introduction

The actuator domain (A-domain) is flexible to take different positions imposed by other domains to regulate the occlusion and extrusion of ions [79]. The A-domain plays role for coupling the ATP hydrolysis with structural rearrangements of the transmembrane segments. The domain contains a loop with a conserved TGE sequence motif which its geometric configuration presumably facilitates interactions with the P-domain [159]. In the crystal structure of Ca<sup>2+</sup>-ATPase, the TGE motif contacts the phosphorylation site closely in the *E2* and *E2P* states, but in *E1* state it is ~30 Å away from the phosphorylated aspartate in P-domain [22]. The glutamate residue of TGE motif is critical for the dephosphorylation of *E2* and *E2P*, but is of little functional importance in *E1* and *E1P* [160].

Here, we addressed the questions of whether or not the TGE motif can bind to the PN domain, independently of the rest of A-domain sequence, and what its impacts on the structure and function of the other cytosolic domains and transmembrane segments of LpCopA. Therefore, we designated model peptides derived from the TGE loop sequence of A-domain in LpCopA and studied the kinetics binding and affinity of these peptide to the PN-domain using Stopped-flow fluorescence. Our data show that peptides binding to the PN domain induce structural changes at cytosolic headpiece and TM-MBS.

## Results and discussion

### 6.1 Synthesis of Actuator-derived peptides

Synthetic peptides were used in spectroscopic, calorimetric and functional assays to investigate the nature of cytosolic domain interactions between the actuator and PN domain. The concept behind this is the use of peptides as putative inhibitors of these interactions. Thereby, catalytic intermediates may become enriched under steady state conditions or the Post-Albers cycle arrested in the extreme case.

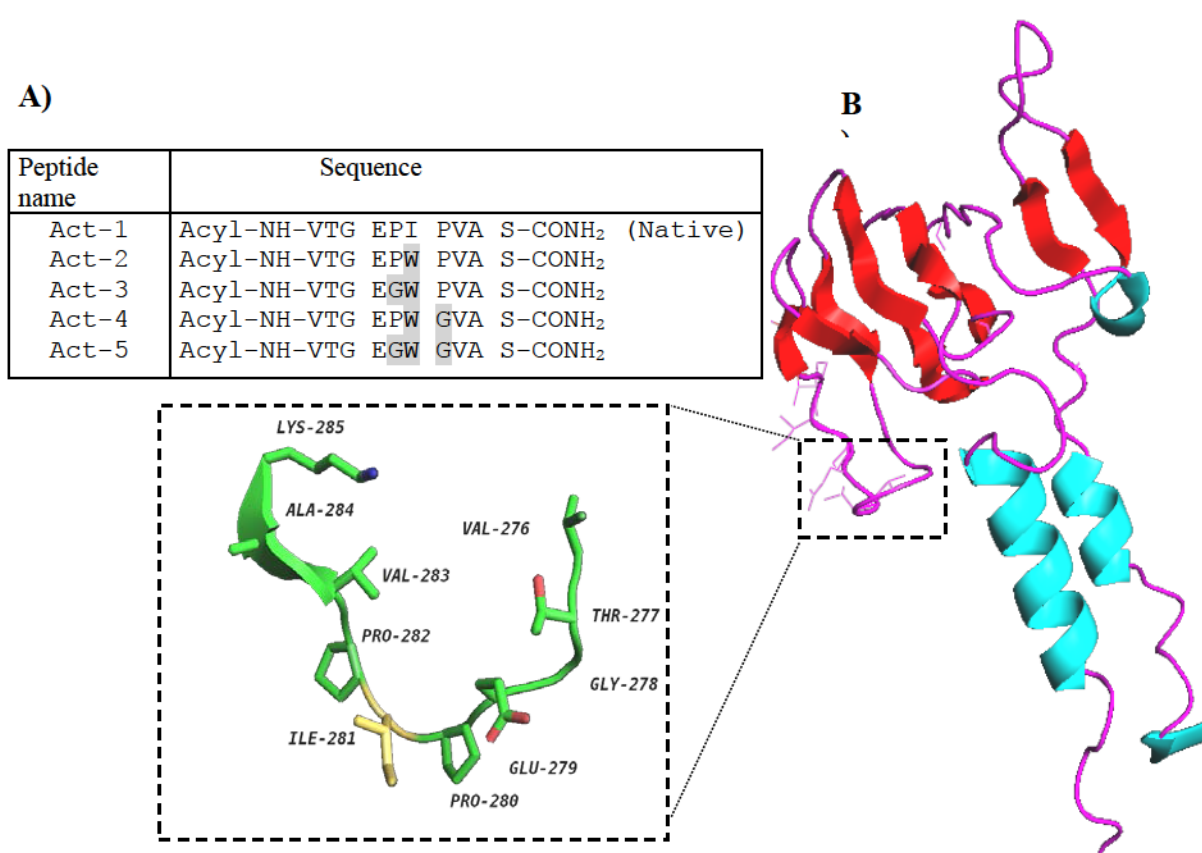


**Figure 6.1. Design of synthetic peptide models derived from Actuator domain.**

The synthetic peptides are derived from the conserved TGE-containing site of the Actuator domain that catalyzes dephosphorylation of the P domain of LpCopA. A) list of peptide sequences that were designed to mimic the conserved TGE motif of Actuator domain. The gray color indicates the mutated residues from wild-type sequence. B) Cartoon representation of the TGE loop in the Actuator domain of LpCopA (PDB entry: 3RFU visualized by PyMOL software).

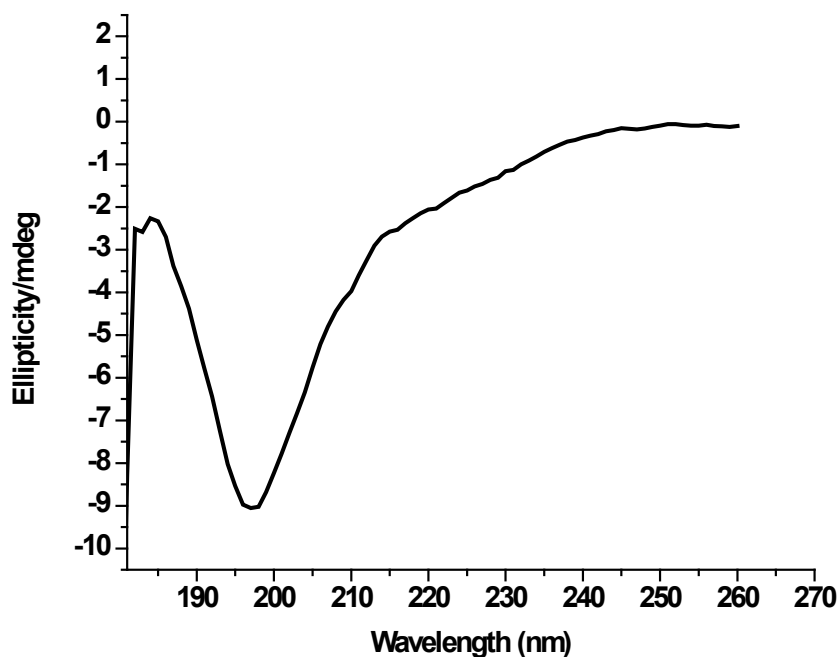


**Figure 6.2. CD spectrum of Act1 peptide in Phosphate buffer.**

50  $\mu\text{M}$  Act1 peptide in 7 mM  $\text{KH}_2\text{PO}_4$  buffer pH 7.4 was measured from 185-260 nm in 1 mm cell using Jasco J-815 Circular Dichroism (CD) Spectropolarimeter.

The actuator domain (A-domain) is involved in the  $E1P \leftrightarrow E2\sim P$  conversion by replacing the N domain from the active surface of the P domain. The A-domain contains a highly conserved TGE motif, which has an important role in the dephosphorylation of the  $E2\sim P$  catalytic state of P-type ATPases. In SERCA, mutation within the TGE motif inhibits the dephosphorylation of  $E2\sim P$  without a reduction of  $\text{Ca}^{2+}$  binding and phosphorylation capacity [161-163].

Here, we investigate the physical nature of domain interactions at the TGE site independently of the full A-domain sequence. Based on the LpCopA crystal structure (PDB ID: 3RFU), we designed peptides whose sequences are derived from the putative interaction site of the actuator domain with the PN domain. There is a conserved hydrophobic cluster next to the conserved TGE-motif (Fig. 6.1) composed of prolines, isoleucine, valine and alanine. The peptides were synthesized with modification at both ends with N-terminal acetylation and C-terminal amidation, which remove the respective terminal charges to mimic the natural peptide backbone. The peptide-based approach to the study of domain interactions requires sufficient affinity of the peptide to its native binding epitope. Therefore, it was necessary to also provide a corresponding observable of peptide protein interactions. To monitor the latter fluorometrically, the



Act-1-peptide (wild-type sequence) was modified by replacing the central isoleucine (corresponding to I281 in actuator domain) by tryptophan as a natural fluorophore in the novel peptide Act-2. Moreover, the prolines in wild-type sequence were further replaced with glycines individually or the two of them in the synthetic peptides Act-3 / Act-4 and Act-5, respectively. The motivation of these replacements is to address the role of the prolines for molecular recognition of the binding epitope at the P domain. The CD spectrum of Act-1 peptide (Fig 6.2) reveals that the peptide is neither helical nor  $\beta$ -sheet but more similar to a random coil as we expected from the crystal structure shown in Fig. 6.1.

## 6.2 Thermal stabilization of PN domain

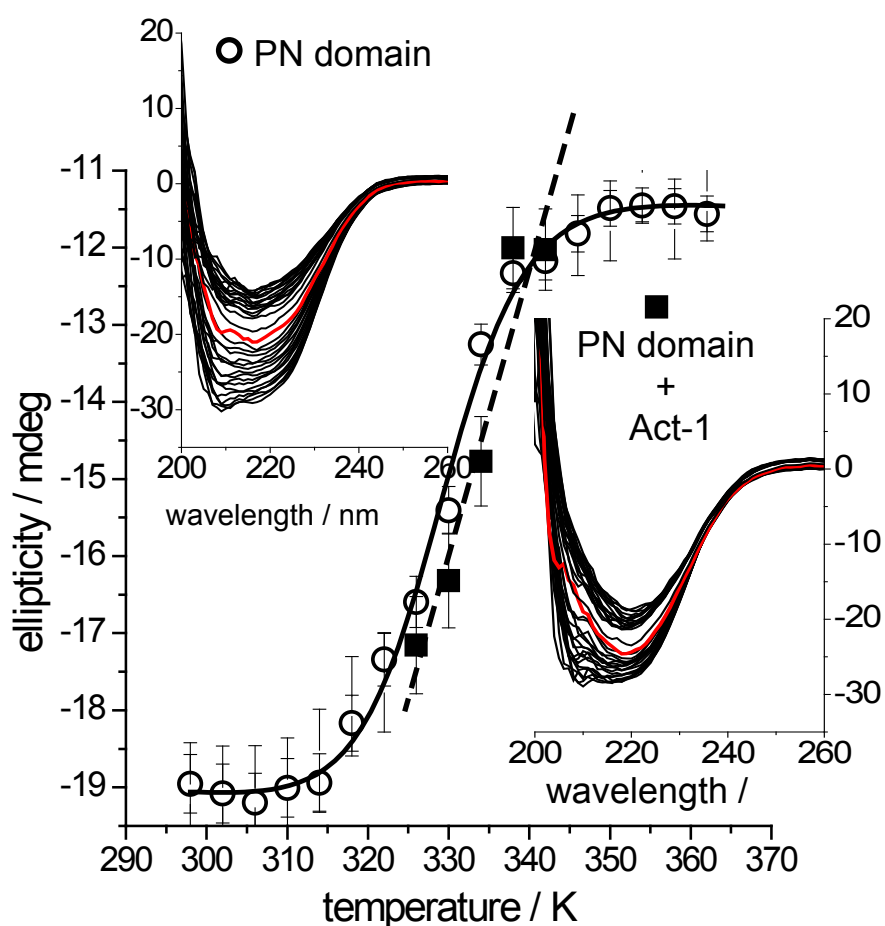


**Figure 6.3. Thermal stabilization of the PN domain by peptide Act-1.**

The thermal stability of PN domain was monitored in function of Act-1 by CD spectroscopy. The data points were taken from the thermally induced CD-spectral changes shown in the insets between 232 to 222 nm (heating rate of 2°C/min). Open circles: PN domain alone at 5  $\mu$ M, filled square: PN domain at 5  $\mu$ M in the presence of 50  $\mu$ M Act-1 peptide. Experiments were performed in 10 mM phosphate buffer pH 7.2, 3 mM MgSO<sub>4</sub> using a 1cm cuvette with stirrer.

Thermal denaturation of the PN domain in the presence of the synthetic Act-1 peptide was performed to investigate the capability of the Act-1 peptide to bind and thereby thermally stabilize the PN domain. Circular dichroism (CD) spectroscopy was used because it allows observing secondary structural changes in real time. The thermal denaturation of the PN domain was monitored by measuring the temperature-dependent CD spectra of 5  $\mu\text{M}$  PN domain in the absence and presence of 50  $\mu\text{M}$  Act-1 peptide as shown in Fig. 6.3. We have evaluated the temperature-induced loss of the integral CD signal between 230 and 222 nm, where the CD of  $\alpha$ -helical structure dominates the spectrum (as a negative signal). Thereby, the unfolding of the PN domain was observed in a range that does not overlap with the peptide signal. The sigmoidal shape of the resulting denaturation curve was fitted to the data with a two state unfolding model, leading to an unfolding enthalpy and entropy of 174 kJ and 528 J, respectively, reproducing the both the unfolding midpoint temperature of  $T_m = 56.0$  °C and the steepness of the transition. In the presence of the actuator Act-1 peptide, the unfolding curve is shifted by  $\sim 4$  K to higher temperature, indicating a stabilization of the PN domain in the presence of the peptide. The more complicated transition composed of both unfolding of the PN domain and unbinding of the peptide prevents the fit of a simple two state model across the entire unfolding regime. However, from the shift of  $\Delta T_m$  by  $\sim 4$  K, a  $\Delta\Delta H > 2$  kJ mol<sup>-1</sup> can be estimated (Material and Methods), assuming an unchanged unfolding entropy. An upper boundary can be derived from the maximal slope of the unfolding curve in the presence of the peptide which results in an estimate of  $\Delta\Delta H < 20$  kJ.

The data show qualitatively that the Act-1 peptide binds to the PN domain. How can the affinity, i.e., the  $K_D$  of the peptide binding be estimated from these data? In the realm of a two state model, the unfolding curve of the PN domain alone can be used because it predicts the degree of denaturation of the free PN domain at the any temperature. Therefore, the amount of unfolded free PN domain is known also for denaturation of the PN domain in the presence of Act-1.

In this case, the  $T_m$  is 59.5 °C. With the definition for the concentration ratio of denatured (D) to native state (N) of the PN domain  $K_{den} = [D]/[N]$  one obtains

$$K_{den} = \exp(528 \text{ JK}^{-1}/R) \cdot \exp(-174 \text{ kJ}/(R \cdot T))$$

In the presence of an additional peptide-bound state (NP), the fraction S of denatured protein as determined from the CD denaturation curve is

$$S = [D] / ([N] + [NP] + [D])$$

$$= K_{den} / (1 + [NP]/[N] + K_{den}) \text{ which leads to:}$$

$$[NP] / [N] = K_{den} \cdot (S^{-1} - 1) - 1.$$

With the total concentration of the native protein  $[N_{tot}] = [N] + [NP]$  one obtains:

$$[N_{tot}] / [N] = K_{den} \cdot (S^{-1} - 1),$$

$[N_{tot}] = (1-S) \cdot C_{tot}$ , with  $C_{tot}$  the total protein concentration. Therefore

$$[N] = (1-S) \cdot C_{tot} / (K_{den} \cdot (S^{-1} - 1))$$

$$[NP] = [N_{tot}] - [N] = C_{tot} (1 - S (1 + K_{den}^{-1}))$$

$$[P] = [P_{tot}] - [NP]$$

Thus the concentrations of free native protein [N], its peptide-bound form [NP] and the free peptide concentration [P] are all known from experiment.

Consequently the  $K_D$  of peptide binding to the PN domain can be determined. Using this approach, the affinity of the Act-1 peptide is 50-100  $\mu\text{M}$  and for PN concentrations of 5 to 50  $\mu\text{M}$  and thus not affected by errors in the determination of the absolute protein concentration. The evaluation assumes binding of the Act-1 peptide only to the native PN domain.

### 6.3 Fluorometric binding assay of peptide Act-2 to PN domain

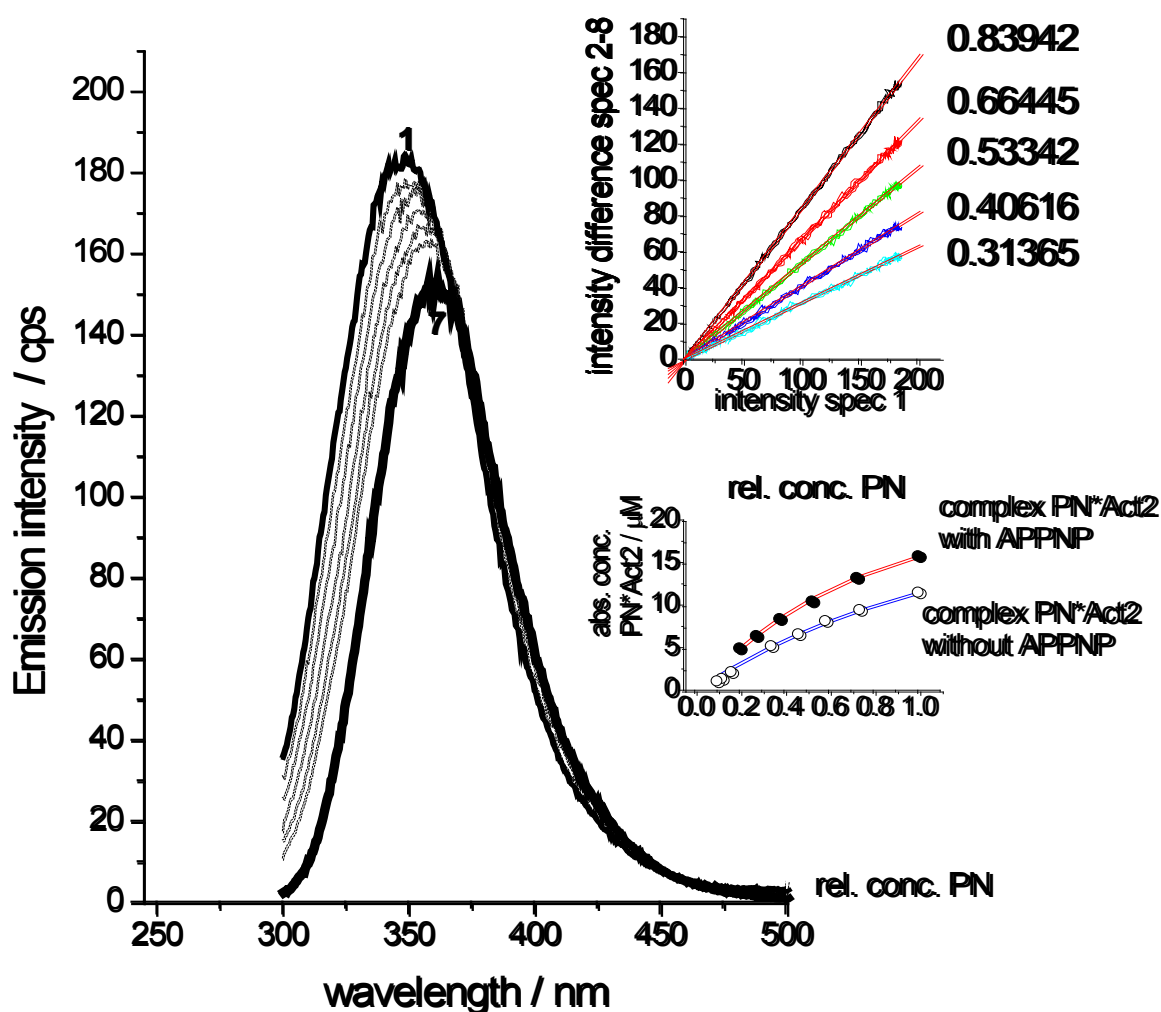


**Figure 6.4.** Trp emission spectra of Act-2 peptide with decreasing in concentration of PN domain.

Traces from 1-7 correspond to various PN concentrations from 55 to 10.9  $\mu\text{M}$ , respectively, and a constant concentration of Act-2 peptide (25  $\mu\text{M}$ ). The Act-2 was excited at 280 nm.

We have addressed the binding of the actuator peptide to the PN domain by an alternative approach using fluorescence spectroscopy. For that purpose the isoleucine corresponding to ILE 281 in the native sequence was replaced by a tryptophan in the Act-2 peptide, rendering it a fluorescence sensor of binding to the PN domain. Figure 6.4 shows the decrease of Trp emission as a function of increasing the Act-2/PN ratio at a constant concentration of Act-2 peptide. This was accomplished by diluting a solution with excess PN domain over Act-2 with aliquots of an Act-2 solution that contained the

identical peptide concentration as the initial mix. Expecting sufficient hydrophobicity of a TRP side chain to become buried into the equivalent environment of the PN domain as the native ILE, a blue shift of the TRP emission was expected upon the transition from the aqueous to the PN-domain-bound state of the peptide. The apparent dissociation constant  $K_D$  was calculated as  $\sim 30\text{-}100\ \mu\text{M}$ . Here, the ratio of free and bound peptide was determined by subtracting the spectrum obtained with excess PN domain (bound state of the peptide) from the fluorescence spectra measured at all other PN concentrations. The subtraction constant was chosen such that the resulting spectrum after the subtraction has the identical shape as that of the free peptide. The criterion for this is the linearity of the plot of the emission spectrum of the free peptide vs. the spectral result from the subtraction as shown in Fig. 6.4 (inset).

The slopes are the relative concentrations between bound and free peptide. The corresponding absolute concentration of the protein-bound peptide is thus obtained from the known (constant) total peptide concentration. In this way, the amount of bound peptide could be determined as a function of the PN domain as shown in the lower panel of the inset. The evaluation leads to a similar peptide affinity as that determined by thermal denaturation.

#### 6.4 Stopped-flow kinetics of Act-2 interaction with PN domain

The above described equilibrium experiments indicate that actuator domain-derived peptides bind to the PN domain with apparent  $K_d$  in the  $30\text{-}100\ \mu\text{M}$  range. We have asked whether a consistent description is possible also under non-equilibrium conditions, when the reaction of the PN domain with a peptide is monitored in a time dependent experiment. Therefore, we have used stopped flow Trp emission experiments to determine rate constants of association and dissociation of Act-2 with PN.

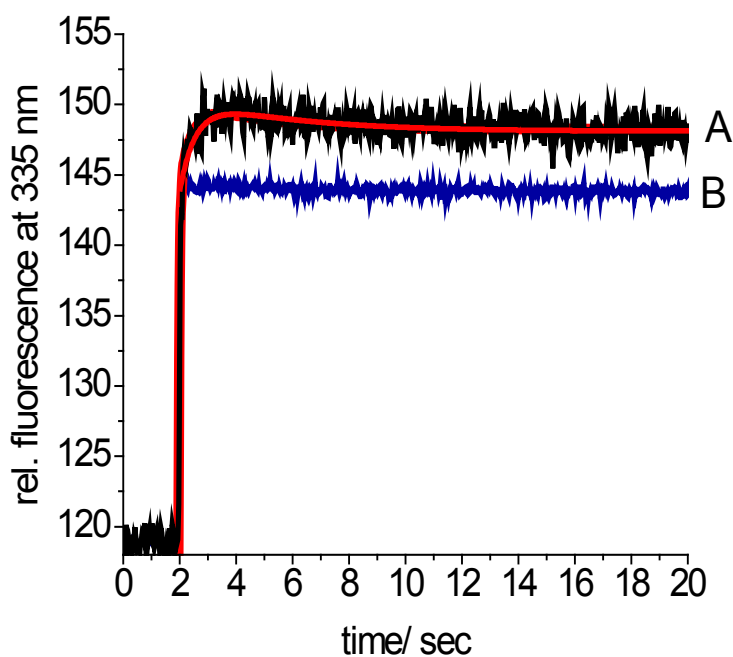


**Figure 6.5. Stopped-flow fluorescence kinetics of peptide Act-2/ PN domain interaction.** A) Tryptophan emission changed upon rapid mixing of 25  $\mu\text{M}$  Peptide Act-2 (final conc.) with 21  $\mu\text{M}$  the PN domain (final conc.). The excitation was at 285 nm and emission accumulated at 335 nm. B) Mixing of peptide Act-2 with buffer (Blue) was taken as a control. Red color indicates the model fit.

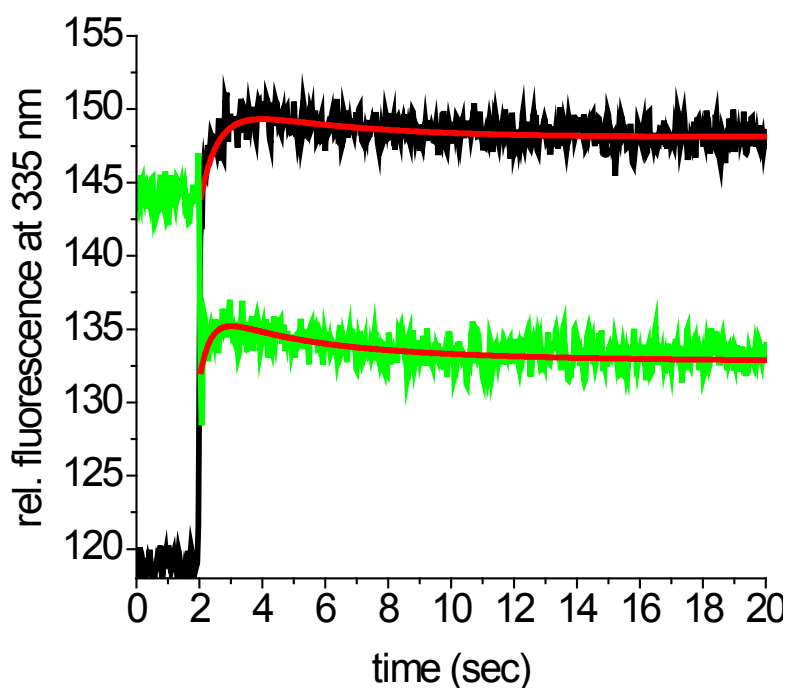
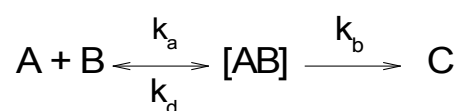


**Figure 6.6. The effect of ATP analog on the kinetics of the Act-2/PN domain interaction.**

Stopped-flow traces of Trp emission in Act-2 peptide (25  $\mu\text{M}$ , final conc.) were recorded upon mixing with the PN domain (21  $\mu\text{M}$ , final conc.) in absence (black color) and in presence (green color) of 100  $\mu\text{M}$  AppNp. The rate constants for association and dissociation were 1) 22000  $\text{M}^{-2}\text{s}^{-1}$  and 0.7  $\text{M}^{-1}\text{s}^{-1}$  in absence of AppNp and 2) 20000  $\text{M}^{-2}\text{s}^{-1}$  and 1.0  $\text{M}^{-1}\text{s}^{-1}$  in presence of 100  $\mu\text{M}$  AppNp, respectively. The apparent dissociation constant  $K_D$  is 30-50  $\mu\text{M}$ .

The fluorescence traces fit best to the mode:



**PN domain +Act2**

$$\begin{aligned} k_a &= 22000 \text{ M}^2\text{s}^{-1} \\ k_d &= 0.7 \text{ M}^{-1}\text{s}^{-1} \\ k_b &= 0.4\text{s}^{-1} \\ K_D &= k_d/k_a = 31.8 \text{ }\mu\text{M} \end{aligned}$$

**PN domain +Act2 +AppNp**

$$\begin{aligned} k_a &= 20000 \text{ M}^2\text{s}^{-1} \\ k_d &= 1.0 \text{ M}^{-1}\text{s}^{-1} \\ k_b &= 0.8\text{s}^{-1} \\ K_D &= k_d/k_a = 50.0 \text{ }\mu\text{M} \end{aligned}$$

Figures 6.5 and 6.6 show the results from fluorescence stopped flow experiments. The emission of the peptide act-2 was excited at 285 nm and measured at 330 nm, i.e. at the blue side of the emission band, where the maximal emission increase occurs upon a binding-induced blue shift. In contrast to the CD data, a five-fold higher amount of the PN-domain (21  $\mu\text{M}$ ) and a reduced concentration of the Act-2 peptide (25  $\mu\text{M}$ ) was used to increase the ratio of bound to unbound peptide. Upon rapid mixing of equal volumes of PN and Act-2 solutions, a fast fluorescence increase was observed within the first two seconds after mixing, which was followed by a slower slight decrease to a final emission level established after  $\sim 10$  seconds. The initial reaction was modelled by a bimolecular reaction with an association and dissociation rate constant  $k_a = 22000 \text{ M}^2\text{s}^{-1}$  and  $k_d = 0.7 \text{ M}^{-1}\text{s}^{-1}$ , respectively, leading to a dissociation constant  $K_D = k_d/k_a = 32 \text{ }\mu\text{M}$ . The ensuing slow decrease to the final emission level (which is still higher than the initial state of the peptide emission in the absence of the PN domain) can be described by a monomolecular reaction of the PN-peptide complex with a rate constant of  $k_b = 0.4 \text{ s}^{-1}$ . Mechanistically, the affinity of the actuator to the PN-domain in LpCopA requires the opening of the P and N domain interface.

This interface is not accessible when ATP links the two domains in the *E1* state. Therefore, we have asked whether the affinity of the act-2 peptide to the isolated PN domain is regulated by the conformational state of the nucleotide-binding pocket of the P-domain. Comparison of the stopped flow data in Fig.6.6 shows that the TRP emission increase is affected but not abolished in the presence of the non-hydrolyzable ATP analogue, AppNp. From the kinetic analysis rate constants of  $k_a = 20000 \text{ M}^{-2}\text{s}^{-1}$  and  $k_d = 1.0 \text{ M}^{-1}\text{s}^{-1}$  are obtained which correspond to a slightly increased dissociation constant  $K_D = 50 \text{ }\mu\text{M}$ , i.e. a slightly reduced affinity of the peptide to the nucleotide-bound state of the PN-domain. A slow ensuing emission change was observed in the presence of the nucleotide as well, indicating that the initial fast binding event is probably followed by a rearrangement of the peptide within the binding site in an induced fit process.

In summary, the on and off rates of peptide binding to the PN domain reproduce the apparent  $K_D$  values in the 30-100  $\mu\text{M}$  range that were found also by equilibrium measurements in the temperature-dependent CD and fluorescence experiments.

## 6.5 Thermodynamics parameters of Act-2/PN domain interaction

The above results have revealed the 30-100  $\mu\text{M}$  affinity of actuator domain-derived peptides to the PN domain. The data do not allow, however, specifying the entropic and enthalpic contributions. Knowledge of the latter is of interest, because these quantities are directly related to the binding mode. Therefore, isothermal titration calorimetry was applied to determine both terms in the binding constant.



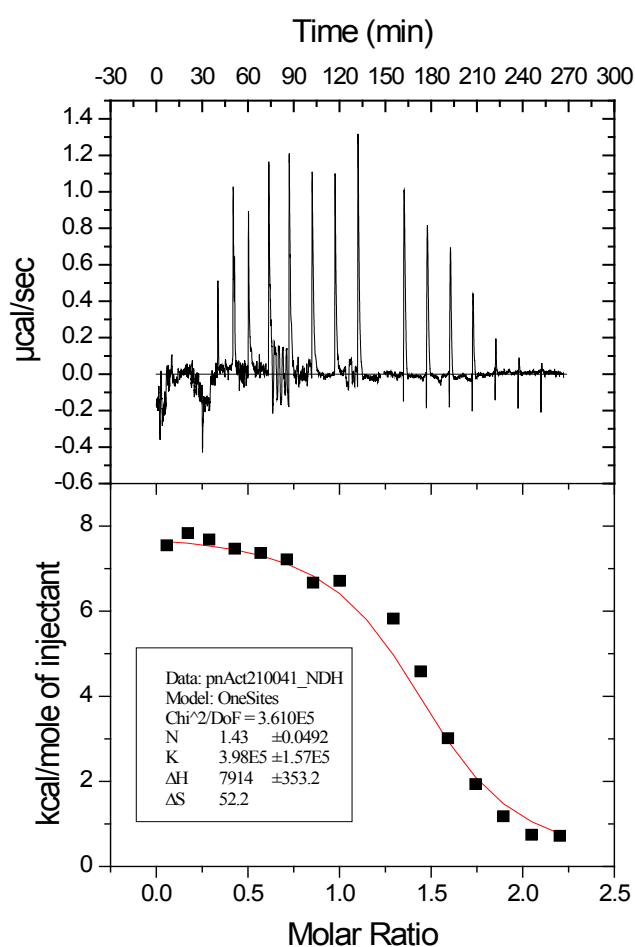


**Figure 6.7. Isothermal titration calorimetry (ITC) of peptide Act-2 with 50  $\mu$ M PN domain**

Dissociation constants ( $K_D$ ) were determined by integrated heat effects normalized to the amount of injected protein and curve fitted based on a 1:1 binding model. in 50 mM Tris-HCl pH7.4, 200 mM KCl, 1 mM MgCl<sub>2</sub> and 10% glycerol

Isothermal Titration Calorimetry (ITC) was used to measure the binding constants for the interaction of Act-2 and the PN domain. The binding reaction was performed in buffer containing physiological salt concentration; 50 mM Tris-HCl pH7.4, 200 mM KCl, 1mM MgCl<sub>2</sub> and 10% glycerol. 2 mM Act-2 peptide was titrated into 50  $\mu$ M PN domain solution with 5 min time intervals.

Qualitatively, the ITC results show an endothermic reaction (a positive ITC signal corresponds to heat uptake upon binding) and thus a positive  $\Delta H$  for the binding reaction as shown in Fig. 6.7. Thus, binding is not driven by lowering of the enthalpy, as for example in electrostatic attraction, but must be driven by a favorable  $T\Delta S$ . The

entropically driven binding of the Act-2 peptide is an indication for hydrophobic interactions. This would agree with the hydrophobic nature of the central region of the peptide and the hydrophobic epitope on the PN domain, seen in the crystal structure. The stoichiometry obtained from the fit of the ITC data (one site) was 1.2, within error this agrees with the expected 1:1 binding of Act-2 peptide to the PN domain.

## 6.6 The effect of actuator peptides on transmembrane helices structure

As shown above, the actuator peptides exhibit the capability to bind to the PN domain and cause structural changes. Now, the question is whether the binding of the peptides at cytosolic domain can result in structural changes at the transmembrane helices which may affect the ATPase activity of LpCopA.

Here, we try to answer these questions by measuring the reactivity of the conserved CPC motif toward a thiol-reactive dye. Furthermore, the catalytic activity of LpCopA was addressed with an ATPase assay of LpCopA in dependence of actuator-derived peptides.

### 6.6.1 Inhibitory effect of Actuator-derived peptides on ATPase activity

The ATPase activity assay of LpCopA was carried out at 37 °C in the presence of the Act-1 peptide varying from 0-200  $\mu$ M under reducing conditions. The activity was induced by adding 80  $\mu$ M CuSO<sub>4</sub> and 2 mM ATP.

The data show that the Actuator-derived peptide Act-1 weakly but reproducibly inhibits the ATPase activity of the full length LpCopA as shown in Fig. 6.8. In the context of the binding studies of Act-1 and Act-2 to the isolated PN domain, we assign the inhibitory effect of the peptides to their interference with PN-Actuator interactions close to the TGE binding interface. Remarkably, this inhibitory effect is also seen with other related peptides, where the flanking prolines have been replaced by glycines individually as simultaneously (Fig.6.9). Therefore, we conclude that the binding interface between the PN and A-domain becomes accessible to hydrophobic interactions with soluble peptides that mimic part of the actuator surface in the PN-Actuator interface. Thereby, they interfere with the post-Albert cycle during repetitive ATPase turnovers.

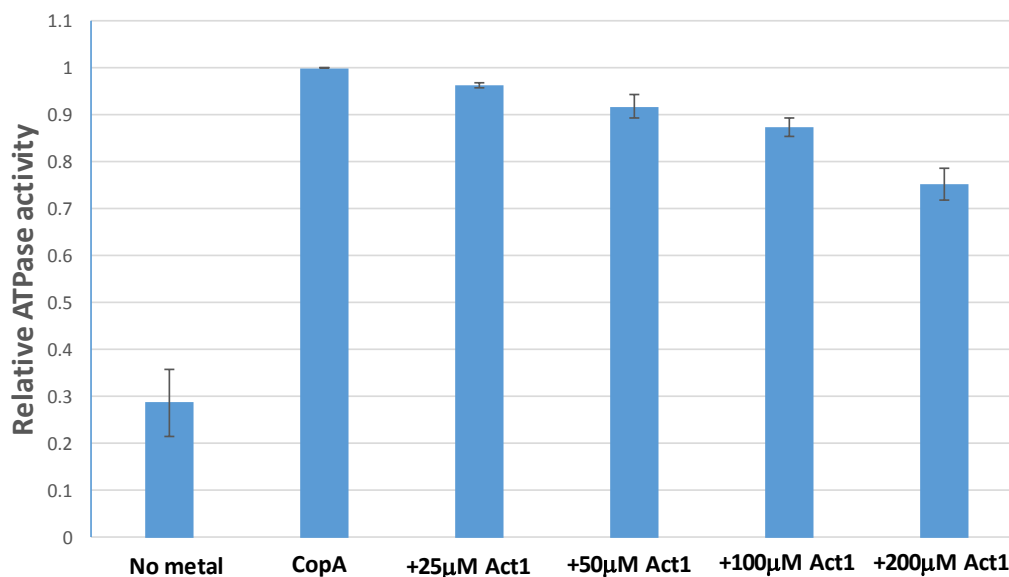


**Figure 6.8. ATPase activity of LpCopA as a function of Act1 peptide**

10-20 µg N-term 6x His-tagged LpCopA in buffer of 30 mM HEPES-NaOH pH 7.4, 100 mM KCl, 3 mM MgCl<sub>2</sub>, 1 mM β-ME, 0.05% DDM and 1mg/ml Asolectin was induced by 80 µM CuSO<sub>4</sub> and 2 mM ATP in presence of various concentrations of Act-1. Plotted data are averages of 3 experiments and values are normalized to activity in the absence of Act-1.

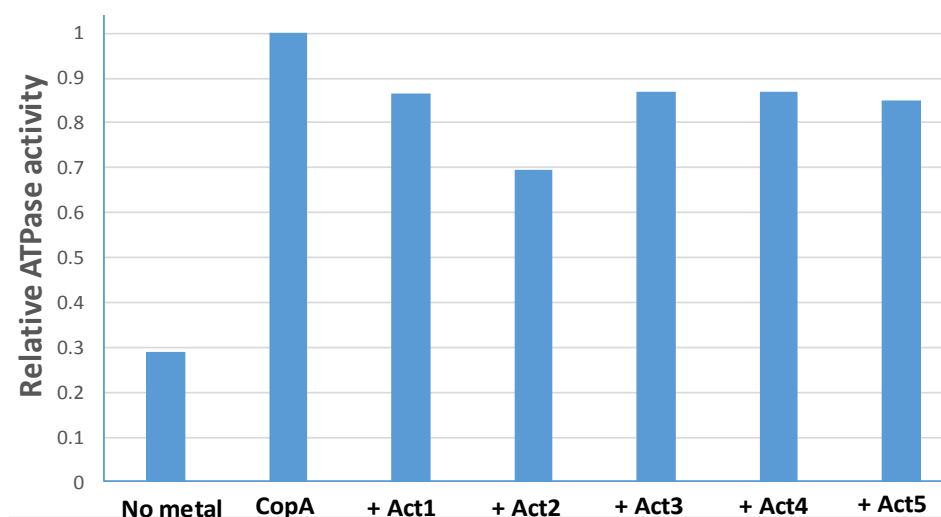


**Figure 6.9. ATPase activity of LpCopA with different actuator-driven peptides.**

Under the same condition in Fig 6.8, the ATPase activity of N-term 6x His-tagged LpCopA was measured in presence of various peptides (at 100 µM final concentrations) whose sequences are variety based on prolines replacement by glycines. The values are normalized to activity in the absence of peptides.

## 6.6.2 Structural impact of peptide Act-1 on the Cys384 residue in the CPC motif

### 6.6.2.1 Fluorometric assay

We have asked whether the demonstrated interference of the actuator-derived peptides affect also the transmembrane domain at the conserved CPC motif. For this purpose, the LpCopA $\Delta$ HMBD was produced by truncation of the metal-binding domain (MBD) from LpCopA which is a cysteine-rich domain that would otherwise interfere with thiol-reactivity at the CPC motif. In addition, the cysteine residue at position 384 in LpCopA $\Delta$ HMBD was replaced by serine to study the accessibility of the C382 residue to the dye. We have used the thiol-reactive dye “7-diethylamino-3-(4'-maleimidylphenyl)-4-methylcoumarin (CPM)” which exhibits increased fluorescence yield upon reaction with cysteine. The 4 mg/ml CPM in DMSO was diluted in assay buffer with ratio 1:40, “working solution” and then added at 1.5 time of protein concentration. The full spectra were recorded (from 400-550 nm) every 1-min for 20 min as shown in Fig. 6.10 and 6.11. Observing the fluorescence increase overtime during reaction with LpCopA $\Delta$ HMBD, we are able to address the accessibility of the CPC motif as a function of the Act-1 peptide interference at the PN-actuator interface.

The data show that LpCopA $\Delta$ HMBD was more influenced by actuator peptide, Act-1, more than the C384S mutant (Fig. 6.12 & 6.13). However, the CPM stability in aqueous solution is still controversial. To reduce the exposure time of CPM to the aqueous solution, the same experiments were repeated by replacing the buffer of the working solution with DMSO, i.e. the final DMSO conc.in assay was raised from ~0.04% to 1.6% to increase the CPM stability; the data was reproduced.

In summary, the data show that C384 residue is more strongly affected by the presence of the Act-1 peptide, but both conserved cysteines are accessible to CPM.

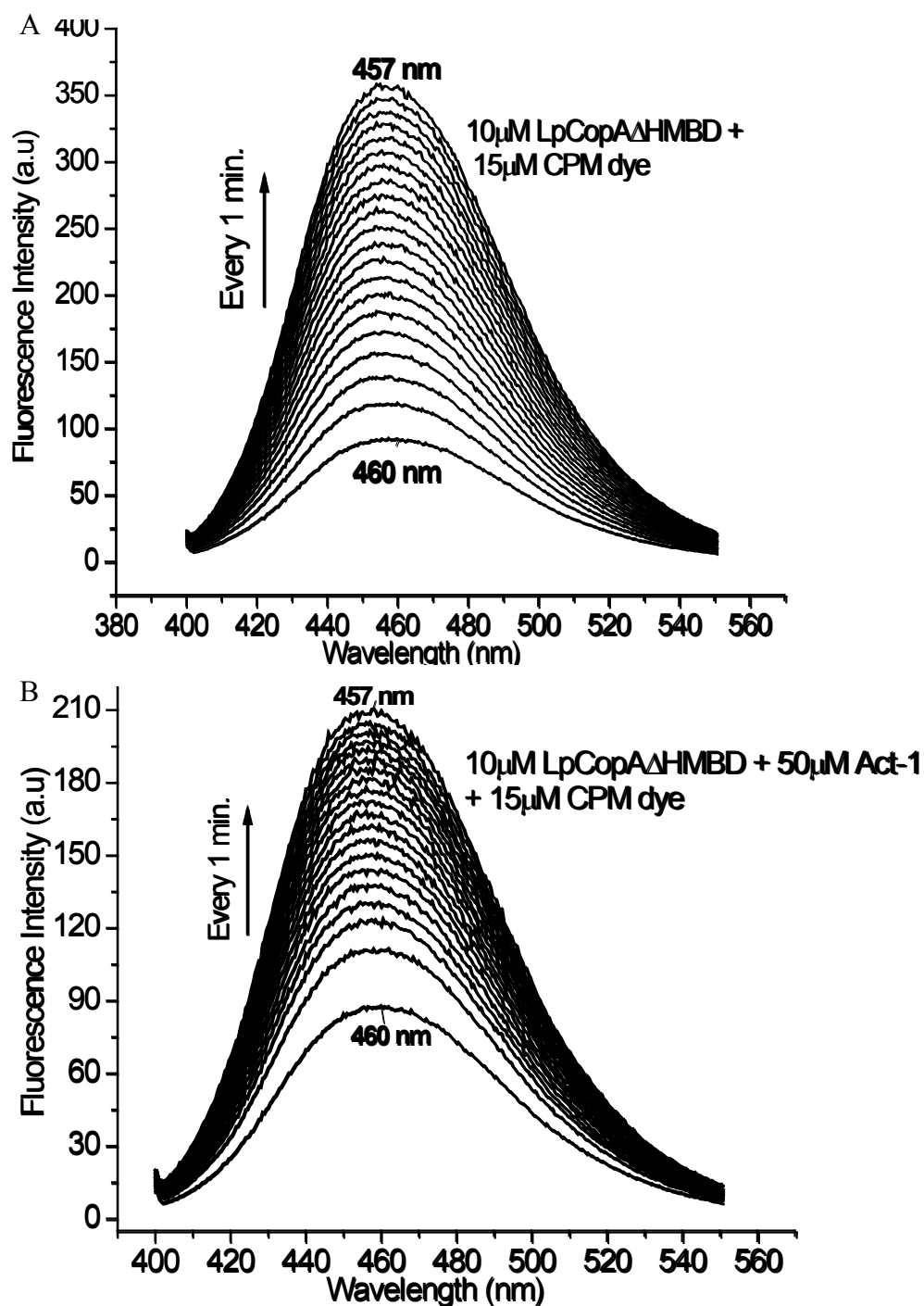


**Figure 6.10. Fluorometric assay of cysteine(s) reactivity of the conserved CPC motif of LpCopA $\Delta$ HMBD**

CPM dye ( $\lambda_{\text{ex}}$  387nm) used as a probe to monitor accessibility of cysteine residues. Full fluorescence spectra of LpCopA $\Delta$ HMBD (10  $\mu$ M) with CPM probe (15  $\mu$ M) were recorded every 1min in **A**) absence and **B**) presence of 50  $\mu$ M Act-1. The assay carried out in a buffer containing 0.1%DDM and 1mg/ml Asolectin at RT (See Materials and Methods, Chapter 2).

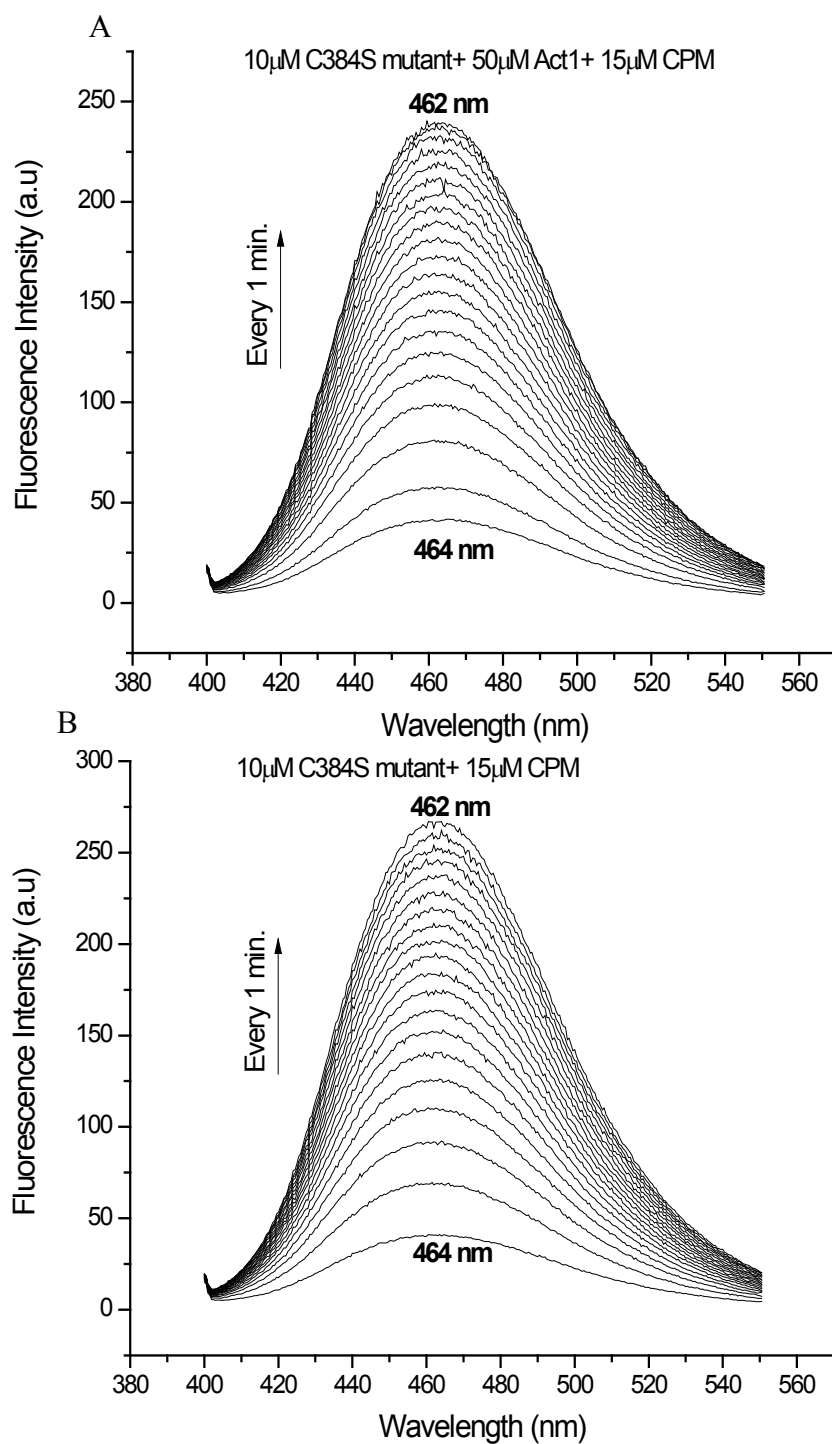


**Figure 6.11. Fluorescence spectra of thiol reactivity of cysteine at 382 in the C384S mutant**

The reactivity of C384S mutant (10  $\mu\text{M}$ ) with CPM (15  $\mu\text{M}$ ) was recorded every 1 min under the same conditions mentioned above; **A**) in absence and **B**) in presence of 50  $\mu\text{M}$  Act-1.

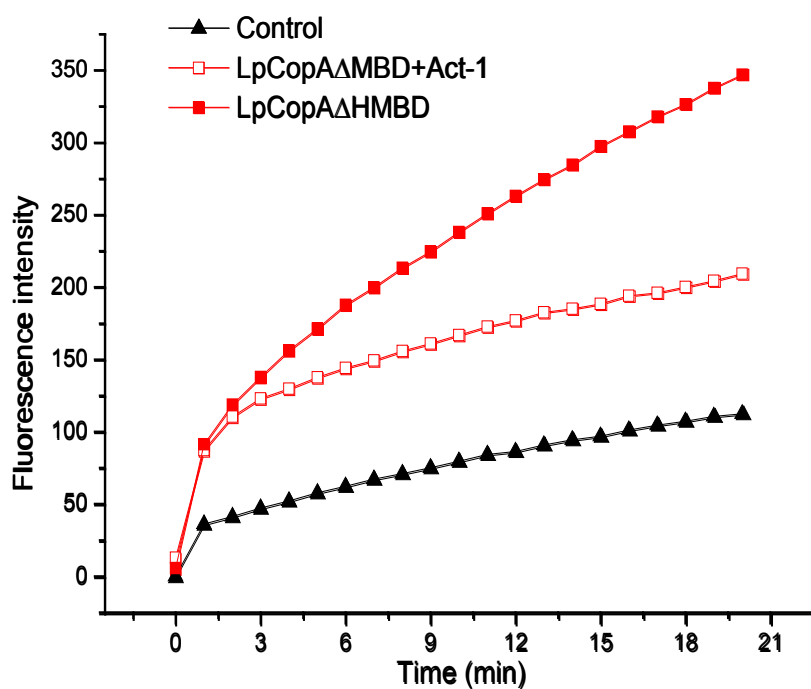


**Figure 6.12. Time course of the peak intensity of the CPM-Cys adduct for LpCopAΔHMBD**

The reaction was occurred without (■) and with 50  $\mu$ M Act-1 (□). CPM background (▲) was measured during the assay.

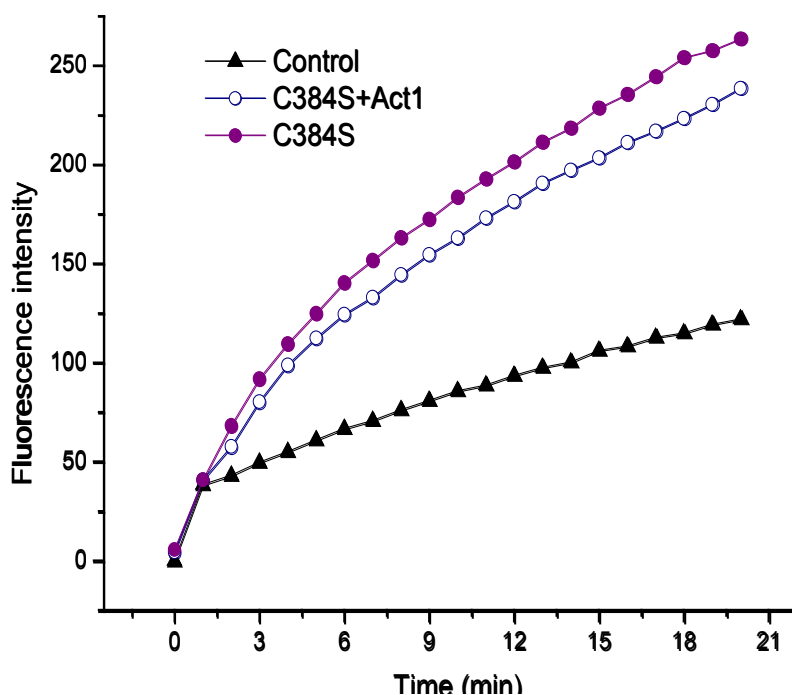


**Figure 6.13. Time course of the peak intensity of the CPM-Cys adduct for the C384S mutant**

The reaction was occurred without (●) and with 50  $\mu$ M Act-1 (○). CPM background (▲) was recorded during the assay.

### 6.6.2.2 Colorimetric assay

In parallel measurement, the accessibility of the cysteines in the CPC-motif of LpCopA $\Delta$ HMBD in function of peptide Act-1 was also investigated using an alternative colorimetric method. The 4,4-dithiodipyridine (4-DPS), thiol-reactive agent, reacts with cysteine forming 4-thiopyridone (4-TP) which absorbs strongly at 324 nm. Figure 6.14 shows the reactivity of LpCopA $\Delta$ HMBD with 4-DPS was inhibited in presence of 50 M Act-1.

In summary, the results conclude that the actuator-derived peptide Act-1 induces structural changes at C384 residue in the transmembrane CPC motif. This conclusion is emphasized by Time-Correlated Single Photon Counting (TCSPC) measurements in Chapter 7- section 7.4.2.2.

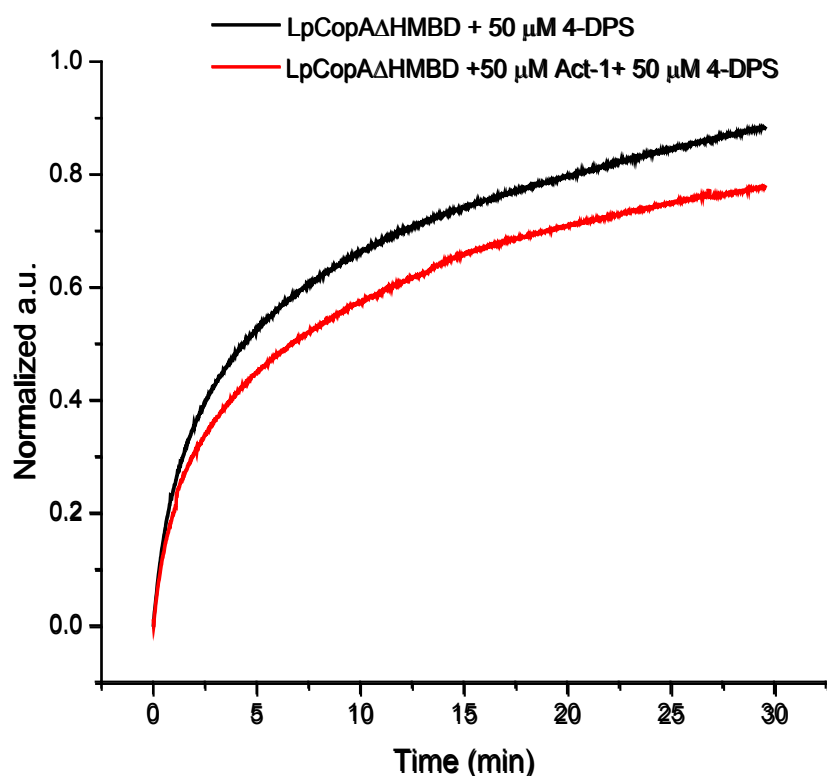


**Figure 6.14. Time course of thiol reactivity of LpCopA $\Delta$ HMBD with 4-DPS**

In 250  $\mu$ l total assay volume, 50  $\mu$ M 4-DPS (final conc.) was added to 5  $\mu$ M LpCopA $\Delta$ HMBD with (red trace) and without (black trace) 50  $\mu$ M peptide Act-1 in 50 mM Tris-HCl pH 7.4, 150 mM NaCl, 3mM MgCl<sub>2</sub>, 0.1% DDM, 1 mg/ml Asolectin buffer. The conversion rate of 4-DPS to 4-TP was monitored by measuring the absorbance at 326nm



## Summary and discussion

It is well-known that A-domain is primarily responsible for cleavage of aspartyl-phosphate bond in the dephosphorylation step and ion release. We addressed question of the role of highly conserved TGE motif in A-domain in the stimulation of conformational changes in transmembrane domain independently of the rest of the A-domain structure. To answer this question, decameric peptides driven from the conserved TGE motif of A-domain sequence, Acyl-NH-VTGE<sub>10</sub>(I/W)PVAS-CONH<sub>2</sub>, were synthesized.

The data analysis of circular dichroism and stopped-flow fluorescence spectroscopy reveal that the actuator-driven peptide binds to the PN domain with  $K_D$  varying from 30-50  $\mu$ M with a weakly ATP-dependent fashion, and induces structural changes in PN domain at the expense of  $\alpha$ -helical content. We suppose that the peptide binds at the phosphorylation site in closely comparative position to that of A-domain as the peptide exhibits a weak inhibitory effect for ATPase activity of LpCopA. The peptide not only cause a conformation change at cytosolic part, but also at transmembrane helical core of LpCopA; this change has been detected by blue-shifting in a static fluorescence of BADAN-labeled TM-MBS of LpCopA $\Delta$ HMBD (see chapter 7) and also by inhibiting the rate of the online thiol labeling of the CPC motif by the CPM fluorophore when it reacted with this mutant, on the other hand, the thiol reactivity of C384S mutant did not inhibit. This indicates that C384 residue is much affected by the peptide binding.

## Chapter 7

### Time-resolved Structural Dynamics of the Transmembrane CPC Motif in LpCopA: Time-correlated Single-photon Counting Technique (TCSPC)

#### Introduction

The structural changes in cytosolic headpiece of CopA, induced by ligand binding, transmit to the transmembrane domain for ion occlusion or extrusion. Recently, the molecular dynamics (MD) simulations of LpCopA suggested that TM domains of the  $E2\sim P_i$  and  $E2P$  states are both open toward the extracellular side as shown in Fig 7.1 ; the extracellular bulk water penetrates the TM-MBS and reach the M717, C382 and C384 residues (from high to low water density, respectively) [34].

Here, we investigate the water accessibility and mobility of the TM-MBS in function of ligands and membrane lipids by applying Time Correlated Single Photon Counting (TCSPC) to site-specifically fluorescently labeled LpCopA. Our data in collaboration with Prof. Martin Hof presented the first experimental evidence on a luminal-open conformation of  $E2\sim P_i$  state of a hydration gradient along the TM-MBS of LpCopA.

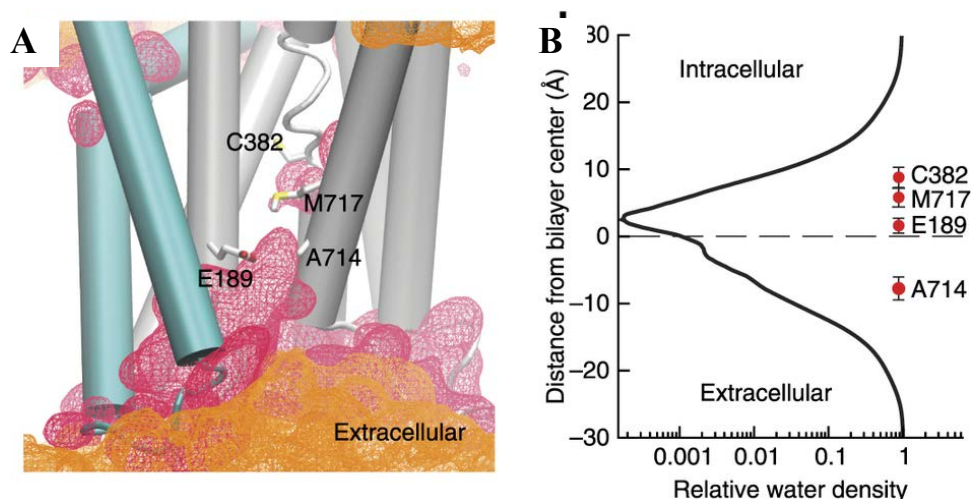


**Figure 7.1. Previous MD simulations suggest the  $E2\sim P_i$  and  $E2P$  states to be open in LpCopA.**

A) Cartoon representation from the previous simulation study [34] of the LpCopA in  $E2\sim P_i$  state show lipid phosphates and water in orange and red density, respectively [34]. B) Water density plot show the water distribution in TM domain. The number of water molecules within 7 Å from the protein relative to bulk solution along the membrane normal (intracellular side is positive). The figure is adapted from [34].

## Results and discussion

### 7.1 Fluorescence properties of BADAN dye: for lifetime measurements

BADAN (6-Bromoacetyl-2-Dimethylaminonaphthalene) is a thiol-reactive probe to monitor the protein conformations and ligand binding due to the environmental sensitivity of its fluorescence. It reacts covalently with cysteine to form a very strong and stable alkylated bond. The alkylation of cysteine is achieved by reaction of the thiol group with the  $\alpha$ -bromide carbonyl of BADAN.

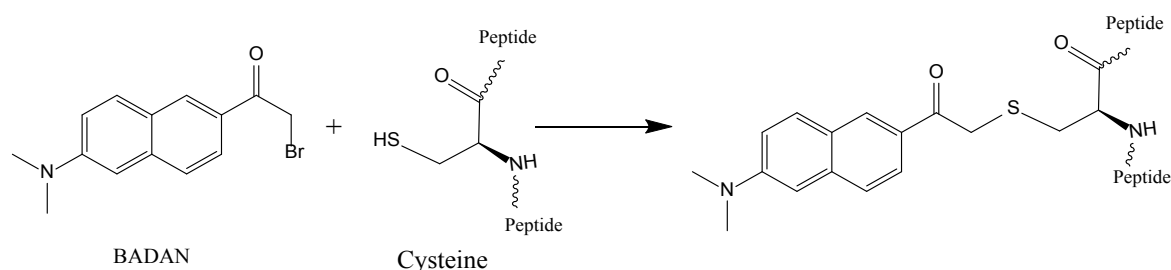


**Figure 7.2. Covalent chemical reaction of thiol residue of a protein with Fluorescent BADAN**

The sensitivity of the chromophore to both solvent polarity and solvent mobility is the basis for the use of BADAN to assess water mobility in proteins. Here, BADAN was used to address the water accessibility and mobility of the copper-binding site of LpCopA. Since the latter is obtained in a detergent-solubilized state, the effect of DDM on BADAN fluorescence needed to be measured as a control. The emission spectrum of BADAN was blue-shifted and the intensity was slowly and continuously increased as soon as 0.3% DDM detergent was added to the assay buffer. This agrees with the expected effect of increased hydrophobicity in the molecular environment of the chromophore and indicates that the hydrophobic property of the dye causes its partitioning into the detergent micelles. Therefore, the BADAN was diluted into assay buffer containing 0.3% DDM and incubated at 4 °C for overnight to stabilize the fluorescence intensity prior to starting the reaction with the membrane proteins. The maximum emission spectrum of BADAN under previous conditions is at 496 nm as shown in Fig. 7.3.

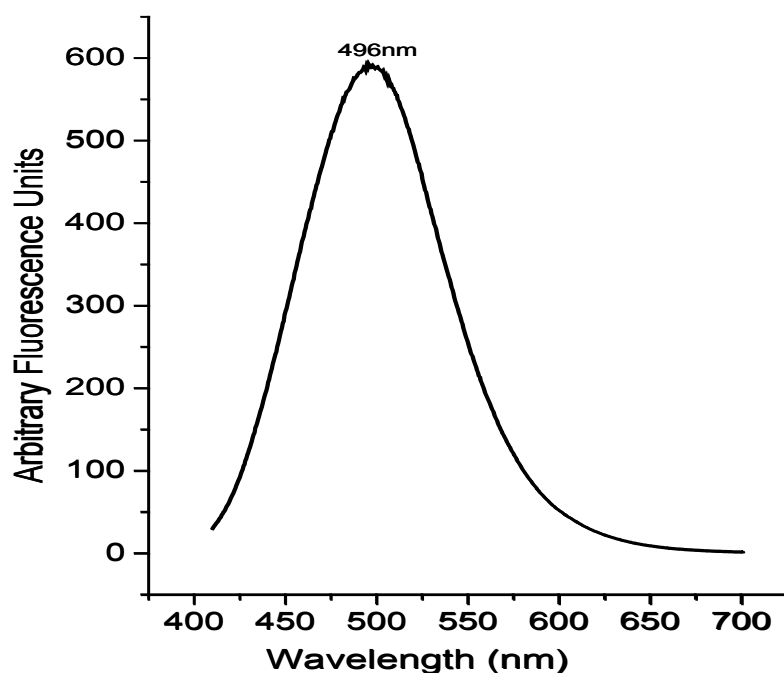


**Figure 7.3. Fluorescence emission spectrum of BADAN.**

10  $\mu\text{M}$  BADAN incubated in buffer containing 0.3%DDM was excited at 390 nm. Continuous emission spectra were measured till obtaining a stable intensity.

BADAN is structurally similar to RODAN and LAURDAN in which the excited state can be either a non-hydrogen-bonded intramolecular charge transfer (ICT) state, or a hydrogen-bonded intramolecular charge transfer (HICT) state (Fig 7.4). In the excited state, a previously non-bonded state can evolve into a state that is hydrogen-bonded to solvent molecules and the latter can further reorient in the excited state in a process called "solvent relaxation" [164]. Thus, the charge distribution around BADAN changes during the life time of the excited state, and result in the reorientation of the solvent molecules into an energetically favorable state with respect to the charge distribution of the electronically excited BADAN [165]. This leads to the stabilization of the negative charge on the carbonyl moiety by the hydrogen bond and a further reduction of the energy gap between the ground and excited state, respectively [164].

As the energy of the excitation state is lowered, the relaxation process causes a continuous red-shift of the recorded time-resolved emission spectra (TRES). Thus, solvent polarity and the local environment have thorough effects on the emission spectra of BADAN [165].

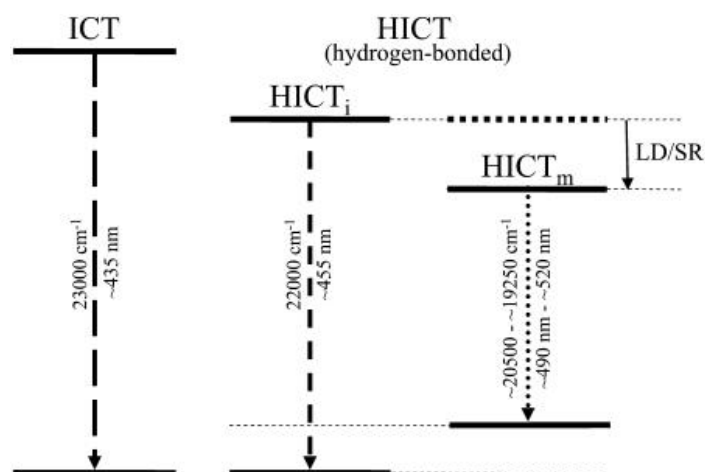


**Figure 7.4. Schematic excited level diagram of BADAN**

The non-hydrogen-bonded ICT state is lowered to hydrogen-bonded HICT state in an immobilized environment (HICT<sub>i</sub>) and in a mobile environment (HICT<sub>m</sub>). The LD and SD stand for internal label dynamics and solvent relaxation, respectively. the diagram is captured from [164].

## 7.2 Site-directed labeling of transmembrane metal-binding site

LpCopA contains six cysteine residues that interact with copper; four are localized in the cytosolic heavy metal-binding domain (HMBD) and the other two in the C382-P-C384 motif of the transmembrane metal-binding site. The transmembrane cysteines in the CPC motif are highly conserved in all ATPases CopA. The C382 localizes closer to the extracellular side where the copper ion exits, while C384 is closer to the cytosol, where copper enters the ATPase. Therefore, the study of the solvent polarity at the CPC motif bears structural information about the accessibility of the two cysteines during the catalytic ATPase cycle. Using a water-sensitive monitor at this site will particularly address the question of the fate and possible role of hydration water in the transport mechanism, because copper enters the pump as a fully hydrated ion. To monitor the local environment at the CPC motif by site-specific BADAN labeling, the HMBD had to be truncated from the LpCopA structure, leading to the construct denoted as LpCopAΔHMBD. In this construct both transmembrane cysteines can potentially react with BADAN. In addition, C384 side chain of LpCopAΔHMBD was further replaced with serine, denoted as C384S mutant, in order to study the local environment at the single cysteine at position 382. Serine was selected for the replacement to mimic the steric conditions of the cysteine. Furthermore, this mutant putatively maintains the ability of the metal-binding site to bind to ions as inferred from the conserved CPX motif of copper-transporting ATPase from other prokaryotes [29, 166].

### 7.2.1 BADAN labeling assay of LpCopA mutants

The kinetic labeling assay of LpCopA $\Delta$ HMBD and C384S mutant with BADAN was performed to find the optimal conditions and time required for completing the labeling. In the beginning, the labeling assay was carried out in buffer containing 0.1% DDM at room temperature but it was found that the LpCopA $\Delta$ HMBD and C384S mutant were unstable and precipitated during the assay. This precipitation may be due to the hydrophobicity of BADAN that results in accumulation with DDM detergent and consequently reduces the micelles around the membrane proteins. Therefore, the DDM concentration was increased to 0.3% and the temperature lowered to 15 °C to slow down the reaction. Equivalent volumes of LpCopA $\Delta$ HMBD or C384S mutant were rapidly mixed with a BADAN solution which was pre-incubated overnight in buffer containing 0.3% DDM. During the reaction of the fluorophore with LpCopA $\Delta$ HMBD, the emission spectra of BADAN was blue-shifted from 496 nm to 488nm in about 30 seconds after mixing, and then over 20 min, the emission intensity slowly increased and the peak shifted further to 484 nm as shown in Fig.7.5.

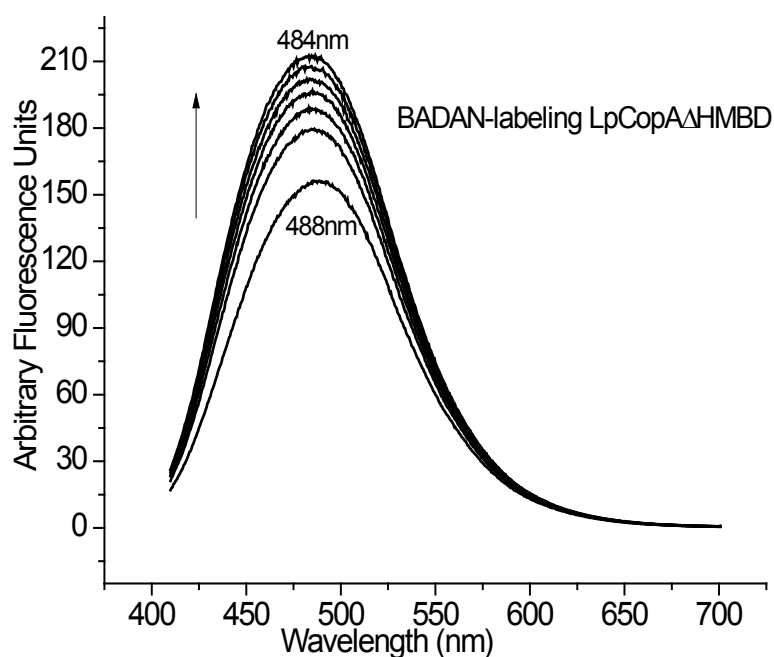


**Figure 7.5. Kinetic assay of BADAN-labeling LpCopA $\Delta$ HMBD.**

The fluorescence emission spectra of 13  $\mu$ M BADAN reacting with 6  $\mu$ M LpCopA $\Delta$ HMBD was recorded every 6 min in the assay buffer containing 0.3% DDM. The excitation wavelength was at 390 nm and emission spectra were collected from 410-700 nm. The arrow indicates to the intensity increasing with time.

While the emission spectra of BADAN reactivity with C384S mutant was blue-shifted to 494 nm within 30 seconds and stabilized at 490 nm over 20 min (Fig. 7.6), the emission spectra of a BADAN-labeled C382S mutant, prepared in a parallel project of a colleague in our group, showed similarity to that of BADAN-labeled LpCopAΔHMBD (data not shown), i.e. a more pronounced blue-shift, indicative of a more hydrophobic molecular environment of BADAN. These findings indicate that C384 residue is preferentially labeled, even when both cysteines of the CPC motif are present. The C382 residue is embedded deeper within the transmembrane helical core than C384 residue. This could lead to a situation that labeling of C384 residue blocks that of C382 residue if the entrance of BADAN to the transmembrane helices occurs favorably via the cytosolic side. The presented data further show that C382 samples a more hydrophilic part of the copper entry site although it is deeper within the protein than C384.

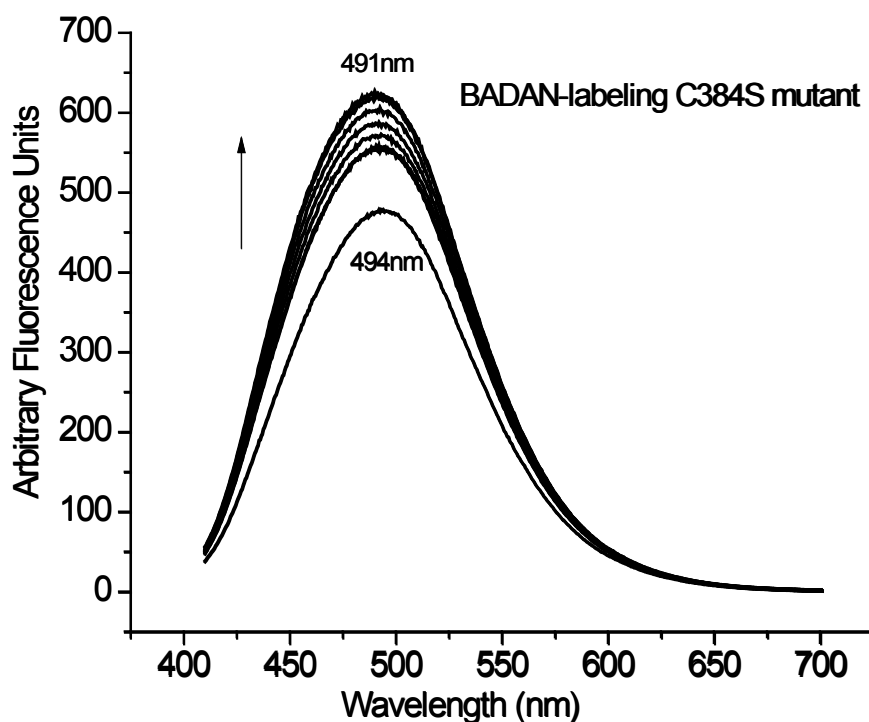


**Figure 7.6. Kinetics of BADAN-labeling C384S mutant.**

The fluorescence emission spectra of 10  $\mu$ M BADAN reaction with 10  $\mu$ M C384S mutant was recorded every 6 min in the same assay conditions as mentioned above. The arrow indicates to the intensity increasing with time.

### 7.2.2 On-Column BADAN labeling

Although, the BADAN labeling of LpCopA $\Delta$ HMBD and C384S mutant was successfully monitored in solution, the Time-Correlated Single Photon Counting (TCSPC) experiments of the labeled membrane proteins prepared in this way, indicated the presence of non-reacted BADAN based on a large fraction of a very fast solvent relaxation component typical of "free" water exposed BADAN. Apparently, the dialysis and PD-10 desalting methods were unable to remove free BADAN; perhaps this is due to the integration of BADAN into detergent micelles. To overcome this problem, LpCopA $\Delta$ HMBD and the C384S mutant were labeled with BADAN when the membrane protein was still bound to the Ni-NTA column after the washing steps. After incubation with BADAN, the column was further washed with buffer and the removal of unbound BADAN was fluorometrically monitored (Fig. 7.7.).

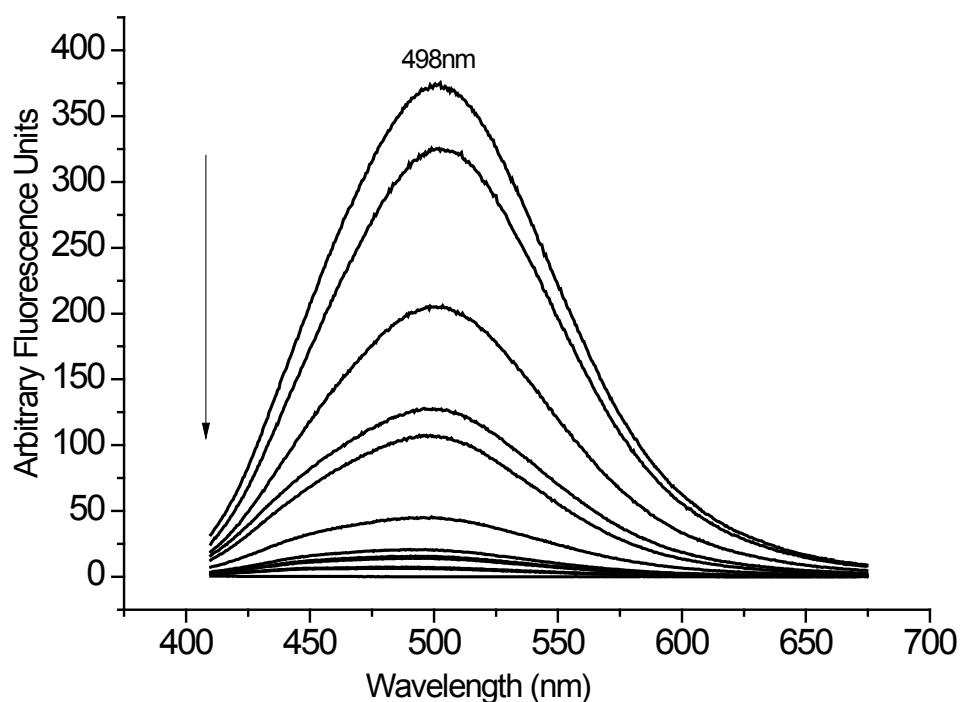


**Figure 7.7. Removal of excess BADAN dye from Ni-NTA column**

The fluorescence emission spectra of BADAN waste were recorded during the washing of BADAN-labeling membrane proteins bound to the Ni-NTA column. The excitation wavelength was at 390 nm and emission spectra were collected from 410-700 nm. The arrow indicates the successive removal of BADAN from the wash buffer.



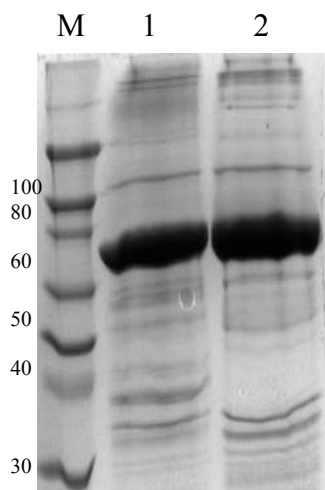


**Figure 7.8. SDS-PAGE analysis of purified BADAN-labeled membrane proteins**

Lane M: Molecular weight marker, lane1: the elution of BADAN-labeled LpCopA $\Delta$ HMBD (72 kDa), and lane2: that of BADAN-labeled C384 from Ni-NTA column. Membrane protein fractions were separated by 11% acrylamide gel.

After removing unbound BADAN, the LpCopA $\Delta$ HMBD and the C384S mutant were eluted with elution buffer containing 0.05% DDM, and imidazole was removed by a PD-10 desalting column; Figure 7.8 shows the purification pattern of BADAN-labeled proteins. The emission spectra of “on column” BADAN-labeled LpCopA $\Delta$ HMBD showed a further blue-shifted to 480 nm (Fig. 7.9) as compared to the sample labeled in solution (Fig. 7.5). This behavior was expected for an enrichment of protein-bound (more hydrophobic) over “free” BADAN (more hydrophilic) BADAN. In contrast, the C384S mutant labeling did not show an equivalent peak shift after on-column labeling. This indicates that C384 is mainly responsible for providing the hydrophobic environment sampled by BADAN when it reacts with the intact CPC motif as already inferred from the data of the BADAN reaction in solution. On the other hand, the fact that also the C384 mutant reacts with BADAN shows that C382 is also accessible for the dye but places it in a more hydrophilic environment. Taking the two results together, it can be concluded that C384 reacts preferentially (over C382) with BADAN in the presence of both conserved cysteines. Upon removal of Cys384, however, C382 also reacts with BADAN. This means both cysteines are solvent accessible but unexpectedly, the more cytosolic one (C384) resides in a more hydrophobic environment, probably; the labeling of C384 impedes the labeling of the second cysteine (C382) by steric constraints. The data show that: 1) the labeling on column is an efficient method to improve protein-specific labeling and 2) there is a strong hydration gradient within the single helical turn at the CPC motif.

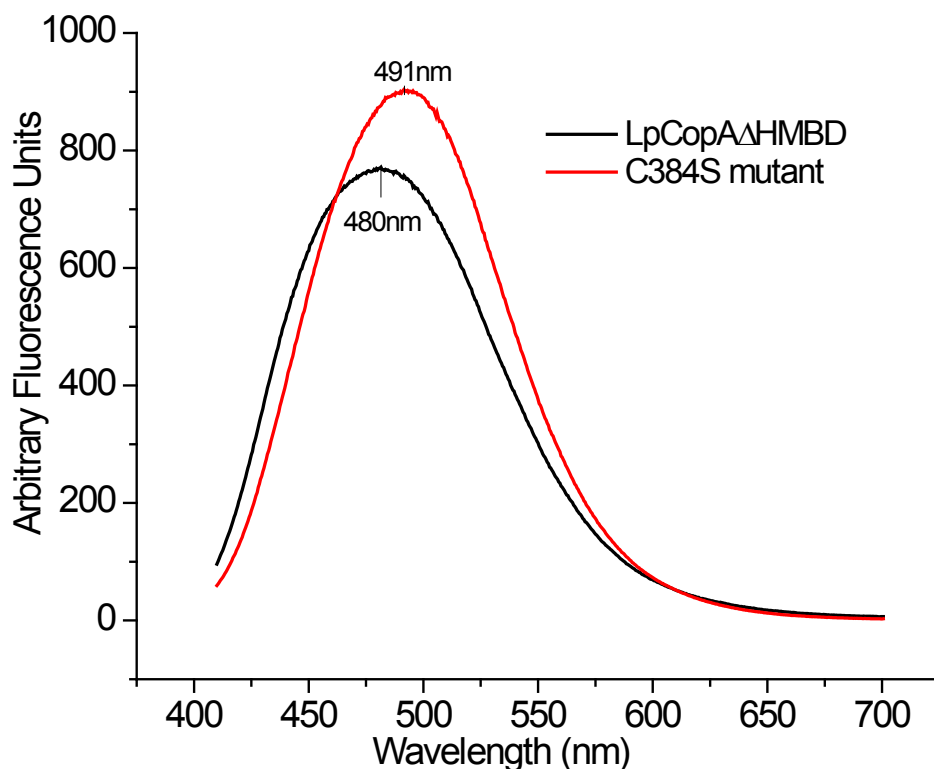


**Figure 7.9. Fluorescence emission spectra of on-column BADAN-labeled C384S mutant and LpCopAΔHMBD.**

While the membrane proteins were bound to Ni-NTA resin, the column was washed with BADAN solution. The excess of un-reacted BADAN was removed by washing with buffer. The excitation wavelength was at 390 nm.

### 7.3 Reconstitution of BADAN-labeled membrane proteins

Reconstitution of membrane proteins into lipid bilayers is a powerful tool to study their structure and function in a native-like environment. The lipid packing affects the rigidity and conformation of membrane proteins and also the solutes and solvent mobility. Thus, the lipid reconstitution is an attractive system to study the mobility of solvent molecules at transmembrane helices of the BADAN-labeled ATPase mutants. For this purpose time-correlated single photon counting (TCSPC) is a sensitive technique to measure local solvent relaxation times in the pure protein or independence on ligand binding. The detergent-mediated reconstitution method has been successfully used for many transporters; e.g. various kinds of ATPase [167], bacteriorhodopsin [168], lactose transport protein (LacS) [169], and ABC transporters [94, 170].

The LpCopA $\Delta$ HMBD and C384S mutant were reconstituted into soybean phospholipid (Asolectin) liposomes using detergent-mediated reconstitution according to [94] with some modifications. Asolectin, a mixture of phosphatidylethanolamine, phosphatidylcholine, and several minor lipids, is frequently used for reconstitution of ATPases [146, 171-173].

According to Geertsma and his coworkers [94], large unilamellar vesicles (LUVs) were prepared using liposome extruder with approximately 100 nm in diameter pore and then titrated with Triton X-100 below the onset of total lipid solubilization ( $R_{sol}$ ) to form detergent-destabilized liposomes. The DDM-solubilized ATPase LpCopA $\Delta$ HMBD and C384S mutant were mixed with Triton X-100-destabilized preformed liposomes and the detergents were subsequently removed by adsorption onto polystyrene Bio-Beads SM-2 to form tightly sealed proteoliposomes. LpCopA $\Delta$ HMBD was successfully incorporated into liposomes and its concentration estimated from SDS-PAGE gel as 0.4-0.5 mg/ml; whereas C384S mutant did not incorporate (Fig. 7.10).

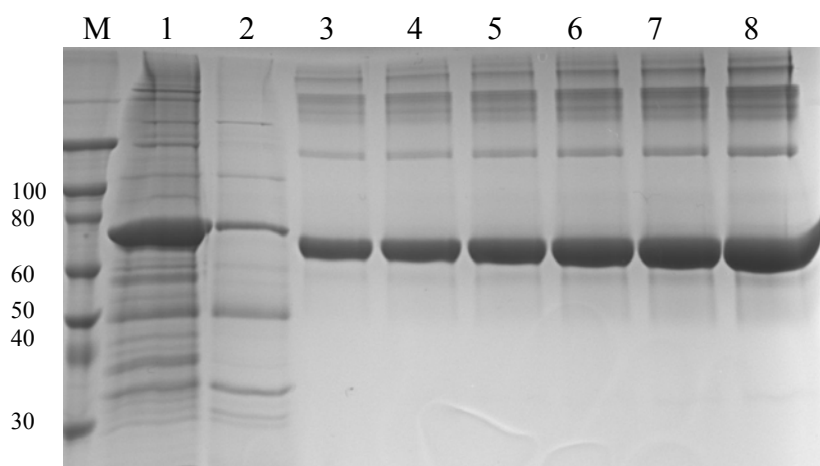


**Figure 7.10. SDS-PAGE analysis of the reconstituted BADAN-labeled LpCopA $\Delta$ HMBD and C384S mutant.**

Concentration of reconstituted BADAN-labeled membrane proteins was estimated by running a series of BSA standard concentrations in 11% acrylamide gel. Lane M: Molecular weight marker (kDa), Lane 1, reconstituted on-column BADAN-labeled LpCopA $\Delta$ HMBD; lane 2, reconstituted on-column BADAN-labeled C384S mutant; lane 3, 0.1 mg/ml BSA; lane 4, 0.2 mg/ml BSA; lane 5, 0.3 mg/ml BSA; lane 6, 0.4 mg/ml BSA.

The efficiency of protein incorporation and orientation into liposomes are controlled by several factors; i.e. detergent concentration and type, protein to lipid ratio, salts and the way of detergent removal [167, 168, 174]. For example, slow detergent removal was found to be more appropriate than a rapid one [175]. Thus, the use of Bio-Beads SM-2 satisfies all the criteria that make the procedure a powerful and better alternative to dialysis or dilution for proteoliposome reconstitution [174]. The change in protein/lipid ratio of  $\text{Na}^+/\text{K}^+$ -ATPase reconstitution from 1:10 to 1:75 caused an increase in the inside-out-oriented molecules to 30% [167].

Triton X-100 is more efficient than other detergents in mediating membrane reconstitution. It has been reported for several membrane proteins that Triton X-100 often mediates the membrane protein incorporation in an unidirectional orientation, whereas the reconstitution with DDM has led to random orientations [94, 167, 170, 176]. However, other works have determined also a bidirectional arrangement of protein molecules (Fig. 7.11) in Triton X-100- mediated incorporation [167, 177, 178].

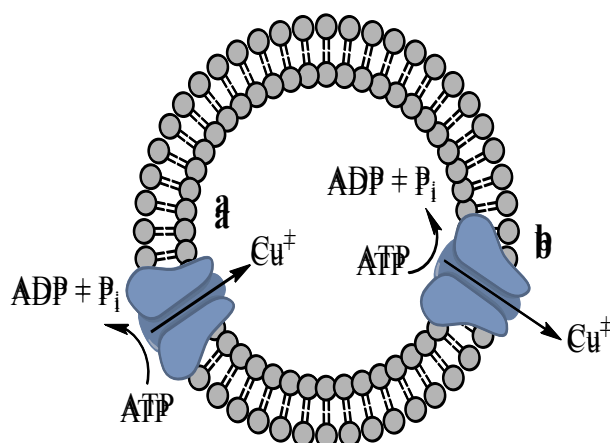


**Figure 7.11. Scheme for proposed  $\text{Cu}^+$ -ATPase orientation in liposome**

The protein orientation inside liposomes can be **a)** inside-out, and **b)** right-side-out.

In this study, it was difficult to investigate the protein orientation because the HMBD-truncated ATPase is unable to either hydrolyze ATP molecules or transfer metal ions. However, according to Table III.1, most membrane proteins have inserted unidirectionally, in either the inside-out or right-side-out orientation.

**Table 7.1 Comparison of the membrane proteins orientation in Triton X-100-mediated proteoliposomes**

| Membrane proteins                       | Inside-out (Right-side-out) orientation % | Reference |
|-----------------------------------------|-------------------------------------------|-----------|
| Bacteriorhodopsin                       |                                           |           |
| • partial solubilization                | 80-85% (20-15%)                           | [168]     |
| • total solubilization                  | 65-70% (35-30%)                           | [168]     |
| ABCC3 transporter                       | 25% (75%)                                 | [170]     |
| LacS protein                            | ~100% (0)                                 | [176]     |
| Ca <sup>2+</sup> -ATPase                | 25% (75%)                                 | [179]     |
|                                         | 40-50% (60-50%)                           | [180]     |
|                                         | 58% (42%)                                 | [177]     |
| Na <sup>+</sup> /K <sup>+</sup> -ATPase | 14% (86%)                                 | [178]     |

## 7.4 Time-resolved Fluorescence measurements

### 7.4.1 The principle of time-correlated single photon counting (TCSPC) fluorescence decay lifetime

As discussed in section 7.1, the polar solvent molecules are oriented so that their dipole moments compensate for the dipole moment of the fluorophore in order to minimize the total energy of the fluorophore and solvation envelope as shown in Fig 7.10. Upon the fluorophore excitation, the charge redistribution causes reorientation of the fluorophore's dipole moment to an energetically unfavourable state. The system again relaxes through reorientation of fluorophore's solvation envelope to a state of lower energy, i.e. leading to the red shift of the emission spectrum. The time-scale of the solvent relaxation depends on the mobility of fluorophore's solvation envelope. The increasing in the solvent polarity leads to the larger red-shift of the fluorophore's emission spectrum, and vice versa. Thus, the solvent relaxation process causes a continuous red-shift of the recorded time-resolved emission spectra (TRES).

In principle Time Correlated Single Photon Counting (TCSPC) is measuring the time between the excitation of the sample and the consecutive emission of a single

photon. The fluorescence decay curves are then reconstructed from the individual delay times. The fluorescence signal is attenuated so that typically only one photon per 1000 excitation pulses is detected. The time, measured between the excitation pulse and the observed photon, is stored in a histogram. A typical histogram is an exponential decay curve which can be fitted to single or multiple exponential decay function to extract the fluorescence lifetime [181].

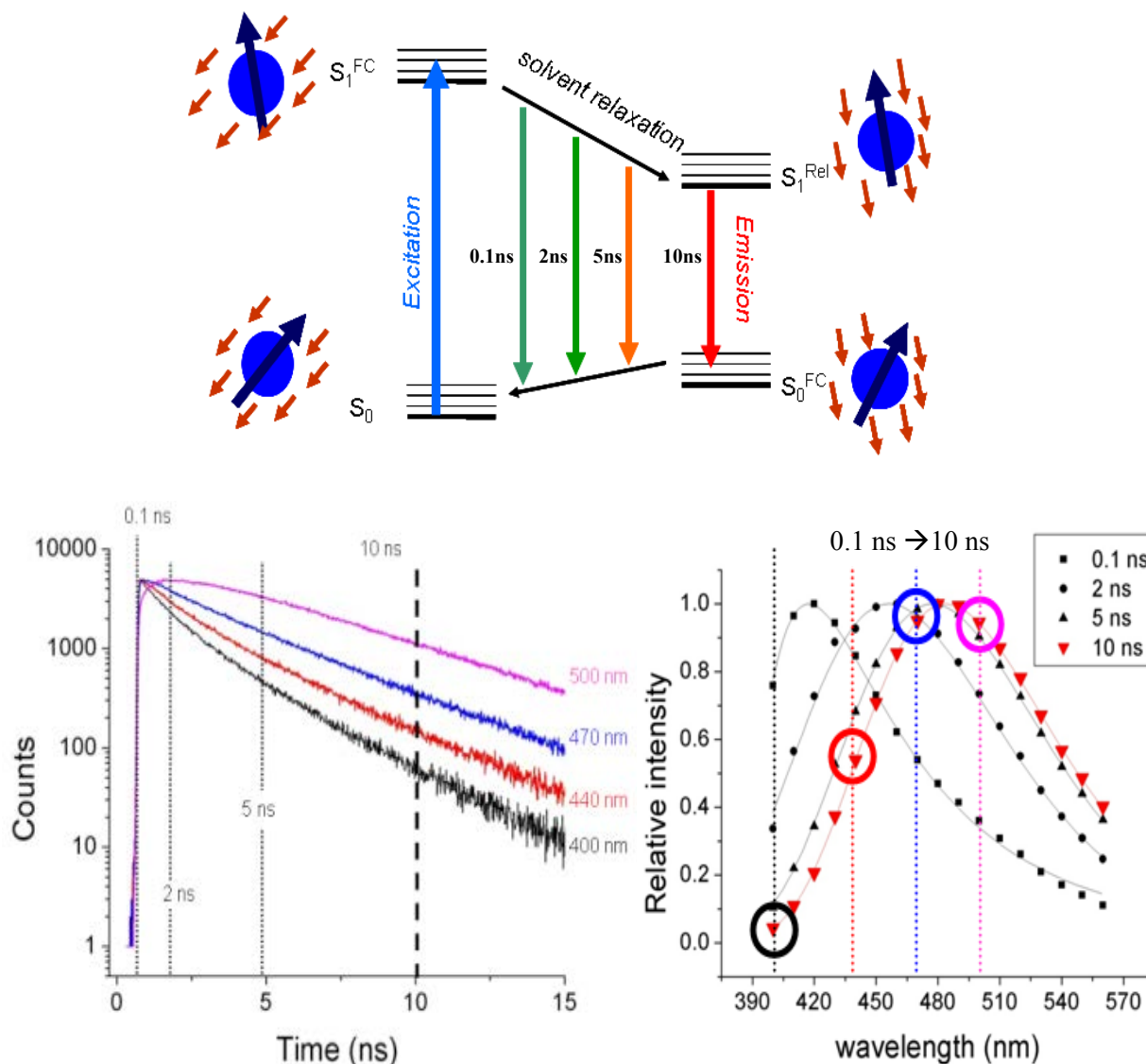


**Figure 7.12 Fluorescence lifetime decay of a fluorophore in the solvent relaxation process.**

The change in the dipole moment of the fluorophore (in blue arrow) upon excitation causes reorientation of the dipole moment of solvent molecules (in red arrows) in a time-dependent on the environment viscosity. Time-Resolved Emission Spectra (TRES) are recorded with nanosecond scale and plotted as intensity vs. wavelength. The figures are adapted from Prof. Hof's lectures, available at ([www.jh-inst.cas.cz/~fluorescence/lectures.html](http://www.jh-inst.cas.cz/~fluorescence/lectures.html)).

### 7.4.2 Solvent relaxation around the CPC motif measured by Time Correlated Single Photon Counting

Here, we utilize the environment-sensitive dye BADAN to investigate the solvent accessibility of transmembrane CPC motif using TCSPC technique and to measure the time scale of solvation response under different conditions. Upon excitation, a large change in dipole momentum is produced between the tertiary amine and ketone at opposite ends of BADAN structure (Fig. 7.13), and the energy is lowered during the excited state life time as the result of solvent relaxation, i.e., water molecules re-orienting around the strong dipole.

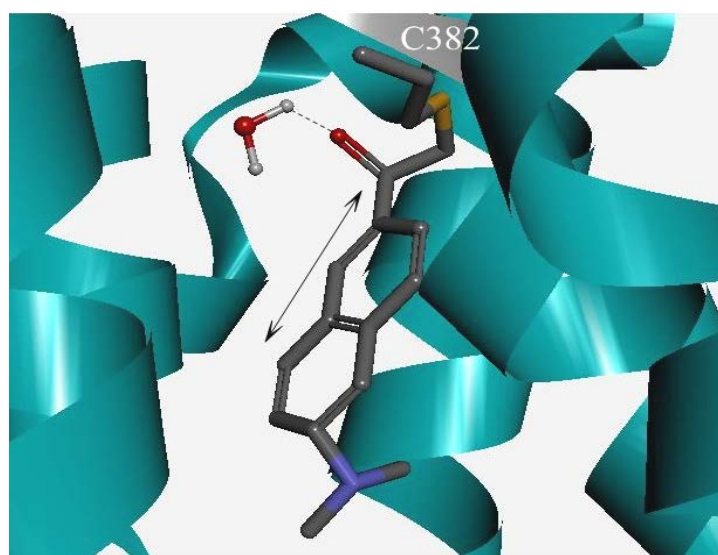


**Figure 7.13. Dipole moment generated upon BADAN excitation**

Cartoon diagram shows structure of BADAN linked to Cys382 of LpCopA $\Delta$ HMBD (PDB entry: 3RFU) with hydrogen bond with a water molecule via its carbonyl group (dashed line). The arrow represents the excitation dipole.

For lifetime measurements, both BADAN-labeled LpCopA $\Delta$ HMBD and the C384S mutant were excited by a pulsed laser, and the emitted fluorescence photons collected. For each detected photon, the decay of emission on the nanosecond time scale, measured by TCSPC, shows a correlation between the lifetime of the BADAN probe and the degree of solvent exposure. The kinetics measured at any discrete wavelength is affected by solvation processes that occur on a comparable time scale; therefore, the lifetime of the probe was determined by fitting the integrated intensity of the time-resolved emission spectra (TRES). All TRES experiments were performed in collaboration with Prof. D.Sc. Martin Hof's lab (J. Heyrovský Institute of Physical

Chemistry of the ASCR, Prague) and data analyzed by Petr Pospisil (PhD student, Prof. Hof group). In essence, the data allow reconstructing a full emission spectrum for each sampled time point. Here, typically 20 ns have been covered and the results are displayed as the shift of the emission maximum as a function of time after excitation. At time zero, the maximal Stoke shift between the excitation (373 nm) and emission energy is measured. For BADAN this is  $22000\text{ cm}^{-1}$  and rather independent of the environment, which makes BADAN a preferred fluorescent monitor for time-dependent Stoke shift analyses. The proposed location of BADAN at the C382PC384 motif is displayed in Fig. 7.14.

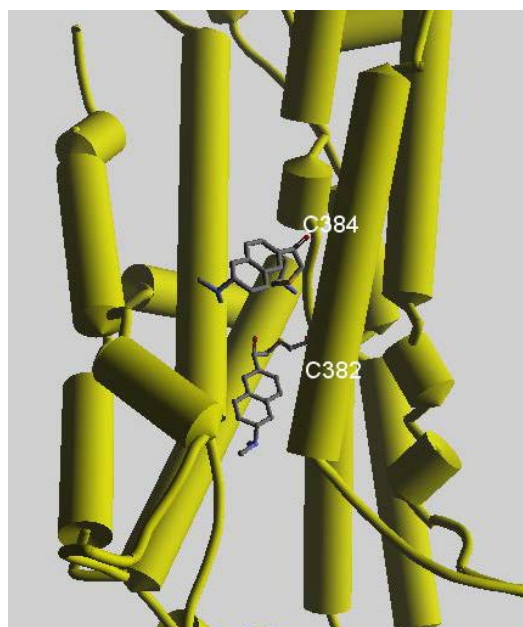


**Figure 7.14. Cartoon diagram represents a proposed location of BADAN in CPC motif.** The alkylation of transmembrane cysteine residues by BADAN was generated in Accelrys Discovery Studio Visualizer software with coordinates of PDB file 3RFU. Shown as gray stick models are the side chain of Cys384 and Cys382, and the BADAN molecule. The orientation of the BADAN relative to the rest of LpCopA helices is hypothetical and was carried by minimizing visually steric clashes between the Cys-BADAN and surrounding amino-acid side chains. Software-based energy minimization of Cys-BADAN was not attempted.



#### 7.4.2.1 Time-Resolved Fluorescence measurements of the CPC motif in mixed micelles and liposomes

The TRES analysis of BADAN-labeled LpCopA $\Delta$ HMBD embedded in 0.3% DDM micelles solution, with both cysteines i.e. the C384 is preferentially labeled, shows slower emission decay than that of BADAN-labeled C384S mutant (Fig.7.15), indicating on immersion of C384 residue of LpCopA $\Delta$ HMBD into high hydrophobic environment while C382 residue is exposed to hydrophilic side.

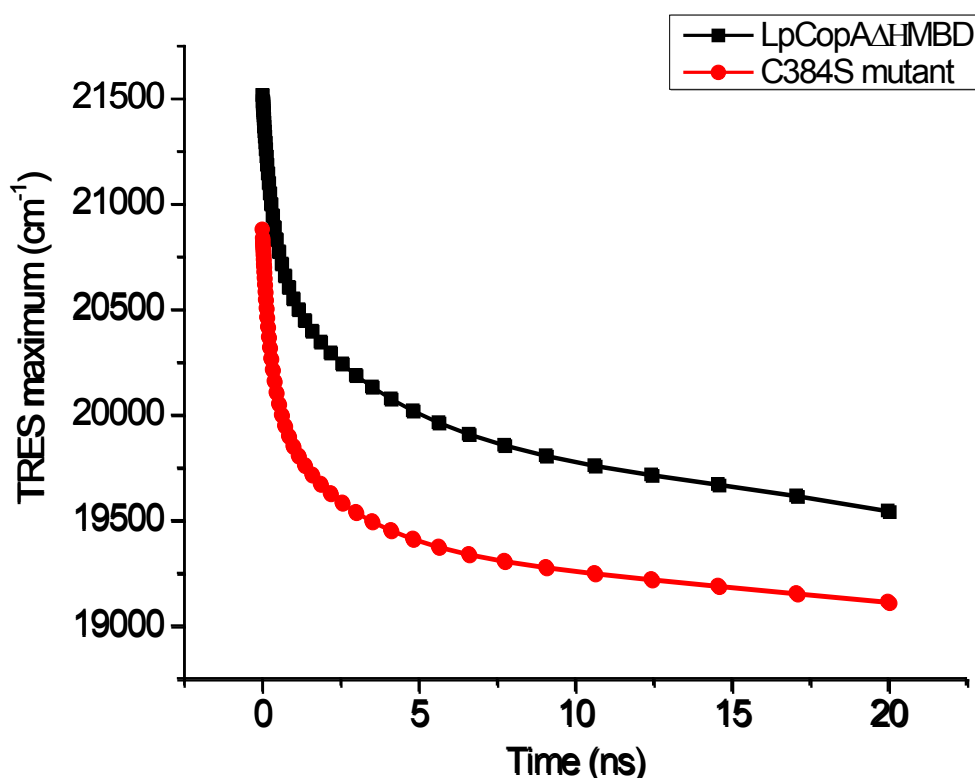


**Figure 7.15 Time-resolved emission spectra (TRES) of LpCopA $\Delta$ HMBD and C384S mutant in detergent micelles solution.**

5  $\mu$ M BADAN-labeled LpCopA $\Delta$ HMBD and C384S mutant was excited at 370 nm at 15 °C and the time decay of emission maximum of C384S mutant was faster than that of LpCopA $\Delta$ HMBD.

In all TRES experiments, LpCopA mutants were dissolved in buffer containing high concentrations of sulfate salts. It is worth pointing out that the sulfate ion acts as phosphate analogue in the phosphorylation domain of ATPases [72, 133, 182]; it binds at the identical phosphate-binding site as has been assigned in the structures of the *E2-P<sub>i</sub>* intermediate state in rabbit SERCA1 [72] and *Sulfolobus solfataricus* CopB-B [133]. Consequently, the structure of BADAN-labeled CopA under TRES experiment conditions is likely to prefer the *E2-P<sub>i</sub>* like conformation but probably fluctuates between *E2-E1* states, because the detergent provides little structural constraints.

In the *E2-P<sub>i</sub>* state, LpCopA, embedded in a dioleoylphosphocholine (DOPC) lipid bilayer, has been proposed to be open at the luminal side and water molecules penetrate the transmembrane domain to reach Cys382, Met717, Glu189 and Ala714 according to Molecular Dynamics (MD) simulation study [100]. Taken together, the TRES results of LpCopA $\Delta$ HMBD and C384S mutant are consistent with MD stimulation study [100] to be the first experimental study providing the solvent accessibility difference between Cys384 and Cys382 of transmembrane metal-binding site of ATPase CopA in *E2-P<sub>i</sub>* state.

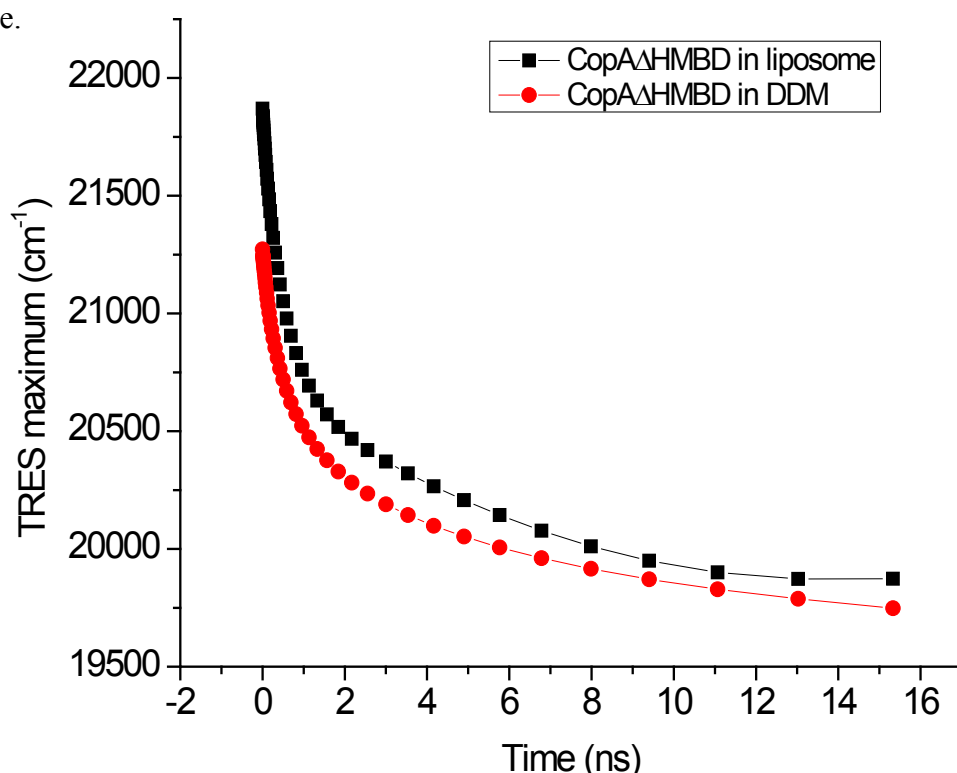


**Figure 7.16 TRES comparison between LpCopA $\Delta$ HMBD in liposome and detergent micelles solution**

Either BADAN-labeled LpCopA $\Delta$ HMBD in 0.3% DDM detergent solution or reconstituted in liposome was excited at 370 nm at 15 °C. The time decay of emission maximum of reconstituted LpCopA $\Delta$ HMBD is slower than that in detergent solution.

To address the role of lipid bilayers on the membrane protein structure and intra-protein water mobility at the CPC region of the LpCopA transmembrane helices, the fluorescence lifetime was measured on the nanosecond time scale also for BADAN-labeled LpCopA $\Delta$ HMBD embedded into liposomes. The comparison between TRES data of LpCopA $\Delta$ HMBD in liposomes and DDM detergent (Fig. 7.15) shows a slower decay of the Stoke shift for proteoliposomes. This shows that the Asolectin lipid bilayer induces a tighter packing of the transmembrane helices and thereby reduces the water mobility at the conserved CPC motif. To our knowledge, this is the first study utilizing site-directed labeling and TCSPC method to investigate the water dynamics at the active core of transmembrane the helices in a P-type ATPase and to address lipid protein interactions. Other studies have used voltage-sensitive membrane dyes (e.g. RH421, Oxonol VI and Laurdan) to detect changes of membrane potential associated with the activity of ATPases [183-185]. This underlying effect is produced by dye-lipid interaction and does not give structural information on pump function. In addition, these dyes exhibit a in terms of phototoxicity and photochemical instability [186]. The TCSPC method was used to characterize the cytoplasmic PN domain of the Na<sup>+</sup>/K<sup>+</sup>-ATPase [187] and of the SERCA1 [188] to measure the fluorescence decays of single-tryptophan mutants and a fluorescein isothiocyanate (FITC) probe, respectively. Although informative on structural transitions, these data do not report on the specific role of water mobility inside the transmembrane helical domains of these proteins.

The finding reported here for LpCopA, although preliminary, can be considered a platform for further work on the effect of the lipidic phase, its compositions, thickness and fluidity on the transmembrane core of ATPase and specifically the mobility of intra-protein water.

#### 7.4.2.2 Modulation of the water relaxation by functionally relevant ligands

The changes in water relaxation of LpCopA $\Delta$ HMBD and the C384S mutant were measured as function of lipid, nucleotides and the actuator domain-derived peptide Act-1. Starting with DDM micelles of LpCopA $\Delta$ HMBD or the C384S mutant, the conditions were changed during the TCSPC experiment by adding to the cuvette appropriate aliquots of stock solutions to supplement the sample in the following order with 1 mM Asolectin first and then either 100  $\mu$ M nucleotides or 100  $\mu$ M Act-1. Figures 17, 19, 20A show that there was no obvious change in TRES of either LpCopA $\Delta$ HMBD or the C384S mutant in detergent micelles and in liposome. However, the static emission spectra were altered upon addition of these additives (Figs. 18 and 21). For example, in proteoliposomes, the Act-1 peptide slightly changed the TRES of LpCopA $\Delta$ HMBD by lowering the rate of the Stoke shift decay (Fig. 20B), indicative with lower water mobility. In line with this observation, the corresponding emission spectrum was blue-shifted (Fig. 21B) indicative of a more hydrophobic environment.

The latter findings are consistent with the fluorometric CPM assay of the CPC motif (Chapter 6) and both emphasize that the actuator-derived peptide induces conformational changes at the cytosolic domains which thereby transmitted into transmembrane domain, shifting C384 residue to more hydrophobic environment.

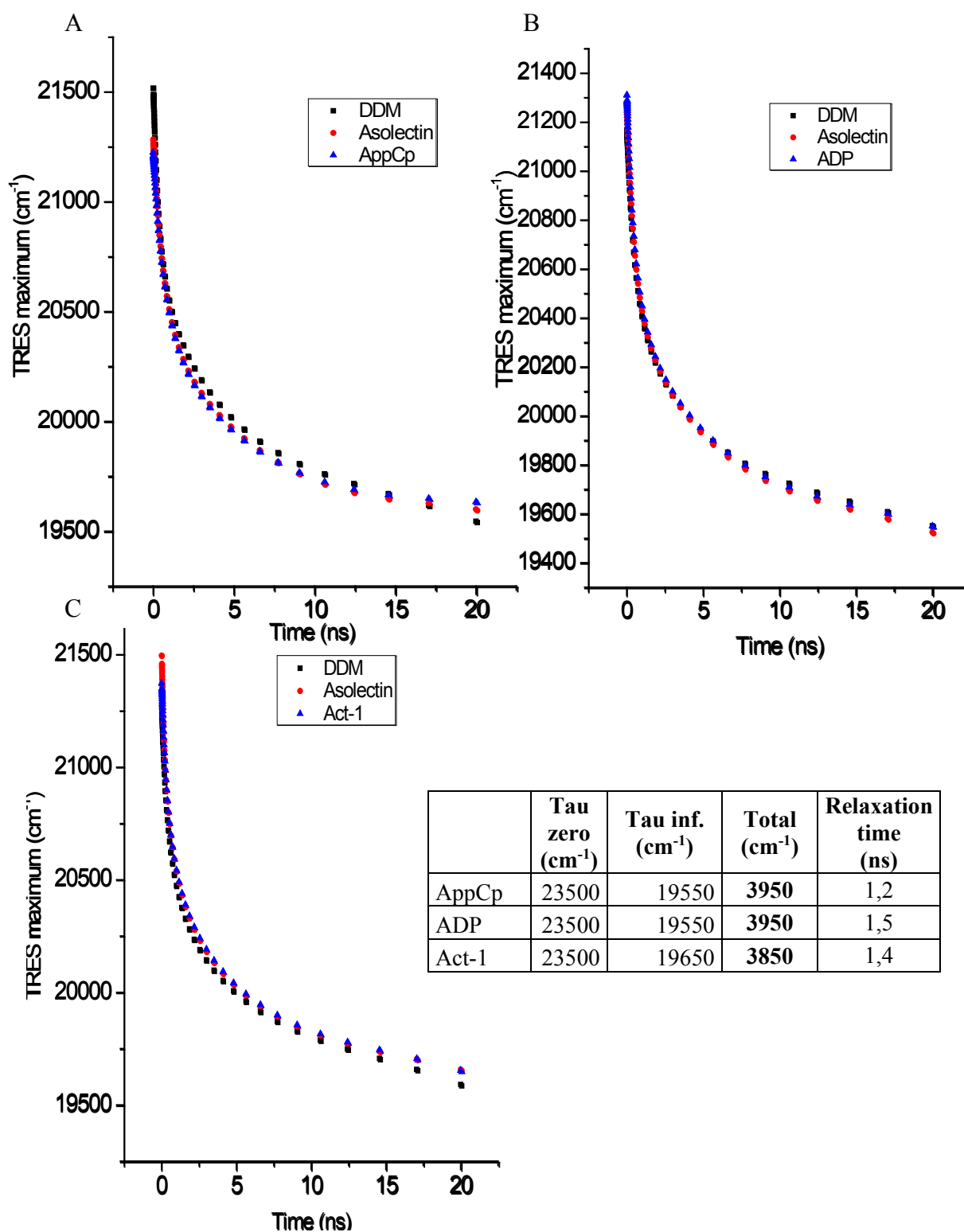


**Figure 7.17 TRES analysis of BADAN-labeled LpCopAΔHMBD with ligands in mixed micelles.**

In all measurements, 7 μM LpCopAΔHMBD was measured first in 0.3% DDM detergent solution, and then followed by addition of 1 mM Asolectin lipid and lastly: A) 100 μM AppCp, B) 100 μM ADP or C) 100 μM peptide Act-1. The protein dissolved in 50 mM HEPES pH 7.5, 150 mM Na<sub>2</sub>SO<sub>4</sub>, 5 mM MgSO<sub>4</sub> and 0.3% DDM. The legends in each panel (top to bottom) show the measurements in the order.

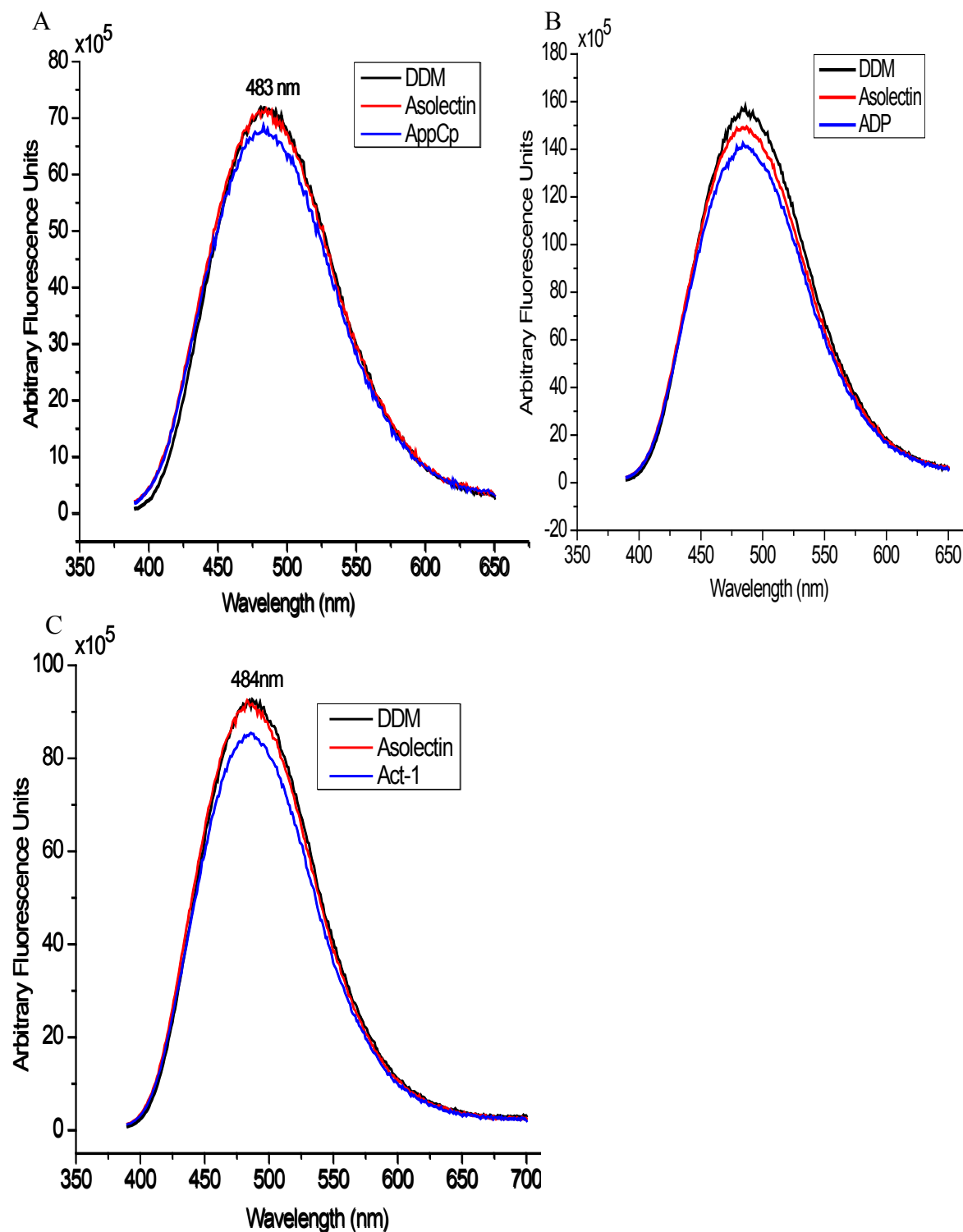


**Figure 7.18** Fluorescence emission spectra of BADAN-labeled LpCopA $\Delta$ HMBD in mixed micelles.

The spectra are according to the measurements in Fig. 7.17. The ligands **A)** 100  $\mu$ M AppNp nucleotide, **B)** 100  $\mu$ M ADP or **C)** 100  $\mu$ M peptide Act-1 was added to 7  $\mu$ M protein in buffer containing 0.3% DDM.

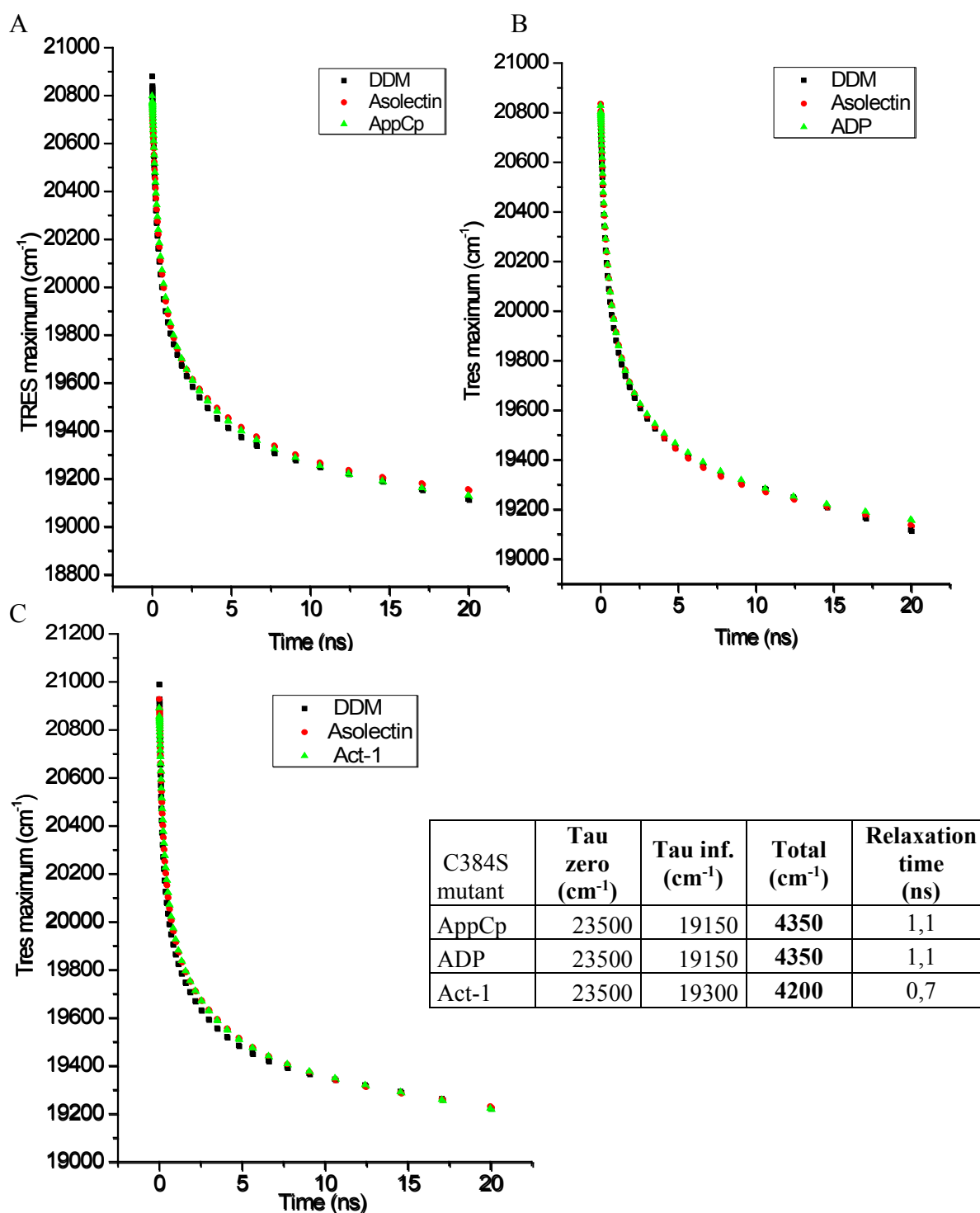


**Figure 7.19 TRES analysis of BADAN-labeled C384S mutant with ligands in mixed micelles.**

In all measurements, 7  $\mu\text{M}$  C384S mutant was measured first in 0.3% DDM detergent solution, and then followed by addition of 1 mM Asolectin lipid and lastly: **A)** 100  $\mu\text{M}$  AppCp, **B)** 100  $\mu\text{M}$  ADP or **C)** 100  $\mu\text{M}$  peptide Act-1. The protein dissolved in 50 mM HEPES pH 7.5, 150 mM Na<sub>2</sub>SO<sub>4</sub>, 5mM MgSO<sub>4</sub> and 0.3% DDM. The legends in each panel (top to bottom) show the measurements in the order.

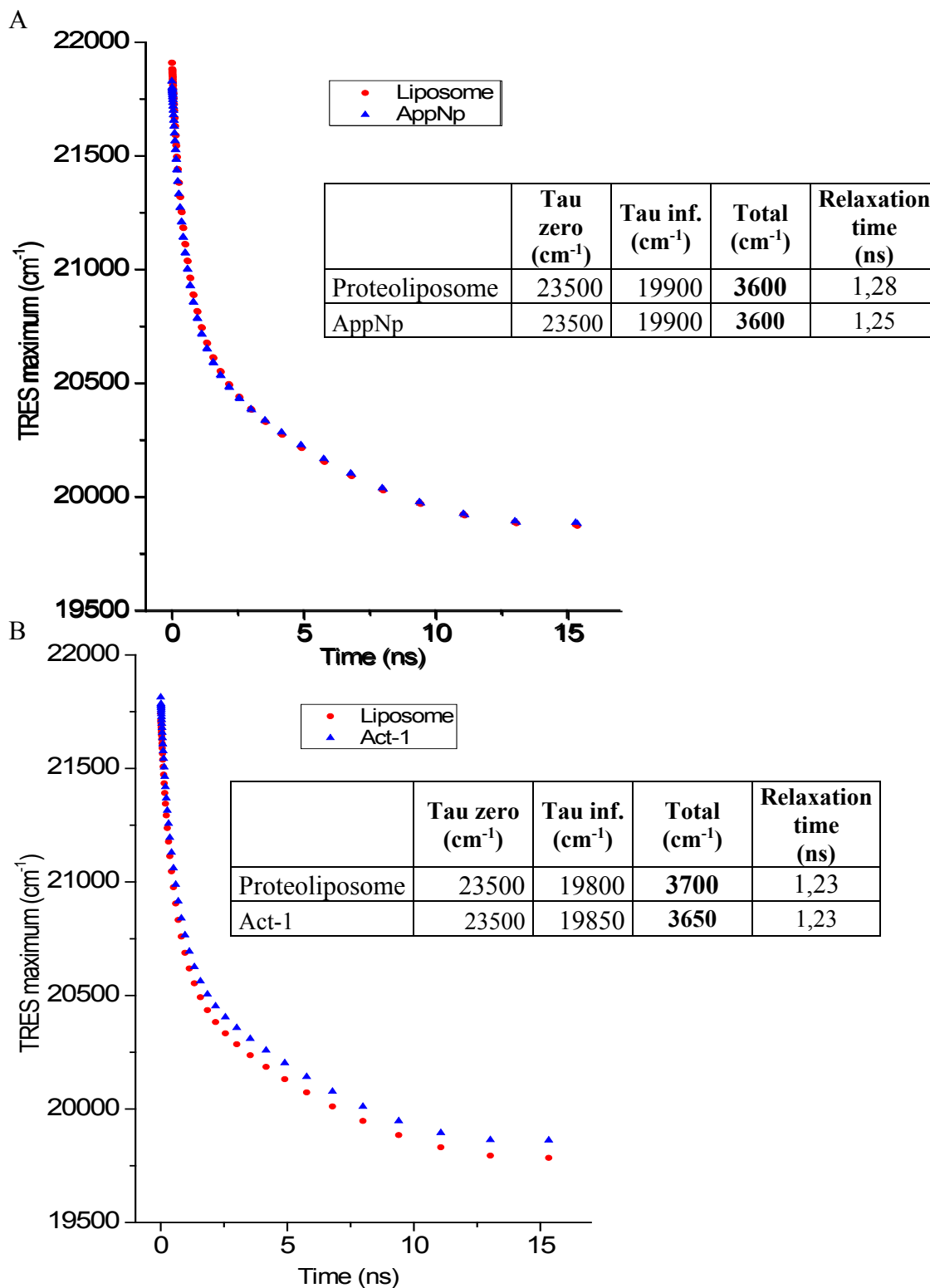


**Figure 7.20 TRES analysis of lipid reconstituted BADAN-labeled LpCopA $\Delta$ HMBD with ligands.**

In all measurements, 1  $\mu$ M reconstituted BADAN-labeled LpCopA $\Delta$ HMBD was measured in 50 mM HEPES pH 7.5, 150 mM Na<sub>2</sub>SO<sub>4</sub>, 5mM MgSO<sub>4</sub>. In function of ligand, **A**) 100  $\mu$ M AppNp nucleotide or **B**) 100  $\mu$ M Act-1 was added to the reconstituted protein. The buffer is 50 mM HEPES pH 7.5, 150 mM Na<sub>2</sub>SO<sub>4</sub>, 5mM MgSO<sub>4</sub>.



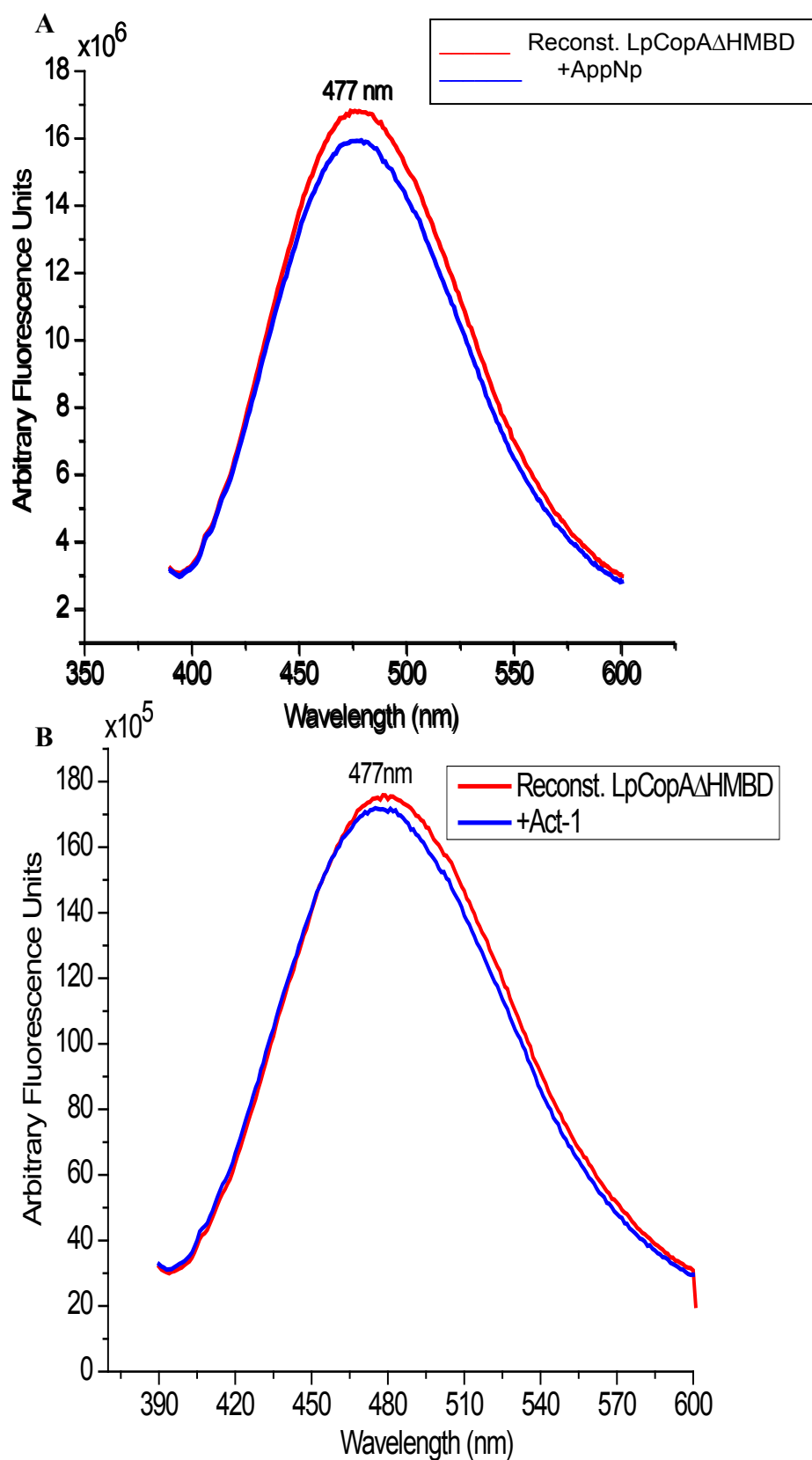


**Figure 7.21** Fluorescence emission spectra of BADAN-labeled LpCopA $\Delta$ HMBD in liposomes.

The spectra are according to the measurements in Fig 7.20. The ligands A) 100  $\mu$ M AppNp nucleotide or B) 100  $\mu$ M peptide Act-1 was added to 1  $\mu$ M reconstituted protein.

## Summary and discussion

The study of water distributions in the transmembrane domain of LpCopA improves our understanding to the entry/exit ion pathway. Therefore, the water accessibility and mobility of the transmembrane metal binding site (TM-MBS) was investigated by measuring the changes in the time-dependent Stokes shift of BADAN specifically labeled the thiol residues of C382PC384 and C382PS384 motif in LpCopA $\Delta$ HMBD and C384S mutant, respectively. The measurements were performed using Time Correlated Single Photon Counting (TCSPC) in collaboration with Prof. Martin Hof. BADAN, a fluorescent environment-sensitive dye, labeled the proteins in innovative method in which the protein was labeled during binding to the Ni-NTA column to facilitate removing of the excess unreacted dye. We postulate that BADAN entered to the TM-MBS through the cytosolic side of LpCopA $\Delta$ HMBD, labeling the C384 residue which, in turn, blocked the labeling of C382 residue as shown in Fig 7.22. This hypothesis is based on the close similarity between the emission spectra of BADAN-labeled LpCopA $\Delta$ HMBD and BADAN-labeled C382S mutant prepared in a parallel project in our lab (where the C384 is only labeled). The BADAN-labeled proteins were dissolved in buffer containing sulfate anion which behaves as phosphate analog assigning the protein to *E2~P*-like state according to our data (see Chapter 4) and other studies [72, 133].

The analysis of the time-resolved emission spectra (TRES) with either preferential labeling of C384 or exclusive labeling at C382 shows a slower Stokes shift for the labeling at position 384 than position 382. This indicates that C384 residue is highly exposed to hydrophobic environment more than C382 residue in the *E2~P*-like conformation in agreement with the recent MD simulation study of LpCopA [100]; this MD simulation study concluded that the luminal ion gate is open in *E2P* or *E2~P* states to extracellular side, allowing the water molecules penetrate TM domain to reach as far as the metal-binding site [100]. Moreover, the impact of membrane lipid and ligands on the solvent accessibility of the CPC motif were also studied. The reconstitution of LpCopA $\Delta$ HMBD in lipid bilayer caused more decay of the TRES than in detergent micelles, indicating on the insertion of C384 residue in more hydrophobic environment; this decay was slightly increased in presence of the peptide Act-1 (Fig. 7.20). This latter observation emphasizes the influence of the actuator-derived peptide on the structural conformation of transmembrane domain of LpCopA.

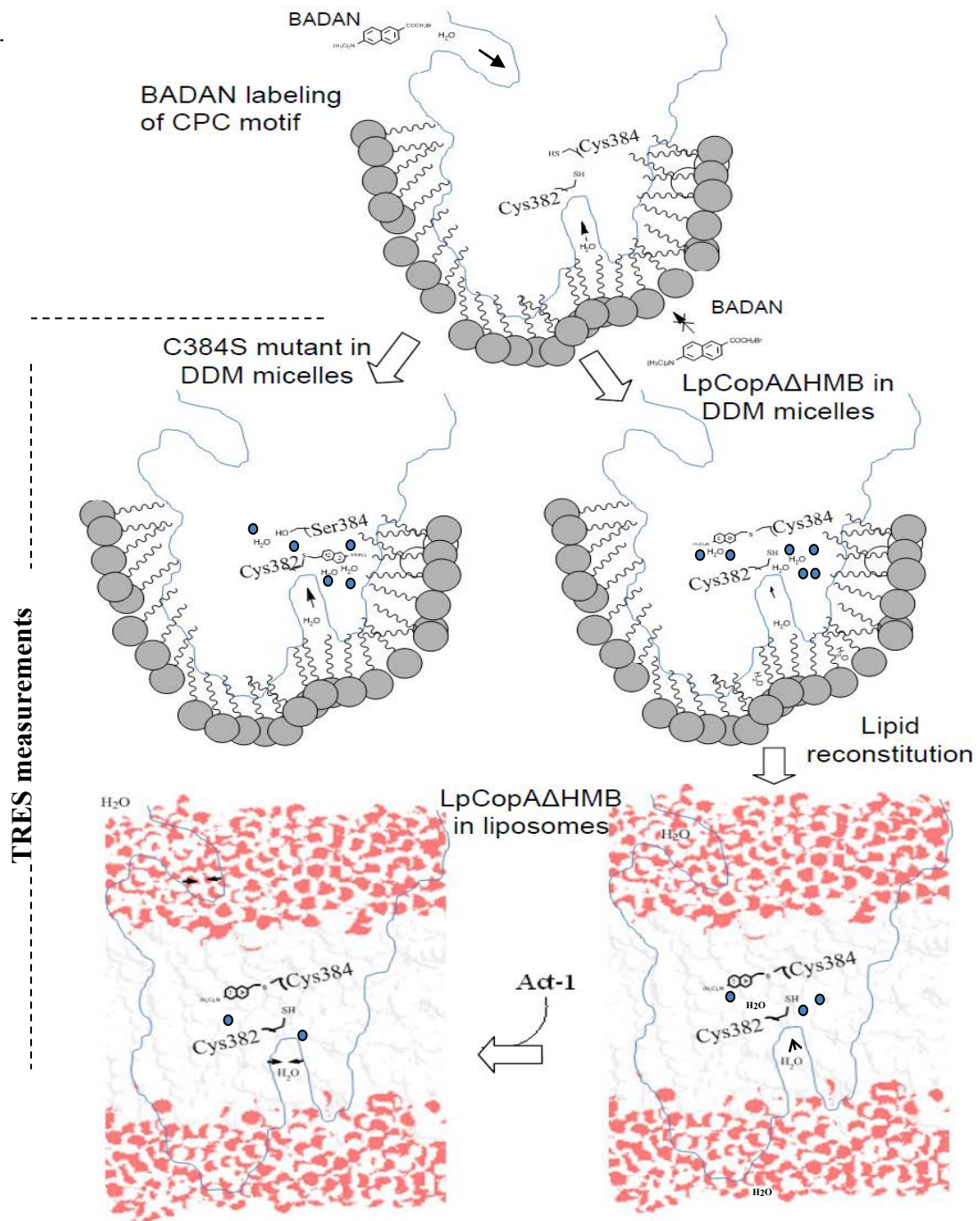


**Figure 7.22. Schematic diagram illustrates the putative BADAN labeling mechanism of the CPC motif and its environments impact on the water distributions.**

BADAN enters to the TM-MBS through the cytosolic side, labeling C384 of LpCopA $\Delta$ HMBD and C382 of the C384S mutant in *E2~P* like conformation. The C384 residue is exposed to more hydrophobic environment (less water; blue circles) than C382 residue. Embedding LpCopA $\Delta$ HMBD into the lipid bilayer lowers the water molecules distribution in TM domain. Addition of peptide Act-1 induces conformational changes, moving the C384 residue in more hydrophobic environment, probably by closing the ion gate.

## Chapter 8 Conclusion and outlook

P-type ATPases comprise a big family of homologous enzymes which are involved in transporting a wide variety of ions across cell membranes using ATP hydrolysis as an energy source. The Cu(I)-transporting ATPase (CopA), the most widespread among P<sub>1B</sub>-type ATPases, has received considerable attention during recent years from several groups, because the defect in the human copper-translocating membrane proteins ATP7A and ATP7B is the direct cause of the severe Menkes' and Wilson's diseases, respectively. *Legionella pneumophila* CopA (LpCopA) is one such ATPase shown to transport selectively Cu (I). In 2011, The crystal structure of LpCopA was solved in a transition state of dephosphorylation (*E*<sub>2</sub>~P state) in the copper-free state [32].

Here, the recombinant LpCopA and its expressed cytosolic domains were used as model for P<sub>1B</sub>-ATPases to investigate the interaction between its cytosolic domains. They are organized as functional modules that rearrange upon ATP binding, hydrolysis and phosphorylation, thereby inducing the conformational changes in the transmembrane domain that lead to metal transport. The data presented here have revealed a strong Cu<sup>+</sup>-dependent binding between the N-terminal heavy metal binding domain (HMBD) and the actuator domain (A-domain) in their isolated state in solution. In agreement with previous studies of Hatori et al. [74, 150] on another, we postulate that the A-domain interaction with the Cu<sup>+</sup>-loaded HMBD is required for forming a catalytically compact headpiece with other cytosolic domains for launching the catalytic turnover and copper transport. This result suggests that in the presence of copper, i.e., during catalytic turnover, this interaction could be crucial in positioning the A-domain relative to the phosphorylation and nucleotide-binding domain (PN-domain), thereby opening or closing the ATP-binding site at the PN-A interface. The data, can thus explain an autoinhibitory action of the HMBD in LpCopA [47]. Since the truncation of the HMBD, however, also abolishes ATP hydrolysis, it is very likely that the HMBD-A association is transiently formed and broken as a part of the catalytic cycling through structural intermediates and not only in an initial de-inhibition step. Our spectroscopic and biochemical data on Cu<sup>+</sup>-binding to the HMBD-A complex thus imply that the HMBD would not be constantly copper-loaded. Instead, it may participate directly in turnover by mediating Cu<sup>+</sup>-transfer to the transmembrane transport sites. In this view,

the HMBD is a copper sensor (autoinhibition in the absence of copper) and a chaperon-like cytosolic domain involved in both induction of conformational changes (A-domain binding) and copper transfer (transient copper binding and release).

In the full length LpCopA the cytosolic domain interactions lead to transmembrane helix rearrangements. The opening and closing of the PN-A interface, which is proposed here to be HMBD- and copper-dependent, is a central step in the catalytic cycle and experiments were designed how this opening may affect the solvent accessibility at the copper entry near the conserved transmembrane copper-binding CPC-motif. Combining peptide synthesis, site-directed mutagenesis, site-specific fluorescent labeling and time-resolved fluorescence spectroscopy, it could be shown here that the blockage of the PN-A interface by a peptide mimetic leads to the reduction of the water accessibility to the protein interior. The peptide interference further leads to the expected reduction of catalytic turnover measured by ATPase assays that were specifically modified in this study. Taken together with the copper-dependent HMBD-A interactions, the data are consistent with an initial cytosolic copper loading step at the HMBD, followed by its association with the A-domain which then leads to a “closure” of the entry site from the bulk water phase. This hydrophobization of the copper entry site may be a crucial step in shielding  $\text{Cu}^+$ -CPC-motif from the cytosolic side such that it will not react back (putatively to the HMBD from which it was released to the transmembrane domain) but move to the next transmembrane copper-binding site of the catalytic cycle.

A model that is consistent with the data, although not fully proven, is shown in the Fig. 8.1. It emphasizes the chaperone-like function of the HMBD and rationalizes the occlusion of the copper entry site from the solvent in preparing for the intramolecular copper transfer from the HMBD to the conserved transmembrane CPC-motif.

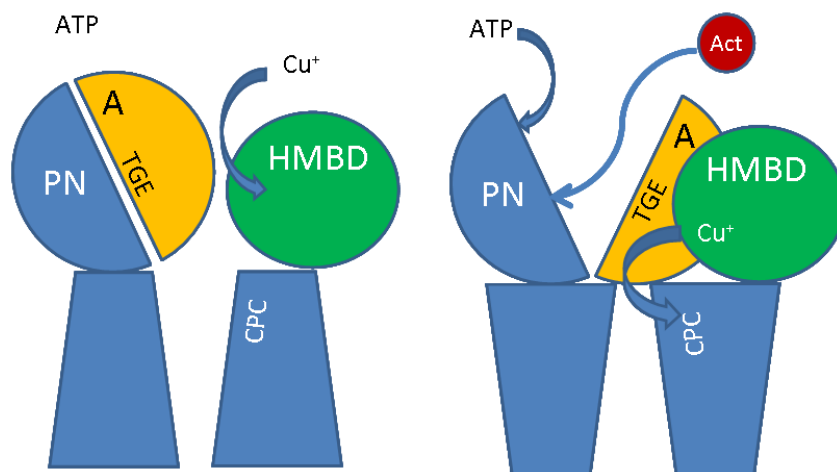


**Figure 8.1. Model of cytosolic domain interactions and their influence on membrane domain accessibility for copper and solvent**

The model emphasizes the proposed Copper chaperone-like function of the HMBD and its copper-dependent association with the A-domain demonstrated in this study.

**Left panel** (autoinhibited state): No HMBD-A interaction, ATP-binding site inaccessible, CPC motif with high solvent accessibility.

**Right panel** (copper-activated state): HMBD-A association, opening of the ATP-binding site, shielding of the CPC-motif from solvent, copper-transfer from the HMBD to CPC-motif in the occludes state of the entry to the transmembrane domain. The interaction site on the PN-domain of an A-domain-derived synthetic peptide (Act), carrying the conserved TGE motif, is shown and blocks the closure of the PN-A interface and occludes the copper entry site near the CPC motif (even in the absence of the HMBD as shown in this study by time-resolved fluorescence spectroscopy). A: actuator domain, PN: phosphorylation and nucleotide-binding domain, HMBD: N-terminal heavy metal-binding domain, Act: synthetic peptide derived from the TGE-carrying conserved sequence in the A domain involved in dephosphorylation of the PN-domain.

On another hand, it has been recently concluded from molecular dynamics (MD) simulations that extracellular water molecules have access to the TM-MBS of LpCopA in *E2*-P (as well as *E2*P state) suggesting a unique  $\text{Cu}^+$  release mechanism that does not require the fully occluded state of the transported ion and is thus distinct from that of SERCA [34]. Here, we presented the first experimental evidence on a luminal-open conformation of *E2*~P state of a hydration gradient along the TM-MBS of LpCopA applying Time Correlated Single Photon Counting (TCSPC) to site-specifically fluorescently labeled LpCopA (collaboration with Prof. Martin Hof). The technique observes the changes in the Stokes shift of the fluorophore bound to one of the

conserved transmembrane cysteines in LpCopA which allows deducing the reorientation of dipole moments of neighboring water molecules after excitation. The LpCopA $\Delta$ HMBD, with native C382PC384 sequence and mutated C382PS384 sequence (C384S mutant), is labeled with thiol-reactive BADAN, a Fluorescent environment-sensitive dye, using innovative labeling method in which the protein was labeled during binding to the Ni-NTA column to facilitate removing of the excess unreacted dye. The analysis of the time dependent Stokes shift (TDSS) with either preferential labeling of C384 or exclusive labeling at C382 in sulfate buffer shows a slower Stoke shift for the labeling at position 384 than position 382. Thus the more cytosolic cysteine resides nevertheless in a more hydrophobic environment than the more membrane inserted cysteine 382. Considering the sulfate a phosphate analog occupying the phosphorylation site of the P-domain in *E2-P* state [72, 133], the TCSPC data indicate that C384 residue is highly exposed to hydrophobic environment more than C382 residue in the *E2-P*-like conformation. This supports the existence of a hydrated cavity in the transmembrane part of the ATPase, consistent with the MD simulation [34].

In the light of these data, we also examined the effect of membrane lipid, detergent and cytosolic ligands on the intraprotein water at the TM-MBS. The lipidic phase surrounding LpCopA $\Delta$ HMBD reduced the water penetration to C384 residue as compared to the detergent micelle system, while cytosolic ligands did not induce remarkable changes in the TDSS of LpCopA $\Delta$ HMBD and the C384S mutant. As a future plan, we would study the interaction of HMBD and A-domain within the entire LpCopA structure using mutagenesis and labeling methods. In combination with TCSPC more specific questions can be addressed, such as the effect of lipid composition on water accessibility of the transmembrane domains.

---

## References

1. Palmer, T. and P.L. Bonner, *Enzymes: Biochemistry, Biotechnology, Clinical Chemistry*. 2007: Elsevier Science.
2. Fraga, C.G., *Relevance, essentiality and toxicity of trace elements in human health*. Mol Aspects Med, 2005. **26**(4-5): p. 235-44.
3. Solioz, M., et al., *Response of gram-positive bacteria to copper stress*. J Biol Inorg Chem, 2010. **15**(1): p. 3-14.
4. Rensing, C. and G. Grass, *Escherichia coli mechanisms of copper homeostasis in a changing environment*. FEMS Microbiol Rev, 2003. **27**(2-3): p. 197-213.
5. da Silva, J.J.R.F. and R.J.P. Williams, *The Biological Chemistry of the Elements: The Inorganic Chemistry of Life*. 2001: OUP Oxford.
6. Roat-Malone, R.M., *Bioinorganic Chemistry: A Short Course*. 2007: Wiley.
7. Kidd, S.P., *Stress Response in Pathogenic Bacteria*. 2011: CABI.
8. Permyakov, E., *Metalloproteomics*. 2009: Wiley.
9. Turski, M.L. and D.J. Thiele, *New roles for copper metabolism in cell proliferation, signaling, and disease*. J Biol Chem, 2009. **284**(2): p. 717-21.
10. Leone, A. and J.F.B. Mercer, *Copper Transport and Its Disorders: Molecular and Cellular Aspects ; [proceedings of a Satellite Meeting of the European Human Genetic Society on Copper Transport and Its Disorders: Molecular and Cellular Aspects, Held May 21 - 25, 1997, in Sestri Levante, Italy]*. 1999: Springer US.
11. Lee, J., J.R. Prohaska, and D.J. Thiele, *Essential role for mammalian copper transporter *Ctr1* in copper homeostasis and embryonic development*. Proc Natl Acad Sci U S A, 2001. **98**(12): p. 6842-7.
12. Simpson, J.A., et al., *Free-radical generation by copper ions and hydrogen peroxide. Stimulation by Hepes buffer*. Biochem. J, 1988. **254**: p. 519-523.
13. Rensing, C. and G. Grass, *Escherichia coli mechanisms of copper homeostasis in a changing environment*. FEMS microbiology reviews, 2003. **27**(2 - 3): p. 197-213.
14. Nies, D.H. and S. Silver, *Molecular Microbiology of Heavy Metals*. 2007: Springer.
15. Field, L.S., E. Luk, and V.C. Culotta, *Copper chaperones: personal escorts for metal ions*. J Bioenerg Biomembr, 2002. **34**(5): p. 373-9.
16. Osman, D. and J.S. Cavet, *Chapter 8 - Copper Homeostasis in Bacteria*, in *Advances in Applied Microbiology*, S.S. Allen I. Laskin and M.G. Geoffrey, Editors. 2008, Academic Press. p. 217-247.
17. Kim, E.-H., et al., *Switch or funnel: how RND-type transport systems control periplasmic metal homeostasis*. Journal of bacteriology, 2011. **193**(10): p. 2381-2387.
18. Krick, M.H. and C.T. Dameron, *Copper I transfer between *Enterococcus hirae* *CopA*, *CopZ* and *CopY* in vitro*. Journal of Biotech Research [ISSN: 1944-3285], 2013. **5**: p. 1-8.
19. Chaturvedi, K.S. and J.P. Henderson, *Pathogenic adaptations to host-derived antibacterial copper*. Frontiers in cellular and infection microbiology, 2014. **4**.
20. Prasad, N.V., *Metals in the Environment: Analysis by Biodiversity*. 2001: Taylor & Francis.



21. Mandal, A.K., W.D. Cheung, and J.M. Arguello, *Characterization of a thermophilic P-type Ag<sup>+</sup>/Cu<sup>+</sup>-ATPase from the extremophile Archaeoglobus fulgidus*. J Biol Chem, 2002. **277**(9): p. 7201-8.
22. Kuhlbrandt, W., *Biology, structure and mechanism of P-type ATPases*. Nat Rev Mol Cell Biol, 2004. **5**(4): p. 282-95.
23. Axelsen, K.B. and M.G. Palmgren, *Evolution of substrate specificities in the P-type ATPase superfamily*. J Mol Evol, 1998. **46**(1): p. 84-101.
24. Arguello, J.M., E. Eren, and M. Gonzalez-Guerrero, *The structure and function of heavy metal transport PIB-ATPases*. Biometals, 2007. **20**(3-4): p. 233-48.
25. Odermatt, A., et al., *Primary structure of two P-type ATPases involved in copper homeostasis in Enterococcus hirae*. J Biol Chem, 1993. **268**(17): p. 12775-9.
26. Bissig, K.D., T.C. Voegelin, and M. Solioz, *Tetrathiomolybdate inhibition of the Enterococcus hirae CopB copper ATPase*. FEBS Lett, 2001. **507**(3): p. 367-70.
27. Inesi, G., *Calcium and copper transport ATPases: analogies and diversities in transduction and signaling mechanisms*. J Cell Commun Signal, 2011. **5**(3): p. 227-37.
28. Mana-Capelli, S., A.K. Mandal, and J.M. Arguello, *Archaeoglobus fulgidus CopB is a thermophilic Cu<sup>2+</sup>-ATPase: functional role of its histidine-rich-N-terminal metal binding domain*. J Biol Chem, 2003. **278**(42): p. 40534-41.
29. Solioz, M. and C. Vulpe, *CPx-type ATPases: a class of P-type ATPases that pump heavy metals*. Trends Biochem Sci, 1996. **21**(7): p. 237-41.
30. Mattle, D., et al., *On allosteric modulation of P-type Cu(+)-ATPases*. J Mol Biol, 2013. **425**(13): p. 2299-308.
31. Guerra, G., et al., *Role of transmembrane segment M8 in the biogenesis and function of yeast plasma-membrane H(+)-ATPase*. Biochim Biophys Acta, 2007. **1768**(10): p. 2383-92.
32. Gourdon, P., et al., *Crystal structure of a copper-transporting PIB-type ATPase*. Nature, 2011. **475**(7354): p. 59-64.
33. Bissig, K., et al., *Structure-function analysis of purified Enterococcus hirae CopB copper ATPase: effect of Menkes/Wilson disease mutation homologues*. Biochem. J, 2001. **357**: p. 217-223.
34. Andersson, M., et al., *Copper-transporting P-type ATPases use a unique ion-release pathway*. Nature structural & molecular biology, 2013.
35. Allen, G.S., et al., *The architecture of CopA from Archaeoglobus fulgidus studied by cryo-electron microscopy and computational docking*. Structure, 2011. **19**(9): p. 1219-1232.
36. Wang, K., et al., *Structure and mechanism of Zn<sup>2+</sup>-transporting P-type ATPases*. Nature, 2014.
37. Gourdon, P., et al., *Structural models of the human copper P-type ATPases ATP7A and ATP7B*. Biol Chem, 2012. **393**(4): p. 205-16.
38. Fu, D., T.J. Beeler, and T.M. Dunn, *Sequence, mapping and disruption of CCC2, a gene that cross-complements the Ca(2+)-sensitive phenotype of csg1 mutants and encodes a P-type ATPase belonging to the Cu(2+)-ATPase subfamily*. Yeast, 1995. **11**(3): p. 283-92.
39. Tabata, K., et al., *Cloning of a cDNA encoding a putative metal-transporting P-type ATPase from Arabidopsis thaliana*. Biochim Biophys Acta, 1997. **1326**(1): p. 1-6.
40. Sambongi, Y., et al., *Caenorhabditis elegans cDNA for a Menkes/Wilson disease gene homologue and its function in a yeast CCC2 gene deletion mutant*. J Biochem, 1997. **121**(6): p. 1169-75.

41. Adams, M.D., et al., *The genome sequence of Drosophila melanogaster*. Science, 2000. **287**(5461): p. 2185-95.
42. Wu, J., et al., *The LEC rat has a deletion in the copper transporting ATPase gene homologous to the Wilson disease gene*. Nat Genet, 1994. **7**(4): p. 541-5.
43. Vulpe, C., et al., *Isolation of a candidate gene for Menkes disease and evidence that it encodes a copper-transporting ATPase*. Nat Genet, 1993. **3**(1): p. 7-13.
44. Tanzi, R.E., et al., *The Wilson disease gene is a copper transporting ATPase with homology to the Menkes disease gene*. Nat Genet, 1993. **5**(4): p. 344-50.
45. Okkeri, J. and T. Haltia, *The metal-binding sites of the zinc-transporting P-type ATPase of Escherichia coli. Lys693 and Asp714 in the seventh and eighth transmembrane segments of ZntA contribute to the coupling of metal binding and ATPase activity*. Biochim Biophys Acta, 2006. **1757**(11): p. 1485-95.
46. Bal, N., et al., *A possible regulatory role for the metal-binding domain of CadA, the Listeria monocytogenes Cd<sup>2+</sup>-ATPase*. FEBS Lett, 2001. **506**(3): p. 249-52.
47. Wu, C.C., W.J. Rice, and D.L. Stokes, *Structure of a copper pump suggests a regulatory role for its metal-binding domain*. Structure, 2008. **16**(6): p. 976-85.
48. Markossian, K.A. and B.I. Kurganov, *Copper chaperones, intracellular copper trafficking proteins. Function, structure, and mechanism of action*. Biochemistry (Mosc), 2003. **68**(8): p. 827-37.
49. Harrison, M.D., et al., *Intracellular copper routing: the role of copper chaperones*. Trends Biochem Sci, 2000. **25**(1): p. 29-32.
50. Schreiter, E.R., et al., *Crystal structure of the nickel-responsive transcription factor NikR*. Nat Struct Biol, 2003. **10**(10): p. 794-9.
51. Rosenzweig, A.C. and T.V. O'Halloran, *Structure and chemistry of the copper chaperone proteins*. Curr Opin Chem Biol, 2000. **4**(2): p. 140-7.
52. Rosenzweig, A.C., et al., *Crystal structure of the Atx1 metallochaperone protein at 1.02 Å resolution*. Structure, 1999. **7**(6): p. 605-17.
53. Palumaa, P., *Copper chaperones. The concept of conformational control in the metabolism of copper*. FEBS Lett, 2013. **587**(13): p. 1902-10.
54. Lu, Z.H., C.T. Dameron, and M. Solioz, *The Enterococcus hirae paradigm of copper homeostasis: copper chaperone turnover, interactions, and transactions*. Biometals, 2003. **16**(1): p. 137-43.
55. Agarwal, S., et al., *Structure and interactions of the C-terminal metal binding domain of Archaeoglobus fulgidus CopA*. Proteins, 2010. **78**(11): p. 2450-8.
56. Banci, L., et al., *Solution structure of the N-terminal domain of a potential copper-translocating P-type ATPase from Bacillus subtilis in the apo and Cu(I) loaded states*. J Mol Biol, 2002. **317**(3): p. 415-29.
57. Wernimont, A.K., et al., *Structural basis for copper transfer by the metallochaperone for the Menkes/Wilson disease proteins*. Nat Struct Biol, 2000. **7**(9): p. 766-71.
58. Gajewski, E., D.K. Steckler, and R.N. Goldberg, *Thermodynamics of the hydrolysis of adenosine 5'-triphosphate to adenosine 5'-diphosphate*. J Biol Chem, 1986. **261**(27): p. 12733-7.
59. Widdas, W.F., *A reconsideration of the link between the energetics of water and of ATP hydrolysis energy in the power strokes of molecular motors in protein structures*. Int J Mol Sci, 2008. **9**(9): p. 1730-52.
60. Contributors, W., *Human Physiology*. Blackscleet River.
61. Tsivkovskii, R., R.G. Efremov, and S. Lutsenko, *The role of the invariant His-1069 in folding and function of the Wilson's disease protein, the human copper-transporting ATPase ATP7B*. J Biol Chem, 2003. **278**(15): p. 13302-8.

62. Voskoboinik, I., J. Mar, and J. Camakaris, *Mutational analysis of the Menkes copper P-type ATPase (ATP7A)*. *Biochem Biophys Res Commun*, 2003. **301**(2): p. 488-94.
63. Gonzalez-Guerrero, M., D. Hong, and J.M. Arguello, *Chaperone-mediated Cu<sup>+</sup> delivery to Cu<sup>+</sup> transport ATPases: requirement of nucleotide binding*. *J Biol Chem*, 2009. **284**(31): p. 20804-11.
64. Tsivkovskii, R., B.C. MacArthur, and S. Lutsenko, *The Lys1010-Lys1325 fragment of the Wilson's disease protein binds nucleotides and interacts with the N-terminal domain of this protein in a copper-dependent manner*. *J Biol Chem*, 2001. **276**(3): p. 2234-42.
65. Zheng, J., et al., *Crystal structure of the catalytic subunit of cAMP-dependent protein kinase complexed with MgATP and peptide inhibitor*. *Biochemistry*, 1993. **32**(9): p. 2154-61.
66. Okkeri, J., L. Laakkonen, and T. Haltia, *The nucleotide-binding domain of the Zn<sup>2+</sup>-transporting P-type ATPase from Escherichia coli carries a glycine motif that may be involved in binding of ATP*. *Biochem J*, 2004. **377**(Pt 1): p. 95-105.
67. Wang, W., et al., *Structural characterization of the reaction pathway in phosphoserine phosphatase: crystallographic "snapshots" of intermediate states*. *J Mol Biol*, 2002. **319**(2): p. 421-31.
68. Aravind, L., M.Y. Galperin, and E.V. Koonin, *The catalytic domain of the P-type ATPase has the haloacid dehalogenase fold*. *Trends Biochem Sci*, 1998. **23**(4): p. 127-9.
69. Moller, J.V., et al., *The sarcoplasmic Ca<sup>2+</sup>-ATPase: design of a perfect chemi-osmotic pump*. *Q Rev Biophys*, 2010. **43**(4): p. 501-66.
70. Zoltner, M., *Structural and Functional Characterization of Prokaryotic CPX-ATPases: Evidence for a Novel Cobalt Exporting P-type ATPase: Strukturelle und Funktionelle Charakterisierung Von Prokaryotischen CPx-ATPasen: Beweis Für Eine Neuartige Kobalt Exportierende P-Type ATPase*, 2007.
71. Olesen, C., et al., *Dephosphorylation of the calcium pump coupled to counterion occlusion*. *Science*, 2004. **306**(5705): p. 2251-5.
72. Toyoshima, C., et al., *Crystal structures of the calcium pump and sarcolipin in the Mg<sup>2+</sup>-bound E1 state*. *Nature*, 2013. **495**(7440): p. 260-4.
73. Clausen, J.D., et al., *Critical interaction of actuator domain residues arginine 174, isoleucine 188, and lysine 205 with modulatory nucleotide in sarcoplasmic reticulum Ca<sup>2+</sup>-ATPase*. *J Biol Chem*, 2008. **283**(51): p. 35703-14.
74. Hatori, Y., et al., *Domain organization and movements in heavy metal ion pumps: papain digestion of CopA, a Cu<sup>+</sup>-transporting ATPase*. *J Biol Chem*, 2007. **282**(35): p. 25213-21.
75. Fu, Y., et al., *A new structural paradigm in copper resistance in Streptococcus pneumoniae*. *Nat Chem Biol*, 2013. **9**(3): p. 177-83.
76. Daiho, T., et al., *Stable structural analog of Ca<sup>2+</sup>-ATPase ADP-insensitive phosphoenzyme with occluded Ca<sup>2+</sup> formed by elongation of A-domain/M1'-linker and beryllium fluoride binding*. *J Biol Chem*, 2010. **285**(32): p. 24538-47.
77. Pedersen, B.P., et al., *Crystal structure of the plasma membrane proton pump*. *Nature*, 2007. **450**(7172): p. 1111-4.
78. Crichton, R., *Biological Inorganic Chemistry: A New Introduction to Molecular Structure and Function*. 2012: Elsevier Science.
79. Toyoshima, C. and G. Inesi, *Structural basis of ion pumping by Ca<sup>2+</sup>-ATPase of the sarcoplasmic reticulum*. *Annu Rev Biochem*, 2004. **73**: p. 269-92.

80. Argüello, J., *Identification of ion-selectivity determinants in heavy-metal transport P1B-type ATPases*. The Journal of membrane biology, 2003. **195**(2): p. 93-108.
81. Okkeri, J., et al., *Introducing Wilson disease mutations into the zinc-transporting P-type ATPase of Escherichia coli. The mutation P634L in the 'hinge' motif (GDGXNDXP) perturbs the formation of the E2P state*. Eur J Biochem, 2002. **269**(5): p. 1579-86.
82. Arguello, J.M., M. Gonzalez-Guerrero, and D. Raimunda, *Bacterial transition metal P(1B)-ATPases: transport mechanism and roles in virulence*. Biochemistry, 2011. **50**(46): p. 9940-9.
83. Toyoshima, C., *How Ca<sup>2+</sup>-ATPase pumps ions across the sarcoplasmic reticulum membrane*. Biochim Biophys Acta, 2009. **1793**(6): p. 941-6.
84. Moller, J.V., et al., *Transport mechanism of the sarcoplasmic reticulum Ca<sup>2+</sup> -ATPase pump*. Curr Opin Struct Biol, 2005. **15**(4): p. 387-93.
85. Toyoshima, C., et al., *Trinitrophenyl derivatives bind differently from parent adenine nucleotides to Ca<sup>2+</sup>-ATPase in the absence of Ca<sup>2+</sup>*. Proc Natl Acad Sci U S A, 2011. **108**(5): p. 1833-8.
86. Olesen, C., et al., *The structural basis of calcium transport by the calcium pump*. Nature, 2007. **450**(7172): p. 1036-42.
87. Toyoshima, C., H. Nomura, and T. Tsuda, *Lumenal gating mechanism revealed in calcium pump crystal structures with phosphate analogues*. Nature, 2004. **432**(7015): p. 361-8.
88. Jensen, A.M., et al., *Modulatory and catalytic modes of ATP binding by the calcium pump*. EMBO J, 2006. **25**(11): p. 2305-14.
89. Clausen, J.D., et al., *Modulatory ATP binding affinity in intermediate states of E2P dephosphorylation of sarcoplasmic reticulum Ca<sup>2+</sup>-ATPase*. J Biol Chem, 2011. **286**(13): p. 11792-802.
90. Bublitz, M., J.P. Morth, and P. Nissen, *P-type ATPases at a glance*. J Cell Sci, 2011. **124**(Pt 15): p. 2515-9.
91. Vallejo, A.N., R.J. Pogulis, and L.R. Pease, *PCR Mutagenesis by Overlap Extension and Gene SOE*. CSH Protoc, 2008. **2008**: p. pdb prot4861.
92. Inoue, H., H. Nojima, and H. Okayama, *High efficiency transformation of Escherichia coli with plasmids*. Gene, 1990. **96**(1): p. 23-8.
93. Lanzetta, P.A., et al., *An improved assay for nanomole amounts of inorganic phosphate*. Anal Biochem, 1979. **100**(1): p. 95-7.
94. Geertsma, E.R., et al., *Membrane reconstitution of ABC transporters and assays of translocator function*. Nat Protoc, 2008. **3**(2): p. 256-66.
95. Laemmli, U.K., *Cleavage of structural proteins during the assembly of the head of bacteriophage T4*. Nature, 1970. **227**(5259): p. 680-5.
96. Bradford, M.M., *A rapid and sensitive method for the quantitation of microgram quantities of protein utilizing the principle of protein-dye binding*. Analytical biochemistry, 1976. **72**(1): p. 248-254.
97. Banik, U. and S. Roy, *A continuous fluorimetric assay for ATPase activity*. Biochem J, 1990. **266**(2): p. 611-4.
98. Stoychev, G., B. Kierdaszuk, and D. Shugar, *Interaction of Escherichia coli purine nucleoside phosphorylase (PNP) with the cationic and zwitterionic forms of the fluorescent substrate N(7)-methylguanosine*. Biochim Biophys Acta, 2001. **1544**(1-2): p. 74-88.
99. Brenner, A.J. and E.D. Harris, *A quantitative test for copper using bicinchoninic acid*. Anal Biochem, 1995. **226**(1): p. 80-4.

100. Andersson, M., et al., *Copper-transporting P-type ATPases use a unique ion-release pathway*. Nat Struct Mol Biol, 2014. **21**(1): p. 43-8.
101. Wimmer, R., et al., *NMR structure and metal interactions of the CopZ copper chaperone*. J Biol Chem, 1999. **274**(32): p. 22597-603.
102. Hearnshaw, S., et al., *A tetranuclear Cu(I) cluster in the metallochaperone protein CopZ*. Biochemistry, 2009. **48**(40): p. 9324-6.
103. Banci, L., et al., *X-ray absorption and NMR spectroscopic studies of CopZ, a copper chaperone in Bacillus subtilis: the coordination properties of the copper ion*. Biochemistry, 2003. **42**(8): p. 2467-74.
104. Urvoas, A., et al., *Metal-binding stoichiometry and selectivity of the copper chaperone CopZ from Enterococcus hirae*. Eur J Biochem, 2004. **271**(5): p. 993-1003.
105. Kihlken, M.A., A.P. Leech, and N.E. Le Brun, *Copper-mediated dimerization of CopZ, a predicted copper chaperone from Bacillus subtilis*. Biochem J, 2002. **368**(Pt 3): p. 729-39.
106. Gordon, E., et al., *Reprint of: Effective high-throughput overproduction of membrane proteins in Escherichia coli*. Protein Expr Purif, 2011.
107. Fan, J., et al., *An efficient strategy for high throughput screening of recombinant integral membrane protein expression and stability*. Protein Expr Purif, 2011. **78**(1): p. 6-13.
108. Filip, C., et al., *Solubilization of the cytoplasmic membrane of Escherichia coli by the ionic detergent sodium-lauryl sarcosinate*. J Bacteriol, 1973. **115**(3): p. 717-22.
109. Konings, W.N., H.R. Kaback, and J.S. Lolkema, *Transport Processes in Eukaryotic and Prokaryotic Organisms*. 1996: Elsevier Science.
110. Bodemer, G.J. and T.U.o.W.-. Milwaukee, *An Investigation of OmcA from Shewanella Oneidensis MR-1: Redox and Structural Characterization*. 2008: University of Wisconsin - Milwaukee.
111. Frankel, S., R. Sohn, and L. Leinwand, *The use of sarkosyl in generating soluble protein after bacterial expression*. Proc Natl Acad Sci U S A, 1991. **88**(4): p. 1192-6.
112. Schlager, B., A. Straessle, and E. Hafen, *Use of anionic denaturing detergents to purify insoluble proteins after overexpression*. BMC Biotechnol, 2012. **12**: p. 95.
113. Hewawasam, G.S. and U.o.K. Chemistry, *Studies on Interactions of Sarco/Endoplasmic Reticulum Calcium Ion-ATPase (SERCA) with Antiapoptotic Protein Bcl-2*. 2008: University of Kansas.
114. Fritz, M., et al., *An intermediate step in the evolution of ATPases: a hybrid F(0)-V(0) rotor in a bacterial Na(+) F(1)F(0) ATP synthase*. FEBS J, 2008. **275**(9): p. 1999-2007.
115. Ferguson, S.A., S. Keis, and G.M. Cook, *Biochemical and molecular characterization of a Na<sup>+</sup>-translocating F1Fo-ATPase from the thermoalkaliphilic bacterium Clostridium paradoxum*. J Bacteriol, 2006. **188**(14): p. 5045-54.
116. Sarin, J., et al., *B-subunit of phosphate-specific transporter from Mycobacterium tuberculosis is a thermostable ATPase*. J Biol Chem, 2001. **276**(48): p. 44590-7.
117. Rahman, S., et al., *Sarkosyl is a good regeneration reagent for studies on vacuolar-type ATPase subunit interactions in Biacore experiments*. Anal Biochem, 2011. **418**(2): p. 301-3.

118. Curtis-Fisk, J., R.M. Spencer, and D.P. Weliky, *Isotopically labeled expression in E. coli, purification, and refolding of the full ectodomain of the influenza virus membrane fusion protein*. *Protein Expr Purif*, 2008. **61**(2): p. 212-9.
119. Healthcare, G., *Purifying Challenging Proteins: Principles and Methods*. 2007: GE Healthcare.
120. Lorsch, J., *Laboratory Methods in Enzymology: Protein*. 2014: Elsevier Science.
121. Frosch, M. and M.C.J. Maiden, *Handbook of Meningococcal Disease: Infection Biology, Vaccination, Clinical Management*. 2008: Wiley.
122. Acton, Q.A., *Surface-Active Agents—Advances in Research and Application: 2012 Edition*. 2012: ScholarlyEditions.
123. Eshaghi, S., et al., *An efficient strategy for high-throughput expression screening of recombinant integral membrane proteins*. *Protein Sci*, 2005. **14**(3): p. 676-83.
124. Lund, S., et al., *Detergent structure and associated lipid as determinants in the stabilization of solubilized Ca<sup>2+</sup>-ATPase from sarcoplasmic reticulum*. *J Biol Chem*, 1989. **264**(9): p. 4907-15.
125. Deigweier, K., et al., *Expression, isolation, and crystallization of the catalytic domain of CopB, a putative copper transporting ATPase from the thermoacidophilic archaeon Sulfolobus solfataricus*. *J Bioenerg Biomembr*, 2004. **36**(1): p. 151-9.
126. Pratap, P.R., O. Dediu, and G.U. Nienhaus, *FTIR study of ATP-induced changes in Na<sup>+</sup>/K<sup>+</sup>-ATPase from duck supraorbital glands*. *Biophys J*, 2003. **85**(6): p. 3707-17.
127. Mukhopadhyay, S., M.S. Hasson, and D.A. Sanders, *A continuous assay of acetate kinase activity: measurement of inorganic phosphate release generated by hydroxylaminolysis of acetyl phosphate*. *Bioorg Chem*, 2008. **36**(2): p. 65-9.
128. Gupta, A. and S. Lutsenko, *Evolution of copper transporting ATPases in eukaryotic organisms*. *Curr Genomics*, 2012. **13**(2): p. 124-33.
129. Solioz, M. and A. Odermatt, *Copper and silver transport by CopB-ATPase in membrane vesicles of Enterococcus hirae*. *J Biol Chem*, 1995. **270**(16): p. 9217-21.
130. Futai, M., Y. Wada, and J.H. Kaplan, *Handbook of ATPases: Biochemistry, Cell Biology, Pathophysiology*. 2006: Wiley.
131. Puig, O., et al., *The tandem affinity purification (TAP) method: a general procedure of protein complex purification*. *Methods*, 2001. **24**(3): p. 218-29.
132. Lutsenko, S., et al., *N-terminal domains of human copper-transporting adenosine triphosphatases (the Wilson's and Menkes disease proteins) bind copper selectively in vivo and in vitro with stoichiometry of one copper per metal-binding repeat*. *Journal of Biological Chemistry*, 1997. **272**(30): p. 18939-18944.
133. Lubben, M., et al., *Sulfate acts as phosphate analog on the monomeric catalytic fragment of the CPx-ATPase CopB from Sulfolobus solfataricus*. *J Mol Biol*, 2007. **369**(2): p. 368-85.
134. Whitmore, L. and B. Wallace, *DICHROWEB, an online server for protein secondary structure analyses from circular dichroism spectroscopic data*. *Nucleic acids research*, 2004. **32**(suppl 2): p. W668-W673.
135. Pelton, J.T. and L.R. McLean, *Spectroscopic methods for analysis of protein secondary structure*. *Anal Biochem*, 2000. **277**(2): p. 167-76.
136. Havlikova, M., et al., *Fluorone dyes have binding sites on both cytoplasmic and extracellular domains of Na,K-ATPase*. *Biochim Biophys Acta*, 2013. **1828**(2): p. 568-76.

137. Kubala, M., et al., *Phe(475) and Glu(446) but not Ser(445) participate in ATP-binding to the alpha-subunit of Na(+)/K(+)-ATPase*. *Biochem Biophys Res Commun*, 2002. **297**(1): p. 154-9.
138. Kubala, M., et al., *Protein modeling combined with spectroscopic techniques: an attractive quick alternative to obtain structural information*. *Physiol Res*, 2004. **53 Suppl 1**: p. S187-97.
139. Liu, M. and A. Barth, *TNP-AMP binding to the sarcoplasmic reticulum Ca(2+)-ATPase studied by infrared spectroscopy*. *Biophys J*, 2003. **85**(5): p. 3262-70.
140. Mangialavori, I.C., et al., *Conformational changes produced by ATP binding to the plasma membrane calcium pump*. *J Biol Chem*, 2013. **288**(43): p. 31030-41.
141. Tran, C.M. and R.A. Farley, *Catalytic activity of an isolated domain of Na,K-ATPase expressed in Escherichia coli*. *Biophys J*, 1999. **77**(1): p. 258-66.
142. Vollmecke, C., et al., *Spectroscopic investigation of the reaction mechanism of CopB-B, the catalytic fragment from an archaeal thermophilic ATP-driven heavy metal transporter*. *FEBS J*, 2009. **276**(21): p. 6172-86.
143. Suzuki, H., et al., *Existence of a low-affinity ATP-binding site in the unphosphorylated Ca2(+)-ATPase of sarcoplasmic reticulum vesicles: evidence from binding of 2',3'-O-(2,4,6-trinitrocyclohexadienylidene)-[3H]AMP and -[3H]ATP*. *Biochemistry*, 1990. **29**(30): p. 7040-5.
144. Yatsunyk, L.A. and A.C. Rosenzweig, *Cu(I) binding and transfer by the N terminus of the Wilson disease protein*. *J Biol Chem*, 2007. **282**(12): p. 8622-31.
145. Gonzalez-Guerrero, M., et al., *Structure of the two transmembrane Cu+ transport sites of the Cu+ -ATPases*. *J Biol Chem*, 2008. **283**(44): p. 29753-9.
146. Gonzalez-Guerrero, M. and J.M. Arguello, *Mechanism of Cu+-transporting ATPases: soluble Cu+ chaperones directly transfer Cu+ to transmembrane transport sites*. *Proc Natl Acad Sci U S A*, 2008. **105**(16): p. 5992-7.
147. Owusu-Apenten, R., *Food Protein Analysis: Quantitative Effects On Processing*. 2002: Taylor & Francis.
148. Arguello, J.M. and M. Gonzalez-Guerrero, *Cu+ -ATPases brake system*. *Structure*, 2008. **16**(6): p. 833-4.
149. Allen, G.S., et al., *The architecture of CopA from Archaeoglobus fulgidus studied by cryo-electron microscopy and computational docking*. *Structure*, 2011. **19**(9): p. 1219-32.
150. Hatori, Y., et al., *Intermediate phosphorylation reactions in the mechanism of ATP utilization by the copper ATPase (CopA) of Thermotoga maritima*. *J Biol Chem*, 2008. **283**(33): p. 22541-9.
151. Jayakanthan, S., *Structural and Functional Characterization of the Cytosolic Domains of the Copper Transporting PIB-ATPase CopB from Archaeoglobus fulgidus*, 2011, University of Arizona: Tucson, Arizona. p. 208 leaves.
152. Jayakanthan, S., *Structural and Functional Characterization of the Cytosolic Domains of the Copper Transporting PIB-ATPase CopB from Archaeoglobus fulgidus*. 2011.
153. Locatelli-Hoops, S.C. and A.A. Yeliseev, *Use of Tandem Affinity Chromatography for Purification of Cannabinoid Receptor CB2*, in *Protein Affinity Tags*. 2014, Springer. p. 107-120.
154. Lubben, M., et al., *Structural model of the CopA copper ATPase of Enterococcus hirae based on chemical cross-linking*. *Biometals*, 2009. **22**(2): p. 363-75.
155. Toyoshima, C. and T. Mizutani, *Crystal structure of the calcium pump with a bound ATP analogue*. *Nature*, 2004. **430**(6999): p. 529-35.

156. Tsuda, T. and C. Toyoshima, *Nucleotide recognition by CopA, a Cu<sup>+</sup>-transporting P-type ATPase*. EMBO J, 2009. **28**(12): p. 1782-91.
157. Liu, X., et al., *Roles of interaction between actuator and nucleotide binding domains of sarco(endo)plasmic reticulum Ca<sup>2+</sup>-ATPase as revealed by single and swap mutational analyses of serine 186 and glutamate 439*. J Biol Chem, 2009. **284**(37): p. 25190-8.
158. Sitthisak, S., et al., *Molecular characterization of the copper transport system in Staphylococcus aureus*. Microbiology, 2007. **153**(Pt 12): p. 4274-83.
159. Sazinsky, M.H., et al., *Structure of the actuator domain from the Archaeoglobus fulgidus Cu<sup>+</sup>-ATPase*. Biochemistry, 2006. **45**(33): p. 9949-55.
160. Clausen, J.D., et al., *Glutamate-183 in the conserved TGES motif of domain A of sarcoplasmic reticulum Ca<sup>2+</sup>-ATPase assists in catalysis of E2/E2P partial reactions*. Proc Natl Acad Sci U S A, 2004. **101**(9): p. 2776-81.
161. Anthonisen, A.N., J.D. Clausen, and J.P. Andersen, *Mutational analysis of the conserved TGES loop of sarcoplasmic reticulum Ca<sup>2+</sup>-ATPase*. J Biol Chem, 2006. **281**(42): p. 31572-82.
162. Clarke, D.M., T.W. Loo, and D.H. MacLennan, *Functional consequences of mutations of conserved amino acids in the beta-strand domain of the Ca<sup>2+</sup>-ATPase of sarcoplasmic reticulum*. J Biol Chem, 1990. **265**(24): p. 14088-92.
163. Moller, J.V., B. Juul, and M. le Maire, *Structural organization, ion transport, and energy transduction of P-type ATPases*. Biochim Biophys Acta, 1996. **1286**(1): p. 1-51.
164. Koehorst, R.B., R.B. Spruijt, and M.A. Hemminga, *Site-directed fluorescence labeling of a membrane protein with BADAN: probing protein topology and local environment*. Biophys J, 2008. **94**(10): p. 3945-55.
165. Jurkiewicz, P., et al., *Solvent relaxation in phospholipid bilayers: principles and recent applications*. J Fluoresc, 2005. **15**(6): p. 883-94.
166. Zielazinski, E.L., et al., *Characterization of a cobalt-specific P(1B)-ATPase*. Biochemistry, 2012. **51**(40): p. 7891-900.
167. Villalobo, A., *Reconstitution of ion-motive transport ATPases in artificial lipid membranes*. Biochim Biophys Acta, 1990. **1017**(1): p. 1-48.
168. Rigaud, J.L., B. Pitard, and D. Levy, *Reconstitution of membrane proteins into liposomes: application to energy-transducing membrane proteins*. Biochim Biophys Acta, 1995. **1231**(3): p. 223-46.
169. Knol, J., K. Sjollem, and B. Poolman, *Detergent-mediated reconstitution of membrane proteins*. Biochemistry, 1998. **37**(46): p. 16410-5.
170. Zehnpfennig, B., I.L. Urbatsch, and H.J. Galla, *Functional reconstitution of human ABCC3 into proteoliposomes reveals a transport mechanism with positive cooperativity*. Biochemistry, 2009. **48**(20): p. 4423-30.
171. Portmann, R. and M. Solioz, *Purification and functional reconstitution of the human Wilson copper ATPase, ATP7B*. FEBS Lett, 2005. **579**(17): p. 3589-95.
172. Justesen, B.H., et al., *Active plasma membrane P-type H<sup>+</sup>-ATPase reconstituted into nanodiscs is a monomer*. J Biol Chem, 2013. **288**(37): p. 26419-29.
173. Leviatan, S., et al., *Combinatorial method for overexpression of membrane proteins in Escherichia coli*. J Biol Chem, 2010. **285**(31): p. 23548-56.
174. Rigaud, J.L. and D. Levy, *Reconstitution of membrane proteins into liposomes*. Methods Enzymol, 2003. **372**: p. 65-86.
175. Levy, D., et al., *A systematic study of liposome and proteoliposome reconstitution involving Bio-Bead-mediated Triton X-100 removal*. Biochim Biophys Acta, 1990. **1025**(2): p. 179-90.



- 
176. Knol, J., et al., *Unidirectional reconstitution into detergent-destabilized liposomes of the purified lactose transport system of Streptococcus thermophilus*. J Biol Chem, 1996. **271**(26): p. 15358-66.
  177. Inesi, G., et al., *Functional characterization of reconstituted sarcoplasmic reticulum vesicles*. J Biol Chem, 1983. **258**(24): p. 14804-9.
  178. Jackson, R.L., et al., *Asymmetric incorporation of Na<sup>+</sup>, K<sup>+</sup>-ATPase into phospholipid vesicles*. Arch Biochem Biophys, 1980. **200**(1): p. 269-78.
  179. Levy, D., et al., *Reconstitution of the sarcoplasmic reticulum Ca(2<sup>+</sup>)-ATPase: mechanisms of membrane protein insertion into liposomes during reconstitution procedures involving the use of detergents*. Biochim Biophys Acta, 1992. **1107**(2): p. 283-98.
  180. Gould, G.W., et al., *Uptake of Ca<sup>2+</sup> mediated by the (Ca<sup>2+</sup> + Mg<sup>2+</sup>)-ATPase in reconstituted vesicles*. Biochim Biophys Acta, 1987. **904**(1): p. 36-44.
  181. Abbyad, P., et al., *Measurement of solvation responses at multiple sites in a globular protein*. J Phys Chem B, 2007. **111**(28): p. 8269-76.
  182. Gao, Y.Q., W. Yang, and M. Karplus, *A structure-based model for the synthesis and hydrolysis of ATP by F1-ATPase*. Cell, 2005. **123**(2): p. 195-205.
  183. A, F., J. C., and A. H-J, *Properties of the SR Ca-ATPase in an Open Microsomal Membrane Preparation*. Open Biochem J, 2008. **2**: p. 91-9.
  184. Mahmmoud, Y.A., et al., *Inhibition of K<sup>+</sup> transport through Na<sup>+</sup>, K<sup>+</sup>-ATPase by capsazepine: role of membrane span 10 of the alpha-subunit in the modulation of ion gating*. PLoS One, 2014. **9**(5): p. e96909.
  185. Sotomayor, C.P., et al., *Modulation of pig kidney Na<sup>+</sup>/K<sup>+</sup>-ATPase activity by cholesterol: role of hydration*. Biochemistry, 2000. **39**(35): p. 10928-35.
  186. Amoroso, S., et al., *Photochemical behavior and Na<sup>+</sup>,K<sup>+</sup>-ATPase sensitivity of voltage-sensitive styrylpyridinium fluorescent membrane probes*. Photochem Photobiol, 2006. **82**(2): p. 495-502.
  187. Grycova, L., et al., *ATP and magnesium drive conformational changes of the Na<sup>+</sup>/K<sup>+</sup>-ATPase cytoplasmic headpiece*. Biochim Biophys Acta, 2009. **1788**(5): p. 1081-91.
  188. Autry, J.M., et al., *Nucleotide activation of the Ca-ATPase*. J Biol Chem, 2012. **287**(46): p. 39070-82.

## Versicherung

### Erklärung entsprechend §5.5 der Promotionsordnung

Hiermit versichere ich, dass ich die vorliegende Arbeit ohne unzulässige Hilfe Dritter und ohne Benutzung anderer als der angegebenen Hilfsmittel angefertigt habe; die aus fremden Quellen direkt oder indirekt übernommenen Gedanken sind als solche kenntlich gemacht. Die Arbeit wurde bisher weder im Inland noch im Ausland in gleicher oder ähnlicher Form einer anderen Prüfungsbehörde vorgelegt.

Die Dissertation wurde im Zeitraum von Oktober 2010 bis September 2014 angefertigt und von Prof. Dr. Karim Fahmy, Abteilung Biophysik, Institut für Ressourcenökologie, Helmholtz-Zentrum Dresden-Rossendorf betreut.

Meine Person betreffend erkläre ich hiermit, dass keine früheren erfolglosen Promotionsverfahren stattgefunden haben.

Hiermit erkenne ich die Promotionsordnung der Fakultät Mathematik und Naturwissenschaften der Technischen Universität Dresden.

Datum, Unterschrift

Ahmed Sayed